



Provided by the author(s) and University of Galway in accordance with publisher policies. Please cite the published version when available.

Title	Paralympic tandem cycling and hand-cycling: Computational and wind tunnel analysis of aerodynamic performance
Author(s)	Mannion, Paul
Publication Date	2019-03-27
Publisher	NUI Galway
Item record	http://hdl.handle.net/10379/15064

Downloaded 2024-04-23T15:56:28Z

Some rights reserved. For more information, please see the item record link above.





OÉ Gaillimh
NUI Galway



Paralympic tandem cycling and hand-cycling: Computational and wind tunnel analysis of aerodynamic performance

by

Paul Mannion

B.E.

A thesis presented for the Degree of

Doctor of Philosophy

at

National University of Ireland, Galway

College of Engineering and Informatics, Department of Civil Engineering

and

Eindhoven University of Technology

Department of the Built Environment

2019

Academic Supervisors: Dr. Eoghan Clifford, Dr. Magdalena Hajdukiewicz, Prof. Dr. Bert Blocken, Dr.

Yasin Toparlar

Declaration

I, the undersigned, hereby declare that this thesis, entitled, '*Paralympic tandem cycling and hand-cycling: Computational and wind tunnel analysis of aerodynamic performance*', is entirely my own work. This thesis has been submitted to the National University of Ireland, Galway and Eindhoven University of Technology as part of a dual-degree contract. The research chapters of this thesis have also been submitted to scientific journals for publication. However, this thesis has not been submitted in whole or in part to any other University or Institution outside of NUI Galway and Eindhoven University of Technology. All sources used have been acknowledged and referenced in the text.

Paul Mannion

Acknowledgements

I would sincerely like to thank Dr. Eoghan Clifford and Dr. Magdalena Hajdukiewicz for initiating this project, and for providing me with the opportunity to work in this field of research. I would also like to thank them for their unwavering support, guidance, and boundary-less enthusiasm for my research.

I would like to thank Prof. Bert Blocken for agreeing to supervise me and for including me into his research group. He showed true interest and dedication to this project and pushed me to only ever try and achieve the highest standard and nothing less. I would also like to express my gratitude and thanks to Dr. Thomas Andrienne for contributing his expertise and facilities to the experimental side of this work.

A special word of thanks needs to be provided for Dr. Yasin Toparlar, for his endless patience, whose guidance was nothing less than invaluable, and who helped me to overcome the problems and bottlenecks within this research.

I would like to thank my colleagues Thijs, Fabio and Alessio, whose experience and advice helped to propel my research, and also aided in retaining my focus. I would also like to extend my thanks to Geert-Jan Maas, Stan van Asten, Arjan Wiskerke, and Jan Diepens for their technical support and much loved good humour. To Maryrose, Thijs and Nurul for the many lunch breaks and company throughout the years, I enjoyed every minute. I would like to express my gratitude and thanks to Corentin Cerutti from INSA Lyon for undertaking a master's internship under my research. Furthermore, I would like to thank Thierry Marchal from ANSYS, whose encouragement and enthusiasm for my research was very much appreciated.

I would like to express my thanks to the staff of Cycling Ireland, in particular to Neill Delahaye, Tommy McGowan, and Eoin Murphy, for their encouragement during this research. I would also like to thank para-athlete Declan Slevin for his involvement in this research and his enthusiasm, and Peter Ryan, Sean Hahessey and Ronan Grimes for participating in wind tunnel experiments.

My parents, family, friends and girlfriend Aigera were the last pieces in the puzzle to help me through my PhD. For their unwavering belief in me and their support, I will always be grateful. Mum, for the endless conversations on the research and writing, and Dad, for the technical help and ideas. John, Maria and Clara, for making me feel less alone when I needed somebody on the other end of the phone the most. Aigera, for the never-ending support you always provided.

I would like to thank the College of Engineering and Informatics in NUI Galway and the Department of the Built Environment in TU Eindhoven for supporting this research, my GRC committee Prof. Padraic O'Donoghue and Dr. Stephen Nash, and the staff and my colleagues in NUI Galway and TU Eindhoven for making my experience so enjoyable. I would also like to thank my supervisor from my bachelor's degree final year project, Dr. Nathan Quinlan, who introduced me to both aerodynamics and computational fluid dynamics, and set me on the course needed to acquire my desired career.

Lastly, to my grand-aunt Mary Mannion and my grandmother, Kathleen Mannion. Kathleen (Nana) was one of the greatest sources of joy and happiness in my life growing up and especially in my college years. She was a second mother to me. My grand-aunt Mary held the greatest belief and pride in me, and her kindness and generosity will not be forgotten. This thesis is dedicated to their memories.

Table of contents

Abstract	x
Chapter 1	
Introduction	1
1.1 <i>Cycling and para-cycling aerodynamics background</i>	1
1.2 <i>Research aims</i>	2
1.3 <i>Structure of the thesis</i>	4
1.4 <i>References</i>	5
Chapter 2	
Methods and literature review	6
2.1 <i>Numerical and experimental methodology</i>	6
2.1.1 <i>CFD and its application in cycling</i>	6
2.1.2 <i>Wind tunnel experiments</i>	19
2.2 <i>Literature review</i>	24
2.2.1 <i>Aerodynamics testing methods in the literature</i>	24
2.2.2 <i>Cyclist posture and positioning</i>	32
2.2.3 <i>Cycling equipment</i>	36
2.2.4 <i>Crosswinds</i>	40
2.2.5 <i>Drafting in cycling</i>	41
2.2.6 <i>Hand-cycling and recumbents</i>	46
2.2.7 <i>Tandem cycling</i>	47
2.3 <i>Discussion and conclusions</i>	50
2.3.1 <i>Discussion</i>	50
2.3.2 <i>Conclusions</i>	51
2.3.3 <i>References</i>	52

Part I: Tandem cycling

Chapter 3

Improving CFD prediction of drag on Paralympic tandem athletes: influence of grid resolution and turbulence model 63

- 3.1 Introduction..... 64*
- 3.2 CFD simulations - initial findings..... 65*
 - 3.2.1 Computational parameters 65
 - 3.2.2 Drag findings 69
- 3.3 Wind tunnel experiments 72*
 - 3.3.1 Experimental setup..... 72
 - 3.3.2 Experimental results..... 74
- 3.4 Impact of grid resolution and turbulence model on tandem drag 74*
 - 3.4.1 Computational settings 74
 - 3.4.2 Results 75
- 3.5 Discussion 81*
- 3.6 Conclusions 83*
- 3.7 References 83*

Chapter 4

On the effects of crosswinds in tandem aerodynamics: an experimental and computational study 87

- 4.1 Introduction..... 88*
- 4.2 Wind tunnel experiments 90*
 - 4.2.1 Experimental setup..... 90
 - 4.2.2 Results from the wind tunnel experiments 92
- 4.3 CFD simulations: Validation study 94*
 - 4.3.1 Computational grid and boundary conditions 94
 - 4.3.2 Solver settings 97
 - 4.3.3 Turbulence model study 97
 - 4.3.4 Validation study 99
- 4.4 CFD simulations: Aerodynamic analysis of crosswind conditions 102*
 - 4.4.1 Computational settings 102
 - 4.4.2 Crosswind force predictions 104
- 4.5 Discussion 106*

4.6 Conclusions.....	110
4.7 References.....	111

Chapter 5

Aerodynamic drag in competitive tandem para-cycling: road race versus time-trial positions115

5.1 Introduction	116
5.2 Wind tunnel experiments.....	118
5.3 Validation study.....	120
5.3.1 Computational domain and boundary conditions	120
5.3.2 Computational grid.....	121
5.3.3 Governing equations & solver settings.....	122
5.3.4 Comparison of results with wind tunnel experiments.....	123
5.4 Comparison of tandem setup variations	124
5.4.1 Geometrical models.....	124
5.4.2 Simulation settings and parameters	125
5.4.3 Aerodynamic analysis of different setups.....	126
5.5 Discussion.....	130
5.5.1 Evaluation of the numerical findings.....	130
5.5.2 Comparison with prior research.....	131
5.5.3 Limitations and future perspectives.....	134
5.6 Conclusions.....	135
5.7 References.....	136

Chapter 6

Impact of pilot and stoker torso angles in tandem para-cycling aerodynamics139

6.1 Introduction	140
6.2 Numerical methodology.....	141
6.2.1 Tandem geometrical models.....	141
6.2.2 Validation studies	142
6.2.3 Boundary conditions.....	143
6.2.4 Numerical parameters.....	143
6.2.5 Numerical grid.....	144
6.3 Results.....	145
6.4 Discussion.....	149

6.5 Conclusions	152
6.6 References	153

Part II: Hand-cycling

Chapter 7

CFD analysis of hand-cycle aerodynamics: turbulence model and grid sensitivity analyses and the impact of wheel selection..... 158

7.1 Introduction.....	159
7.2 Wind tunnel experiments	161
7.3 CFD simulations: validation study and sensitivity analysis	163
7.3.1 Geometry and boundary conditions	163
7.3.2 Computational settings.....	164
7.3.3 Computational grid and grid convergence study.....	164
7.3.4 Turbulence model sensitivity	166
7.4 CFD simulations: analysis of hand-cycle aerodynamics	168
7.4.1 Wheel geometries.....	168
7.4.2 Aerodynamics investigations	169
7.4.3 Impact of wheel diameter.....	172
7.5 Discussion	175
7.6 Conclusions	176
7.7 References	177

Chapter 8

Analysis of crosswind aerodynamics for competitive hand-cycling

8.1 Introduction.....	182
8.2 Wind tunnel experiments	183
8.3 CFD simulations	185
8.3.1 Computational domain and boundary conditions.....	185
8.3.2 Solver settings	186
8.3.3 Computational grid	186
8.4 Results	189
8.4.1 Validation study	189

8.4.2 Crosswind aerodynamics	191
8.4.3 Breakdown of forces	196
8.5 Discussion	197
8.6 Conclusion	198
8.7 References	199

Chapter 9

Aerodynamics analysis of wheel configurations in Paralympic hand-cycling: a computational study .202

9.1 Introduction	203
9.2 Simulation setups	205
9.2.1 Geometrical models	205
9.2.2 Boundary conditions and solver settings	207
9.2.3 Computational grids	209
9.3 Validation studies	213
9.3.1 Isolated rotating wheels	213
9.3.2 Hand-cycle validation studies	217
9.4 Results	219
9.4.1 Rear wheel spacing	220
9.4.2 Crosswinds investigation	223
9.5 Discussion	228
9.6 Conclusions	231
9.7 References	232

Chapter 10

The impact of arm-crank position on the drag of a Paralympic hand-cyclist237

10.1 Introduction	238
10.2 Validation of CFD simulations with wind tunnel data.....	240
10.2.1 CFD simulations: Settings and parameters	240
10.2.2 Wind tunnel experiments and comparison with CFD results	244
10.3 Results	246
10.4 Discussion	248
10.5 Conclusion	251

10.6 References 252

Chapter 11

Discussion and future perspectives..... 255

11.1 Discussion 255

11.2 Future perspectives 261

11.3 References 263

Chapter 12

Conclusions..... 265

About the author..... 269

Publications and dissemination 269

Abstract

There are several key resistive forces affecting the speed of cyclists; namely aerodynamic resistance, gravity induced by road gradients, rolling resistance, and drive train and wheel bearing resistances. Of these, in most scenarios, aerodynamic resistance is the leading challenge for cyclists to overcome. Aerodynamic improvements, particularly on flat to rolling terrain, offer the greatest potential for improvements in cycling speed. On flat roads, descents and inclines of up to about 5%, air resistance is the single biggest force a cyclist must overcome. For example, at speeds in excess of 50 km/h on flat terrain the aerodynamic resistance is up to 90% of the total resistance experienced by the cyclist. The power to overcome aerodynamic resistance acting on a body is proportional to the cube of speed, meaning small increases in speed require significant increases in power.

Para-cycling (competitive cycling for people with physical disabilities) has not experienced the same level of aerodynamics research that has been invested in able-bodied cycling. However, Para-athletes compete at the highest level of sporting events in the Paralympics and world championships. There is a diverse range of cycling categories within competitive Para-cycling, including hand-cycling, tricycle, tandem and traditional cycling (with a standard bicycle). Within each category there are additional sub-categories for different disability types which minimise the impact of impairment on the result of the competition. Para-cyclists can reach the velocities typically achieved by able-bodied cyclists, and in the case of hand-cyclists during a hill descent, they can exceed the velocities capable by able-bodied cyclists. Thus, aerodynamics play an important role in para-cycling, and is a key area for performance optimisation.

This research focused on the aerodynamics of tandem cycling and hand-cycling (classes H1-H4) within the competitive UCI Para-cycling categories and uses computational fluid dynamics simulations for the aerodynamics analysis, supported by wind tunnel tests on reduced-scale models. A tandem cycling setup is composed of a sighted (pilot) and a visually impaired (stoker) athlete competing on a tandem bicycle. Aerodynamic equipment for tandem cycling is largely derived from traditional able-bodied cycling; including helmets, skinsuits and wheels. Cycling aerodynamics is typically considered to be a bluff body aerodynamics problem, and tandem cycling presents a unique case in cycling with two bluff bodies in close proximity to each other. Parallels can be drawn to two solo cyclists drafting, but the aerodynamics of tandem cycling has not been explored in the literature prior to this research. Hand-cycling differs from traditional able-bodied cycling to a greater degree than tandem cycling. Within the H1-H4 competition classes, the athletes adopt a recumbent position on the hand-cycle and provide propulsion power with their arms.

A key output of this research includes mapping the influence of the near-wall grid resolution, and Reynolds-Averaged Navier-Stokes turbulence modelling for tandem cycling and hand-cycling. It was found that there was no single turbulence model suitable for tandem cycling, with the SST $k-\omega$ turbulence model found to be most suitable for yaw angles of 0° and 5° , and the $k-kl-\omega$ turbulence model for 10° , 15° and 20° yaw. Tandem-cycling also exhibited a dependence on the near-wall grid resolution, with counter-intuitive and incorrect flow occurrences at y^* values exceeding 30. The locations for flow separation were incorrectly predicted if parameters outside of the aforementioned grid requirements and turbulence model were used, inferred by the incorrect drag predictions where the stoker experienced a larger drag than the pilot. Road race and time-trial setups for competitive race events were investigated to determine aerodynamic benefits associated with unique tandem setups such as the so-called ‘frame-clench’ time-trial position. In addition, the aerodynamic interaction between the pilot and the stoker athletes was explored by considering the drag of each athlete with respect to a solo cyclist in equivalent positions. It was found that the pilot and stoker can experience up to 92.7% and 47.8%, respectively, of the drag of an equivalent solo cyclist for a standard road race setup. This new knowledge was further expanded upon with torso angle studies and crosswind investigations that broadened the knowledge of the aerodynamic interactions between the pilot and stoker athletes.

Hand-cycling did not exhibit the same pronounced dependencies on grid resolution and turbulence modelling as tandem cycling. However, the SST $k-\omega$ turbulence model coupled with a low y^* grid was found to provide accurate results at 0° yaw and in crosswind conditions. The wheel selection for hand-cycling proved to have the largest impact on the aerodynamic drag. The athlete and frame reside within the vertical profiles of the three wheels utilised by a hand-cyclist, and the three wheels exhibit strong aerodynamic interactions with each other, the athlete, and the hand-cycle frame geometry. 20-inch diameter spoked wheels on the rear axle were found to be more favourable aerodynamically than 26-inch wheels. In addition, a front disk wheel coupled with two rear spoked wheels was found to provide the best combination of low drag and low lateral forces in crosswind conditions; improving stability and aerodynamic performance.

These results were leveraged to develop best practice guidelines for the modelling of hand-cycling and tandem aerodynamics using computational fluid dynamics, supported by reduced-scale wind tunnel experiments to validate the numerical simulations. This research provides knowledge to athletes, coaches, and researchers regarding tandem and hand-cycling aerodynamics, and provides directions to attain improved aerodynamic performances.

Chapter 1

Introduction

1.1 Cycling and para-cycling aerodynamics background

The aerodynamic drag of a cyclist comprises of viscous and form drag. Viscous drag results from skin friction at the surface of cyclists and bicycles, while form drag results from the bluff body shape of the cyclist and bicycle. Elite cyclists and para-cyclists often optimise their cycling positions to reduce their drag by means of wind tunnel testing, computational fluid dynamics, or controlled field tests (e.g. in a velodrome). In many cases, aerodynamic improvements are gained through trial and error. Thus, additional knowledge on the fundamental characteristics of cycling aerodynamics can significantly aid in performance optimisation. Defraeye et al. (2010a) demonstrated that form drag contributes to more than 90% of the drag from the cyclist's body alone, and this can be alleviated by improving pressure recovery on the object of interest. The wake flow from a cyclist can also provide key information on how to reduce the form drag, as the wake flow is a direct product of a cyclist's bluff body. Skin suits can be optimised to reduce both viscous and form drag. Indeed, placing the seams in the clothing in specific locations can transition the surface bound flow from laminar to turbulent early, causing the flow to remain attached to the surface for longer, improving pressure recovery, and thus reducing drag.

Kieffer et al. (2006) highlighted that innovations are often closely protected, with technological advancements often only published after they have become obsolete. As a consequence, they do not always hold a competitive advantage after being released to public knowledge. However, it is evident over the history of cycling that significant performance gains have been made; primarily due to the advancement of technology and the understanding of the underlying physics. For example, a performance improvement index was developed by Haake (2009) to allow for comparison between athletes and for a comparison between sports, where a higher index indicated a greater improvement in the sport. The results for cycling were impressive, with a 221% increase in the performance improvement index in the Union Cycliste Internationale (UCI) one-hour track cycling record (measured by the distance cycled in one hour) over a 111 year period.

Para-cycling is a younger sport than its able-bodied equivalent. Both para-cycling and traditional able-bodied cycling are governed by the UCI. Paralympic cycling has a world cup, world

championships, and Paralympic/Olympic races. Road cycling made its Paralympic debut in 1984, and track cycling appeared in 1996. The first tandem cyclists competed in 1992 (Paralympics, 2018). Athletes with visual impairments (known as the stoker) sit on the rear of the tandem while a second athlete, the pilot, steers the tandem; both athletes provide propulsion power. Hand-cycling was introduced to the Paralympics in 2004 for lower body amputees and paraplegics to compete in road cycling events. There are five classes (H1-H5) (UCI, 2017). Athletes with impairments which affect their co-ordination or balance compete using tricycles within two classes (T1-T2) (UCI, 2017). Athletes with prosthetics, cerebral palsy, or other conditions who can ride a traditional bicycle use modified bicycles within five classes (C1-C5) (UCI, 2017). A class with a lower number (e.g. C1 as opposed to C3) indicates a more severe impediment to the athlete. Aerodynamics influence the outcomes of competitive para-cycling events as it does in able-bodied cycling. Athletes competing using a tricycle or bicycle hold some similarities to able-bodied cycling, where some research (e.g., postures, athlete apparel) from the able-bodied sport is applicable to these Paralympic categories. However, the aerodynamic characteristics for each para-cycling category does not have significant research backing in the literature, and the aerodynamics for tandem cycling and hand-cycling are often not well understood by Paralympic athletes or coaches. The velocities para-cyclists can achieve are in the same range as able-bodied cyclists, and thus, aerodynamics is an equally important consideration in para-cycling as its able-bodied counterpart.

1.2 Research aims

The objective of this research was to conduct an analysis of hand-cycling and tandem cycling aerodynamics, using CFD as the primary research tool and supported by wind tunnel experiments. By providing knowledge focused on the specific disciplines of tandem cycling and hand-cycling, participating athletes, coaches and other researchers can be aided in understanding the typical aerodynamic features and underlying physics. Furthermore, guidelines for reliable CFD modelling of tandem and hand-cycling aerodynamics were developed. Detailed studies were carried out to understand the primary causes of aerodynamic drag and the corresponding drag area ($C_D A$) values associated with typical case studies; thus, assisting in the aerodynamic optimisation of future athletes. $C_D A$ values are typically used to compare aerodynamic drag in the cycling industry instead of the drag coefficient (C_D), due primarily to the difficulty in measuring the frontal area of cyclists. A sub-objective of this research was to bridge the knowledge gap between para-cycling and able-bodied

cycling; specifically, for tandem and hand-cycling. Able-bodied cycling has dominated the cycling aerodynamics research scene (see reviews by Crouch et al. (2017) and Lukes et al. (2005)) with few publications in para-cycling.

This thesis aims to address the following key knowledge gaps in para-cycling aerodynamics, specific to tandem cycling and hand-cycling:

- **Determining computational fluid dynamics (CFD) techniques and parameters required for reliable and accurate simulations.** Existing sensitivity studies for traditional able-bodied cyclists show that turbulence model selection can strongly affect the accuracy of CFD simulations (Defraeye et al., 2010b). Both tandem cycling and hand-cycling differ geometrically from a traditional cyclist, with the impact of turbulence modelling, to date, not yet explored for these para-cycling categories.
- **Determining the influence of crosswinds on the drag and lateral forces experienced by tandem and hand-cyclists.** Crosswinds are a hindrance for both able-bodied and disabled cyclists and are experienced in almost all outdoor events. Given the significantly different geometries involved when compared to solo cyclists, understanding the aerodynamic loads applied to tandem and hand-cyclists under crosswind conditions can help to improve safety, and improve aerodynamic performance to reduce drag.
- **Analysing the impact of athlete postures/positioning on aerodynamic drag.** The posture adopted by an athlete is key to his/her aerodynamic performance, with more extreme low-drag postures being developed in able-bodied cycling in recent years (Blocken et al., 2018). Postures and positioning hold similar importance in para-cycling. For example, tandem cycling contains a large number of possible posture combinations with two athletes on the single bicycle.
- **Analysing the impact of equipment (e.g. wheel choice) on the aerodynamic drag.** Helmet and wheel choice hold importance for tandem and hand-cycling aerodynamics. Wheel choice is expected to hold greater significance for hand-cycling aerodynamics than traditional able-bodied cycling; where three wheels are present for the former opposed to two for the latter. Furthermore, the athlete's body and hand-cycle frame are within the vertical coordinate of the wheels, indicating that the wake flow from the front wheel and interference drag from the two rear wheels may impact the aerodynamic drag.

1.3 Structure of the thesis

The chapters of this thesis are divided into two main parts: (I) tandem cycling aerodynamics, and (II) hand-cycling aerodynamics. A methodology and literature review chapter precede the research chapters. Both part (I) and (II) of this thesis contain four chapters each. Each research chapter is based on papers that are published, under review, or in preparation for submission to leading peer-reviewed scientific journals. The chapters within part (I) and (II) discuss sensitivity analyses to CFD parameters, postures and positioning, and crosswind investigations for competitive tandem and hand-cycling respectively. Figure 1.1 visually illustrates the structure of the thesis and the link between the research aims and each chapter.

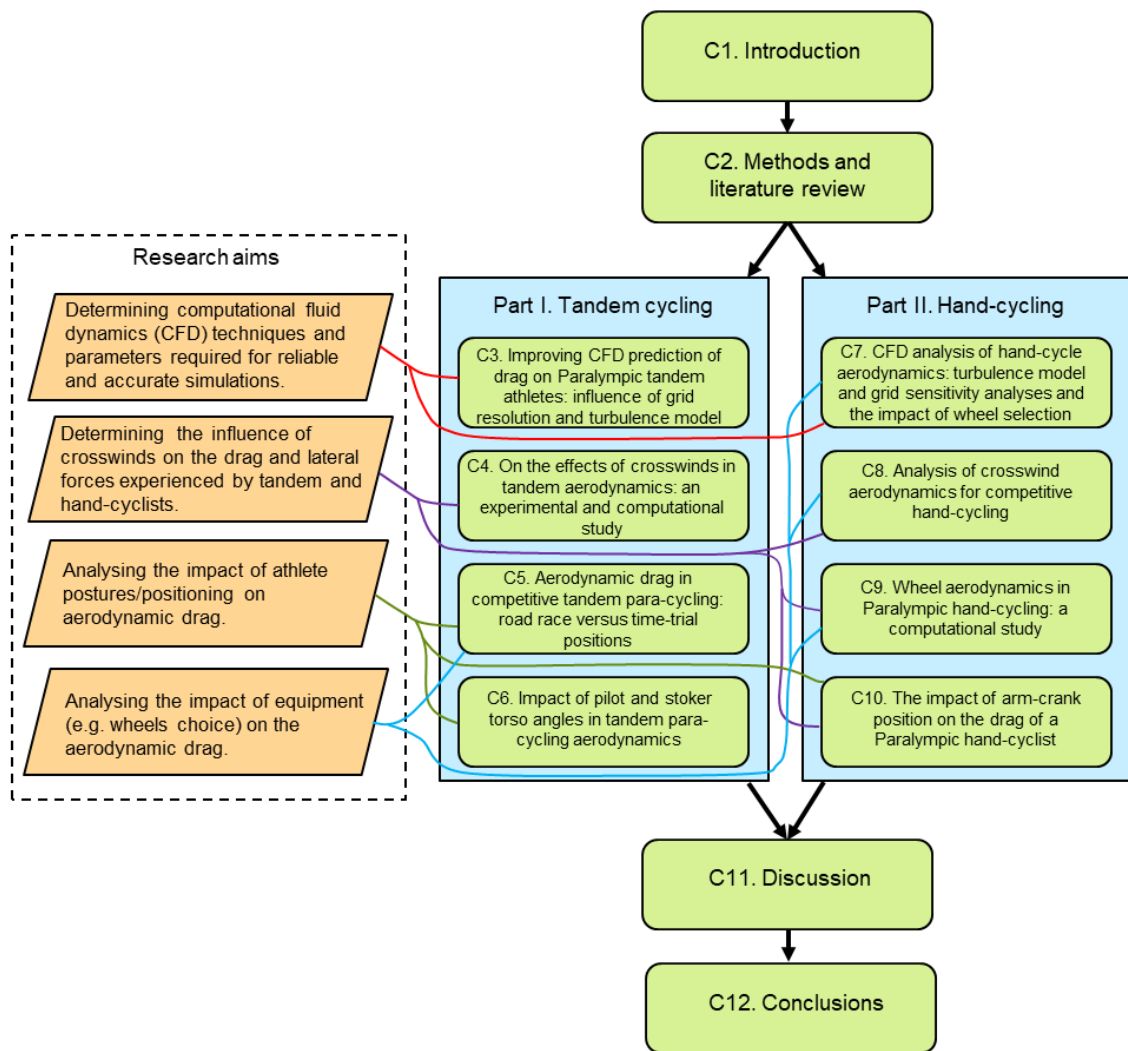


Figure 1.1. A roadmap of the thesis structure and research aims.

1.4 References

- Blocken, B., Druenen, T. Van, Toparlar, Y., Andrienne, T., & Marchal, T. (2018). Numerical analysis of drag of different cyclist positions for hill descent. *Journal of Wind Engineering & Industrial Aerodynamics*, 31(c), 8595. <https://doi.org/10.1016/j.jweia.2018.08.010>
- Crouch, T. N., Burton, D., LaBry, Z. A., & Blair, K. B. (2017). Riding against the wind: a review of competition cycling aerodynamics. *Sports Engineering*, 20(2), 81–110. <https://doi.org/10.1007/s12283-017-0234-1>
- Defraeye, T., Blocken, B., Koninckx, E., Hespel, P., & Carmeliet, J. (2010a). Aerodynamic study of different cyclist positions: CFD analysis and full-scale wind tunnel tests. *Journal of Biomechanics*, 43(7), 1262–1268. <https://doi.org/10.1016/j.jbiomech.2010.01.025>
- Defraeye, T., Blocken, B., Koninckx, E., Hespel, P., & Carmeliet, J. (2010b). Computational fluid dynamics analysis of cyclist aerodynamics: Performance of different turbulence-modelling and boundary-layer modelling approaches. *Journal of Biomechanics*, 43(12), 2281–2287. <https://doi.org/10.1016/j.jbiomech.2010.04.038>
- Haake, S. J. (2009). The impact of technology on sporting performance in Olympic sports. *Journal of Sports Sciences*, 27(13), 1421–1431. <https://doi.org/10.1080/02640410903062019>
- Kieffer, W., Moujaes, S., & Armbya, N. (2006). CFD study of section characteristics of Formula Mazda race car wings. *Mathematical and Computer Modelling*, 43(11–12), 1275–1287. <https://doi.org/10.1016/j.mcm.2005.03.011>
- Lukes, R. a, Chin, S. B., & Haake, S. J. (2005). The understanding and development of cycling aerodynamics. *Sports Engineering*, 8, 59–74. <https://doi.org/10.1007/BF02844004>
- Paralympics. (2018). Para-cycling: A brief history of the sport. Retrieved April 12, 2018, from <https://www.paralympic.org/news/para-cycling-brief-history-sport>
- UCI. (2017). Cycling Regulations, Part 16 Para-Cycling, version on 01/02/2017. Union Cycliste Internationale. Retrieved from http://www.uci.ch/mm/Document/News/Rulesandregulation/16/26/73/16-PAR-20170201-E_English.PDF

Methods and literature review

This chapter is divided into two parts: the methods used for this research and a literature review. The former details the primary techniques for the numerical and experimental approaches. The approaches to geometrical modelling are discussed, which was an important step bridging the applicability of CFD simulations from simplified geometries to those accurately representing the unique features of athletes. The governing equations for the numerical approaches applied in this study are discussed, and finally, the details of the wind tunnel facilities and experimental setups used in this research are explained.

The second part of this chapter discusses the literature in relation to cycling and para-cycling aerodynamics. New innovations in aerodynamics testing are highlighted that are significant for the future of optimising cycling aerodynamics. In addition, a concise summary is presented of previous and state of the art research in the field of cycling and para-cycling aerodynamics. Key discussion points include athlete postures and positioning, cycling equipment, crosswinds and drafting.

2.1 Numerical and experimental methodology

2.1.1 CFD and its application in cycling

Computational Fluid Dynamics (CFD) refers to the ensemble of techniques for the numerical solution of the governing flow equations or approximate forms of these equations, to provide insights into fluid flow phenomena. The governing equations represent the mathematical expressions of three conservation laws; the conservation of mass, momentum, and energy. CFD application in sports aerodynamics goes back as far as 1992 (Hanna, 2012) and has seen rapid development in the late 20th century and early 21st century, largely thanks to the aeronautical and automotive fields. There are several numerical discretisation approaches applied in CFD, with the Finite Volume Method (FVM) being the most commonly used in modern commercial and open-source codes. As with all modelling approaches, errors can occur with CFD modelling and these include spatial discretisation errors,

temporal discretisation errors, and iterative convergence errors. Physical modelling errors and ‘user’ errors are another source. Best practice guidelines exist to aid in achieving accurate and reliable simulation results. Many of these hold importance for simulating cycling aerodynamics, such as (Blocken, 2015a; Franke et al., 2007; Tominaga et al., 2008). These guidelines include determining the size of the computational domain. A number of factors can be considered here, including the blockage ratio to be less than 3%. Furthermore, the inlet, outer top and lateral boundary conditions of the fluid domain should be a minimum of $5H_{MAX}$ (H_{MAX} is the largest arbitrary height of the geometrical model) from the geometrical model. The outlet boundary condition should be a minimum of $10H_{MAX}$ from the geometrical model. Prismatic grids, 2nd order discretisation schemes, grid convergence studies, time convergence studies, appropriate computational domain boundary conditions, stringent convergence criteria, and appropriate validation studies are among the guidelines also relevant to simulating tandem cycling aerodynamics. Key factors for CFD simulations in cycling aerodynamics include the approximate form of the governing equations such as Reynolds-averaged Navier-Stokes (RANS) or Large-Eddy Simulation (LES), the boundary conditions employed, and spatial and temporal discretisation. Both the LES and Detached-Eddy Simulation (DES) approaches have been used in the literature for cycling aerodynamics applications at a high computational cost (Defraeye et al., 2010; Fintelman et al., 2015a). However, the RANS numerical approach was used for this research for a number of reasons. Firstly, the RANS approach has been successful in the literature for cycling aerodynamics as demonstrated by numerous authors (Blocken et al., 2013; Blocken et al., 2016; Fintelman et al., 2015a; Griffith et al., 2014). Secondly there is a lesser computational expense associated with this approach by comparison to LES/DES, enabling a wider comparative study. Furthermore, this thesis aimed to provide a feasible yet accurate computational methodology, and throughout the early stages of this research it was concluded that when applied with the appropriate settings, RANS can provide sufficiently accurate results. This renders DES/LES as a computationally expensive alternative.

2.1.2.1 Governing equations

Cycling aerodynamics can be described assuming that air is a homogeneous, isotropic and viscous Newtonian fluid. In this thesis, only isothermal and incompressible flow will be considered, at 15°C and 101325 Pa. The motion of such a fluid can be described by mass conservation and momentum conservation in incompressible form (Equations 2.1-2.4), which form a simplified expression of the Navier-Stokes equations. In addition, no body forces such as gravity are considered.

Conservation of mass:

The mass of a system remains constant over time, and is neither created nor destroyed (Ferziger & Peric, 2002; Malalasekera & Versteeg, 2007).

$$\text{div}(\mathbf{u}) = 0 \quad (2.1)$$

where the divergence operator is indicated by *div*, and \mathbf{u} is the instantaneous velocity vector.

Conservation of momentum:

The rate of change of momentum is the equal of the sum of forces acting on the fluid (Ferziger & Peric, 2002; Malalasekera & Versteeg, 2007).

$$\text{X momentum: } \frac{\partial u}{\partial t} + \text{div}(u \mathbf{u}) = -\frac{1}{\rho} \frac{\partial p}{\partial x} + \nu \text{div}(\text{grad } u) \quad (2.2)$$

$$\text{Y momentum: } \frac{\partial v}{\partial t} + \text{div}(v \mathbf{u}) = -\frac{1}{\rho} \frac{\partial p}{\partial y} + \nu \text{div}(\text{grad } v) \quad (2.3)$$

$$\text{Z momentum: } \frac{\partial w}{\partial t} + \text{div}(w \mathbf{u}) = -\frac{1}{\rho} \frac{\partial p}{\partial z} + \nu \text{div}(\text{grad } w) \quad (2.4)$$

where u , v and w are the Cartesian components of the instantaneous velocity vector, t is time, ν is the kinematic viscosity, ρ is the density, p is the instantaneous pressure, and *grad* is the gradient operator.

2.1.2.2 Turbulence modelling

Turbulence occurs at high Reynolds numbers, and is an unsteady three-dimensional viscous phenomenon that can be described as a series of eddies of varying dimensions that interact with each other through time (Ferziger & Peric, 2002). It results from the viscous and inertia momentum terms interacting, and is deemed chaotic (Ferziger & Peric, 2002). Turbulence is diffusive, and highly sought after for enhanced mixing or similar occurrences (Ferziger & Peric, 2002). However, the diffusive nature of turbulence results in thicker boundary layers and shear layers than laminar counterparts. Turbulence is often parameterised by the Reynolds number; the ratio of inertial forces to viscous forces (Malalasekera & Versteeg, 2007). Low Reynolds number flows are dominated by viscous forces, while high Reynolds number flows are dominated by inertia forces. The flow transitions from laminar into turbulent flow as the Reynolds number increases (Malalasekera & Versteeg, 2007). The damping effect of viscosity becomes too small at higher Reynolds numbers to prevent disturbances to the flow from amplifying, and these disturbances grow and interact with neighbouring disturbances, forming a cascade (Malalasekera & Versteeg, 2007). Thus, turbulence is

highly complex and difficult to model, and models are often used that predict the statistical quantities of turbulent flows.

Turbulent flows are generated around bluff bodies such as cyclists and are an important aspect of the flow physics. Solving the Navier-Stokes equations directly, termed Direct Numerical Simulation (DNS), is beyond the reach of computational resources for high-Reynolds number flows, but is applicable for low-Reynolds number flows albeit at a high computational expense. Approaches such as LES and Detached Eddy Simulation (DES) are generally also prohibitively expensive for the complex and high-Reynolds numbers flows in cycling aerodynamics, and thus, the RANS equations are commonly solved for cycling problems. The statistics of the flow are solved for RANS and the Reynolds decomposition is adopted, as described by equations 2.5-2.9: Mean and fluctuating components are separated from the instantaneous velocity vector and instantaneous pressure:

$$u = U + u' \quad (2.5)$$

$$v = V + v' \quad (2.6)$$

$$w = W + w' \quad (2.7)$$

$$\mathbf{u} = \mathbf{U} + \mathbf{u}' \quad (2.8)$$

$$p = P + p' \quad (2.9)$$

where U , V and W are the mean components of their respective Cartesian velocities. u' , v' and w' are the fluctuating components of their respective Cartesian velocities. \mathbf{U} and \mathbf{u}' are the mean and fluctuating components respectively of the instantaneous velocity vector, and P and p' are the mean and fluctuating components respectively of the instantaneous pressure.

By replacing the instantaneous variables in equations 2.1-2.4 by equations 2.5-2.9 and time averaging (or ensemble averaging) of the resulting equations, the following equations 2.10-2.13 are obtained for conservation of mass and momentum, which are the Reynolds averaged Navier-Stokes (RANS) equations:

Conservation of mass:

$$\text{div}(\mathbf{U}) = 0 \quad (2.10)$$

X momentum:

$$\frac{\partial U}{\partial t} + \text{div}(\mathbf{U} \mathbf{U}) = -\frac{1}{\rho} \frac{\partial P}{\partial x} + \nu \text{div}(\text{grad } U) + \frac{1}{\rho} \left[\frac{\partial(-\rho \overline{u'u'})}{\partial x} + \frac{\partial(-\rho \overline{u'v'})}{\partial y} + \frac{\partial(-\rho \overline{u'w'})}{\partial z} \right] \quad (2.11)$$

Y momentum:

$$\frac{\partial V}{\partial t} + \text{div} (V \mathbf{U}) = -\frac{1}{\rho} \frac{\partial P}{\partial y} + \nu \text{div} (\text{grad} V) + \frac{1}{\rho} \left[\frac{\partial(-\rho \overline{u'v'})}{\partial x} + \frac{\partial(-\rho \overline{v'v'})}{\partial y} + \frac{\partial(-\rho \overline{v'w'})}{\partial z} \right] \quad (2.12)$$

Z momentum:

$$\frac{\partial W}{\partial t} + \text{div} (W \mathbf{U}) = -\frac{1}{\rho} \frac{\partial P}{\partial z} + \nu \text{div} (\text{grad} W) + \frac{1}{\rho} \left[\frac{\partial(-\rho \overline{u'w'})}{\partial x} + \frac{\partial(-\rho \overline{v'w'})}{\partial y} + \frac{\partial(-\rho \overline{w'w'})}{\partial z} \right] \quad (2.13)$$

The Reynolds stress matrix (equation 2.14) is composed of the means of the products of the fluctuating components in equations 2.11-2.13.

Reynolds stress matrix:

$$R_e = \begin{bmatrix} \overline{u'u'} & \overline{u'v'} & \overline{u'w'} \\ \overline{u'v'} & \overline{v'v'} & \overline{v'w'} \\ \overline{u'w'} & \overline{v'w'} & \overline{w'w'} \end{bmatrix} \quad (2.14)$$

These fluctuating components (equation 2.14) which represent the influence of turbulence on the mean flow are unknown and hence, equations 2.10 to 2.13 are not a closed set of equations. Turbulence models are thus required for closure. Turbulence models can be identified by their number of extra transport equations, and the models pertinent to this research are discussed below.

Spalart Allmaras

This turbulence model contains a single transport equation (equation 2.15), for turbulent kinematic eddy viscosity (ν). The Spalart-Allmaras turbulence model was developed for aerodynamic flows (Spalart & Allmaras, 1992) as an economical computational model for boundary layers in external aerodynamics. It is suitable for aerofoil applications and provides good performance in boundary layers with adverse pressure gradients. Common industrial use includes application in turbomachinery applications. However, it is difficult to define the length scale for complex geometries and thus the model can be unsuitable for general internal flows. Thus, the Spalart-Allmaras turbulence model is not considered a general-purpose CFD turbulence model (Malalasekera & Versteeg, 2007).

The transport equation for ν (equation 2.15) is:

$$\frac{\partial(\rho v)}{\partial t} + \frac{\partial(\rho v u_i)}{\partial x_j} = G_v + \frac{1}{\sigma_v} \left[\frac{\partial}{\partial x_j} \left\{ (\mu + \rho v) \frac{\partial v}{\partial x_j} \right\} + C_{b2} \rho \left(\frac{\partial v}{\partial x_j} \right)^2 \right] - Y_v + S_v \quad (2.15)$$

where Y_v is the turbulent viscosity destruction, G_v is the turbulent viscosity production, σ_v and C_{b2} are model constants, and S_v is a source term.

Standard k - ε

The standard k - ε turbulence model (Jones & Launder, 1972) solves two transport equations; turbulent kinetic energy (k) and turbulent kinetic energy dissipation rate (ε). The standard k - ε model is only valid for fully turbulent flows, and provides good accuracy for many industrial relevant flows including free-shear layer flows (Malalasekera & Versteeg, 2007). This turbulence model is considered a high-Reynolds number model. However, limitations of the k - ε turbulence model include inferior performance in adverse pressure gradients, no-slip walls and strong curvatures compared to other turbulence models. The k - ε turbulence model requires a two layer approach or wall functions based on the log-law to model near-wall flows, instead of solving the near-wall flow directly. Disproportionate levels of turbulent shear stress lead to the prevention of flow separation on curved walls (Malalasekera & Versteeg, 2007), limiting the usefulness of this turbulence model for some applications within external flow simulation. Furthermore, the k - ε turbulence model predicts high levels of turbulence in stagnation/impingement regions, which can result in excessive heat transfer in reattachment regions (Malalasekera & Versteeg, 2007). The k - ε turbulence model is still a widely used and often validated turbulence model and is categorised as a general-purpose CFD turbulence model (Malalasekera & Versteeg, 2007). Successful predictions in a variety of recirculating flows and thin shear layer flows have been obtained with this model, and it can also perform well in confined flows where Reynolds shear stresses hold importance (Malalasekera & Versteeg, 2007). However, far wake flows, mixing layers, and rotating flows result in less successful predictions, along with other unconfined flows.

The following transport equations are used by the k - ε turbulence model for k (equation 2.16) and ε (equation 2.17) respectively:

$$\frac{\partial(\rho k)}{\partial t} + \frac{\partial(\rho k u_i)}{\partial x_i} = \frac{\partial}{\partial x_j} \left[\left(\mu + \frac{\mu_t}{\sigma_k} \right) \frac{\partial k}{\partial x_j} \right] + G_k + G_b - \rho \varepsilon - Y_M + S_k \quad (2.16)$$

$$\frac{\partial(\rho \varepsilon)}{\partial t} + \frac{\partial(\rho \varepsilon u_i)}{\partial x_i} = \frac{\partial}{\partial x_j} \left[\left(\mu + \frac{\mu_t}{\sigma_\varepsilon} \right) \frac{\partial \varepsilon}{\partial x_j} \right] + C_{1\varepsilon} \frac{\varepsilon}{k} (G_k + C_{3\varepsilon} G_b) - C_{2\varepsilon} \rho \frac{\varepsilon^2}{k} + S_\varepsilon \quad (2.17)$$

where Y_M is the contribution of the fluctuating dilatation in compressible turbulence to the dissipation rate, G_k represents turbulent kinetic energy generation, G_b is the turbulence kinetic energy generation

due to buoyancy, $C_{1\varepsilon}$, $C_{2\varepsilon}$, and $C_{3\varepsilon}$ are all modal constants, σ_ε and σ_k are the respective turbulent Prandtl numbers for ε and k , S_ε and S_k are both source terms defined by the user, and μ_t is the dynamic eddy viscosity.

Standard k - ω

The standard k - ω turbulence model (Wilcox, 1993) also solves two transport equations; the turbulence kinetic energy (k) and the specific dissipation rate (ω). This turbulence model is considered a low-Reynolds number model and can be integrated through the viscous sublayer. It does not require the application of wall-damping functions in low Reynolds number flows. However, this model may not provide reliable predictions for flows outside of the shear layer (free-shear flows) (Menter, 2009). This turbulence model can be useful for external aerodynamics applications but free-stream flows exhibit a dependency on the assumed non-zero free-stream value of ω applied at inlet boundaries. A typical application where the standard k - ω turbulence model provides superior performance than many other turbulence models is the flow over a backward-facing step (Malalasekera & Versteeg, 2007).

The following transport equations are used by the k - ω turbulence model for k (equation 2.18) and ω (equation 2.19) respectively:

$$\frac{\partial(\rho k)}{\partial t} + \frac{\partial(\rho k u_i)}{\partial x_i} = \frac{\partial}{\partial x_j} \left[\Gamma_k \frac{\partial k}{\partial x_j} \right] + G_k - Y_k + S_k \quad (2.18)$$

$$\frac{\partial(\rho \omega)}{\partial t} + \frac{\partial(\rho \omega u_i)}{\partial x_i} = \frac{\partial}{\partial x_j} \left[\Gamma_\omega \frac{\partial \omega}{\partial x_j} \right] + G_\omega - Y_\omega + S_\omega \quad (2.19)$$

where S_ω and S_k are source terms, Y_ω and Y_k characterise the dissipation of ω and k respectively due to turbulence, G_ω is ω generation and G_k is k generation from mean velocity gradients, and Γ_ω and Γ_k characterise the effective diffusivities of ω and k , respectively.

Shear Stress Transport k - ω

The Shear Stress Transport (SST) k - ω turbulence model is a hybrid model where the k - ε model is used in the fully turbulent region far from wall bounded flows, and the k - ω model is used for the near-wall region (Menter, 1994). Blending functions are used to attain smooth transitions between both models where numerical instabilities may arise. The k equation remains the same as in

the k - ω model (equation 2.18) throughout the SST model. The ε equation transforms into an ω equation through the $\varepsilon = k\omega$ relationship. The SST k - ω model accounts for the transport of turbulent shear stress through its definition of turbulent viscosity (Menter, 1994). In addition, the SST k - ω model contains the refinements of the baseline (BSL) k - ω model (not described in this thesis), which features a damped cross-diffusion derivative term in the ω equation and refined model constants. As a result of these features, the SST k - ω model is more reliable than the standard k - ω and BSL k - ω models for a wider range of flows including adverse pressure gradient flows and transonic shock waves. Thus, the SST k - ω model is commonly used as a general-purpose model, and has seen significant use in aerospace and external aerodynamics applications (Malalasekera & Versteeg, 2007).

The following transport equations are used by the SST k - ω turbulence model for k (equation 2.20) and ω (equation 2.21) respectively:

$$\frac{\partial(\rho k)}{\partial t} + \frac{\partial(\rho k u_i)}{\partial x_i} = \frac{\partial}{\partial x_j} \left[\Gamma_k \frac{\partial k}{\partial x_j} \right] + G_k - Y_k + S_k \quad (2.20)$$

$$\frac{\partial(\rho \omega)}{\partial t} + \frac{\partial(\rho \omega u_i)}{\partial x_i} = \frac{\partial}{\partial x_j} \left[\Gamma_\omega \frac{\partial \omega}{\partial x_j} \right] + G_\omega - Y_\omega + D_\omega + S_\omega \quad (2.21)$$

where D_ω characterises the cross-diffusion term.

The transport behaviour of the turbulent shear stress is attained by a limiter to the formulation of the eddy-viscosity:

$$\mu_t = \frac{\rho k}{\omega} \left(\frac{1}{\max\left[\frac{1}{\alpha^*}, \frac{SF}{\alpha_1 \omega}\right]} \right) \quad (2.22)$$

where S is the magnitude of the strain rate, α^* is turbulent viscosity damping coefficient, and F is a blending function.

Transition SST k - ω

The transition SST k - ω (T-SST) turbulence model is a 4-equation model adding two additional transport equations to the SST k - ω turbulence (Menter et al., 2006); the intermittency transport equation (γ) and the transition momentum thickness Reynolds number transport equation ($R\tilde{e}_{\theta t}$), the latter of which determines the criteria for the onset of transition. This model is applicable

for modelling transition from laminar flow to turbulent flow in wall bounded flows only, and predicts free-stream flows as fully turbulent. The application for the transition SST k - ω turbulence model focuses on classical boundary layer flows with non-zero free-stream velocities. This, this model is not suitable for fully developed pipe or channel flows however, where no free-stream velocity is present (Fluent, 2017). An advantage of this turbulence model is its wall roughness correlation modification possible with $R\tilde{e}_{\theta t}$ which is not possible with other low-Reynolds number turbulence models.

The transport equations for γ (equation 2.23) and $R\tilde{e}_{\theta t}$ (equation 2.24) are as follows:

$$\frac{\partial(\rho\gamma)}{\partial t} + \frac{\partial(\rho\gamma u_j)}{\partial x_j} = \frac{\partial}{\partial x_j} \left[\left(\mu + \frac{\mu_t}{\sigma_\gamma} \right) \frac{\partial \gamma}{\partial x_j} \right] + P_{\gamma 1} - E_{\gamma 1} + P_{\gamma 2} - E_{\gamma 2} \quad (2.23)$$

$$\frac{\partial(\rho R\tilde{e}_{\theta t})}{\partial t} + \frac{\partial(\rho R\tilde{e}_{\theta t} u_j)}{\partial x_j} = \frac{\partial}{\partial x_j} \left[\sigma_{\theta t} (\mu + \mu_t) \frac{\partial R\tilde{e}_{\theta t}}{\partial x_j} \right] + P_{\theta t} \quad (2.24)$$

where $P_{\gamma 1}$ and $E_{\gamma 1}$ are transmission sources, $P_{\gamma 2}$ and $E_{\gamma 2}$ are destruction/re-laminarization sources, $P_{\theta t}$ is a source term, and $\sigma_{\theta t}$ is a model constant.

k-kl- ω

The k - kl - ω turbulence model is a 3-equation model that can be used to predict the onset of transition from laminar to turbulent in boundary layer flows (Walters & Cokljat, 2008). The application area of this turbulence model is similar to that of the T-SST turbulence model; boundary layer flows and external aerodynamics applications. Due to the recent development of this model, there is still little information available regarding its applications and limitations. The transport equations are turbulent kinetic energy (k_T), laminar kinetic energy (k_L) and inverse turbulent time scale (ω). The transport equations k_T (equation 2.25), k_L (equation 2.26) and ω (equation 2.27) are described as:

$$\frac{Dk_T}{Dt} = P_{K_T} + R + R_{NAT} - \omega k_T - D_T + \frac{\partial}{\partial x_j} \left[\left(\nu + \frac{\alpha_T}{\alpha_k} \right) \frac{\partial k_T}{\partial x_j} \right] \quad (2.25)$$

$$\frac{Dk_L}{Dt} = P_{K_L} - R - R_{NAT} - D_L + \frac{\partial}{\partial x_j} \left[\nu \frac{\partial k_L}{\partial x_j} \right] \quad (2.26)$$

$$\frac{D\omega}{Dt} = C_{\omega 1} P_{K_L} \left(\frac{\omega}{k_T} \right) + \left(\frac{C_{\omega R}}{f_W} - 1 \right) (R + R_{NAT}) \left(\frac{\omega}{k_T} \right) - C_{\omega 2} \omega^2 + C_{\omega 3} f_\omega \alpha_T f_W^2 \left(\frac{\sqrt{k_T}}{d^3} \right) + \frac{\partial}{\partial x_j} \left[\left(\nu + \frac{\alpha_T}{\alpha_\omega} \right) \frac{\partial \omega}{\partial x_j} \right] \quad (2.27)$$

where R is the averaged effect of the breakdown of the stream-wise fluctuations to turbulence during transition, R_{NAT} is the natural transition production, f_ω is intermittency damping term, f_W is the ratio of effective length scale to turbulent length scale, α_T is the turbulent scalar diffusivity, $C_{\omega 1}$, $C_{\omega 2}$, $C_{\omega 3}$ and $C_{\omega R}$ are model constants, D_T and D_L are the near-wall dissipation terms for turbulent and laminar flow respectively, and P_{K_T} and P_{K_L} are the production of turbulent and laminar kinetic energy respectively.

2.1.2.3 Near-wall modelling

Accurate representations of near-wall flow are important for accurate aerodynamic predictions using CFD. The near-wall region of a turbulent boundary layer can be divided into three layers (Figure 2.1). The first layer in proximity to the wall is the viscous sublayer, where the flow is almost laminar and molecular viscosity has a dominant role in momentum, heat and mass transport. A buffer layer exists after the viscous sublayer, where viscous and turbulent effects are equally important. A log-law region separates the buffer layer and the outermost layer, where turbulence has the dominant role. The extent of the outermost layer is dependent on the Reynolds number.

The refinement level of a grid relative to the boundary layer flow can be identified through the non-dimensional wall distance y^+ (equation 2.28), or alternatively, y^* (equation 2.30). The y^+ values associated with the viscous sublayer, buffer layer, and logarithmic layer are identified in Figure 2.1. A y^+ or y^* of the first cell in the region of 1-5 is typically required to resolve the viscous sublayer. While both the y^+ and y^* parameters generally provide approximately equal values, y^* is used within this research instead of y^+ . As observed by Blocken & Toparlar (2015), the formulation for y^* holds an advantage over y^+ for cycling aerodynamics applications as y^* does not get calculated as zero if the shear stress is zero (e.g. locations of flow stagnation and flow reattachment which occur in cycling aerodynamics) and thus can be used to specify the grid requirements also in these locations.

Equation 2.28: Non-dimensional wall distance y^+_p for wall-bounded flow at a first cell height with centre point P:

$$y^+_p = \frac{u_\tau y_p}{\nu} \quad (2.28)$$

where ν is the local kinematic viscosity and y_p is the normal distance from the wall to the centre point P of the first cell at the wall surface. u_τ is the friction velocity, defined by:

$$u_\tau = \sqrt{\frac{\tau_w}{\rho}} \quad (2.29)$$

where ρ is the density of the fluid in the wall bounded flow, and τ_w is the wall shear stress.

Equation 2.30: Non-dimensional wall distance y^*_P for wall-bounded flow at a first cell height with centre point P:

$$y^*_P = \frac{u^* y_P}{\nu} \quad (2.30)$$

The friction velocity u^* is defined as:

$$u^* = C_\mu^{\frac{1}{4}} k_P^{\frac{1}{2}} \quad (2.31)$$

where C_μ is a model constant, and k_P is the turbulent kinetic energy at P. P is the centre point of the first cell at the wall surface.

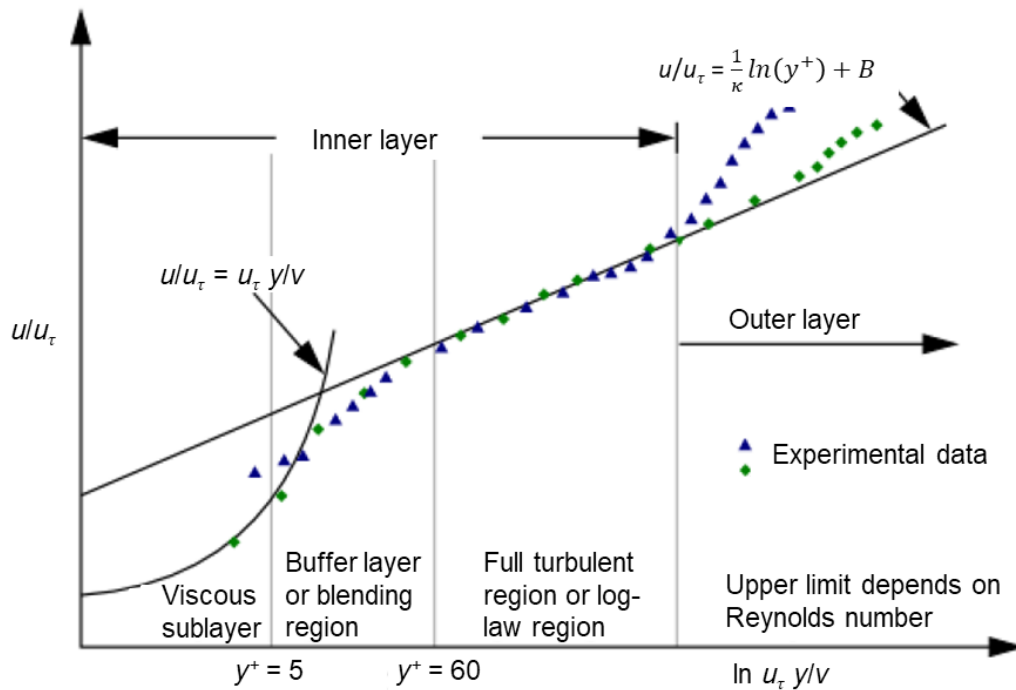


Figure 2.1. An illustration of the y^+ value associated with the different layers of wall bounded flow. Figure from (Fluent, 2015).

There are two traditional methods for modelling the flow in near-wall regions, termed ‘wall functions’ and ‘Low Reynolds Number Modelling’ (LRNM). The LRNM method allows the viscosity affected layers at the wall to be resolved, but, requires an appropriate high-resolution grid. The quality of the numerical results for the wall bounded flow is directly dependent on the grid resolution. For

good grid quality, prism layers are required with unstructured grids, with a recommended y^* of 1 to place the cell centre height (y_p) of the first prism layer within the viscous sublayer (Tucker & Mosquera, 2001). The growth ratio of the cells from the wall surface is also an important factor for resolving the near-wall flow. Typically, a growth ratio of 1.2 or less is recommended for low-Reynolds number turbulence models (Tucker & Mosquera, 2001). In addition, inappropriate grid resolution can confine the growth of the boundary layer, and it is recommended that the height of the total number of prism layers, normal to the wall, should be greater than the height of the boundary layer.

Wall functions do not resolve the viscous sublayer and the buffer layer, but instead employ semi-empirical formulas to bridge the viscosity affected layers. The standard wall functions by Launder & Spalding (1974) use the log law of the wall to describe mean velocity (equation 2.32). However, wall functions are strictly only suitable between y^* ranges of about 30 to about 300, and numerical results deteriorate for highly refined near-wall grids with y^* values less than 15. In addition, wall functions can be unreliable for flows with large pressure gradients that lead to boundary layer separation. Figure 2.2 illustrates the difference in grid requirements for both the LRMN and wall function methods.

The log law of the wall for mean velocity is described as:

$$U^+ = \frac{1}{\kappa} \ln(y^+) + B \quad (2.32)$$

where U^+ is the dimensionless velocity, κ is the von Kármán constant, and B is a constant.

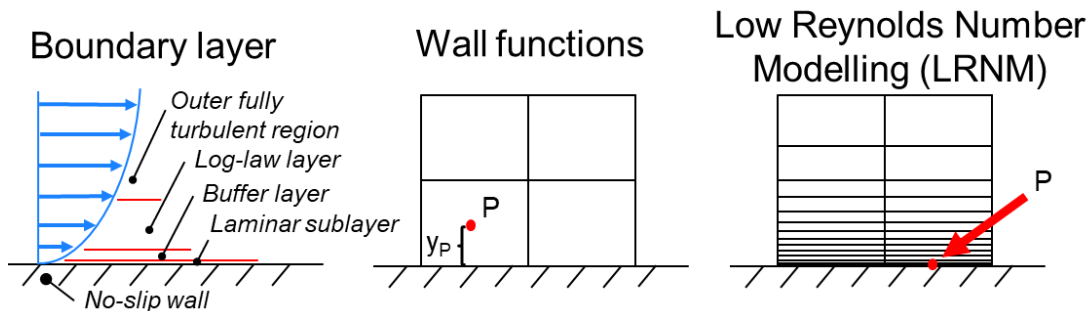


Figure 2.2. An illustration of the grid types for the wall function approach and LRNM approach to boundary layer flow modelling. y_p [m] is the normal distance from the wall to the centre point P of the first cell.

Within ANSYS Fluent (Fluent, 2015), the CFD software utilised for this research, the near-wall modelling method for the $k-\epsilon$ turbulence models combines a two-layer model with so-called ‘enhanced’ wall functions. The two-layer approach subdivides the complete flow domain into a

viscosity affected zone and a fully turbulent zone, determined by a turbulent Reynolds number that is wall distance based. Thus, this model allows for the viscous sublayer to be resolved if the near-wall grid is sufficiently fine ($y^* \approx 1$). The one-equation model by Wolfshtein (Wolfshtein, 1969) is used to solve the flow in the viscosity affected zone. If the grid is not sufficiently refined, the enhanced wall functions blend the logarithmic layer formulation with the laminar formulation. The Spalart-Allmaras model and turbulence models with an ω -equation do not require the two-layer approach of the ε -equation, and can be integrated through the viscosity affected zone all the way down to the wall. The grid resolution again plays an important role, and the viscosity affected zone formulation and the logarithmic layer formulations are blended based on y^* .

Standard wall functions have been used by Fintelman et al. (2015) for able-bodied cycling aerodynamics, and scalable wall functions (Grotjans & Menter, 1998) have been used by Blocken and Toparlar (2015), and Blocken et al. (2016) for cyclist applications in proximity to other road vehicles. However, LRNM was applied in this research as opposed to the wall functions approach, due to the former's accuracy for near-wall flow predictions, despite the complexities of the grid requirements for complex three-dimensional objects (athletes, bicycles) and the associated increase in computational cost resulting from higher total cell counts.

2.1.2.4 Geometric modelling

The geometrical modelling for this research can be separated into two categories; the athletes and the bicycles (both tandem and hand-cycle). The geometries for the athletes and their helmets was acquired via 3D structured light scanning using an Artec Eva scanner (Artec, 2017). The structured light scanner does not use a laser similar to conventional scanners. It projects a grid onto the surface being scanned using light emitting diodes at a typical frequency of 14-15 frames per second and measures the deformation between each point in the grid as it moves over the surface. The Artec Eva is specified to have an accuracy of 0.1 mm (Artec, 2017), which is sufficient for the purposes of athlete scanning. The portability of the hand-held Artec Eva allowed for a complete scan of a cyclist to be acquired in four minutes or less. The native modelling software that accompanied the 3D scanner, Artec Studio, was used to post-process all scans. The surface tessellation density (tessellation is where a surface is meshed using a series of geometric shapes) was reduced in an appropriate manner to ensure that the small geometrical features were captured but to also allow for an export using the stereolithography (.STL) format with a file size acceptable for import into computer aided design (CAD) software. This model was then converted to a standard ACIS text (.SAT) format to create a solid body useable for conventional 3D CAD modelling methods. The quality of the cells from the

.STL file is low as the cells are highly skewed, and hence unsuitable to be directly used for CFD calculations.

There were two athletes in this research. Informed consent was provided by both athletes prior to 3D scanning. For the tandem studies, a volunteer was 3D scanned in an aggressive drops (crouched) position, an upright position, and a time-trial (TT) position. A Bontrager Ballista road helmet was used for the crouched and upright positions, and a standard tear-drop TT helmet was used for the TT position. A H3 class hand-cyclist was 3D scanned along with his hand-cycle (TopEnd brand) at four different arm-crank positions. Two helmets were also scanned with the hand-cyclist; a Kelly road helmet and a Casco TT helmet.

The bicycle frames and wheels for the tandem and solo bicycles used in this research were modelled in CAD software (Autodesk Inventor) and were designed as generic wheel shapes that were not based on any particular brand, unless where stated otherwise for the Zipp 404 and Zipp Sub9 wheels. The bicycle and athlete geometries were combined in Autodesk Inventor, after which they were imported to ANSYS Design Modeller for CFD pre-processing.

2.1.2 Wind tunnel experiments

Wind tunnel experiments are the traditional method for cycling aerodynamics research, with the first experiments (to the best of the author's knowledge) dating back to the 1970s, as mentioned by Zdravkovich (1992). Wind tunnel experiments are also a reliable method for validating Computational Fluid Dynamics (CFD) simulations and can themselves be considered a simulation. The flow conditions in a wind tunnel are controlled and are not always fully representative of the wind conditions found in the outdoor or indoor environments that competitive cyclists are competing in. However, the control over the flow conditions in a wind tunnel allows for repeatability which cannot be attained in outdoor environments. There are two primary types of wind tunnels; open circuit and closed circuit. A closed-circuit wind tunnel (see example Figure 2.3) utilises turning vanes in the corners to aid in recirculating the flow to reduce operating costs. An open circuit wind tunnel is cheaper to construct but is sensitive to the ambient conditions with higher operating costs. This research utilised a closed-circuit wind tunnel for all experiments.

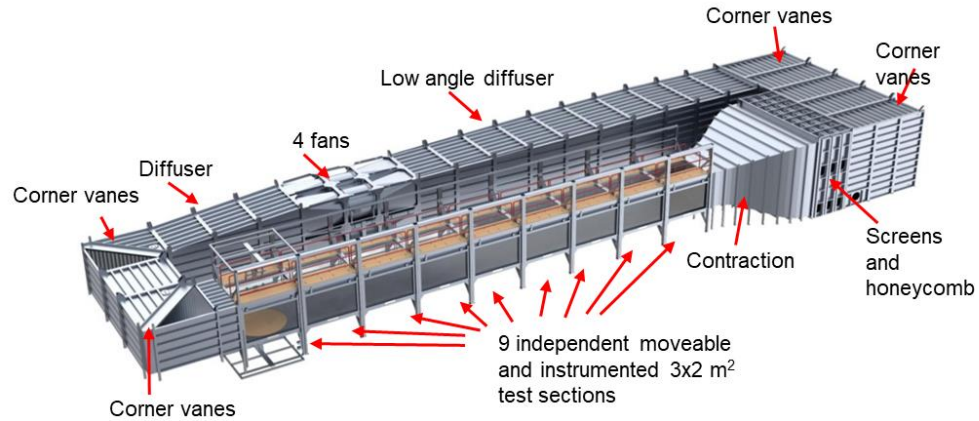


Figure 2.3. An example of a closed-circuit atmospheric boundary layer wind tunnel. © Eindhoven University of Technology.

Experiments were conducted at the University of Liège using quarter-scale tandem and hand-cycling geometries. The aeronautical test section measured (in cross-section) 2 m wide x 1.5 m high (i.e. 3 m²). Geometric similarity between the wind tunnel geometry and the digital geometry was maintained, with both geometries derived from a single model. Dynamic similarity is required to match the aerodynamic force values of the quarter-scale wind tunnel geometries with full-scale counterparts. This can be achieved through Reynolds number matching. The Reynolds number is described in equation 2.33, and describes the nature of the flow (laminar-transitional-turbulent) through the ratio of inertial forces to viscous forces. To match the Reynolds numbers of the quarter-scale experiments with full-scale velocities, the velocity was required to be four times larger for the experiments. Hence, to replicate the Reynolds number at a competitive cycling velocity of 15 m/s, the air velocity in the test section of the wind tunnel was 60 m/s (216 km/h). Kinematic similarity between experimental and numerical models was maintained by keeping geometric similarity and Reynolds number matching.

$$Re = \frac{\rho VL}{\mu} \quad (2.33)$$

where ρ is density, V is the freestream velocity, L is the characteristic length scale, and μ is the dynamic viscosity.

Another scaling parameter important for aerodynamic forces is the Mach number (M), described in equation 2.34. The Mach number is the ratio of the freestream velocity to the speed of sound. Mach number similarity is important for compressible flows and can be considered for flows with a Mach number greater than 0.3. However, the maximum speed of cyclists occur at a Mach number range where density is near-constant; $< 0.3 M$ (Barlow et al., 1999). At quarter-scale with a

velocity of 60 m/s, the Mach number is 0.175 (dry air at 15°C). Thus, Mach number similarity was not required for these experiments.

$$M = \frac{V}{a} \quad (2.34)$$

where a is the speed of sound.

The geometries for the quarter-scale tandem and hand-cycling models were manufactured using Computer Numerical Control (CNC) milling from acrylonitrile butadiene styrene (ABS) plastic. The minimum size feature allowable for the manufacturing process was 3 mm. Thus, the diameter of the spokes was limited to this size for both the tandem and hand-cycle wheel geometries (equivalent to 12 mm diameter spokes in full-scale). A baseplate connected the para-cycling geometries to the force sensor(s), (Figure 2.4a). The baseplates were manufactured with the para-cycling geometries so that they were a single unit, to which the force sensor could be attached. Support structures were included in the geometries at the intersection of the wheel geometry and the baseplate (Figure 2.4a-c). These structures provided a secure connection between the para-cycling geometries and the baseplate, and added stiffness to the geometries to reduce/remove vibrations when under wind load (216 km/h). The tandem geometry was split into four components, each highlighted using colour in Figure 2.4c. The pilot and the stoker were the primary geometrical components of interest and were isolated from the tandem bicycle. The tandem bicycle was divided into two components, front and rear with a split in the middle of the frame. Dividing the tandem geometry into four components allowed for drag measurements to be obtained from the pilot and stoker individually and simultaneously. The two components of the tandem bicycle were not in contact with the geometry of the pilot or stoker, and did not have their own force sensors for drag or lateral force measurements. Tight fitting sleeves were fitted over the split in the frame tubes that separated the front and rear halves of the tandem geometry. These sleeves were placed to connect the front and rear halves of the tandem frame during the experiments to prevent the ends of the frame tubes from vibrating.

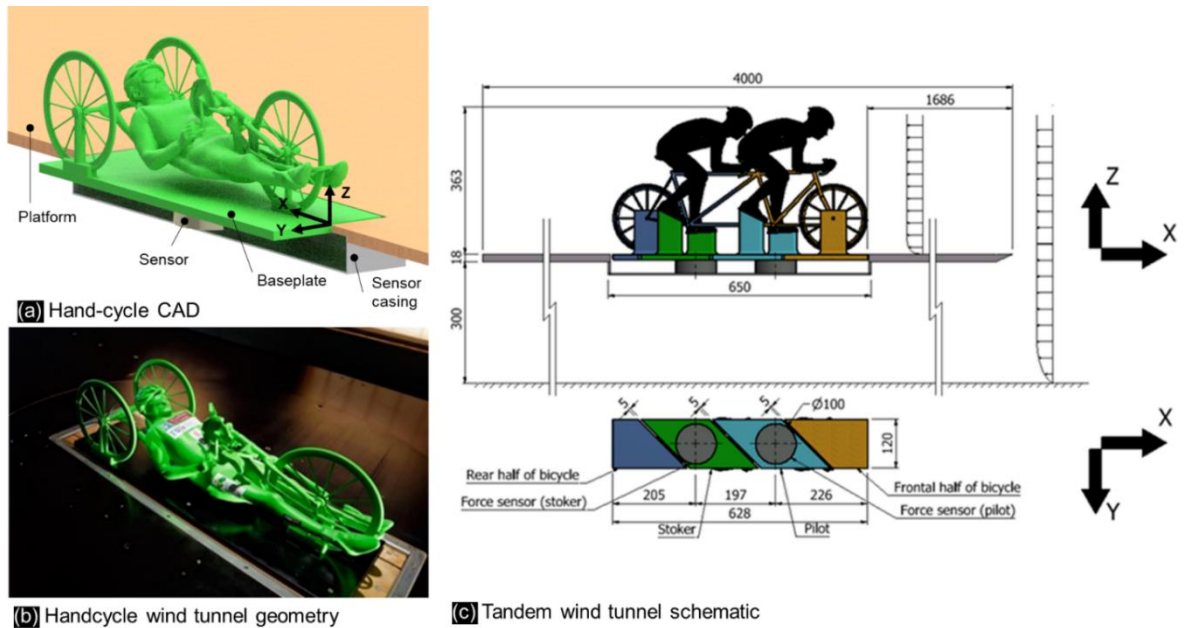


Figure 2.4. (a) CAD representation of quarter-scale hand-cycle wind tunnel setup. (b) Photo of hand-cycle model in the wind tunnel. (c) Schematic of the quarter-scale tandem geometry for wind tunnel experiments. Dimensions are in mm.

The test geometries were placed on a sharp-edged platform raised 0.3 m from the test-bed of the wind tunnel. The purpose of the sharp-edged raised platform was to remove the test geometries from the boundary layer on the test-bed of the wind tunnel. The boundary layer at the bed of the wind tunnel would have impacted the aerodynamic investigations on the quarter-scale para-cyclist geometries. A 60 mm boundary layer was measured on the raised platform, which was determined as small enough to not significantly impact the para-cyclist geometries. Incorporated into the centre of the platform was a rotational plate, to allow for yaw angles to be investigated. A container was built into the rotational plate to which the force sensors could be attached, while removing them from the oncoming airflow. The baseplates of the tandem and hand-cycle geometries were flush with the upper surface of the platform, while the container extruded downwards from the lower surface of the platform (Figure 2.4 a-c).

ATI Delta six-axis force/torque sensors were used for both the tandem and hand-cycle quarter-scale experiments. All sensors were calibrated within 0.75% of the maximum load of 165 N for drag and lateral forces within a 95% confidence interval, resulting in a maximum error range of ± 1.24 N. A single sensor was attached to the baseplate of the hand-cycle geometry. Two sensors were used for the separated geometries of the pilot and stoker for the tandem geometry, providing individual and simultaneous measurements. All sensors were positioned in vertical alignment with the centre of gravity of their respective geometries.

Each force sensor was biased in the wind tunnel with the test geometry in place, prior to imparting any wind load. After the test velocity of 60 m/s had been achieved in the tunnel, a settling period of 30 s was provided before force measurements were recorded for 180 s. The sampling rate was 10 Hz. The temperature inside the test section of the tunnel was recorded to correct the force measurements to 15°C for any fluctuations between the experiments. The velocity in the test section was also recorded using a pitot tube, and corrections were also applied to the force measurements for any velocity fluctuations from the set velocity of 60 m/s. The turbulence intensity of the free-stream air was 0.2%. The settling time period of 30 s at full wind load, and the recorded period of 180 s were acquired from tracking the moving average of the aerodynamic force data. It was determined that the average reading converged after a 30 s initialisation period and that the flow was stable. A period of 180 s for recording purposes was determined to be required to achieve statistically steady-state results. These parameters were also selected in agreement with the successful wind tunnel test campaign from the research by Blocken et al. (2016), who conducted quarter-scale wind tunnel experiments in cycling aerodynamics at the same Reynolds number, and using the same facilities and force transducer. The parameters of the wind tunnel test campaign for this research were based off the learnings from this research.

Corrections for blockage, due to the wind tunnel cross sectional area being too small relative to the frontal area of the test object, must be taken into account for reduced-scale and full-scale experiments where required. Solid blockage is an important parameter for the validity of wind tunnel data (Barlow et al., 1999). The walls of the wind tunnel can compress the streamlines and increase the velocity of the fluid over the test object. This local speed is thus higher than the reference wind tunnel speed causing inaccuracies with aerodynamic force measurements. The blockage ratio (equation 2.35) determines if blockage corrections are required (Maskell, 1965). The blockage ratio is the ratio of the frontal area of all items within the test section, and the cross-section of the test section. Typically, correction is required if the blockage ratio is between 1-10% (Barlow et al., 1999), and experiments with higher blockage ratios are not typically advised. Thorn's short-form equation (Barlow et al., 1999) for solid blockage correction was used for this research and is provided in equation 2.36. A value of 0.96 was used for the form factor 'K' for 3D bodies approximating a body of revolution, e.g. cylinders (Barlow et al., 1999). Solid blockage corrections were only applied where stated in each chapter of this thesis.

$$BR = \frac{A}{C} \tag{2.35}$$

BR is the blockage ratio, A is the frontal area of the model (including plate and support structures if present) and C is the cross-sectional area of the wind tunnel test section.

$$\epsilon_{SB} = \frac{\Delta V}{V} = \frac{KM}{C^2} \quad (2.36)$$

ϵ_{SB} is the velocity correction ratio, ΔV is the velocity correction, V is the uncorrected velocity, K is the form factor, and M is the model volume.

2.2 Literature review

Optimising cycling aerodynamics generally requires wind tunnel testing, computational fluid dynamics or track testing (or a combination thereof). Most of the aerodynamics research in cycling has focused on elite road cycling (road races and time-trials) and track cycling. This is due to the tight margins within these disciplines at the elite level, the significant role played by aerodynamics in both cycling speed and tactics and the economic and media benefits that excellent performances can bring to teams, individual cyclists and sponsors. A number of recent publications have sought to shine light on the complex nature of cycling aerodynamics across a broader cycling community, including both professional and amateur cyclists (Blocken et al., 2018; Blocken et al., 2016; Crouch et al., 2016; Fintelman et al., 2014a). Traditional methods used in the literature for cycling aerodynamics research are discussed in this sub-chapter, along with new innovations. Moreover, advances in aerodynamics knowledge regarding athlete postures and positions, cycling equipment, and cycling tactics are reviewed and discussed.

2.2.1 Aerodynamics testing methods in the literature

2.2.1.1 Wind tunnel testing

Wind tunnel testing as reported in the literature has almost exclusively focused on road cycling and time-trial (TT) cycling for able-bodied athletes. However, other cycling categories, in particular human powered vehicle projects have been subject to experiments as well (Epema et al., 2012). Pressure and force data can be acquired from wind tunnel experiments using pressure taps and

force transducers, respectively. Pressure taps allow for a more complete understanding of the flow over a cyclist if used in sufficient numbers. Defraeye et al. (2010b) utilised pressure taps on a half-scale model of a cyclist to provide a more comprehensive suite of wind tunnel data for the validation of CFD simulations. Pressure coefficients at each point location for the CFD simulations were found to generally be within 25% of the wind tunnel experiments. Such methodologies to attain validation data for CFD simulations from wind tunnel testing are difficult to apply using actual athletes due to the difficulties with repeatability, but are useful for static, scaled models. Force transducers in turn can obtain aerodynamic forces and moments which are also useful for CFD validation purposes. Force transducers are typically the most common tool for cycling aerodynamics investigations in wind tunnels. An example of a typical full-scale setup from (Defraeye et al., 2010a) in Figure 2.5 illustrates a raised plate to which a force transducer is attached, along with a position system for the athlete. Chowdhury et al. (2011, 2012) discussed a full-scale testing methodology for the measurement of aerodynamic properties as a function of cyclist's body positions along with various cycling accessories under a range of flow velocities. The methodology was designed to allow for both static and dynamic testing. A six-component force sensor under the platform provided force and moment measurements. The problem of repeatability with athlete positioning was addressed using a camera system. However, a drawback of this methodology was the lack of loaded rotors to provide a set resistance to the cyclist under dynamic testing conditions, along with the inability to transfer the rotation to the front wheel; a feature that has been widely used elsewhere in the literature (Barry et al., 2015b; Belloli et al., 2014; Gibertini et al., 2008). García-López et al. (2008) addressed the sensitivity of aerodynamic drag in wind tunnel testing with recommendations for future research. These include (i) pedalling at a race pace to adequately represent the mean power maintained over the course of the event, (ii) allowing the front wheel to rotate at the same pace as the rear wheel, (iii) including a power meter in the experimental setup, and (iv) synchronization of the force balance and the bicycle's crank.

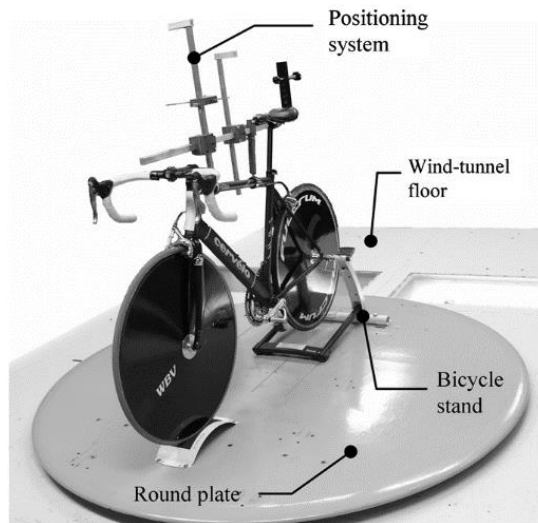


Figure 2.5. A bicycle setup for wind tunnel experiments. Figure obtained from (Defraeye et al., 2010a).

Studying the flow-field around a cyclist can be challenging. Wind tunnel testing often presents aerodynamic improvements solely through evaluating drag reduction, as detailed flow-field information can be difficult to obtain (Defraeye et al., 2010a, 2010b). Flow visualisation techniques can yield information on why different cycling positions generate different drag, providing a means to further lower the drag profile of a cyclist. There are various methods available for flow visualisation in wind tunnel testing, the most common of which are smoke tests. Oil and ink flow methods are additional options. Crouch et al. (2012) concluded that there is the potential to improve rider aerodynamics through a targeted approach at reducing the drag associated with the vortex flow structures that develop at various locations on the rider's body. The study utilised various wind tunnel flow visualisation techniques such as a series of detailed time-averaged velocity-field wake surveys, skin friction flow visualisations, wool tuft flow visualisations, and time-averaged surface pressure measurements for varying leg positions. Crouch et al. (2014) demonstrated how aerodynamic drag can be assessed from the perspective of the fluid through which the cyclist moves. Such techniques enabled analysis of how drag forces were generated. Crouch et al. (2016) mapped the flow topology of the near wake of a model cyclist, in both static and dynamic wind tunnel experiments, making comparisons over the full 360° rotation of the crank using time and phase-averaging techniques. The primary wake flow features were found to be consistent across the range of pedalling frequencies tested, and it was suggested that only limited reductions in aerodynamic drag may be available through adjusting cycling cadence with conventional pedal strokes.

Wind tunnel testing is a reliable method for cycling aerodynamic analyses, allowing a higher level of repeatability than track testing, and with generally less uncertainty than numerical methods.

It is clear that there are further options for flow visualisation in wind tunnel environments, but at additional costs. However, understanding the underlying physics of the flow around cyclists is key to acquiring further optimisations.

2.2.1.2 Computational fluid dynamics

Computational fluid dynamics (CFD) tools can be a useful asset to obtain whole flow-field data, i.e. data of all relevant variables at every point in space (and time) (Figure 2.6), while wind tunnel testing can require additional investment in time and materials where flow visualisation is required. CFD models can analyse the wake flows of athletes; thus, identifying the additional causes of drag. However, CFD can be expensive with regards to the hardware required and associated costs, and with regards to time to solution for transient methods. The benefits of CFD are recognised within the cycling community, and are well established within other sports including motorsport, swimming, skiing and bobsleighbing; to some extent running has also embraced its potential (Dabnichki & Avital, 2006; Hart, 2006; Rouboa et al., 2006). Olympic gold medals can be won by tenths of a second (Hart, 2006), and it is possible to use CFD to find aerodynamic enhancements which lead to additional speed and time savings. Hanna (2012) discussed the impact of computer hardware advances to CFD users in sporting applications. A key aim of aerodynamic testing is discovering new cycling positions that conform to the International Union of Cycling (UCI) rules while providing aerodynamic benefits. Similar procedures have been found to be successful in other sports such as bobsleigh aerodynamics. Computational modelling in bobsleighs on the positioning of the internal crew members has yielded aerodynamic benefits without breaching regulations (Dabnichki & Avital, 2006). Rules and regulations that pose design constraints in elite sports are intended to reduce the impact of equipment on the outcome of competitive events, and to ensure the safety of competing athletes.

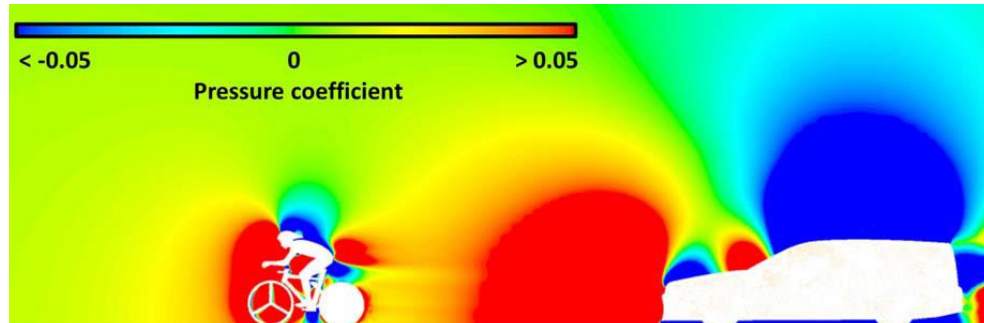


Figure 2.6. Static pressure coefficient map illustrating the aerodynamic effect of a trailing car on a cyclist (Blocken & Toparlar, 2015).

CFD has also enabled the study of flow-field information and aerodynamic forces on individual surface components within a larger simulation. However, simplified geometries (to some extent) are common across CFD simulations in order to simplify spatial discretisation (Blocken and Toparlar, 2015; Defraeye et al., 2010a). Simplifications include the smoothing of the athlete's geometry and the neglecting of smaller items such as brake cables, gears, derailleurs etc. These components are highly detailed, but small in scale, which would require a computationally expensive grid to capture the geometrical features with sufficient accuracy.

Defraeye et al. (2010b) conducted one of the first comprehensive studies into the accuracy of CFD for cycling applications. Only the rider was included (whose geometry was acquired through high-resolution 3D scanning) in the computational model with no bicycle geometry. A reduced-scale model (1/2) of the cyclist produced by rapid prototyping was used to validate the CFD models using wind tunnel experiments. In addition to three-component forces and moments, high-resolution surface pressure measurements were taken from the scale model's surface at 115 locations, which provided detailed information on the flow-field. The data provided from the wind tunnel tests were used to compare the performance of several Reynolds-averaged Navier-Stokes (RANS) turbulence models, large-eddy simulations (LES), and boundary layer modelling methods with low-Reynolds number modelling (LRNM) and wall functions. The RANS shear-stress transport (SST) $k-\omega$ model provided the best overall performance, followed closely by LES. LES provided valuable transient information but at a high computational cost. Furthermore, the additional temporal sensitivity analysis that is required for LES makes and its associated cost render it less attractive for practical calculations. LRNM was shown to provide superior performance for drag predictions, in comparison to wall functions.

Defraeye et al. (2011) performed the only study concerning aerodynamics and convective heat transfer from a cyclist found by this review. CFD was used to investigate if a link exists between aerodynamic performance and heat transfer from an athlete's body. Nineteen body segments of a cyclist for three different body positions were analysed for an increased insight into drag reduction mechanisms and the thermo-physiological response of cyclists related to heat stress and hydrothermal performance of clothing. A high degree of variability of the drag area was found for individual body segments at different cyclist positions, in contrast to the convective heat losses for the same body parts which were not as sensitive to the cyclist's position. High drag values were found for the head, legs and arms, with high convective heat transfer coefficients (CHTC) found for the legs, arms, hands and feet, and Defraeye et al. (2011) summarised that a direct relationship may not exist between high drag forces and convective heat transfer from the athlete.

The variation in drag force and associated downstream flow structure with crank angle was investigated numerically and experimentally by Griffith et al. (2014). CFD under-predicted drag measurements by 15%, however, the author put this partially down to the simplification of the geometry of the athlete and bicycle. A good match of the downstream flow structure was found between the CFD and wind tunnel results. Minimum drag was observed at a crank angle of 15°, when the two thighs of the cyclist were aligned. The maximum drag was observed at a crank angle of 75°, when one leg is at full extension and the other leg is raised towards the rider's torso. The transient nature of the entire flow-field was revealed by these CFD studies. Griffith et al. (2014) concluded that there is a dependency between the drag force experienced by the rider and the downstream vortex flow structures from the cyclist. The strength of the vorticity structure can be linked to the drag force as shown by the alignment of either thigh perpendicular to the flow, aggregating the power of downstream vortex structures. The authors also indicated that caution should be exercised when modelling components isolated from the entire cycling geometry, as the positioning of the legs affected not only the drag force on the legs, but the drag force on the rider's torso.

CFD is becoming more commonly used in cycling aerodynamics research, due in part to its capability to provide whole flow-field data, which aids in understanding the flow structures and phenomena behind the aerodynamic forces. However, CFD is not without its limitations, and requires verification as well as validation through experimental means to ensure reliable and accurate information is attained from the simulations. It is noted that common drawbacks of CFD testing in the literature include the neglect of varying roughness on riders TT suits. LRNM and wall functions (Blocken and Toparlar, 2015; Blocken et al., 2013a; Defraeye et al., 2011) have been used in the past to model the surface of the rider, with little or no difference between the skin, suit and helmet surface modelling. Wall functions allow for some roughness to be considered. However, they assume certain flow conditions without actually solving the viscous sub-layers near the (no-slip) wall

surface, which is the case with LRNM. It may be possible that this may be overcome in future research by using specially adapted models such as the transition SST $k-\omega$ turbulence model, which can be used to control roughness and has already been successfully applied in cycling aerodynamics applications (Blocken et al., 2018).

2.2.1.3 Track and laboratory testing

Track (outdoor or indoor – velodrome) testing can replicate the cycling conditions a cyclist will compete in. However, it can be difficult to qualitatively and quantitatively obtain aerodynamic metrics such as drag in such tests. These tests also provide an idealised environment when compared to outdoor events. Changes in outdoor track topography and atmospheric conditions can present challenges to determining definitive aerodynamic improvement, unless properly accounted for. Velodromes can provide more controlled wind conditions than outdoor tracks allowing for improved repeatability between experiments. Simplifications often present in both wind tunnel testing and CFD simulations can detract from the real-world applicability of the results. These problems are negated when using velodrome testing. For example, Tour De France cyclists are invariably subject to crosswinds, while only direct forward-facing flow (0° yaw) is commonly tested using CFD and wind tunnel methods – an outdoor track where weather conditions are carefully monitored around the track can offer more “real-life” conditions. Power and drag measurements are possible for the entire bike/rider system. Typically, the power output of the cyclist is acquired from Schoberer Rad Messtechnik (SRM) power meters, or power-taps. By varying athlete postures and cycling equipment in an indoor track circuit, aerodynamic advantages can be measured through time savings around a measured lap distance. The power output by athletes to overcome aerodynamic resistance is simply the aerodynamic force times the velocity of the athlete in still air, as described in equation 2.37.

$$W = 0.5\rho C_D AV^3 \quad (2.37)$$

where W is the power, ρ is the air density, V is the athlete velocity, A is the frontal area, and C_D is the drag coefficient.

A mathematical model for individual pursuit cyclists in an indoor velodrome was developed by Underwood and Jermy, (2010a). Using this model, the velocity of the centre of mass and the finishing time for athletes could be predicted using forward integration and were accurate to within 3% with the available input data at the time of this research. This model accounted for the actual position of the rider on the track and the effects of leaning in the bends using data collected by a SRM power meter. This provided an assessment of the energy expended due to aerodynamics from the

realistic predictions of the athlete's position on the velodrome. Lim et al. (2011) concluded that commercially available power meters, which can be used in velodrome testing, are sensitive enough to detect the changes in aerodynamic resistance associated with changes in body position. García-López et al. (2013) also demonstrated the validity, reliability and sensitivity of velodrome tests to detect small changes in aerodynamic drag in elite cycling by comparison to wind tunnel experiments.

Recent efforts have been made to develop quantitative and qualitative flow visualisation techniques for on-site sport aerodynamics optimisation (Sciacchitano et al., 2015). The proposed method utilises tomographic particle image velocimetry (tomo-PIV) to measure the velocity-field in a three-dimensional domain. The 3D spatial distribution of tracer particles that are illuminated within a volume are acquired by images from cameras at various viewing angles. It has been proposed that the flow tracers could be comprised of helium filled soap bubbles (HFSB). PIV is a standard tool for the investigation of turbulent flow, whereby a velocity field is measured from which pressure field and aerodynamic forces can be retrieved. Large-scale tomo-PIV opens new and unprecedented possibilities for investigating sports aerodynamics. Non-intrusive pressure and force measurements could be conducted, eliminating the need for sensors on the subject being tested. Quantitative visualisation of the flow-field such as flow separation, wake flows, vortex structures and boundary layer characteristics would become possible during track testing. The 'ring of fire' concept (cyclist travelling through HFSB concentrated in one location of the velodrome) for a velodrome would provide on-site measurements with no alterations to the cyclist or cycling equipment. Sciacchitano et al. (2015) addressed the suitability of HFSB for flow visualisation in cycling applications by experimentally analysing the flow around a horizontal axis wind turbine (HAWT). It was determined that HFSB as flow tracers allow velocity measurements in a volume exceeding 10,000 m³. Spoelstra et al. (2018) applied the 'ring of fire' method to cyclist aerodynamics, and found that the drag measured did not directly match wind tunnel results. This difference was attributed to the support structures required to hold the bicycle upright in the wind tunnel. The difference between a TT and upright position was measured as 25% which compares to the 15-30% range in drag reduction reported in the literature for these two positions (Defraeye et al., 2010a; Grappe et al., 1997; Jeukendrup & Martin, 2001). This method is not yet widely used, with the technology in its development and testing phase. However, it may offer a new and innovative approach to determining aerodynamic drag and for flow visualisations in the near future.

Velodrome or outdoor track testing is possibly the least costly method of aerodynamic testing, and perhaps, the most commonplace method. However, the dependency on environmental conditions and the difficulties with visualising flow can make it difficult to determine small

performance improvements, which are typically achieved using either wind tunnel testing, or CFD. However, new emerging technologies may change this trend in the coming years.

2.2.2 Cyclist posture and positioning

Actively adjusting the cyclist position and/or posture during wind tunnel testing is a commonplace method to find reductions in the form drag of cyclists. There are three standard cycling positions used for benchmark purposes in elite cycling; the upright position (UP), dropped position (DP) and time-trial position (TT) (Defraeye et al., 2010a). There are numerous other cycling positions recognised for their aerodynamic properties such as the Obree and superman positions (Grappe et al., 1997); albeit these are currently banned in UCI sanctioned races. Furthermore, recent developments have focused on metabolic and physiological performance data in combination with power output to optimise the balance between aerodynamics and power output (Fintelman et al., 2015b, 2016; Underwood et al., 2011).

Grappe et al. (1997) used velodrome testing to evaluate the aerodynamics of four different cycling positions. The Obree position, a unique aerodynamic cycling position developed by Graeme Obree, was the focus of this research. The reproducibility of tests that determined the drag area using an external mechanical power device was also evaluated. The substantial aerodynamic advantage of the Obree position over the standard upright, dropped and time-trial positions was confirmed. However, there may be possible disadvantages in terms of ventilator and metabolic variables that were not studied in this research. Gnehm et al. (1997) concluded that riding a bicycle in an extreme aerodynamic position increases the metabolic cost of cycling under static conditions on rollers, i.e. when the wind resistance is not taken into account. This increase in metabolic cost was measured by the volume of oxygen (VO_2) that the cyclist intakes. Three cycling positions were analysed, upright cycling, hands on drops, and hands on clip-on aero-handlebars. Heart rate and VO_2 values were significantly higher for dropped and aero-handlebar positions respectively in comparison to the upright position. Gnehm et al. (1997) estimated that 9 W of power could be lost as a result of metabolic restriction, however, this was far smaller than the 100 W of savings expected from the aerodynamic positioning.

Gibertini et al. (2008) showed that a drag reduction in the order of 20% with respect to the traditional cyclist's position can be attained from posture alterations while remaining within the limits of the UCI rules. A model estimating the frontal area of a cyclist as a function of anthropometric properties, postural variations and helmet characteristics in a time-trial position was created by

Barelle et al. (2010). The height and body mass of the cyclist were highlighted as high impact factors for aerodynamic performance. Oggiano et al. (2008) utilised wind tunnel testing to analyse 6 different postures with 11 elite TT cyclists. The posture yielding the lowest aerodynamic drag saved an average of 21.9 W in power output, with an average gain of 0.75 km/h in velocity at a 500 W output.

Defraeye et al. (2010a) conducted an aerodynamic study of different cyclist positions using CFD simulations validated using full-scale wind tunnel experiments. Three cycling positions were investigated, time-trial, dropped and upright positions (Figure 2.7a) with drag areas of 0.219 m², 0.179 m² and 0.150 m² calculated respectively, using RANS methods. Only the cyclist was modelled in this study, therefore interference drag between the rider and the bicycle was neglected. Defraeye et al. (2010a) also provided a useful comparative summary of recorded drag area of cyclist postures in the early literature (1980's – 2000's).

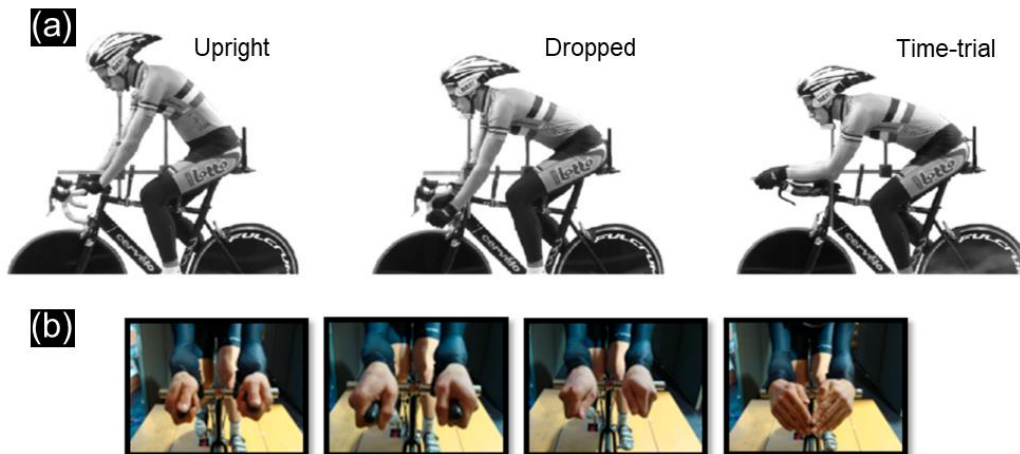


Figure 2.7. (a) The three main cycling positions: Upright position (UP), dropped position (DP) and time-trial position (TTP) respectively from left to right. Figure obtained from (Defraeye et al., 2010a). (b) Four hand positions, normal, thumbs inside, fist grip and arrow grip for individual pursuit athletes. Figure obtained from (Underwood & Jermy, 2010b).

Underwood & Jermy (2010b) collected aerodynamic drag and power output data for elite athletes using a variety of different hand positions to determine whether an optimal hand position existed for individual pursuit athletes. An arrow style hand position (Figure 2.7b) was shown to reduce power output by 30 W. A region of smooth recirculation was found to have developed behind the athlete's thumbs which may be more favourable than the turbulent separation found for all other hand positions tested. Underwood et al. (2011) measured the aerodynamic and biomechanical power of a track cyclist as a function of shoulder and torso angles. Three competitive track cyclists were measured in a wind tunnel at 40 km/h. A custom adjustable handlebar setup was used to ensure repeatability and measurability for changes in shoulder and torso angles. It was found that a low torso

angle (4.5° to 8.6° from the horizontal plane) and a middle shoulder angle (88° to 93° , measured to the torso angle) presented an optimal balance between power output and aerodynamics. It is noted that the UCI has specific constraints which limit the movement of the handlebars and the saddle, which are used for adjusting the elbow, shoulder and torso angles. Chabroux et al. (2012) also investigated the aerodynamics of a cyclist's hand position. By having the hands on the shifters, a 1.6% increase in total drag force resistance was measured in comparison to the classical hands position. A decrease of almost 1.8% in total drag was observed when the cyclist's elbows were joined together. It was also determined that hand positions had negligible impact on the frontal area of the cyclist. Underwood & Jermy (2013) analysed the aerodynamic effect of different handlebar heights using wind tunnel tests on 14 cyclists. The drag area of each position was calculated to identify an optimal handlebar position for each athlete. However, a high degree of variability was found between athletes. Handlebar height had a greater overall influence on the drag compared to the handlebar elbow pad separation.

Fintelman et al. (2014a) predicted the optimal time-trial cycling position as a function of the cycling speed. The question this research posed was at which cycling speed the aerodynamic power losses begin to dominate. The optimal rider torso angle was found to depend strongly on the cycling speeds, with decreasing torso angle more suitable for higher cycling speeds. At a speed of 46 km/h, it was found that aerodynamic losses were greater than physical power losses due to torso angle. However, it was concluded that cyclists should not adopt an almost horizontal torso position on the bicycle despite the aerodynamic gains, instead balancing power output with aerodynamics. The reduction in power output at these almost horizontal torso angles was attributed to a number of factors, including muscles not operating within their optimal range, muscle recruitment, increased pressure on shoulders, neck and arm, and increased adductor activation due to the extreme hip angles to keep the leg movement in the sagittal plane. Fintelman et al. (2015) concluded that a trade-off between aerodynamic drag and physiological functioning should be made for non-elite cyclists. Fintelman et al. (2015) analysed nineteen male cyclists performing incremental tests on a cycle ergometer at five different torso angles, oxygen uptake, carbon dioxide expiration, minute ventilation, heart rate, frontal area, cadence, and gross efficiency being among the recorded variables. Lower torso angles were shown to diminish athlete performance, with the 0° torso angle significantly affecting metabolic and physiological variables. Fintelman et al. (2016) further investigated torso angles to maximise aerodynamic and muscular efficiency for the cyclist, with the hypothesis that small torso angles could yield a forward shift of muscle activation time and crank torque. A significant increase in crank torque range and forward shift in peak torque timing was found at smaller torso angles.

Barry et al. (2015a) recommended that lowering the head and torso of a cyclist would translate into a reduction in aerodynamic drag through a reduction in the velocity defect and turbulence levels in the wake. This study focused on a dynamic cyclist in a wind tunnel environment, where the effect of variations in body posture on aerodynamic drag and its translation to performance were investigated with postures applicable to the standard road bicycle and TT bicycle. It was concluded that it is required to bring the arms inside the silhouette of the torso and hips to fully optimise aerodynamic performance. The traditional drops racing posture represented only a small saving over the hoods posture. However, it was discovered that by lowering the head and torso (into a crouched posture), the power requirement dropped by a further 7% over the standard drops posture. It was also discovered that gripping the hoods with horizontal forearms can reduce the required cyclist power by 13.4% in comparison to the standard hoods posture.

It is noted that there has been no detailed aerodynamic comparison to date of the aerodynamic differences between men and women cyclists. A focused study on the athlete's body geometry using CFD to compare their aerodynamic characteristics in typical competitive postures would provide further insight into potential aerodynamic differences due to male and female anthropometrics. Barelle et al. (2010) discusses how the location of flow separation points and resulting trailing vortices could differ between genders impacting the athletes drag force. In addition, full dynamic simulations of a pedalling cyclist using CFD have not yet been published for cycling to the best knowledge of the authors. There are examples of CFD simulations that capture the pedalling motion of a cyclist in articles on the social media platform LinkedIn, from the employees of a CFD software company (Beves, 2016). However, this has not yet filtered into the research community at the time of the finalisation of this thesis. The simulation performed by (Beves, 2016) demonstrates that modern commercial CFD software has the capabilities to analyse the complexities of a pedalling cyclist. Such instantaneous transient data of a pedalling cyclist would provide valuable aerodynamics data to the cycling community. Some attempts have been made to graphically display flow patterns from a dynamic cyclist using experimental methods (Crouch et al., 2014; 2016). Three-dimensional flows around a full-scale cyclist mannequin were investigated in pursuit of explaining the large variations in aerodynamic drag measured as the mannequin's legs are positioned around the 360° crank cycle. Although providing a major leap forward in the current understanding of cycling aerodynamics, CFD analysis would supplement and extend research of this nature providing a broader and in-depth understanding of the complex dynamic flows.

2.2.3 Cycling equipment

2.2.3.1 Bicycle frame aerodynamics

Many modern road bicycles, though relatively streamlined, often rely on a more rounded frame design for structural and stiffness purposes. However, the time-trial (TT) bicycles almost exclusively rely on a tear drop and thin frame designs. Furthermore, for improved aerodynamics, cables on both road and TT frames are often housed within the frame to reduce turbulence and drag as much as possible. Engineers consider the system as a whole in order to optimise the aerodynamics of the full system (e.g. the interaction of the brakes/cables with the wheels and frame).

Seat-stays and the bicycle frames can be designed to direct air over the brakes and areas of high flow separation can be identified and redesigned/eliminated. It is the ability to build these new designs using a carbon fibre monocoque structure that has dramatically improved bicycle design and performance (Haake, 2009). The monocoque design was banned at first from competitive events by the UCI (Candy & Edmonds, 1996), this ruling was overturned two years after the initial ban however in 1988. Zdravkovich, (1992) used splitter plates to reduce the drag of a bicycles frame. Splitter plates are thin plates added to the leeward side of bicycle frame tubes. The splitter plates were intended to reduce vortex shedding on circular cross section shapes. A 4% reduction to the bicycle frame's drag coefficient resulted from the application of splitter plates to the frame geometry.

Bicycle designs by Mike Burrows embody 10 years of an individual designer's experimentation and innovation (Candy & Edmonds, 1996). In collaboration with Lotus, the LotusSport Pursuit bicycle by Mike Burrows was ridden by Chris Boardman to win a gold medal for the pursuit event in the 1992 Olympic Games. The LotusSport bicycle marked an important conceptual shift in the structural, visual and aerodynamic design aspects of a bicycle. The importance of aerodynamics was placed in the sporting spot-light due to Chris Boardman lapping his fellow competitor in the individual pursuit event, a feat which was unheard of at the time (Tew Sayers, 1999). Following the development of the Lotus bike, the aerodynamic development of the 'Superbike' began in Australia by a team from the Royal Melbourne Institute of Technology and the Australian Institute of Sport (Thompson, 1998). This is one of the earliest attempts in the literature to accurately simulate real cycling conditions. Dynamic testing was achieved using an electric motor to drive the rear and front wheels via a belt drive, with artificial styrofoam legs attached to the pedals. The aerodynamic monocoque design for the superbike required 5% less rider power than the previous tubular frame produced by the Australian Institute of Sport.

2.2.3.2 Bicycle wheel aerodynamics

The importance of wheel aerodynamics has been recognised since early wind tunnel testing began on cycling (Sayers & Stanley, 1994). The rotational speed of the disk wheels has been shown to have relatively minor impacts on the aerodynamic forces. Greenwell et al. (1995), using wind tunnel experiments, demonstrated that although aerodynamic characteristics were strongly dependant on wheel geometry, they were independent of the rotational velocity of the wheel for aerodynamic designs. Wind tunnel experiments were carried out on a number of designs of racing bicycle wheels by Tew & Sayers (1999) ranging from the standard 32 spoke wheel, through wheels with aerodynamic rims and spokes, to a solid disc wheel. The research into the disc wheel yielded significant results that provided new insights into the aerodynamic characteristics of disc wheels, and showed the complexity of balancing improved aerodynamics with other racing considerations. For example, disc wheels are known to have stability issues in some crosswind conditions, as was evidenced by tests which demonstrated at yaw angles up to 8° , fluctuating side forces were experienced, possibly from boundary layer separation. These side force fluctuations may contribute to poor bicycle handling capabilities.

Knupe & Farmer (2009) investigated the suitability of CFD for studying the aerodynamics of wheels. Six different wheels (Figure 2.8) were tested at varying yaw angles using steady state analysis with the standard $k-\varepsilon$ turbulence model. The drag of a disc wheel was shown to decrease with increasing yaw angle, turning negative at 20° . These studies were not validated with experimental testing; however, manufacturers have claimed similar negative drag occurrences for some disc wheels (Prasuhn, 2007). Godo et al. (2009) performed comprehensive aerodynamics research on a commercial bicycle wheel using CFD. The study presented a methodology that used automated pre-processing and post-processing techniques for rapid and consistent aerodynamics studies on a range of bicycle wheel geometries under a large range of flow conditions. Ten different yaw angles were modelled at two speeds of 32 km/h and 48 km/h using steady state RANS analysis with the Spalart-Allmaras turbulence model for closure. In addition to this, transient analysis using delayed detached eddy simulation (DDES) was run for five of the yaw angles at the same two speeds. Flow structures were identified and compared for different yaw angles, and it was observed that a unique transition from a downwards to an upwards acting force occurred as the yaw angle increased. Viscous drag was found to be less than 3% of the overall force, with the remainder a result of pressure drag. The spokes generated a comparable drag to the wheel hub, with the wheel rim and tyres generating most of the drag. Godo et al. (2010) built on the work by Godo et al. (2009) using this methodology to analyse and compare six different wheels. Significant differences between the analysed wheels were shown with deeper rim wheels offering a clear advantage under commonly experienced yaw angles ($5-15^\circ$).

Strong agreement with wind tunnel studies provided further confidence in the results. Figure 2.8 illustrates the aesthetic difference between various wheel types along with the air interaction with each wheel geometry at 10° yaw.

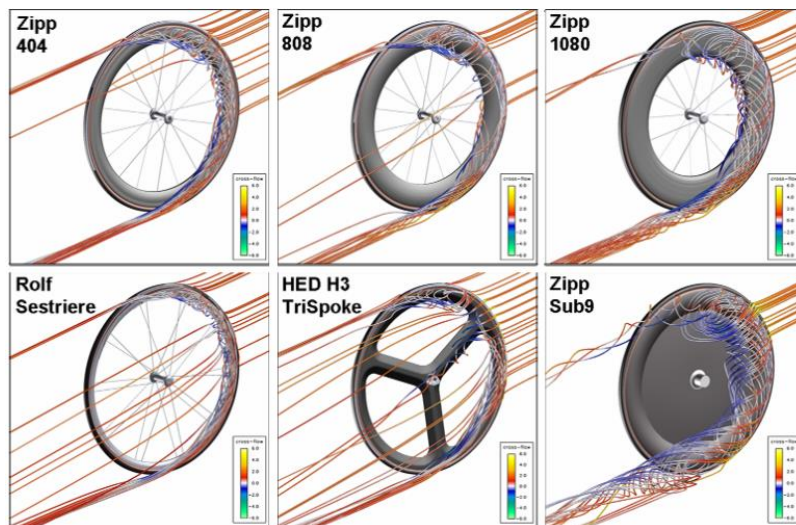


Figure 2.8. Streamlines at a yaw angle of 10° showing recirculation on the suction side of six different wheels. Figure obtained from (Godo et al., 2010).

Barry et al. (2012) reported the aerodynamic results of various styles of bicycle wheels subject to yaw angles between 0° and 30°. Several deep rim wheels of various depths were tested, along with disc wheels and a bladed tri-spoke wheel. The wheels were dynamically tested on the bicycle with an anthropomorphic mannequin. The influence of the wheel type on the drag and side forces, and the yaw and roll moments of the complete bicycle and athlete combination were investigated. It was suggested by Barry et al. (2012) that the assessment of wheel performance based on axial drag is an incomplete approach. The effect of side forces and moments can drastically change the bicycle dynamics under common cycling conditions. Thus, wheel selection should be tailored towards the conditions the athlete will be competing in.

2.2.3.3 Rider apparel

Rider apparel can contribute significantly to the overall drag of a cyclist. This has resulted in developments both in safety equipment such as helmets, and in clothing to reduce aerodynamic drag. Brownlie et al. (2009) documents the development of aerodynamic apparel for elite cycling events. More than 200 stretch fabrics were tested in a wind tunnel on cylinders, limb models and live cyclists. Fabrics were characterised by their ability to induce a drag crisis; a decrease in drag force where the

flow prematurely transitions from laminar to turbulent. A smaller wake flow was also apparent as a result from a drag crisis. The coefficient of drag on cylinder and limb segments was reduced by over 40%. Several successful methods were proven for lowering the drag, such as custom fitting, aligning seams with the airflow and matching fabric textures to specific limb segments. Aerodynamic testing by Chowdhury et al. (2010) on sports textiles concluded that a smooth cylinder with no textile had the highest measured drag force, illustrating the importance of aerodynamic clothing for sports applications even for smooth objects. Such developments have also been a focus for sprinting and skating events (Brownlie & Kyle, 2004).

Brownlie et al. (2010) demonstrated that TT helmets reduce a cyclist's drag during high speed cycling events, and that even a bald mannequin head experienced a larger drag force than when covered in most helmets tested. A 16.8% difference in drag was found between a TT helmet and a modern road helmet, potentially due to the large area of venting and the angle of the vent entry to the wind, coupled with the reduced streamlining in comparison to TT helmets. The correct use of a TT helmet can reduce total cycling power requirements by 2.2% to 6.6% (Brownlie et al., 2010). Alam et al. (2010) studied the aerodynamic efficiency of vents in helmets alongside their impact on thermal comfort. A wide range of speeds, yaw and pitch angles were studied in wind tunnel experiments using an instrumented mannequin. The heat dissipation properties of each helmet as a function of wind speed were used to measure thermal comfort. It was proved that there is scope for improvement in helmet design with modifications made to a helmet indicating that the position of vents can increase aerodynamic efficiency while retaining the same level of thermal comfort. Chabroux et al. (2012) further investigated the influence of helmet characteristics on aerodynamics in time-trial races. The addition of a large visor on the helmet was shown to provide a drag coefficient reduction as a function of the helmet inclination.

Some helmet manufacturers previously introduced dimples on the outer surface of the helmet (e.g. Giro, LG and Lazer). The aerodynamic benefits of dimples became famous with the advent of the modern golf ball. However, the benefits that a dimpled surface can provide are applicable only to specific flow conditions, e.g. a spinning sphere or cylinder. For a golf ball, dimples reduce aerodynamic drag force by delaying the separation of airflow and increasing turbulent flow regime. Alam et al. (2014) set out to test this theory applied by helmet manufacturers, finding no measurable advantage between smooth and dimpled helmets under varied pitch angles and at 0° yaw.

The significance of the number and location of ventilation holes on the aerodynamic performance of a helmet was investigated by Underwood et al. (2015). The design difficulty with helmets is combining safety features (and conforming to regulatory standards) with aerodynamic efficiency, low weight and thermal comfort. Using a 3D printed aero helmet with holes that could be

blocked to simulate different configurations, different head angles and helmet positions on a model head were tested in a wind tunnel. It was determined that the head angle and the nose to helmet distance of the cyclist had larger detrimental effects on the drag force than the number or positioning of ventilation holes. Only a slight reduction in drag force was recorded for a helmet with no ventilation holes compared to having multiple large holes. Hence, a correctly fit helmet was determined to be more important than the ventilation holes when considering aerodynamic drag.

2.2.4 Crosswinds

Crosswind evaluation (Figure 2.9) is one of the most important and underdeveloped areas of research in cycling. Only two studies analysed as part of this review have investigated cross wind effects on athletes in cycling (Fintelman et al., 2014b, 2015). In all outdoor cycling events, cyclists are commonly if not always cycling under various degrees of crosswind conditions. Therefore, typical riding postures and cyclist positions that have been developed under traditional headwind flow conditions may be rendered obsolete if new research emerges with thorough investigations of all traditional rider positions and further variations in postures under varying crosswind conditions.

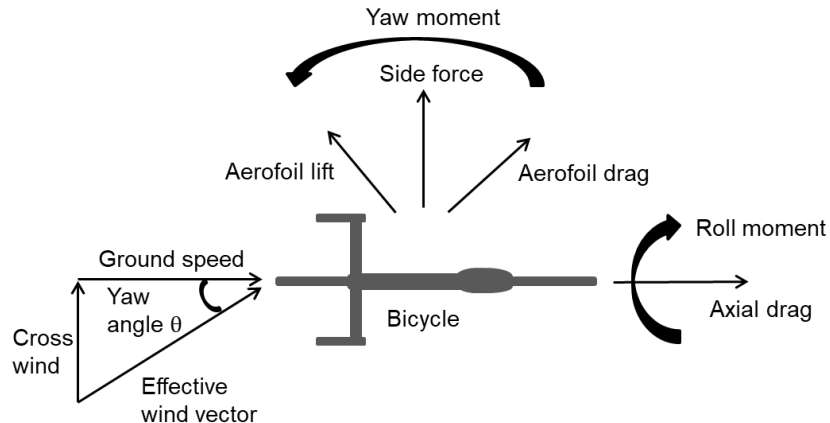


Figure 2.9. Bicycle axis system, adapted from (Barry et al., 2012).

Fintelman et al. (2014b) investigated the effects of crosswinds on cyclists with a focus on cycling stability under adverse crosswind conditions. This study recorded the aerodynamic response (in a wind tunnel) of two different full-scale bikes with and without a mannequin for a variety of crosswind angles in 15° increments (0-90°). It was observed that the bike type had a larger impact on the lateral force coefficient than the torso angle of the cyclist. Drag coefficients of a TT bike were recorded as being up to 50% smaller in comparison to a road bike at 0° yaw. However, the side force

coefficients were up to 34% larger for increasing yaw angles. The rear disc wheel on the TT bike was the major contributor to the difference in the lateral force coefficient between the two bicycles.

Fintelman et al. (2015) used validated CFD simulations to investigate the flow-field around a static cyclist at various yaw angles. RANS simulations (standard $k-\varepsilon$ and SST $k-\omega$) were used to analyse yaw angles ranging between 0° and 90° , while DES and LES were used to analyse only a single yaw angle of 15° due to their increased computational expense. The bicycle was included in the simulation along with the rider. A standard urban road helmet was used instead of an aerodynamic TT helmet as this research was focused more on cycling safety than competitive racing. Discrepancies between different CFD modelling techniques and the wind tunnel results were apparent with 17% difference in drag force between DES and experimental results at a yaw angle of 15° . Geometrical simplifications in the CFD along with interference drag from the wind tunnel test stand could be contributors to these discrepancies.

E-bikes are a new cycling technology with no aerodynamics research present in the literature that this author is aware of, where aerodynamics research and crosswinds research could have key implications for safety and efficiency. Aerodynamic considerations in new designs could potentially promote greater fuel efficiency and thus higher mileage to the users. Thus, consumers could travel farther and potentially faster consuming less energy through a smart aerodynamic design. Understanding how E-bikes and consumer bikes perform under crosswinds could have key safety implications as larger numbers appear on the roads as their popularity increases. As their usage continues to grow, so too does the need for further research (Fishman & Cherry, 2015).

2.2.5 Drafting in cycling

The majority of aerodynamic studies in cycling focus on a single isolated cyclist. Examining multiple cyclists in full-scale wind tunnel experiments can be difficult due to space restrictions. However, field tests have verified the benefits derived from drafting, where two or more cyclists ride in close proximity to each other. Coast down testing has been used in the literature as a method of investigating the separation distance on the aerodynamic drag reduction for drafting cyclists as seen by (Kyle, 1979). For riders at minimum practical spacing, a maximum saving of 35% was observed for the trailing rider. The aerodynamic benefits decreased with increased distance between the riders as expected. McCole et al. (1990) found that cyclists drafting at 32 km/h experienced an 18% reduction in their volume of O_2 (VO_2) consumption in comparison to individual performances. Zdravkovich et al. (1996) recorded a maximum drag reduction of 41-48% for the trailing rider in a

full-scale two cyclist formation, with a reduction in drag observed as the separation distance was reduced.

Efforts have been made to examine the impact of drafting, taking a closer look at the resulting flow-fields around each cyclist using CFD. Blocken et al. (2013) made new observations regarding a two-cyclist drafting formation using CFD, validated with wind tunnel experiments. Only the riders were modelled in the CFD simulations. Interference drag between the rider and the bicycle was neglected. A wheel to wheel distance of 0.15 m was modelled, with an air speed of 15 m/s. The key observation from this study was that the leading rider also benefits from drafting, with a 1.5 – 2.5% drag reduction. This results from the following findings from this study: (i) the absolute value of the under-pressure on the back of the trailing cyclist is reduced by the presence of the leading cyclist, who also reduces the overpressure at the front of the trailing cyclist. Both factors contribute to a reduction in overall drag force, (ii) as the leading cyclist adopts postures that yield lower drag, the drag reduction for the trailing cyclist is decreased. The opposite is true for the leading cyclist who experiences a drag reduction due overpressure in front of the trailing cyclist interacting with the under-pressure on the leading cyclists back. Defraeye et al. (2014) further investigated the drafting phenomena using four individual cyclists (Figure 2.10), each 3D scanned and modelled in different racing postures. Each rider in the pursuit formation was subject to varying rider postures. Such research using numerical studies on cyclists in a pace line has proven extremely useful for determining an optimal cyclist sequence for time-trial events both on the road and in velodromes. It was made clear that the drag of a cyclist is dependent on their position in the pace line. The results indicated a 3% gain was provided to the leading cyclist by the presence of following riders, hence confirming the mechanism found by Blocken et al. (2013). Second and subsequent positions experience drag reductions up to 40% in comparison to a single cyclist not partaking in drafting, with the second from last cyclist receiving the largest aerodynamic benefit from the formation. The wheel to wheel distance between the bicycles was assumed to be quasi-zero in this study. Note that in actual race events, this distance can be less when bicycle wheels overlap and the athletes ride in a slightly staggered formation.

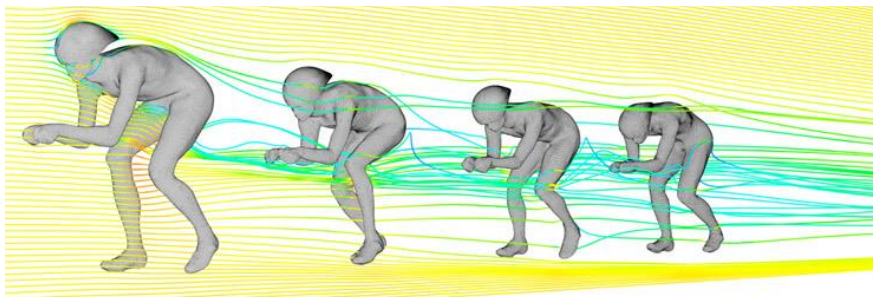


Figure 2.10. Streamlines of the flow around four drafting cyclists. Figure obtained from (Defraeye et al., 2014).

Barry et al. (2014) investigated the effect of spatial position on the aerodynamic interactions between cyclists. Variations in aerodynamic drag for cyclists in various two-rider formations were measured in wind tunnel experiments using static mannequins. Drafting and overtaking formations were analysed by mapping loads experienced by both riders as a function of their relative spatial position. It was demonstrated that drag forces, side forces, yaw momentum and roll moment are strong functions of spatial position. When both riders were drafting inline, there was a maximum drag reduction of 49% for the trailing rider and up to 5% for the lead rider under zero yaw conditions. In a following study, four riders were tested in a wind tunnel with drag on each cyclist measured simultaneously (Barry et al., 2015b). Mean drag savings of 5%, 45%, 55% and 57% for the cyclists in positions 1-4 respectively were measured. All tests were conducted at an airspeed of 18 m/s. Rollers under both wheels provided a testbed for dynamic testing with rotation transferred to the front wheels via belts. The blockage ratio was below 5%, and fixed wheel to wheel separation distance of 120 mm was maintained throughout the testing. Three generic riding postures were evaluated in drafting formations, and Barry et al. (2015b) recognised that general trends were not consistent in testing and that it may be necessary to test the actual athletes in individual teams to fully optimise performance. The strong aerodynamic interactions observed between the drafting riders appeared to be unique functions of individual athlete anthropometrics.

The track testing by Broker et al. (1999) yielded higher drag values than the wind tunnel studies and computational work by Defraeye et al. (2014) for drafting investigations. However, there was less control over the cyclist spatial positioning in track testing where proximity has a large impact on drag results. In addition, the geometry of the bicycles were not included in the numerical simulations by Defraeye et al. (2014). Wind tunnel testing also has disadvantages, and it is possible that the controlled environment can amplify the effects of drafting. The drag reduction on the second cyclist in a two-rider sequence was observed to be in the region of 44% by Barry et al. (2014) for the second rider at an inline wheel to wheel distance of 700 mm from the front rider in wind tunnel tests. All other studies apart from (Barry et al., 2015a) report lower drag savings for the second rider, with a smaller wheel to wheel spacing between the front and rear riders. Figure 2.11a-b illustrates the differences found between different studies in the literature for the percentage drag reduction found by drafting. The differences between the drafting studied in Figure 2.11a are outlined in Table 2.1 for increased clarity; the key differences being the wheel to wheel inline spacing, the air speed, and the method of testing, whether it being dynamic or static and also with geometry assumptions if using CFD, e.g., the bicycles were not included in the numerical studies by Defraeye et al. (2014).

Table 2.1. List of differences between published results in Figure 2.11, illustrating the variability between drafting experiments and numerical simulations.

Publications	Wheel to wheel	Air Speed	Posture	Static/Dynamic testing
	Spacing (mm)	(km/h)		
Barry et al. (2015a): WT	120	65	TT	Dynamic cyclist and bicycle
Defraeye et al. (2014): CFD	0	60	TT	Static cyclist only
Barry et al. (2014): WT	700	65	TT	Static mannequin and bicycle
Blocken et al. (2013): CFD	10	54	TT	Static cyclist only

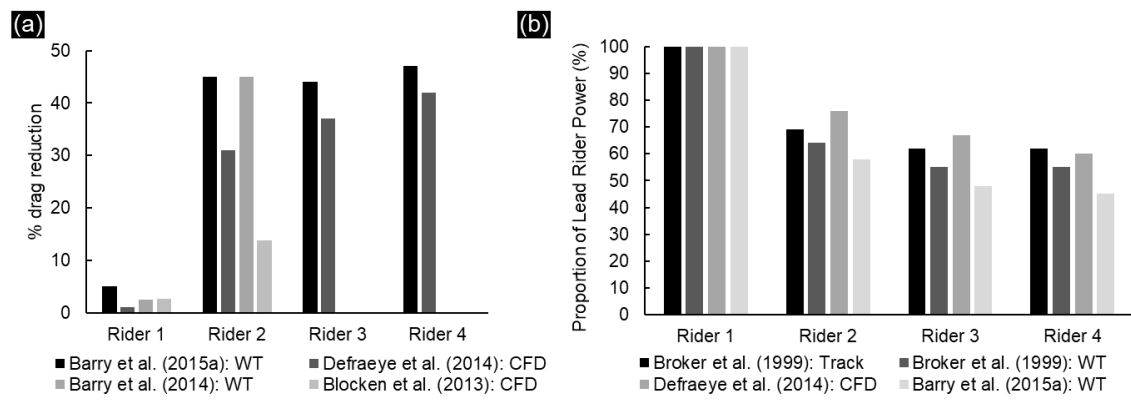


Figure 2.11. (a) The percentage drag reduction of each cyclist in a 2 and/or 4 cyclist sequence, in comparison to their individual drag in a no-drafting scenario. (b) Literature comparisons of differences in power output as a percentage of the lead rider in a 4 athlete formation, adapted from (Barry et al., 2015a).

Blocken & Toparlar (2015) expanded the use of CFD in cycling by exploring other drafting related dynamics in cycling races, i.e. the aerodynamic effects of a trailing car on the drag of a single cyclist. Both a static bicycle and a rider were modelled in this simulation, but with some geometrical simplifications. A reduced scale model of a cyclist was created for wind tunnel validation studies. The results show a potential 3.9 s impact on a 50 km time-trial event. Blocken & Toparlar (2015) recommended to the UCI that the 10 m minimum distance rule should be altered to 30 m to negate this aerodynamic benefit unknowingly availed of by some cyclists. It was noted that during actual races, the 10 m limit is not strictly enforced and that there may be at least one car, if not multiple, potentially influencing the drag of a cyclist. In a following study, the aerodynamic effects of following motorcycles on a single cyclist was investigated (Blocken et al., 2016). It was reported that a single trailing motorcycle could yield a drag reduction of 8.7% for a single cyclist at a separation distance of 0.25 m. In the case of three trailing motorcyclists, a drag reduction of 13.9% was experienced by

2.2.6 Hand-cycling and recumbents

While the racing bicycle for professional or casual use has experienced extensive development with regard to aerodynamics, similar development has not occurred with regard to tandem cycles or hand-cycles that are used by elite para-cyclists. Existing elite hand-cycles are a young technology with little aerodynamic research conducted to enhance their potential. Belloli et al. (2014) performed dynamic wind tunnel testing of two hand-cycle/rider combinations, an arm powered hand cycle (Figure 2.13a), and an arm-trunk powered hand cycle (Figure 2.13b). A specialised system was built for the wind tunnel testing where the hand cycle was mounted on a support frame with each wheel placed on rollers with an adjustable resistance. The study also included a comparison of track testing to the wind tunnel experiments, measuring the torque on the pedals, the bike velocity and the track properties. The aerodynamic force was determined from the energy balance specified by Martin et al. (1998), with assumptions of no-wind conditions. The drag area of the arm powered and arm-trunk powered hand cycles were found to be 0.245 m^2 and 0.202 m^2 respectively from the track tests by Belloli et al. (2014) when the athletes were actively providing propulsion. Wind tunnel experiments found the opposite with the arm-powered hand-cyclist experiencing less drag than the arm-trunk powered hand-cyclist; drag area values of 0.21 m^2 and 0.22 m^2 respectively. Further investigations explored a ‘free-wheeling’ scenario where the athlete does not apply propulsive power but adopts a static aerodynamic posture. Better agreement was found between the track and wind tunnel experiments for the free-wheeling scenarios, with both methods predicting the arm-trunk powered hand-cyclist to yield lower drag than the arm-powered hand-cyclists. Large differences were found for the drag area of the arm-trunk powered hand-cyclist in the wind tunnel where the drag area in the aerodynamic ‘free-wheeling’ position was measured to be 40.9% lower than the propulsive position.

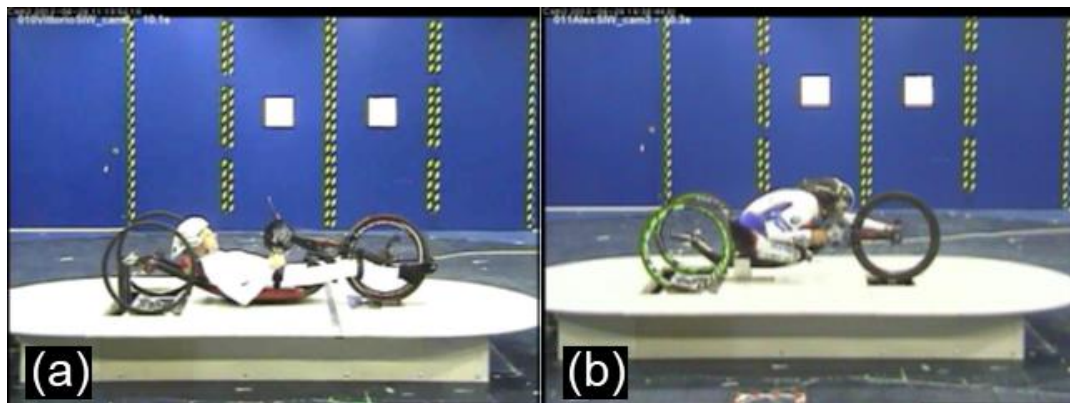


Figure 2.13. (a) An arm powered hand-cyclist, and (b) an arm-trunk powered hand-cyclist, both in aerodynamic postures. Figure obtained from (Belloli et al., 2014).

Hand-cycles make few other appearances in the literature. Their similarity to recumbent cycles is recognised most notably in discussions on fully faired cycles (a bicycle enclosed in an aerodynamic shell), outside of the UCI domain (Gross et al., 1983). French amateur cyclist Charles Mochet changed cycling history after developing a recumbent bicycle with which he won races against the world's elite (Epema et al., 2012). Recumbent cycles were first banned by the UCI in 1938 (Gross et al., 1983). The formation of the International Human Powered Vehicle Association in 1976 introduced a new championship for bicycles banned by the UCI, and has since spurred recumbent bicycle development (Epema et al., 2012). The current world record of a human powered vehicle (HPV) is 144.18 km/h, in a fully faired recumbent bicycle (Bennett, 2016). HPVs appear elsewhere in the literature with some wind tunnel experiments used to analyse the aerodynamics of the outer shell to aid future design iterations. Epema et al. (2012) used oil streak testing to determine the location for the laminar-turbulent transition point. Attempts were made to keep the pressure gradient along the length of the outer shell from changing drastically to delay turbulent transition.

2.2.7 Tandem cycling

Excluding published work from the present research, there have been no other instances of tandem cycling aerodynamics research conducted in the literature to the best knowledge of the author. However, tandem cycling aerodynamics bears some resemblances to other research fields, specifically: two solo cyclists drafting and the aerodynamics of two inline cylinders. The phenomenon of drafting in cycling can consist of two cyclists, cycling inline to each other. At the minimum distance between two drafting riders, some similarities can be drawn between the two athletes on a tandem bicycle, albeit with a larger spacing distance between both athletes when on solo bicycles (see Section 2.2.5).

The aerodynamics of tandem cycling can be simplified to two inline cylinders, in order to gain a fundamental understanding of the interaction of two bluff bodies in close proximity. The aerodynamics of two cylinders has been studied extensively in the literature (Sumner, 2010), with applications in aviation, bridges, cables, off-shore structures and many others. It is noted that the Reynolds number used for investigations of inline cylinder aerodynamics were generally drastically lower than that experienced by tandem cyclists ($> 1e07$), which needs to be accounted for when comparisons are made. Fundamental classical problems of fluid mechanics are found for the flow around a circular cylinder such as the boundary layer, flow separation, vortex dynamics, and the free shear layer (Sumner, 2010). The flow around a single isolated cylinder is well understood, but the

changes to the flow around said cylinder when a second cylinder is introduced in close proximity is less understood, with intricate interactions between the vortices, shear layers and wake flows. There are two types of flow interference associated with flows consisting of two cylinders: wake interference and proximity interference (Sumner, 2010). Wake interference is when one cylinder is partially or fully submerged in the wake of the second cylinder. Proximity interference is when two cylinders are located close to each other but are not directly in the wake of each other (e.g. cylinders located side by side). Wake interference holds similarity to tandem cycling aerodynamics where the rear athlete (the stoker) sits directly in the wake of the front athlete (the pilot). The numerical approach has been less popular than the experimental approach in the literature due to the complexity of the flow around paired or groups of cylinders; which many simulations have confined to 2D flows at low Reynolds numbers ($Re < 300$) (Sumner, 2010).

The process of wake interference results in the incoming flow conditions (i.e. incident vorticity field (Lin et al., 2002)), for the downstream cylinder being modified by the upstream cylinder. In addition, the downstream cylinder interferes with the vortex formation region and the wake of the upstream cylinder. The spacing between both cylinders determines if they behave aerodynamically as a single bluff body or two independent bodies (Lee & Basu, 1997). This spacing is commonly referred to as the ‘pitch ratio (L/D)’, which is the centre to centre longitudinal distance ‘ L ’ between both cylinders divided by the diameter ‘ D ’ of the cylinder. The von Kármán vortex shedding from the upstream cylinder is suppressed when the pitch ratio is small (Zdravkovich, 1987), and if the pitch ratio is enlarged, complex flow behaviour can be observed in the gap between the two cylinders. The critical pitch ratio designates the start of von Kármán vortex shedding from the upstream cylinder, which is sensitive to Reynolds number and turbulence intensity (Ljungkrona et al., 1991). Wake interference can be subdivided into three types of behaviour (Zdravkovich, 1987), single bluff-body behaviour, shear layer reattachment behaviour, and co-shedding of von Kármán vortex streets from both cylinders. All three behaviour types are illustrated in Figure 2.14 (Zhou & Yiu, 2006). However, despite the studies conducted, the flow behaviour in the gap between both cylinders remains obscure with no complete understanding; speculated to be due to the Reynolds number sensitivity of the shear layers (Lin et al. 2002), and the vortex formation length (Ljungkrona et al. 1991). Xu & Zhou (2004) further illustrated the sensitivity of the aerodynamic forces of two inline cylinders to the Reynolds number from Strouhal number data. The critical pitch ratio also displays a high sensitivity to Reynolds number, and varies from an L/D of 3 to 5 in the literature (Sumner, 2010). Staggered cylinders defined by an angle (α°) of incidence can form a simplified representation of tandem cycling under crosswind conditions. Cylinders can experience wake interference and/or proximity interference effects in staggered arrangements, with the possibility for interaction between four separated free shear layers,

two Kármán vortex formatting and shedding processes and the subsequent von Kármán vortex sheets (Sumner, 2010).

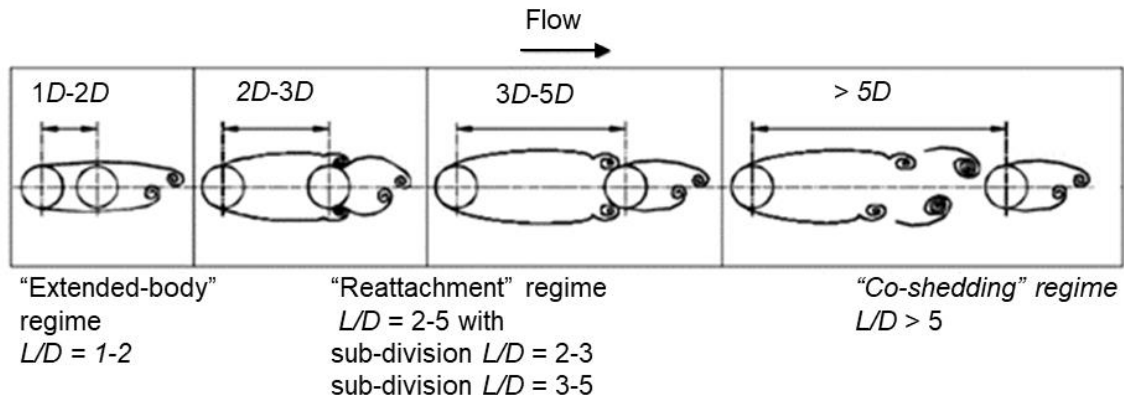


Figure 2.14. An illustration of the single bluff-body behaviour regime, reattachment or extended body regime, the shear layer reattachment regime and co-shedding regime. The Reynolds number is 7000. Figure obtained from Zhou & Yiu, (2006).

One of the objectives of tandem cycling research is to obtain drag force data for both tandem athletes. Force coefficients have been measured for inline cylinders in the literature and display a high degree of complex behaviour with dependencies on factors such as the pitch ratio and Reynolds number (Sumner, 2010). The drag coefficient (C_D) for the upstream cylinder is typically lower than the value for a single isolated cylinder when the pitch ratio is in the shear layer reattachment or single bluff-body behaviour regimes. The downstream cylinder has been found to experience a negative C_D in the single bluff-body behaviour regime, indicating that thrust forces are generated from the aerodynamic behaviour (Sumner, 2010). When the critical pitch ratio was reached, and co-shedding behaviour began for the two cylinders, the mean C_D of the leading cylinder increased to a value close to that of an isolated cylinder.

2.3 Discussion and conclusions

2.3.1 Discussion

The inclusion of CFD methods in recent years had provided diverse and detailed information on new and varying aspects of cycling aerodynamics. It is predicted that virtual modelling of athletes in real time will be possible at future competitive events (Hanna, 2012), in an effort to gain competitive advantages on the day. Physically realistic CFD/multiphysics models of athletes are also predicted to virtually test new equipment or sports textiles suited to individual athletes. A drawback of wind tunnel testing is the difficulty in obtaining whole flow-field data. Wind tunnel studies commonly have investigated only the aerodynamic forces on the cyclist. However the research conducted by (Fintelman et al., 2015a; Crouch et al., 2014, 2016; Blocken & Toparlar, 2015; Blocken et al., 2013b; Defraeye et al., 2011) on cycling aerodynamics has utilised CFD to obtain whole flow-field data, with validation data provided by wind tunnel studies. This combination provides reliable aerodynamics results, yielding new insights into the wake flow of cyclists and the fundamental causes of aerodynamic drag. Some discrepancies remain between CFD simulations and their wind tunnel validation tests. For example, support structures are required for wind tunnel experiments of bicycles and these structures are not commonly included in corresponding CFD studies. It would be recommended that CFD studies should initially mimic the wind tunnel validation tests to the best extent, and upon validation, the support structures can be removed from the model to give a clearer indication of the flow-field around a cyclist.

There have been a number of previous literature reviews into cycling aerodynamics. For example, Lukes et al. (2005) conducted a broad review that examined shortcomings of the current level of cycling aerodynamics knowledge, while Debraux et al. (2011) focused on describing methods used during the last 30 years for the evaluation of the effective and projected frontal area in cycling. Crouch et al. (2017) provided a wide review of competitive cycling aerodynamics overall. However, Para-cycling aerodynamics has not been addressed sufficiently in the literature and has also not been identified in previous literature reviews as an under-developed research field.

The gap in research between able-bodied and para-cycling disciplines is apparent in the literature. Able-bodied road, triathlon and TT cyclists have had extensive aerodynamic research conducted. Athletes' postures and positions have been broadly researched under zero yaw conditions, as have the drafting phenomena, with CFD, wind tunnel and track testing methods being utilised. Some areas of able-bodied cycling aerodynamics research applicable for para-cycling include the

testing of individual cycling components that are used by both disciplines. Bicycle wheels are a key example, which have had some attention in the literature, with both CFD testing and wind tunnel experiments. There are gaps present in the approaches to investigating cycling aerodynamics that would need to be addressed if applied to para-cycling aerodynamics. Bicycles and their riders are not always modelled together using CFD due to the computational expense. Thus interference drag between the rider and the bicycle is neglected if one or the other is left out (Blocken et al., 2013a; Defraeye et al., 2010a, 2010b). Due to the close integration of some para-athletes with their bicycle and equipment, e.g. hand-cyclists, this would not be an option for aerodynamic analysis using CFD. This would neglect interference drag and thus leading to possible discrepancies within results. However, it is noted that when athletes and their bicycles are modelled together, numerous simplifications are made to the model to reduce computational expense. For example, the spokes and cables on the bike are often neglected and the finer details of the cyclist are also neglected (e.g. some facial features).

2.3.2 Conclusions

The future of aerodynamic testing does not see either wind tunnel testing, CFD or track testing being any less included in aerodynamics research. CFD is not by any means replacing wind tunnel testing, but, is providing complementary data for further aerodynamic insights – just as it is doing in other fields of wind engineering (Blocken, 2014, 2015, 2018; Meroney, 2016; Tominaga & Stathopoulos, 2013, 2016; Meroney & Derickson, 2014; Solari, 2007; Baker, 2007; Wilson & Papadopoulos, 2004; Murakami, 1997; Stathopoulos, 1997). This makes the combination of CFD and wind tunnel testing an attractive choice for aerodynamics analysis in para-cycling research. It is worth noting that there is increased potential for track testing to provide a visual information on aerodynamic flows as highlighted by Sciacchitano et al. (2015) and thus could provide an additional validation method for CFD simulations.

Para-cycling and the role of orthotics, prosthetics or other disabilities, have a distinct lack of knowledge of in their respective fields. Some wind tunnel analysis has been conducted on competitive hand-cycles (Belloli et al., 2014; Mazzola et al., 2012), however there is no current knowledge or understanding of the flow around hand-cycles, recumbents and tandems, despite a general agreement in the cycling world that recumbent type cycles yield lower drag than their upright counterparts (Gross et al., 1983). There is no current knowledge of whole flow-field aerodynamics of these cycling categories. Tandem cycling appears untested. Some useful information can be attained from paired

cylinders to inform researchers of the expected complexity for exploring tandem cycling aerodynamics. Reynolds number sensitivity is expected to play a role in measured or simulated drag forces, along with athlete spacing sensitivity, vortex formation, and whether the flow around the two tandem athletes behaves as a single body regime or a shear layer reattachment regime. Such research could have a significant impact on the ability of tandem and hand-cyclists to perform more effectively and efficiently at major Paralympic events. From the wheels, frame design and to the riders' position, there is significant scope for further research.

2.3.3 References

- Alam, F., Chowdhury, H., Elmir, Z., Sayogo, A., Love, J., & Subic, A. (2010). An experimental study of thermal comfort and aerodynamic efficiency of recreational and racing bicycle helmets. *Procedia Engineering*, 2(2), 2413–2418.
<https://doi.org/10.1016/j.proeng.2010.04.008>
- Alam, F., Chowdhury, H., Wei, H. Z., Mustary, I., & Zimmer, G. (2014). Aerodynamics of Ribbed Bicycle Racing Helmets. *Procedia Engineering*, 72(2007), 691–696.
<https://doi.org/10.1016/j.proeng.2014.06.117>
- ANSYS Fluent. (2015). ANSYS Fluent theory guide. *Release 16.1 Documentation*. ANSYS Inc.
- Artec Europe. (2017). Artec Eva, 3D Scanners. Retrieved May 22, 2017, from
<https://www.artec3d.com/3d-scanner/artec-eva>
- Baker, C. J. (2007). Wind engineering-Past, present and future. *Journal of Wind Engineering and Industrial Aerodynamics*, 95(9–11), 843–870. <https://doi.org/10.1016/j.jweia.2007.01.011>
- Barelle, C., Chabroux, V., & Favier, D. (2010). Modeling of the time trial cyclist projected frontal area incorporating anthropometric, postural and helmet characteristics. *Sports Engineering*, 12(4), 199–206. <https://doi.org/10.1007/s12283-010-0047-y>
- Barlow, J. B., Rae, W. H., & Pope, A. (1999). *Low-speed Wind Tunnel Testing* (3rd ed.). John Wiley & Sons.
- Barry, N., Burton, D., Crouch, T., Sheridan, J., & Luescher, R. (2012). Effect of crosswinds and wheel selection on the aerodynamic behavior of a cyclist. In *9th Conference of the International Sports Engineering Association, Procedia Eng.* (Vol. 34, pp. 20–25).
<https://doi.org/10.1016/j.proeng.2012.04.005>
- Barry, N., Sheridan, J., Burton, D., & Brown, N. A. T. (2014). The effect of spatial position on the aerodynamic interactions between cyclists. In *Proceedings of the 2014 conference of the International Sports Engineering Association, Procedia Eng.* (Vol. 72, pp. 774–779). Elsevier

- B.V. <https://doi.org/10.1016/j.proeng.2014.06.131> Barry, N., Burton, D., Sheridan, J., Thompson, M., & Brown, N. A. T. (2015a). Aerodynamic drag interactions between cyclists in a team pursuit. *Sports Engineering*, 18, 93–103. <https://doi.org/10.1007/s12283-015-0172-8>
- Barry, N., Burton, D., Sheridan, J., Thompson, M., & Brown, N. A. T. (2015b). Aerodynamic performance and riding posture in road cycling and triathlon. *Proceedings of the Institution of Mechanical Engineers, Part P: Journal of Sports Engineering and Technology*, 229(1), 28–38. <https://doi.org/10.1177/1754337114549876>
- Belloli, M., Cheli, F., Bayati, I., Giappino, S., & Robustelli, F. (2014). Handbike aerodynamics: wind tunnel versus track tests. In *The 2014 conference of the International Sports Engineering Association, Procedia Eng.* (Vol. 72, pp. 750–755). Elsevier B.V. <https://doi.org/10.1016/j.proeng.2014.06.127>
- Bennett, J. (2016). New Human-Powered Speed Record Set at 89.6 Mph in Egg-Shaped Bike. Retrieved August 22, 2018, from <https://www.popularmechanics.com/technology/a22946/human-powered-speed-record-aerovelo/>
- Beves, C. (2016). *CFD simulation of a pedalling cyclist*. Retrieved from <https://www.linkedin.com/pulse/long-live-revolution-christopher-beves/>
- Blocken, B. (2014). 50 years of Computational Wind Engineering: Past, present and future. *Journal of Wind Engineering and Industrial Aerodynamics*, 129, 69–102. <https://doi.org/https://doi.org/10.1016/j.jweia.2014.03.008>
- Blocken, B. (2015). Computational Fluid Dynamics for urban physics: Importance, scales, possibilities, limitations and ten tips and tricks towards accurate and reliable simulations. *Building and Environment*, 91, 219–245. <https://doi.org/10.1016/j.buildenv.2015.02.015>
- Blocken, B. (2018). LES over RANS in building simulation for outdoor and indoor applications: A foregone conclusion? *Building Simulation*. <https://doi.org/10.1007/s12273-018-0459-3>
- Blocken, B., Defraeye, T., Koninckx, E., Carmeliet, J., & Hespel, P. (2013a). CFD simulations of the aerodynamic drag of two drafting cyclists. *Computers & Fluids*, 71, 435–445. <https://doi.org/10.1016/j.compfluid.2012.11.012>
- Blocken, B., Defraeye, T., Koninckx, E., Carmeliet, J., & Hespel, P. (2013b). Surprises in cycling aerodynamics. *Europhysics News*, 44(1), 20–23. <https://doi.org/10.1051/epn/2013102>
- Blocken, B., & Toparlar, Y. (2015). A following car influences cyclist drag: CFD simulations and wind tunnel measurements. *Journal of Wind Engineering and Industrial Aerodynamics*, 145(0), 178–186. <https://doi.org/10.1016/j.jweia.2015.06.015>
- Blocken, B., Toparlar, Y., & Andrianne, T. (2016). Aerodynamic benefit for a cyclist by a following motorcycle. *Journal of Wind Engineering and Industrial Aerodynamics*, 155, 1–10.

- <https://doi.org/https://doi.org/10.1016/j.jweia.2016.04.008>
- Blocken, B., van Druenen, T., Toparlar, Y., Malizia, F., Mannion, P., Andrienne, T., Marchal, T., Maas, G.J., Diepens, J. (2018). Aerodynamic drag in cycling pelotons: New insights by CFD simulation and wind tunnel testing. *Journal of Wind Engineering and Industrial Aerodynamics*, 179(May), 319–337. <https://doi.org/10.1016/J.JWEIA.2018.06.011>
- Broker, J. P., Kyle, C. R., & Burke, E. R. (1999). Racing cyclist power requirements in the 4000-m individual and team pursuits. *Medicine & Science in Sports & Exercise*, 31(11), 1677. <https://doi.org/10.1097/00005768-199911000-00026>
- Brownlie, L., & Kyle, C. (2004). Reducing the aerodynamic drag of sports apparel: development of the NIKE Swift sprint running and SwiftSkin speed skating suits. *The Engineering of Sport*, 5(1), 90–96. Retrieved from <http://www.biomechanica.com/docs/publications/docs/brownlie-swift.pdf>
- Brownlie, L., Kyle, C., Carbo, J., Demarest, N., Harber, E., MacDonald, R., & Nordstrom, M. (2009). Streamlining the time trial apparel of cyclists: the Nike Swift Spin project. *Sports Technology*, 2(1–2), 53–60. <https://doi.org/10.1002/jst.12>
- Brownlie, L., Ostafichuk, P., Tews, E., Muller, H., Briggs, E., & Franks, K. (2010). The wind-averaged aerodynamic drag of competitive time trial cycling helmets. *Procedia Engineering*, 2(2), 2419–2424. <https://doi.org/10.1016/j.proeng.2010.04.009>
- Candy, L., & Edmonds, E. (1996). Creative design of the Lotus bicycle: Implications for knowledge support systems research. *Design Studies*, 17, 71–90. [https://doi.org/10.1016/0142-694X\(95\)00026-N](https://doi.org/10.1016/0142-694X(95)00026-N)
- Chabroux, V., Barelle, C., & Favier, D. (2012). Aerodynamics of cyclist posture, bicycle and helmet characteristics in time trial stage. *Journal of Applied Biomechanics*, 28, 317–323. [https://doi.org/10.1016/S0765-1597\(01\)00049-1](https://doi.org/10.1016/S0765-1597(01)00049-1)
- Chowdhury, H., Alam, F., & Subic, A. (2010). Aerodynamic performance evaluation of sports textile. *Procedia Engineering*, 2(2), 2517–2522. <https://doi.org/10.1016/j.proeng.2010.04.025>
- Chowdhury, H., Alam, F., & Mainwaring, D. (2011). A full scale bicycle aerodynamics testing methodology. *Procedia Engineering*, 13, 94–99. <https://doi.org/10.1016/j.proeng.2011.05.057>
- Chowdhury, H., & Alam, F. (2012). Bicycle aerodynamics: an experimental evaluation methodology. *Sports Engineering*, 15(2), 73–80. <https://doi.org/10.1007/s12283-012-0090-y>
- Crouch, T. N., Burton, D., Thompson, M. C., Brown, N. A. T., & Sheridan, J. (2016). Dynamic leg-motion and its effect on the aerodynamic performance of cyclists. *Journal of Fluids and Structures*, 65, 121–137. <https://doi.org/10.1016/j.jfluidstructs.2016.05.007>
- Crouch, T. N., Burton, D., Brown, N. a. T., Thompson, M. C., & Sheridan, J. (2014). Flow topology in the wake of a cyclist and its effect on aerodynamic drag. *Journal of Fluid Mechanics*, 748,

5–35. <https://doi.org/10.1017/jfm.2013.678>

Crouch, T. N., Burton, D., LaBry, Z. A., & Blair, K. B. (2017). Riding against the wind: a review of competition cycling aerodynamics. *Sports Engineering*, *20*(2), 81–110.

<https://doi.org/10.1007/s12283-017-0234-1>

Crouch, T., Sheridan, J., Burton, D., Thompson, M., & Brown, N. A. T. (2012). A quasi-static investigation of the effect of leg position on cyclist aerodynamic drag. *Procedia Engineering*, *34*, 3–8. <https://doi.org/10.1016/j.proeng.2012.04.002>

Dabnichki, P., & Avital, E. (2006). Influence of the position of crew members on aerodynamics performance of two-man bobsleigh. *Journal of Biomechanics*, *39*(15), 2733–2742.

<https://doi.org/10.1016/j.jbiomech.2005.10.011>

Debraux, P., Grappe, F., Manolova, A. V., & Bertucci, W. (2011). Aerodynamic drag in cycling: methods of assessment. *Sports Biomechanics*, *10*(3), 197–218.

<https://doi.org/10.1080/14763141.2011.592209>

Defraeye, T., Blocken, B., Koninckx, E., Hespel, P., & Carmeliet, J. (2010a). Aerodynamic study of different cyclist positions: CFD analysis and full-scale wind tunnel tests. *Journal of Biomechanics*, *43*(7), 1262–1268. <https://doi.org/10.1016/j.jbiomech.2010.01.025>

<https://doi.org/10.1016/j.jbiomech.2010.01.025>

Defraeye, T., Blocken, B., Koninckx, E., Hespel, P., & Carmeliet, J. (2010b). Computational fluid dynamics analysis of cyclist aerodynamics: Performance of different turbulence-modelling and boundary-layer modelling approaches. *Journal of Biomechanics*, *43*(12), 2281–2287.

<https://doi.org/10.1016/j.jbiomech.2010.04.038>

Defraeye, T., Blocken, B., Koninckx, E., Hespel, P., & Carmeliet, J. (2011). Computational fluid dynamics analysis of drag and convective heat transfer of individual body segments for different cyclist positions. *Journal of Biomechanics*, *44*(9), 1695–1701.

<https://doi.org/10.1016/j.jbiomech.2011.03.035>

Defraeye, T., Blocken, B., Koninckx, E., Hespel, P., Verboven, P., Nicolai, B., & Carmeliet, J. (2014). Cyclist drag in team pursuit: Influence of cyclist sequence, stature, and arm spacing.

Journal of Biomechanical Engineering, *136*(1), 011005. <https://doi.org/10.1115/1.4025792>

Epema, H. K., van den Brand, S., Gregoor, W., Kooijman, J. D. G., Pereboom, H. P., Wielemaker, D. C., & van der Zweep, C.-J. (2012). Bicycle Design: A different approach to improving on the world human powered speed records. *Procedia Engineering*, *34*, 313–318.

<https://doi.org/10.1016/j.proeng.2012.04.054>

Ferziger, J. H., & Peric, M. (2002). *Computational Methods for Fluid Dynamics*, 423.

[https://doi.org/10.1016/S0898-1221\(03\)90046-0](https://doi.org/10.1016/S0898-1221(03)90046-0)

Fintelman, D. M., Sterling, M., Hemida, H., & Li, F.-X. (2014a). Optimal cycling time trial position models: Aerodynamics versus power output and metabolic energy. *Journal of Biomechanics*,

- 47(8), 1894–1898. <https://doi.org/10.1016/j.jbiomech.2014.02.029>
- Fintelman, D. M., Sterling, M., Hemida, H., & Li, F.-X. (2014b). The effect of crosswinds on cyclists: an experimental study. In *The 2014 conference of the International Sports Engineering Association, Procedia Eng.* (Vol. 72, pp. 720–725). <https://doi.org/10.1016/j.proeng.2014.06.122>
- Fintelman, D. M., Hemida, H., Sterling, M., & Li, F.-X. (2015a). CFD simulations of the flow around a cyclist subjected to crosswinds. *Journal of Wind Engineering and Industrial Aerodynamics*, 144, 31–41. <https://doi.org/10.1016/j.jweia.2015.05.009>
- Fintelman, D. M., Sterling, M., Hemida, H., & Li, F.-X. (2015b). The effect of time trial cycling position on physiological and aerodynamic variables. *Journal of Sports Sciences*, 0414(April 2015), 1–8. <https://doi.org/10.1080/02640414.2015.1009936>
- Fintelman, D. M., Sterling, M., Hemida, H., & Li, F. X. (2016). Effect of different aerodynamic time trial cycling positions on muscle activation and crank torque. *Scandinavian Journal of Medicine and Science in Sports*, 26(5), 528–534. <https://doi.org/10.1111/sms.12479>
- Fishman, E., & Cherry, C. (2015). E-bikes in the Mainstream: Reviewing a Decade of Research. *Transport Reviews*, 1647(July 2015), 1–20. <https://doi.org/10.1080/01441647.2015.1069907>
- Franke, J., Hellsten, A., Schlünzen, H., & Carissimo, B. (2007). Best practice guideline for the CFD simulation of flows in the urban environment. *COST Action 732: Quality Assurance and Improvement of Microscale Meteorological Models*. Hamburg Germany.
- García-López, J., Ogueta-Alday, A., Larrazabal, J., & Rodríguez-Marroyo, J. (2013). The Use of Velodrome Tests to Evaluate Aerodynamic Drag in Professional Cyclists. *International Journal of Sports Medicine*, 35(05), 451–455. <https://doi.org/10.1055/s-0033-1355352>
- García-López, J., Rodríguez-Marroyo, J. A., Juneau, C.-E., Peleteiro, J., Martínez, A. C., & Villa, J. G. (2008). Reference values and improvement of aerodynamic drag in professional cyclists. *Journal of Sports Sciences*, 26(3), 277–286. <https://doi.org/10.1080/02640410701501697>
- Gaul, L. H., Thomson, S. J., & Griffiths, I. M. (2018). Optimizing the breakaway position in cycle races using mathematical modelling. *Sports Engineering*, 0(0), 1–14. <https://doi.org/10.1007/s12283-018-0270-5>
- Gibertini, G., Campanardi, G., Grassi, D., & Macchi, C. (2008). Aerodynamics of Biker Position. In *BBA VI International Colloquium on: Bluff Bodies Aerodynamics & Applications*. Milano, Italy.
- Gnehm, P., Reichenbach, S., Altpeter, E., Widmer, H., & Hoppeler, H. (1997). Influence of different racing positions on metabolic cost in elite cyclists. *Medicine and Science in Sports and Exercise*, 29(6), 818–23. <https://doi.org/10.1097/00005768-199706000-00013>
- Godo, M., Corson, D., & Legensky, S. (2009). An aerodynamic study of bicycle wheel performance

- using CFD. In *47th AIAA Aerospace Sciences Annual Meeting*. Orlando, Florida: AIAA.
<https://doi.org/10.2514/6.2009-322>
- Godo, M., Corson, D., & Legensky, S. (2010). A comparative aerodynamic study of commercial bicycle wheels using CFD. *48th AIAA Aerospace Sciences Meeting*, (2010–1431).
- Grappe, F., Candau, R., Belli, A., & Rouillon, J. D. (1997). Aerodynamic drag in field cycling with special reference to the Obree's position. *Ergonomics*, *40*(12), 1299–1311.
<https://doi.org/10.1080/001401397187388>
- Greenwell, D., Wood, N., Bridge, E. K. L., & Addy, R. (1995). Aerodynamic characteristics of low-drag bicycle wheels. *Aeronautical Journal (1968)*, *99*(983), 109–120.
- Griffith, M. D., Crouch, T., Thompson, M. C., Burton, D., & Sheridan, J. (2014). Computational fluid dynamics study of the effect of leg Position on cyclist aerodynamic drag. *The American Society of Mechanical Engineers, Journal of Fluids Engineering*, *136*.
<https://doi.org/10.1115/1.4027428>
- Gross, A. C., Kyle, C. R., & Malewicki, D. J. (1983). The Aerodynamics of Human-Powered Land Vehicles. *Scientific American*. <https://doi.org/10.1038/scientificamerican1283-142>
- Grotjans, H., & Menter, F. (1998). Wall functions for general application CFD codes. In *Proceedings of the 4th Computational Fluid Dynamics Conference (ECCOMAS'98)* (pp. 1112–1114). John Wiley & Sons.
- Haake, S. J. (2009). The impact of technology on sporting performance in Olympic sports. *Journal of Sports Sciences*, *27*(13), 1421–1431. <https://doi.org/10.1080/02640410903062019>
- Hanna, R. K. (2012). CFD in Sport - a Retrospective; 1992 - 2012. *Procedia Engineering*, *34*, 622–627. <https://doi.org/10.1016/j.proeng.2012.04.106>
- Hart, J. H. (2006). The use of CFD in the chase of Olympic gold. *Sports Engineering*, 1–11.
- Jeukendrup, A. E., & Martin, J. (2001). Improving cycling performance. *Sports Medicine*, *31*(7), 559–569. <https://doi.org/10.2165/00007256-200131070-00009>
- Jones, W. P., & Launder, B. E. (1972). The prediction of laminarization with a two-equation model of turbulence. *International Journal of Heat and Mass Transfer*, *15*(2), 301–314.
[https://doi.org/10.1016/0017-9310\(72\)90076-2](https://doi.org/10.1016/0017-9310(72)90076-2)
- Knupe, J., & Farmer, D. (2009). Aerodynamics of High Performance Race Bicycle Wheels, (April 2009), 1–15.
- Kyle, C. R. (1979). Reduction of Wind Resistance and Power Output of Racing Cyclists and Runners Travelling in Groups. *Ergonomics*, *22*(4), 387–397.
<https://doi.org/10.1080/00140137908924623>
- Launder, B. E., & Spalding, D. B. (1974). The numerical computation of turbulent flows. *Computer Methods in Applied Mechanics and Engineering*, *3*(2), 269–289. <https://doi.org/10.1016/0045->

- Lee, T., & Basu, S. (1997). Nonintrusive measurements of the boundary layer developing on a single and two circular cylinders. *Experiments in Fluids*, *23*, 187–192. Retrieved from Mechanics
- Lim, A. C., Homestead, E. P., Edwards, A. G., Carver, T. C., Kram, R., & Byrnes, W. C. (2011). Measuring Changes in Aerodynamic/Rolling Resistances by Cycle-Mounted Power Meters. *Medicine & Science in Sports & Exercise*, *43*(5), 853–860.
<https://doi.org/10.1249/MSS.0b013e3181fcb140>
- Lin, J. C., Yang, Y., & Rockwell, D. (2002). Flow past two cylinders in tandem: instantaneous and averaged flow structure. *Fluids and Structures*, *16*(8), 1059–1071.
<https://doi.org/10.1006/jfls.2002.0469>
- Ljungkrona, L., Norberg, C., & Sundén, B. (1991). Free-stream turbulence and tube spacing effects on surface pressure fluctuations for two tubes in an in-line arrangement. *Journal of Fluids and Structures*, *5*(6), 701–727. [https://doi.org/10.1016/0889-9746\(91\)90364-U](https://doi.org/10.1016/0889-9746(91)90364-U)
- Lukes, R. a, Chin, S. B., & Haake, S. J. (2005). The understanding and development of cycling aerodynamics. *Sports Engineering*, *8*, 59–74. <https://doi.org/10.1007/BF02844004>
- Malalasekera, W., & Versteeg, H. K. (2007). *An Introduction to Computational Fluid Dynamics - The Finite Volume Method*. *AIAA Journal* (Vol. 44). <https://doi.org/10.2514/1.22547>
- Martin, J. C., Milliken, D., Cobb, J., McFadden, K., & Coggan, A. (1998). Validation of a mathematical model for road cycling power. *Journal of Applied Biomechanics*, *14*, 276–291.
- Maskell, E. C. (1965). A Theory of Blockage Effects on Bulff Bodies and Stalled Wings in a Closed Wind Tunnel. *Her Majesty's Stationery Office*, 1–27.
- Mazzola, M., Andreoni, G., Campanardi, G., Costa, F., Gibertini, G., Grassi, D., & Romero, M. (2012). Effects of seat and handgrips adjustments on a Hand Bike vehicle. An ergonomic and aerodynamic study for a quantitative assessment of Paralympics athletes's performance. *Advances in Usability Evaluation Part I*, (November 2017), 7167–7174.
- McCole, S. D., Claney, K., Conte, J. C., Anderson, R., & Hagberg, J. M. (1990). Energy expenditure during bicycling. *Journal of Applied Physiology (Bethesda, Md. : 1985)*, *68*(2), 748–53. Retrieved from <http://www.ncbi.nlm.nih.gov/pubmed/2318782>
- Menter, F. R. (1994). Two-equation eddy-viscosity turbulence models for engineering applications. *AIAA Journal*, *32*(8), 1598–1605. <https://doi.org/10.2514/3.12149>
- Menter, F. R. (2009). Review of the shear-stress transport turbulence model experience from an industrial perspective. *International Journal of Computational Fluid Dynamics*, *23*(4), 305–316. <https://doi.org/10.1080/10618560902773387>
- Menter, F. R., Langtry, R. B., Likki, S. R., Suzen, Y. B., Huang, P. G., & Völker, S. (2006). A correlation-based transition model using local variables—Part I: model formulation. *Journal*

- of Turbomachinery*, 128(3), 413–422. <https://doi.org/10.1115/1.2184352>
- Meroney, R. N. (2016). Ten questions concerning hybrid computational/physical model simulation of wind flow in the built environment. *Building and Environment*, 96, 12–21. <https://doi.org/10.1016/j.buildenv.2015.11.005>
- Meroney, R. N., & Derickson, R. (2014). Virtual reality in wind engineering: the windy world within the computer. *Journal of Wind Engineering*, 11(2), 11–26.
- Murakami, S. (1997). Current status and future trends in computational wind engineering. *Journal of Wind Engineering and Industrial Aerodynamics*, 67–68, 3–34. [https://doi.org/10.1016/S0167-6105\(97\)00230-4](https://doi.org/10.1016/S0167-6105(97)00230-4)
- Oggiano, L., Leirdal, S., Sætran, L., & Ettema, G. (2008). Aerodynamic Optimization and Energy Saving of Cycling Postures for International Elite Level Cyclists. *The Engineering of Sport* 7, 1(2), 597–604. https://doi.org/10.1007/978-2-287-09411-8_70
- Prasuhn, J. (2007). “Revolutionary Speed: Zipp’s Wind Tunnel Test.” *Triathlete*, June 2004, 192–195.
- Rouboa, A., Silva, A., Leal, L., Rocha, J., & Alves, F. (2006). The effect of swimmer’s hand/forearm acceleration on propulsive forces generation using computational fluid dynamics. *Journal of Biomechanics*, 39(7), 1239–1248. <https://doi.org/10.1016/j.jbiomech.2005.03.012>
- Sayers, A. T., & Stanley, P. (1994). Drag force on rotating racing cycle wheels. *Journal of Wind Engineering and Industrial Aerodynamics*, 53(3), 431–440. [https://doi.org/10.1016/0167-6105\(94\)90094-9](https://doi.org/10.1016/0167-6105(94)90094-9)
- Sciacchitano, A., Caridi, G. C. A., & Scarano, F. (2015). A quantitative flow visualization technique for on-site sport aerodynamics optimization. *Procedia Engineering*, 112, 412–417. <https://doi.org/10.1016/j.proeng.2015.07.217>
- Solari, G. (2007). The International Association for Wind Engineering (IAWE): Progress and prospects. *Journal of Wind Engineering and Industrial Aerodynamics*, 95(9–11), 813–842. <https://doi.org/10.1016/j.jweia.2007.01.010>
- Spalart, P., & Allmaras, S. (1992). A one-equation turbulence model for aerodynamic flows. In *30th Aerospace Sciences Meeting and Exhibit*. American Institute of Aeronautics and Astronautics. <https://doi.org/http://doi.org/doi:10.2514/6.1992-439>
- Spoelstra, A., Terra, W., & Sciacchitano, A. (2018). The Ring of Fire for in-Field Sport Aerodynamic. <https://doi.org/10.3390/proceedings2060221>
- Stathopoulos, T. (1997). Computational wind engineering: Past achievements and future challenges. *Journal of Wind Engineering and Industrial Aerodynamics*, 67–68, 509–532. [https://doi.org/10.1016/S0167-6105\(97\)00097-4](https://doi.org/10.1016/S0167-6105(97)00097-4)

- Sumner, D. (2010). Two circular cylinders in cross-flow : A review. *Journal of Fluids and Structures*, 26(6), 849–899. <https://doi.org/10.1016/j.jfluidstructs.2010.07.001>
- Tew, G. S., & Sayers, a. T. (1999). Aerodynamics of yawed racing cycle wheels. *Journal of Wind Engineering and Industrial Aerodynamics*, 82(1), 209–222. [https://doi.org/10.1016/S0167-6105\(99\)00034-3](https://doi.org/10.1016/S0167-6105(99)00034-3)
- Thompson, L. (1998). Engineering the world’s fastest bicycle. *The Engineering of Sport*.
- Tominaga, Y., Mochida, A., Yoshie, R., Kataoka, H., Nozu, T., Yoshikawa, M., & Shirasawa, T. (2008). AIJ guidelines for practical applications of CFD to pedestrian wind environment around buildings. *Journal of Wind Engineering and Industrial Aerodynamics*, 96(10–11), 1749–1761. <https://doi.org/10.1016/j.jweia.2008.02.058>
- Tominaga, Y., & Stathopoulos, T. (2013). CFD simulation of near-field pollutant dispersion in the urban environment: A review of current modeling techniques. *Atmospheric Environment*, 79, 716–730. <https://doi.org/10.1016/j.atmosenv.2013.07.028>
- Tominaga, Y., & Stathopoulos, T. (2016). Ten questions concerning modeling of near-field pollutant dispersion in the built environment. *Building and Environment*, 105, 390–402. <https://doi.org/10.1016/j.buildenv.2016.06.027>
- Tucker, P., & Mosquera, A. (2001). NAFEMS introduction to grid and mesh generation for CFD. *NAFEMS CFD Working Group*.
- Underwood, L., & Jermy, M. (2010a). Mathematical model of track cycling: the individual pursuit. *Procedia Engineering*, 2(2), 3217–3222. <https://doi.org/10.1016/j.proeng.2010.04.135>
- Underwood, L., & Jermy, M. (2010b). Optimal hand position for individual pursuit athletes. In *8th Conference of the International Sports Engineering Association, Procedia Eng.* (Vol. 2, pp. 2425–2429). <https://doi.org/10.1016/j.proeng.2010.04.010>
- Underwood, L., & Jermy, M. (2013). Optimal handlebar position for track cyclists. *Sports Engineering*, 16(2), 81–90. <https://doi.org/10.1007/s12283-013-0111-5>
- Underwood, L., Jermy, M., Eloi, P., & Cornillon, G. (2015). Helmet position, ventilation holes and drag in cycling. *Sports Engineering*, 18(4), 241–248. <https://doi.org/10.1007/s12283-015-0181-7>
- Underwood, L., Schumacher, J., Burette-Pommay, J., & Jermy, M. (2011). Aerodynamic drag and biomechanical power of a track cyclist as a function of shoulder and torso angles. *Sports Engineering*, 14(2–4), 147–154. <https://doi.org/10.1007/s12283-011-0078-z>
- Walters, D. K., & Cokljat, D. (2008). A three-equation eddy-viscosity model for Reynolds-Averaged Navier–Stokes simulations of transitional flow. *Journal of Fluids Engineering*, 130(12), 121401. <https://doi.org/10.1115/1.2979230>
- Wilcox, D. C. (1993). *Turbulence Modeling for CFD*. DCW Industries, Inc.

- Wilson, D. G., & Papadopoulos, J. (2004). *Bicycling Science*. MIT Press. Retrieved from <https://books.google.com/books?hl=en&lr=&id=0JJo6DIF9iMC&pgis=1>
- Wolfshtein, M. (1969). The velocity and temperature distribution in one-dimensional flow with turbulence augmentation and pressure gradient. *International Journal of Heat and Mass Transfer*, *12*, 301–318. [https://doi.org/10.1016/0017-9310\(69\)90012-X](https://doi.org/10.1016/0017-9310(69)90012-X)
- Xu, G., & Zhou, Y. (2004). Strouhal numbers in the wake of two inline cylinders, *37*, 248–256. <https://doi.org/10.1007/s00348-004-0808-0>
- Zdravkovich, M. M. (1987). The effects of interference between circular cylinders in crossflow. *Fluids and Structures*, 239–261.
- Zdravkovich, M., Ashcroft, M., Chisholm, S., & Hicks, N. (1996). Effect of cyclist's posture and vicinity of another cyclist on aerodynamic drag. In *The Engineering of sport* (1st Ed., pp. 21–30). Balkema, Rotterdam.
- Zdravkovich, M. M. (1992). Aerodynamics of bicycle wheel and frame. *Journal of Wind Engineering and Industrial Aerodynamics*, *40*(1), 55–70. [https://doi.org/10.1016/0167-6105\(92\)90520-K](https://doi.org/10.1016/0167-6105(92)90520-K)
- Zhou, Y., & Yiu, M. W. (2006). Flow structure, momentum and heat transport in a two-tandem-cylinder wake. *Journal of Fluid Mechanics*, *548*, 17–48. doi:10.1017/S002211200500738X

Part I: Tandem cycling

Improving CFD prediction of drag on Paralympic tandem athletes: influence of grid resolution and turbulence model

Chapter 3 is the first chapter of four in Part I of this thesis, which focuses on tandem cycling. This chapter focuses on aspects of CFD modelling central to attaining reliable results specific to tandem cycling. New guidelines for the selection of a suitable turbulence model and grid topology for the analysis of tandem cycling aerodynamics using CFD are outlined based on sensitivity studies. Novel wind tunnel experiments that provided aerodynamic force data for the pilot and stoker independently and simultaneously were used to provide validation data.

This chapter has been published in the international peer-reviewed journal *Sports Engineering*:

Mannion, P., Toparlar, Y., Blocken, B., Hajdukiewicz, M., Andrienne, T., & Clifford, E. (2018). Improving CFD prediction of drag on Paralympic tandem athletes: Influence of grid resolution and turbulence model. *Sports Engineering*, 21(2), 123–135.
<http://doi.org/10.1007/s12283-017-0258-6>

Abstract: Tandem cycling enables visually impaired athletes to compete in cycling in the Paralympics. Tandem aerodynamics can be analysed by track measurements, wind tunnel experiments and numerical simulations by Computational Fluid Dynamics (CFD). However, the proximity of the pilot (front) and the stoker (rear) and the associated strong aerodynamic interactions between both athletes present substantial challenges for CFD simulations, the results of which can be very sensitive to computational parameters such as grid topology and turbulence model. To the best of our knowledge, this paper presents the first CFD and wind tunnel investigation on tandem cycling aerodynamics. The study analyses the influence of the CFD grid topology and the turbulence model on the aerodynamic forces on pilot and stoker and compares the results with wind tunnel measurements. It is shown that certain combinations of grid topology and turbulence model give trends that are opposite to those shown with other combinations. Indeed, some combinations provide counter-intuitive drag outcomes with the stoker experiencing a drag force up to 28% greater than the pilot. Furthermore, the application of a blockage correction for two athlete bodies in close proximity is investigated. Based on a large number of CFD simulations and validation with wind tunnel

measurements, this paper provides guidelines for the accurate CFD simulation of tandem aerodynamics.

3.1 Introduction

Tandem cycling is a specific discipline within para-cycling categories, with races on both the road and track (velodrome). A tandem bicycle accommodates two athletes, the pilot on the front saddle, and the stoker on the rear. Within the para-cycling community, the stoker is visually impaired, hence the necessity for a fully sighted pilot to steer the tandem at road or track race events (UCI, 2017). Methods to improve an athlete's aerodynamic profile include track ergometer measurements, wind tunnel experiments and Computational Fluid Dynamics (CFD) simulations (Blocken, 2014; Blocken & Toparlak, 2015; Blocken et al., 2016; Crouch et al., 2017; Fintelman et al., 2015; Griffith et al., 2014).

CFD provides whole flow-field data in the computational domain which can substantially increase the insight into the flow processes. Para-cycling has, to date, not seen the same knowledge investment compared to its able-bodied counterpart. To the best of our knowledge, there has been no previous analysis of para-cycling aerodynamics that utilised CFD simulations. In relation to other para-cycling disciplines, Belloli et al. (2014) investigated the aerodynamics of Paralympic hand-cycling categories using wind tunnel experiments, while the opportunities for aerodynamics enhancements with regards to prosthetics in cycling were tested by Dyer (2015) on an outdoor velodrome.

The closest aerodynamic analogy to tandem cycling in the literature is the phenomenon of drafting, where two or more cyclists are in close proximity to one another. On a fundamental level, Alam, (2014) addressed the flow characteristics of inline configurations of two cylinders. Drag and lift coefficients were found to be highly sensitive to Reynolds number due to changes in flow structure. Íñiguez-de-la Torre & Íñiguez (2009) performed 2D CFD studies using elliptical inline shapes to represent cyclists, finding drag benefits of up to 5% for the leading cyclist. Blocken et al. (2013) performed CFD simulations and a wind tunnel test revealing for the first time that the leading cyclist experienced a drag reduction up to 2.6% for closely drafting cyclists in time-trial position. This work was expanded to four cyclists by Defraeye et al. (2014) who reported that second from front and subsequent positions in a team pursuit experienced drag reductions up to 40%. Barry et al. (2015) reported mean drag savings of 5%, 45%, 55% and 57% for four cyclists positioned behind each other, respectively. Barry et al. (2016) also experimentally analysed the flow structures occurring in drafting. Parallels between tandem cycling and the physics of drafting can also be drawn with the

work of Blocken & Toparlar, (2015) and Blocken et al. (2016), who investigated the aerodynamic benefit for a cyclist by a trailing/following car and motorcycle, respectively, which they attributed to the subsonic upstream disturbance typical of the elliptical character of the governing Navier-Stokes equations. Although drafting is the closest analogy to tandem cycling, the difference in distance between respective athletes in a tandem setup and a drafting setup is large. Drafting cyclists can have a wheel to wheel distance of 0.12 m (or less), which implies about 1.8 m between each athlete on a regular average sized racing bicycle, measured from the same point on both athletes. In comparison, the equivalent point to point distance between a pilot and stoker on a tandem bicycle is 0.8 m, which is significantly less. The close proximity of the pilot and stoker is expected to result in large aerodynamic interactions between the two athletes.

A variety of turbulence models and near-wall modelling treatments were assessed by Defraeye et al. (2010) for their impact on computed cyclist drag and compared with wind tunnel experiments. Several steady Reynolds-Averaged Navier-Stokes (RANS) turbulence models as well as Large Eddy Simulations (LES) were compared with the experimental data. The Shear Stress Transport (SST) k - ω turbulence model (Menter, 1994) provided the best overall agreement with the experimentally obtained drag (4% difference). Moreover, studies focusing on cycling and automotive aerodynamic interactions found good agreement between experimental data and CFD simulations (Blocken & Toparlar, 2015; Blocken et al., 2016) when using the standard k - ϵ turbulence model (Jones & Launder, 1972) with scalable wall functions (Grotjans & Menter, 1998) to resolve the near-wall flow.

This paper provides new guidelines for CFD simulations for tandem cycling aerodynamics, with specific attention to near-wall grid resolution and turbulence model choice. The application of a wind tunnel solid blockage correction to tandem athletes is explored. Furthermore, the forces experienced by pilot and stoker are investigated separately to provide an understanding of the drag interaction between the pilot and stoker athletes.

3.2 CFD simulations - initial findings

3.2.1 Computational parameters

3.2.1.1 Tandem geometry and computational domain

The tandem cycling setup considered in this study was selected to resemble a road race scenario. Standard road helmets as opposed to more aerodynamic time-trial (TT) helmets were used and simplified spoked wheels were fitted to the tandem bicycle opposed to disk or trispoke wheels.

For the purposes of this study, the bicycle geometry was simplified by neglecting the chain, sprocket, derailleur, brake mechanisms and cables. The wheel spokes were also simplified, with twelve spokes of 0.012 m diameter modelled for front and rear wheel. An Eva (Artec, 2017) structured light 3D scanner provided high resolution 3D models of an athlete and a helmet (Bontrager Ballista). The same athlete geometry was used for pilot and for stoker to provide good comparability without inferring drag bias towards either pilot or stoker. The athlete was scanned in an aggressive dropped posture typically used by both tandem athletes in road races. The full-scale model for the CFD simulations had a frontal area of 0.399 m².

A 80x28x28 m³ cuboid was used for the computational domain (Figure 3.1) with the tandem geometry at 28 m from the inlet (Figure 3.1). The domain size resulted in a blockage ratio of 0.06%, below the 3% recommendation (Blocken, 2015; Casey & Wintergerste, 2000; Franke et al., 2007; Tominaga et al., 2008). Therefore blockage corrections were not required. A gap of 0.025 m between wheel bottom and ground surface was used to avoid skewed and low-quality computational cells.

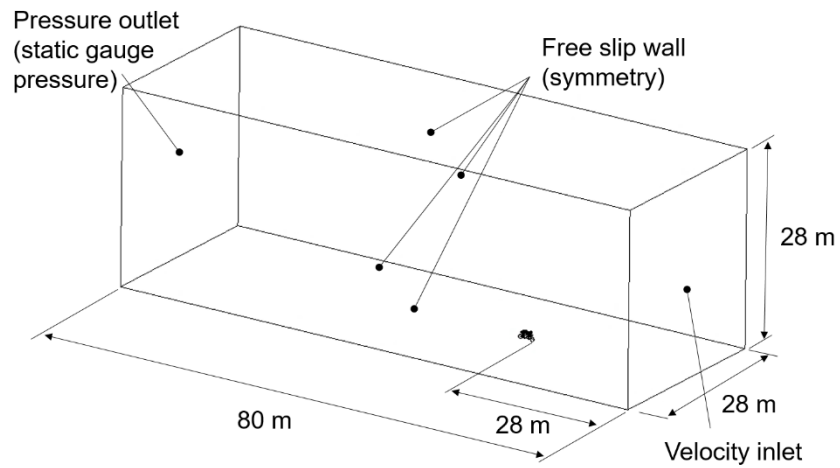


Figure 3.1. Dimensions of the computational domain and positioning of flow boundaries.

3.2.1.2 Computational grid

The grid resolution is assessed based on the dimensionless wall unit y^* :

$$y^* = \frac{u^* y_P}{\nu} \quad (3.1)$$

where u^* is the friction velocity (Eq. 3.2), y_P is the normal distance of the cell centre point P from the wall surface, ν is the local kinematic viscosity.

$$u^* = C_\mu^{\frac{1}{4}} k_P^{\frac{1}{2}} \quad (3.2)$$

where $C_\mu = 0.09$, and k_P the turbulent kinetic energy at P.

The grids generated in this study were based on (Casey & Wintergerste, 2000; Franke et al., 2007; Tominaga et al., 2008; Tucker & Mosquera, 2001). Two different grid topologies were devised; (i) a tetrahedral-only grid and (ii) a combined prismatic-tetrahedral grid, with prismatic cells in the boundary layers and tetrahedral cells beyond.

A grid-sensitivity study, comprising of a coarse, medium and fine tetrahedral-only grid, was conducted, with the surface grid systematically refined with each face size halved for the progressive grids. The boundary layer resolution depended on the tetrahedral cell size at the surfaces of interest for each grid as no prism layers were used. The grid sizes were 11.1, 24.6 and 64.9 million cells, respectively. The medium grid was selected as a reference grid for surface face sizings for subsequent grids, providing a compromise between accuracy and computational expense. Cell face sizes varied depending on the location of the surface on the athlete or bicycle geometry. All facet edge length (m) dimensions are provided in Table 3.1. The dimensions are normalised by the diameter of the athlete’s head (0.2 m). A new grid was created, denoted as grid 1, which stemmed from the medium grid in the grid independence study. Figure 3.2a and Figure 3.2c illustrate segments of the surface grid, and also the volume grid in a vertical centre-plane. The total number of cells in grid 1 was 20.2 million.

Table 3.1. Grid surface face sizes for respective surface components. Dimensions are normalised by the diameter of the athlete’s head (0.2 m).

	Edge length (m)	Normalised length
Torso	0.005	0.025
Legs	0.003	0.015
Head/helmet	0.002	0.01
Arms	0.0018	0.009
Frame	0.002	0.01
Wheel tyres/rims	0.0015	0.0075
Spokes	0.0005	0.0025

For the second grid used in this study, denoted as grid 2, settings for grid 1 were implemented as the background grid with the addition of prism cells to all wall surfaces in the boundary layers, as advised by Tominaga et al. (2008), Tucker & Mosquera, (2001), and Blocken, (2015). This yielded a y_P of 17.5 μm , an average y^* of 0.80 and a max y^* of 2.75. Note that $y^* \approx 1$ and < 5 is required to resolve the thin viscous sublayers to reproduce boundary layer flow and potential separation. The near-wall prism layers are illustrated in Figure 3.2d. 20 prism cells with a growth ratio of 1.2 were used. This combined prismatic-tetrahedral volume grid is denoted as grid 2 (Figure 3.2b,d). The total number of cells in grid 2 was 33.3 million.

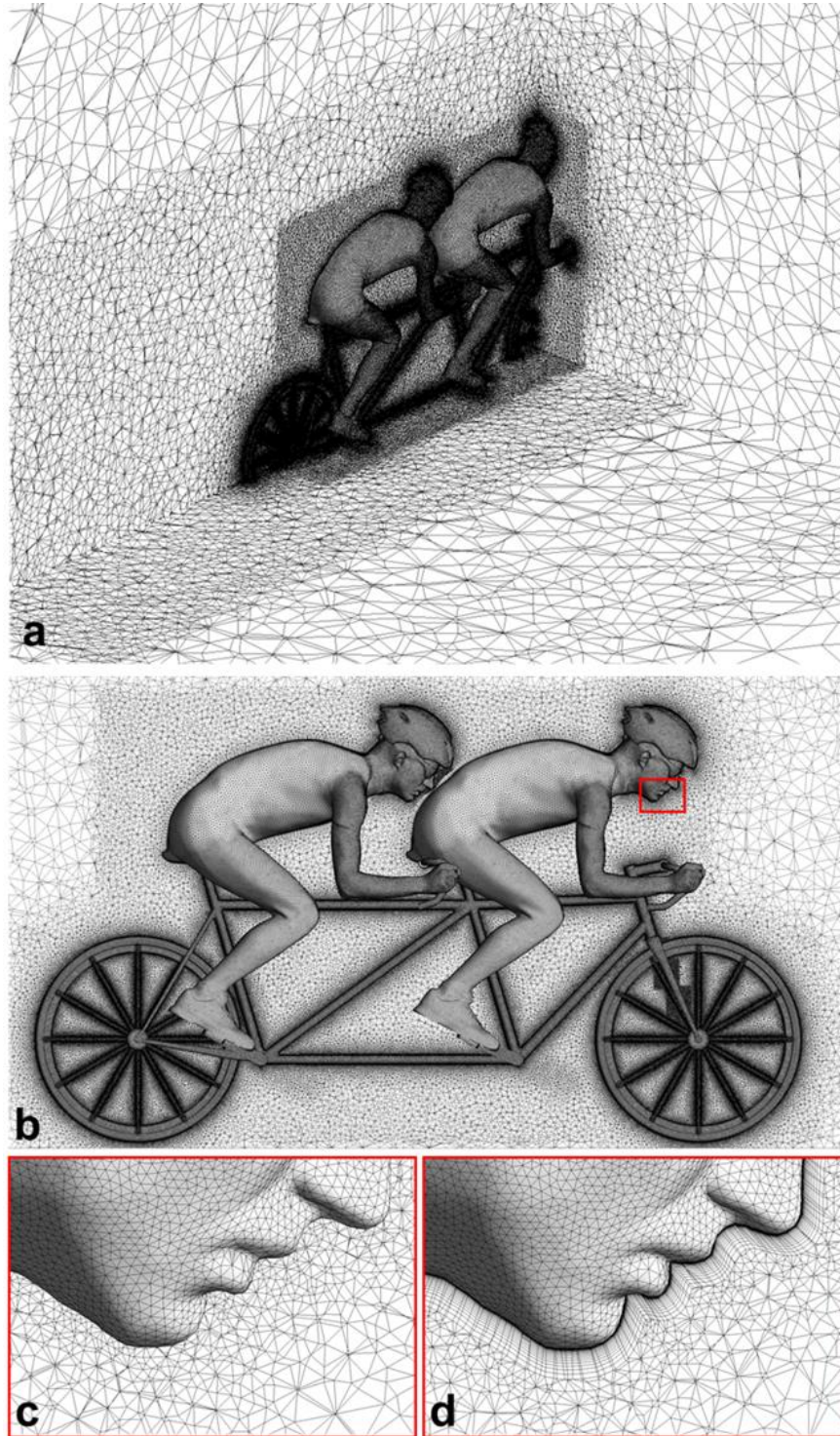


Figure 3.2. (a) Surface grid on the tandem geometry and part of the volume grid surrounding the tandem geometry (grid 2–33.3 million cells), (b) surface and volume grid of tandem geometry (grid 2–33.3 million cells), (c) tetrahedral cell growth from the surface grid on the face of the pilot (grid 1–20.2 million cells), (d) prism layer growth from the surface grid on the face of the pilot (grid 2–33.3 million cells).

3.2.1.3 Boundary conditions

A uniform velocity of 15 m/s with 0.2% turbulence intensity and a hydraulic diameter of 1 m was applied as a velocity inlet condition. Air with a density of 1.225 kg/m³ and a viscosity of 1.789e-5 kg/m.s was specified as the fluid. Zero static gauge pressure was applied to the outlet boundary. A symmetry condition was applied for the lateral boundaries, the top boundary, and also for the ground boundary to represent a free-slip wall. A no-slip wall with zero roughness was applied for the tandem bicycle surfaces and for the athlete surfaces.

3.2.1.4 Governing equations & solver settings

The simulations were performed using ANSYS Fluent 16 (ANSYS, 2015). The RANS equations were solved with the shear stress transport (SST) k- ω turbulence model (Menter, 1994). The Least Squares Cell Based method was used to compute gradients (ANSYS, 2015). The Coupled algorithm was used for pressure-velocity coupling. Second-order pressure interpolation was used, along with second-order discretisation schemes for all equations. Due to the inherent unsteady nature of tandem cycling aerodynamics, the pseudo-transient solver within Fluent was used. Averaging was required for the resulting forces from the pseudo-transient simulations where steady-state convergence was unachievable. A study was conducted to determine a suitable pseudo-transient time-step, with values decreasing by one order of magnitude from 0.1 s to 1e-05 s. Drag values were averaged over 4500 iterations after an oscillatory phase was reached. A negligible difference was found varying time-step size, with a final size of 0.01 s used to allow for sufficient oscillations to occur over 2000 iterations for averaging purposes. All simulations reported were averaged over 2000 iterations after results reached a statistically steady state.

3.2.2 Drag findings

The drag coefficient is described by:

$$C_D = \frac{F_D}{0.5\rho AV^2} \quad (3.3)$$

where F_D is the drag force (N), ρ the density (kg/m³), A the frontal area (m²) and V the velocity (m/s).

The total drag force of bicycle and two riders for grid 1 and grid 2 were 39.6 N and 43.2 N, respectively (C_D of 0.718 and 0.787). It was expected that the stoker would experience a lower drag than the pilot due to drafting. However, Figure 3.3 shows that grid 1 yielded an opposite drag distribution: 35.9% of total drag for the pilot and 46.1% for the stoker. Grid 2 however, yielded 52.5% of total drag for the pilot and 26.9% for the stoker.



Figure 3.3. Drag force (N) on the pilot and stoker using different grids. The details of grid 1 (tetrahedral-only) and grid 2 (tetrahedral-prismatic) are discussed in Section 3.2.1.2.

Figure 3.4 shows the differences in surface pressure coefficient, normalised wall shear stress, and the sum of both these quantities for grids 1 and 2. It is clear that the grid resolution in the boundary layer and its impact on the flow separation locations and resulting wake flow played a critical role in the drag differences between both grids. This is also shown by Figure 3.5. While the over-pressure on the stoker by grid 1 (Figure 3.5a) suggests that the pilot and stoker were acting as independent bodies, the pressure coefficient by grid 2 seemed to suggest that they rather acted as a single body. Two cylinders in tandem were also found to act as a single body when in close proximity (Alam, 2014; Sohankar, 2012). The friction drag was found to contribute only 8.2% and 5.7% to the total drag experienced by the pilot and the stoker respectively for grid 1, and 3.4% and 5.6% for grid 2. The primary difference in the drag forces was in pressure drag, caused by differences in the pressure recovery predictions due to the difference in flow separation locations between grid 1 and grid 2, rather than the magnitude of the friction drag predictions. Note that the athletes experienced a larger viscous drag for grid 1 due to the flow staying attached for longer to the surfaces of the athletes. Figure 3.5b depicts the flow staying attached to the back of the pilot and traversing around the saddle for grid 1, travelling in the opposite direction to the flow in grid 2 at the same location. To further elucidate the opposing results regarding the pilot and stoker's drag forces for two different grids, wind tunnel experiments and CFD simulations with different grid topologies and turbulence models were performed.

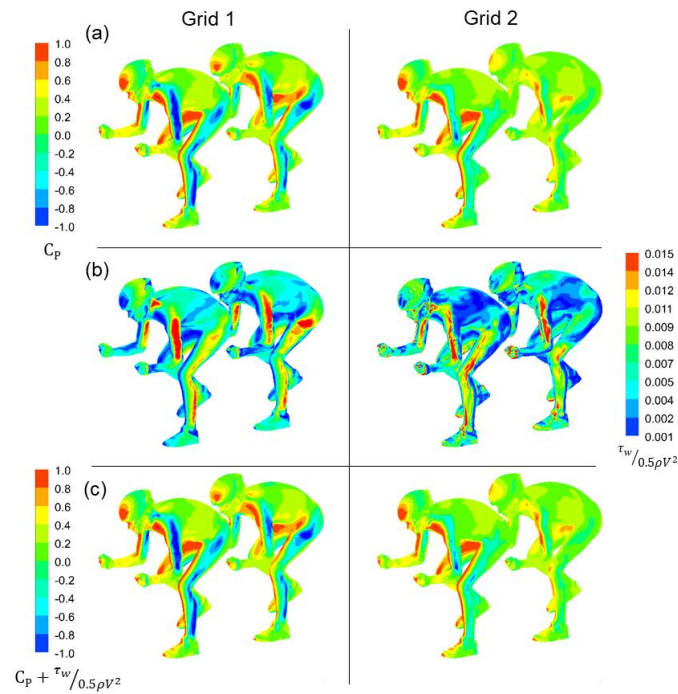


Figure 3.4. Comparison between grid 1 and grid 2 for (a) surface pressure coefficient, (b) normalised shear stress, and (c) sum of the surface pressure coefficient and normalised wall shear stress. C_p is the surface pressure coefficient, τ_w is the wall shear stress, ρ is the density and V is the reference velocity.

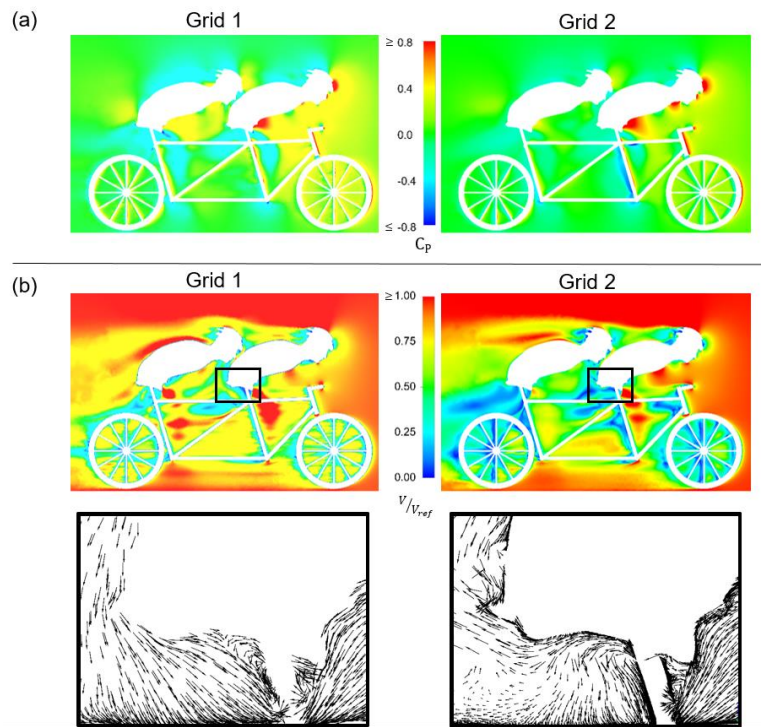


Figure 3.5. Comparison between grid 1 and grid 2 for (a) static pressure coefficient, and (b) normalised velocity in a centre-plane through the fluid domain, and vector plots of the flow under the pilot's saddle.

3.3 Wind tunnel experiments

3.3.1 Experimental setup

The wind tunnel experiment was performed at the University of Liège, Belgium. The test chamber had a cross sectional area of $2 \times 1.5 \text{ m}^2$. A sharp edged horizontal platform was elevated by 0.3 m from the test section floor to separate the test geometries from the boundary layer at the tunnel floor (Figure 3.6). The quarter-scale tandem geometry was divided into 4 separated components (Figure 3.7a-b), and thus, the drag on the bodies of the pilot and stoker was measured separately. The handlebars remained attached to the hands of the athletes, but not to the bicycle frame. The tandem bicycle was separated in the middle to allow for it to be passed through the athletes' legs and reattached with tight fitting sleeves. This was done to remove vibrations at the end of the tube lengths. Both athletes had filleted cuboid supports connecting their feet to individual baseplates, labelled in Figure 3.7b as athlete supports. Both the front and rear bicycle frame and wheel components received additional supports to remove vibrations from the smaller components present. No visible vibrations occurred during testing. The largest supports are labelled as bicycle support in Figure 3.7b. The front forks were simplified to a single cylindrical tube of equal diameter to the head tube. Additional changes implemented for the tandem geometries for the wind tunnel experiments included the removal of pedals, cranks and seat tubes to separate the athlete geometries from that of the tandem bicycle. The athletes and bicycle geometries were manufactured to $\frac{1}{4}$ scale (Figure 3.7c), with the support structures and baseplates included in the geometrical models. This allowed for the athlete geometries to be directly connected to the force sensors without any intermediate connection component. The blockage ratio for the setup including plate and supporting structure was 2.2%. 3D solid blockage corrections by Barlow et al. (1999) were applied, which are applicable in the blockage ratio range of 1-10% (Barlow et al., 1999). A body shape value 'K' of 0.96 was used to approximate the shape of the tandem. A flow velocity of 60 m/s was used to match the Reynolds number of the quarter-scale tests with that of full-scale tandem cyclists at 15 m/s.

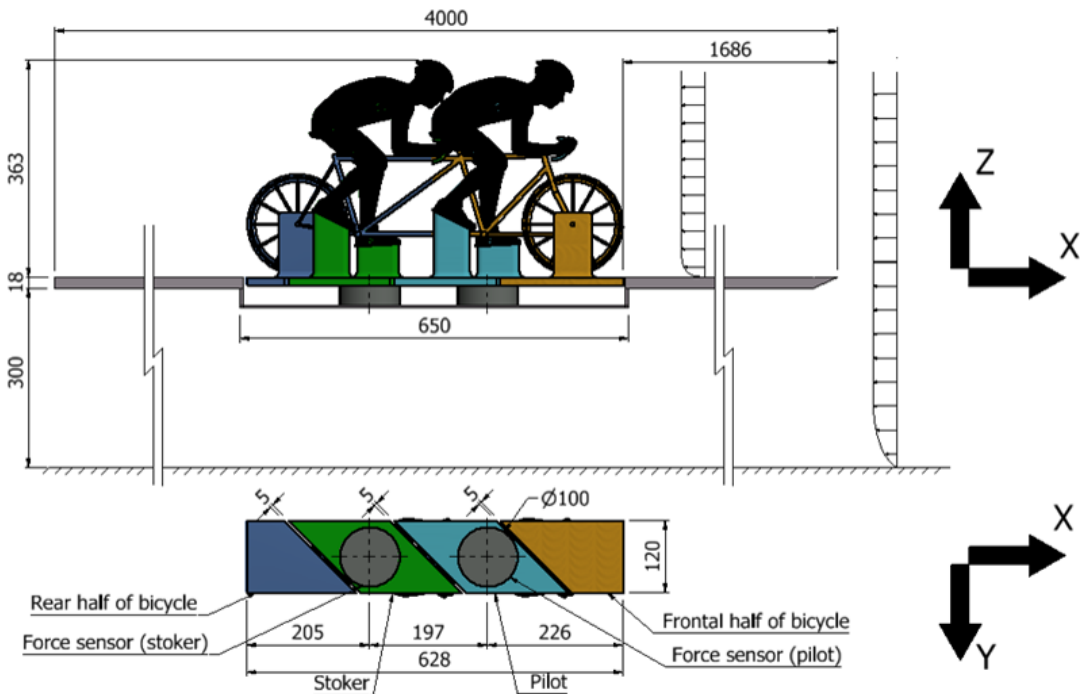


Figure 3.6. Simplified diagram of the wind tunnel setup, adapted from Blocken et al. (2016), utilising the same wind tunnel facilities and platform. All dimensions are in mm. X, Y and Z directions indicated are positive force readout directions from both force sensors.

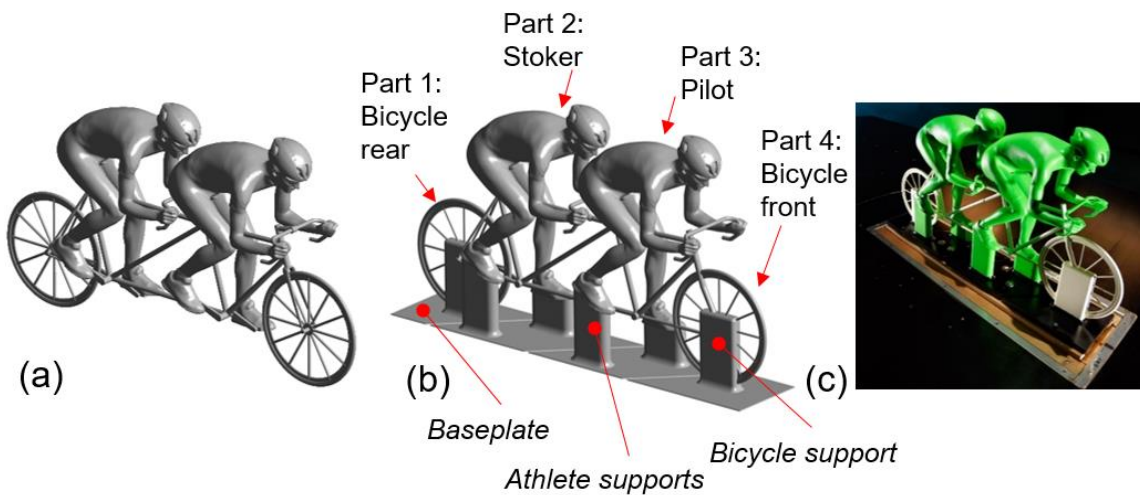


Figure 3.7. (a) An accurate representation of tandem geometry, (b) simplified tandem geometry with additional supports and baseplates required for the wind tunnel experiments, (c) manufactured model in the wind tunnel.

Both athletes were individually attached to separate force transducers, for separate and simultaneous readouts during the experiment. Force was sampled at 10 Hz for 180 s during the experiment. A maximum error of 1.24 N at a 95% confidence interval was provided by the manufacturers for both force transducers. This error included systematic and random errors, the

former of which was removed via biasing the transducers prior to imparting a wind load. Air velocity (x direction, Figure 3.6) was recorded inside the wind tunnel using a pitot tube. Air temperature was also recorded to correct drag measurements to an air density at 15°C, for comparison with the CFD simulations, where an air density of 1.225 kg/m³ was used. The approach-flow longitudinal turbulence intensity was 0.2% (Blocken et al., 2016).

3.3.2 Experimental results

The experiments showed that the stoker experienced 39% less drag than the pilot (15.55 N and 25.52 N respectively), in addition to lower lift and lateral forces (Figure 3.8). The stoker experienced a lateral force negative to the axis direction, which pushed the athlete to his right, while the pilot was pushed to his left. Both the pilot and stoker experienced a positive lift force of 34% and 44% of the drag forces experienced by the pilot and stoker respectively. The counter-intuitive drag findings in section 3.2.2 using grid 1 (section 3.2.2) were incorrect, where the stoker experienced a drag force 40% greater than the pilot. However, grid 2 did provide the correct trend in drag forces of both athletes (section 3.2.2).

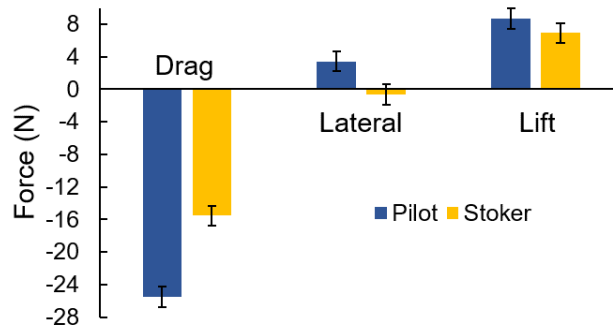


Figure 3.8. Wind tunnel drag, lateral and lift force results on both the pilot and stoker geometries, with error bars ± 1.24 N for systematic and random errors. The drag values are depicted as negative as per the orientation of the force transducers (Figure 3.7).

3.4 Impact of grid resolution and turbulence model on tandem drag

3.4.1 Computational settings

For CFD validation, new digital geometries were made representative of those in the wind tunnel experiment (Figure 3.7b), with foot supports, wheel supports, and baseplate geometries

included. Note that the CFD geometry was made at full-scale. The new frontal area of the tandem bicycle and athlete's wind tunnel geometry with supports included was 0.455 m² at full-scale (0.028 m² at quarter-scale). The drag on the handlebars, supports and baseplates connected to the athletes was included in the drag summations for the pilot and stoker, while the drag on the tandem bicycle was not considered.

A new grid sensitivity study consisting of a coarse, medium and fine tetrahedral-only grid, was conducted on the new geometrical model using the face sizes on athletes and bicycle surfaces as described in section 3.2.1.2. The medium grid was chosen to provide the sizing for a tetrahedral-prismatic grid with prism layers identical to those described in grid 2, section 3.2.1.2. This tetrahedral-prismatic grid, denoted as grid 3a, contained 38.2 million control volumes. A no-slip wall boundary condition was applied to the baseplate and support surfaces. A free-slip wall was applied to the ground surfaces surrounding the geometrical model. The SST k- ω turbulence model (Menter, 1994) was used for this study, with all solver parameters kept the same as in section 3.2.1.4. With this starting point, the impact of near-wall grid resolution (y^*) and turbulence model was investigated.

3.4.2 Results

3.4.2.1 Impact of near-wall grid resolution (y^*)

Seven additional tetrahedral-prismatic grids were created, representative of grid 3a (section 3.4.1). However, the y_P was doubled for each grid, yielding grids b-h (Figure 3.9). The y^* values reported in this section relate to the surfaces of pilot and stoker geometries attached to the force sensors (Figure 3.6). Figure 3.10 illustrates the y^* distribution for grid 3a, which had a y_P of 0.0175 mm, resulting in an average y^* of 0.80, and a maximum y^* of 2.75. An additional tetrahedral-only grid was created with no prism layers growing from wall surfaces, using the grid parameters described for grid 1 (section 3.2.1.2). This grid is denoted as grid 3i. The average y^* of grid 3i was 57.09, with a maximum y^* of 240 due to the variance in y_P resulting from the range of face sizes. For comparison, grid 3g obtained an average y^* value of 58.15 using prism cells, but a maximum y^* value of only 119 was obtained.



Figure 3.9. A comparison of drag force (N) on the pilot and stoker including baseplates, supports and handlebars across computational grids with varying average y^* values. Note that for the tetrahedral grid, the max y_P is provided, where a variety of smaller y_P values are present due to the dependency of y_P on the tetrahedral cell size.

Figure 3.9 presents the drag forces for each grid. Note that drag forces on baseplates, supports and handlebars were included in the CFD outputs for comparison to the wind tunnel data. As the average y^* increased from 0.80 to 108.80, the pilot experienced a reducing drag force while the stoker experienced an increasing drag force. The stoker experienced a larger drag than the pilot at an average y^* of 108.80, when using prism layers at wall surfaces (grid 3h). However, when using tetrahedral cells to resolve the wall bounded flow (grid 3i), this effect was magnified, resulting in the stoker experiencing a drag force 29.4% larger than the pilot. It was observed that separation was delayed or prevented by low boundary layer resolution modelling, causing the disparities between drag forces for high resolution and low resolution grids, as per Figure 3.5.

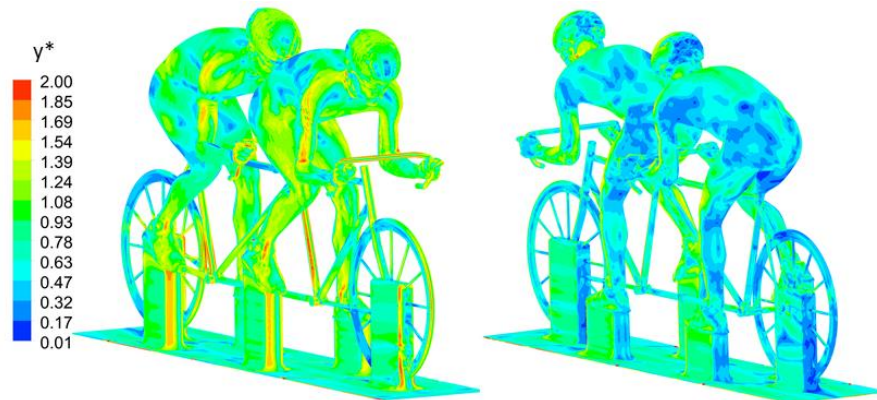


Figure 3.10. y^* contours ranging from ≥ 2 to ≤ 0.01 across the tandem wind tunnel geometry surfaces, with a maximum value of 2.75, for grid 3a.

To determine if the near-wall grid resolution of grid 3a was suitable for transitional turbulence models, an additional grid (grid 3j) was created based on the same geometrical geometry with a y_p of 0.0025 mm, a growth ratio of 1.15, and 36 prism layers, which yielded an average and maximum y^* of 0.10 and 0.89 respectively. The 4-equation transitional SST (T-SST) $k-\omega$ (Menter et al., 2006) turbulence model was tested with both grids. A 0.4% and 2.5% difference was found between grid 3a and grid 3j for drag on the pilot and stoker respectively, which was determined as too small to warrant the additional computational expense of utilising grid 3j. Thus, grid 3a was chosen for a turbulence model sensitivity analysis in section 3.4.2.2.

3.4.2.2 Impact of turbulence model

Eight turbulence models were applied to grid 3a: the T-SST $k-\omega$ (Menter et al., 2006), the $k-kl-\omega$ (Walters & Cokljat, 2008), the intermittency SST $k-\omega$ (Menter et al., 2006), the SST $k-\omega$ (Menter, 1994), the standard $k-\varepsilon$ (Jones & Launder, 1972), the realizable $k-\varepsilon$ (Shih et al., 1995), the renormalization-group (RNG) $k-\varepsilon$ (Choudhury, 1993), and the 1-equation Spalart-Allmaras turbulence model (Spalart & Allmaras, 1992). The 1-equation Wolfshtein model (Wolfshtein, 1969) was used for low Reynolds number modelling with the $k-\varepsilon$ models. Second-order discretisation schemes were used for the convective and viscous terms of all equations. The results are summarised in Figure 3.11 and Table 3.2. The T-SST model provided drag predictions for the pilot and stoker that deviated by -1.0% and -14.4%, respectively, from the wind tunnel results. The T-SST model also failed to predict the correct direction of the lateral force on the pilot. The intermittency SST $k-\omega$ model provided comparable results to the T-SST model, with drag deviations of 2.4% and -13.5% for the pilot and stoker respectively. The $k-kl-\omega$ model under-predicted drag for the pilot by -14.1%, and over-predicted drag on the stoker by 4.6%. However, it predicted all lateral and lift forces to within the error region of the force transducers for both the pilot and stoker. The SST $k-\omega$ models predicted the drag of the pilot and stoker to within -3.7% and -13.9% of the wind tunnel values respectively, and the Spalart-Allmaras model predicted the drag of the pilot and stoker to within -4.0% and -15.9% respectively. The $k-\varepsilon$ models all under-predicted pilot drag forces beyond 30%, with the realizable and standard $k-\varepsilon$ models predicting a larger drag force on the stoker than on the pilot.

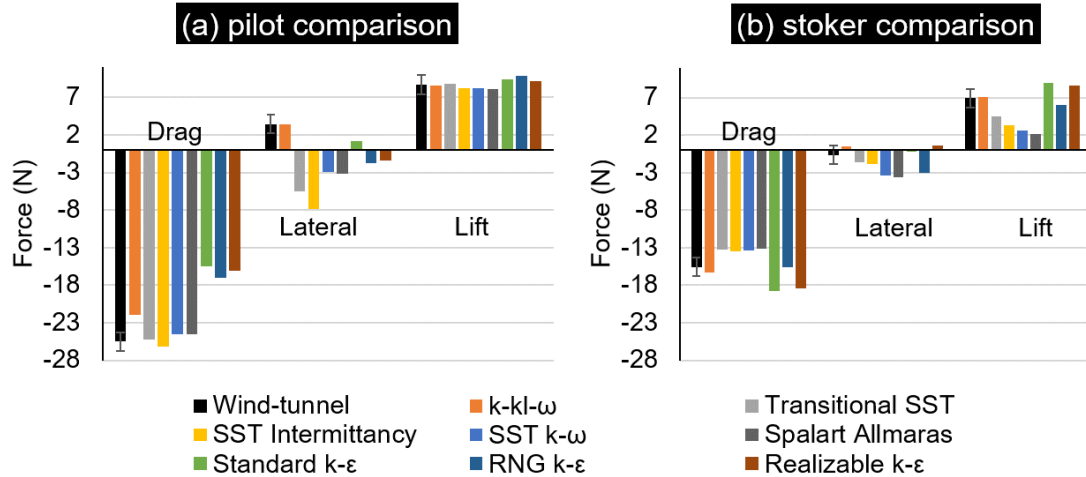


Figure 3.11. (a) Drag, lift and lateral forces (N) acting on the pilot and (b) on the stoker as obtained by various turbulence models. Systematic and random errors within a 95% confidence interval are represented by error bars for the wind tunnel data.

Table 3.2. A comparison of drag, lateral and lift forces (N) obtained using various turbulence models, against wind tunnel data. Blockage corrections (Barlow et al., 1999) have been applied to the wind tunnel results displayed, with one standard deviation included.

	Pilot			Stoker		
	Drag (N)	Lateral (N)	Lift (N)	Drag (N)	Lateral (N)	Lift (N)
Wind-tunnel blockage corrected	-25.52±0.89	3.42±1.25	8.68±0.94	-15.55±0.83	-0.64±1.04	6.91±0.92
Transitional SST k- ω	-25.26	-5.54	8.81	-13.31	-1.63	4.46
Intermittency SST k- ω	-26.14	-7.87	8.23	-13.46	-1.80	3.29
k-kl- ω	-21.92	3.38	8.54	-16.27	0.53	7.08
SST k- ω	-24.58	-2.98	8.24	-13.39	-3.44	2.57
Spalart-Allmaras	-24.51	-3.14	8.10	-13.08	-3.67	2.18
RNG k- ϵ	-17.05	-1.79	9.82	-15.64	-3.06	5.99
Standard k- ϵ	-15.46	1.20	9.41	-18.79	-0.24	8.90
Realizable k- ϵ	-16.05	-1.40	9.18	-18.47	0.65	8.59

3.4.2.3 Blockage effects

The blockage corrections by Barlow et al. (1999) applied to the wind tunnel data, were designed for a single bluff body, not two inline bodies in close proximity as per the tandem athletes of this study. Hence, the validity of these corrections is in question for the comparison against the full-scale tandem CFD simulations in a domain much larger than that of the wind tunnel environment. To further investigate the potential influence of blockage, a new computational domain was created, representing the actual geometry and scale of the wind tunnel environment used for the validation studies (Figure 3.12a-b). The tandem geometry was scaled to quarter-scale as per the wind tunnel

experiment (Figure 3.12c) and a 60 m/s velocity was imposed at the inlet boundary. The geometry included the elevated platform, the closed container containing both force transducers and the supporting columns ($\text{\O} 0.02 \text{ m}$) for the elevated platform. The wind tunnel test section was modelled as 12 m long, with the inlet boundary condition 2.3 m from the frontal edge of the platform surface. Despite the high level of geometrical detail of the wind tunnel environment, there may have been additional blockage effects occurring in the physical wind tunnel due to the boundary layer development on the walls of the closed-loop wind tunnel.

A selection of turbulence models from section 3.4.2.2 were chosen for further investigation, the 4-equation T-SST model (Menter et al., 2006), the 3-equation $k\text{-}k\ell\text{-}\omega$ model (Walters & Cokljat, 2008), the 2-equation SST $k\text{-}\omega$ model (Menter, 1994), and the 1-equation Spalart-Allmaras model (Spalart & Allmaras, 1992). The $k\text{-}\varepsilon$ models were not used due to their previous inaccurate force predictions for the tandem athletes (Figure 3.11). The tandem geometry was representative of Figure 3.7b. The grid sizing's for the tandem geometry were representative of grid 3a, scaled accordingly to quarter-scale. Five prism layers with a first aspect ratio of 10 were placed on the walls of the wind tunnel and the raised platform, which were treated as smooth no-slip walls. The grid was denoted as grid 4. The total number of cells was 36.5 million. All solver parameters followed those outlined in section 3.2.1.4 and section 3.4.1, apart from the pseudo-transient time-step, which was scaled to 0.000625 s to account for the quarter-scale model and 60 m/s air velocity.

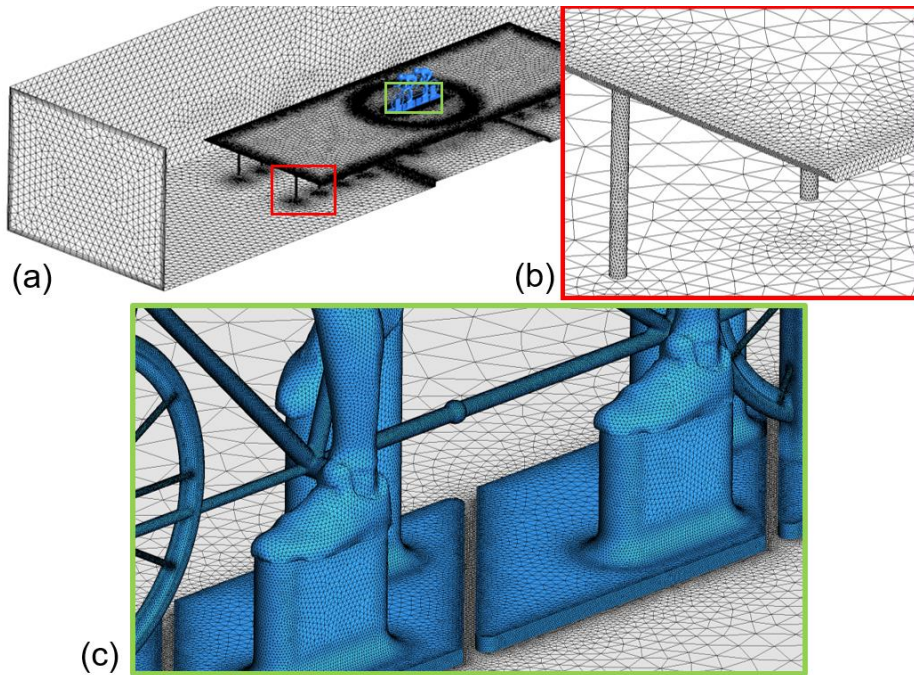


Figure 3.12. (a) Computational grid of the CFD model of the wind tunnel test section (grid 4), (b) a close-up image of the grid density on the platform edges and support columns, (c) grid density on the baseplate and athlete support structures. Cell count was 36.5 million.

Figure 3.13 shows the shifts in drag for the pilot and stoker measurements in the new CFD domain in comparison to the results presented in Figure 3.11. Previously the T-SST turbulence model under-predicted the pilot drag by -3.0%, and the stoker drag by -16.2%, by comparison to the wind tunnel measurements with blockage correction applied. In the new CFD domain, the T-SST model over-predicted the pilot drag by 9.9%, and under-predicted the stoker drag by -7.7%. The k-kl- ω turbulence model experienced a more dramatic increase in total drag, with the pilot drag now over-predicted by 6.4%, and the stoker drag over-predicted by 17.7%. The SST k- ω turbulence model provided the best all-round predictions in the scaled environment, with the pilot drag over-predicted by 4.0% and the stoker drag over-predicted by 4.2%. The Spalart-Allmaras turbulence model did not provide useful drag data, under-predicting pilots drag by -13.2%, and over-predicting the stokers drag by 12.4%. No turbulence model provided lateral force predictions for the pilot within the error range of the force transducers (± 1.24 N). The k-kl- ω turbulence model predicted the lateral force on the stoker to within 2.2%, and the Spalart-Allmaras model predicted the lift force on the stoker to within 1.6%, but the poor performance of both models in all other areas rendered them ineligible for further research purposes. The SST k- ω model was thus chosen as the best performing turbulence model for tandem aerodynamics, due to its close reproduction of the wind tunnel results for drag force (N) on the pilot and stoker, and for the lift force on the pilot (-3.4% difference). All force data are documented in Table 3.3.

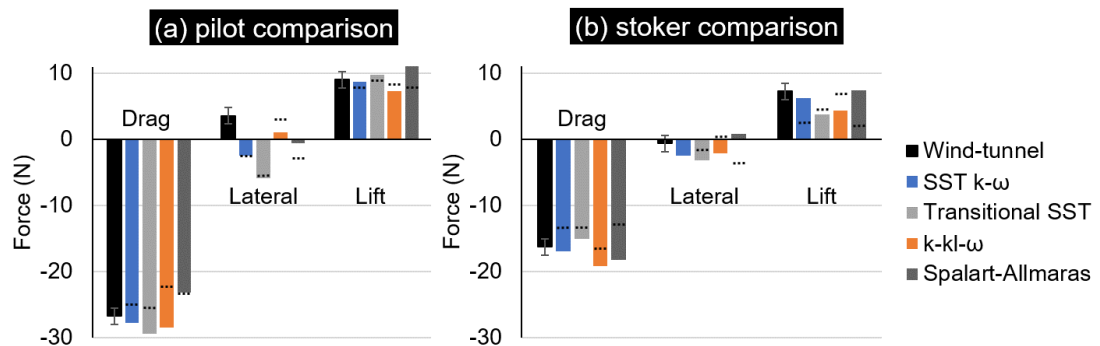


Figure 3.13. Drag, lateral and lift force data on (a) the pilot, and (b) the stoker geometries, from the quarter-scale CFD models simulating the wind tunnel environment. Blockage corrections are not applied to the wind tunnel results in both (a) and (b). Systematic and random errors within a 95% confidence interval are represented by error bars for the wind tunnel data. Dashed lines present the previous predictions from Figure 3.11.

Table 3.3. A comparison of drag, lateral and lift forces (N) obtained using various turbulence models, when modelling the wind tunnel test section geometrically within the CFD model. Blockage corrections have not been applied to the wind tunnel results displayed. One standard deviation is included with the wind tunnel results.

	Pilot			Stoker		
	Drag (N)	Lateral (N)	Lift (N)	Drag (N)	Lateral (N)	Lift (N)
Wind-tunnel not blockage corrected	-26.72±0.93	3.59±1.30	9.08±0.98	-16.28±0.87	-0.67±1.09	7.24±0.96
Transitional SST k- ω	-29.38	-5.87	9.75	-15.03	-3.20	3.73
k-k1- ω	-28.44	1.13	7.31	-19.16	-2.14	4.28
SST k- ω	-27.78	-2.41	8.77	-16.96	-2.53	6.25
Spalart-Allmaras	-23.20	-0.55	12.56	-18.30	0.77	7.35

3.5 Discussion

This study investigated the aerodynamic drag for tandem para-cycling athletes. The grid and turbulence model sensitivity analysis showed that a low y^* grid combined with the SST k- ω turbulence model yielded the lowest drag deviation from the wind tunnel measurements (4.0% and 4.2% for the pilot and stoker respectively). The drag coefficient for the tandem road setup without support structures was 0.787 ($C_{DA} = 0.314 \text{ m}^2$). The pilot and the stoker contributed 52.5% and 26.9% to the total drag, respectively. Without proper selection of near-wall grid resolution and turbulence model, total drag coefficients were obtained that appeared plausible as per section 3.2.2, but were actually the cumulative sum of errors. Counter-intuitive drag distributions were observed, with the near-wall grid resolution (Figure 3.9) and/or the use of a k- ϵ turbulence model (Figure 3.11) identified as reasons for this discrepancy. The use of k- ϵ turbulence models for cycling aerodynamics as reported by Blocken et al. (2016), Fintelman et al. (2015), Blocken & Toparlar, (2015), and Defraeye et al. (2010), did not yield sufficiently accurate results (< 10% deviation from experiments) for a tandem system.

The standard k- ϵ and realizable k- ϵ models predicted drag coefficients for the tandem geometry used in the wind tunnel experiment that deviated by only 5.4% and 5.0%, respectively, from the validated drag coefficient predicted when the SST k- ω turbulence model was utilised, all using the same grid. However, by comparison to wind tunnel experiments, the drag on the pilot was under-predicted by 39.4% when using the standard k- ϵ turbulence model, and over-predicted by 20.8% for the stoker, resulting in the stoker experiencing a larger drag force than the pilot. The total drag force prediction for the k- ϵ models conceals the inaccuracy of the drag predictions on both athletes.

Figure 3.4 illustrated the impact of tetrahedral cells (grid 1) when used for the near-wall grid, through differences in the predictions of surface pressure coefficient and normalised shear stress

between grid 1 and grid 2. As per section 3.2.2, there was only an 8.8% difference between the total C_D of the tandem system when utilising two grids with different near-wall resolutions. However, the flow fields were fundamentally different (Figure 3.5), along with the drag distributions (Figure 3.3) on individual athletes, with only the fine grid resolution at the wall producing a realistic result. It is recommended that a fine near-wall grid producing a $y^* < 1$ using the SST $k-\omega$ turbulence model, is imposed for future CFD studies on tandem cycling research, to predict flow separation from both athletes.

These observations yield both consistencies and partial inconsistencies with the findings reported in the literature. The SST $k-\omega$ turbulence model was found to yield the lowest error for tandem cycling, consistent with the turbulence model sensitivity analysis conducted by Defraeye et al. (2010) for solo cyclists, who determined that it provided the best overall drag, lateral and lift force predictions from a selection of RANS turbulence models. However, the standard $k-\varepsilon$ turbulence model was also found to provide good drag predictions for a solo cyclist, two drafting able-bodied cyclists, and a cyclist followed by a car or motorcycle (Blocken & Toparlar, 2015; Blocken et al., 2016; Defraeye et al., 2010; Fintelman et al., 2015). This turbulence model was found to yield large errors in drag predictions for tandem cycling.

A limitation of the CFD approach followed in this study was the use of a static geometry. The models manufactured for the wind tunnel experiments were static, and accordingly the CFD models were also simulated as static models to validate the simulations. In reality, the athlete's legs would move to power the cranks, resulting in rotating wheels. Vortices generated from the hips and legs of athletes can have a strong effect on the drag (Griffith et al., 2014). Investigations into a dynamic tandem setup exploring the interaction between these vortices and the pilot and stoker could provide a deeper understanding of tandem aerodynamics, and present the opportunity for further optimisation with crank-rotation phase shifts between tandem athletes. Further simplifications in this study included the wall boundary conditions for the athletes which were modelled as no-slip walls with zero roughness. Athletes would have varying roughness over their surfaces in reality due to skin, hair and clothing, which could also affect aerodynamic drag.

The effects of blockage on tandem cycling in a wind tunnel environment are not yet fully understood and require further wind tunnel experiments and CFD simulations to fully investigate the phenomena. In the absence of such information, for CFD validation studies it is recommended to create CFD models that replicate the dimensions of the wind tunnel, and that include a high level of geometrical detail of the test section. After validation, new CFD models should be generated with an enlarged domain to provide more accurate aerodynamics predictions without the influence of blockage. This procedure negates the need to apply blockage corrections to the force data acquired of tandem cyclists. In addition, further investigation is required to determine Reynolds number

dependence/independence of the present results through experimental testing. Reynolds number independence was analysed by Defraeye et al. (2010) for a half-scale model of a solo cyclist. It was found that there were limited effects above a full-scale velocity of 10 m/s, however, it must be verified if this finding is applicable for tandem cyclists through additional research.

3.6 Conclusions

The aerodynamics of a tandem para-cycling road race setup was simulated using CFD, and was found to have a full-scale C_D of 0.787 and C_{DA} of 0.314 m². A grid with coarse near-wall boundary layer resolution was found to yield counter-intuitive drag distributions for individual athletes, with the stoker experiencing a higher drag than the pilot. Wind tunnel experiments proved the counter-intuitive drag distributions to be incorrect, with the stoker experiencing 39% less drag than the pilot. In addition to this grid dependency of achieving an average y^* value close to 1, the CFD simulations were also shown to have a dependency on turbulence models, with the SST $k-\omega$ turbulence model providing the most accurate drag predictions: 4.0% and 4.2% for the pilot and stoker respectively when compared against wind tunnel validation data, and modelling the wind tunnel geometry within the CFD fluid domain. The realizable $k-\varepsilon$ and standard $k-\varepsilon$ models predicted the stoker to experience a larger drag than the pilot, despite the grid meeting the requirement of an average y^* value less than 1, and using low Reynolds number modelling opposed to wall functions. The RNG $k-\varepsilon$ model under-predicted the drag on the pilot beyond 20%. It is recommended that a fine grid with an average y^* value of 1 or less be used in combination with the SST $k-\omega$ turbulence model for future tandem cycling aerodynamics research.

3.7 References

- Alam, M. (2014). The aerodynamics of a cylinder submerged in the wake of another. *Journal of Fluids and Structures*, 51, 393–400. <http://doi.org/10.1016/j.jfluidstructs.2014.08.003>
- ANSYS Fluent. (2015). ANSYS Fluent theory guide. *Release 16.1 Documentation*. ANSYS Inc.
- Artec Europe. (2017). Artec Eva, 3D Scanners. Retrieved May 22, 2017, from <https://www.artec3d.com/3d-scanner/artec-eva>
- Barlow, J. B., Rae, W. H., & Pope, A. (1999). *Low-speed Wind Tunnel Testing* (3rd ed.). John Wiley & Sons.
- Barry, N., Burton, D., Sheridan, J., Thompson, M., & Brown, N. A. T. (2015). Aerodynamic drag

- interactions between cyclists in a team pursuit. *Sports Engineering*, 18, 93–103.
<http://doi.org/10.1007/s12283-015-0172-8>
- Barry, N., Burton, D., Sheridan, J., Thompson, M., & Brown, N. A. T. (2016). Flow field interactions between two tandem cyclists. *Experiments in Fluids*, 57(12), 1–14.
<http://doi.org/10.1007/s00348-016-2273-y>
- Belloli, M., Cheli, F., Bayati, I., Giappino, S., & Robustelli, F. (2014). Handbike aerodynamics: wind tunnel versus track tests. In *The 2014 conference of the International Sports Engineering Association, Procedia Eng.* (Vol. 72, pp. 750–755). Elsevier B.V.
<http://doi.org/10.1016/j.proeng.2014.06.127>
- Blocken, B. (2014). 50 years of Computational Wind Engineering: Past, present and future. *Journal of Wind Engineering and Industrial Aerodynamics*, 129, 69–102.
<http://doi.org/https://doi.org/10.1016/j.jweia.2014.03.008>
- Blocken, B. (2015). Computational Fluid Dynamics for urban physics: Importance, scales, possibilities, limitations and ten tips and tricks towards accurate and reliable simulations. *Building and Environment*, 91, 219–245. <http://doi.org/10.1016/j.buildenv.2015.02.015>
- Blocken, B., Defraeye, T., Koninckx, E., Carmeliet, J., & Hespel, P. (2013). CFD simulations of the aerodynamic drag of two drafting cyclists. *Computers & Fluids*, 71, 435–445.
<http://doi.org/10.1016/j.compfluid.2012.11.012>
- Blocken, B., & Toparlar, Y. (2015). A following car influences cyclist drag: CFD simulations and wind tunnel measurements. *Journal of Wind Engineering and Industrial Aerodynamics*, 145(0), 178–186. <http://doi.org/10.1016/j.jweia.2015.06.015>
- Blocken, B., Toparlar, Y., & Andrienne, T. (2016). Aerodynamic benefit for a cyclist by a following motorcycle. *Journal of Wind Engineering and Industrial Aerodynamics*, 155, 1–10.
<http://doi.org/https://doi.org/10.1016/j.jweia.2016.04.008>
- Casey, M., & Wintergerste, T. (2000). Best Practice Guidelines. *ERCOfTAC Special Interest Group on “Quality and Trust in Industrial CFD.”* ERCOfTAC.
- Choudhury, D. (1993). Introduction to the renormalization group method and turbulence modeling. Fluent Inc. Technical Memorandum TM-107.
- Crouch, T. N., Burton, D., LaBry, Z. A., & Blair, K. B. (2017). Riding against the wind: a review of competition cycling aerodynamics. *Sports Engineering*, 20(2), 81–110.
<http://doi.org/10.1007/s12283-017-0234-1>
- Defraeye, T., Blocken, B., Koninckx, E., Hespel, P., & Carmeliet, J. (2010). Computational fluid dynamics analysis of cyclist aerodynamics: Performance of different turbulence-modelling and boundary-layer modelling approaches. *Journal of Biomechanics*, 43(12), 2281–2287.
<http://doi.org/10.1016/j.jbiomech.2010.04.038>

- Defraeye, T., Blocken, B., Koninckx, E., Hespel, P., Verboven, P., Nicolai, B., & Carmeliet, J. (2014). Cyclist drag in team pursuit: Influence of cyclist sequence, stature, and arm spacing. *Journal of Biomechanical Engineering*, 136(1), 011005. <http://doi.org/10.1115/1.4025792>
- Dyer, B. (2015). The importance of aerodynamics for prosthetic limb design used by competitive cyclists with an amputation: An introduction. *Prosthetics and Orthotics International*, 39 (3), 232–237. <http://doi.org/10.1177/0309364614527121>
- Fintelman, D. M., Hemida, H., Sterling, M., & Li, F.-X. (2015). CFD simulations of the flow around a cyclist subjected to crosswinds. *Journal of Wind Engineering and Industrial Aerodynamics*, 144, 31–41. <http://doi.org/10.1016/j.jweia.2015.05.009>
- Franke, J., Hellsten, A., Schlünzen, H., & Carissimo, B. (2007). Best practice guideline for the CFD simulation of flows in the urban environment. *COST Action 732: Quality Assurance and Improvement of Microscale Meteorological Models*. Hamburg Germany.
- Griffith, M. D., Crouch, T., Thompson, M. C., Burton, D., & Sheridan, J. (2014). Computational fluid dynamics study of the effect of leg Position on cyclist aerodynamic drag. *The American Society of Mechanical Engineers, Journal of Fluids Engineering*, 136. <http://doi.org/10.1115/1.4027428>
- Grotjans, H., & Menter, F. (1998). Wall functions for general application CFD codes. In *Proceedings of the 4th Computational Fluid Dynamics Conference (ECCOMAS'98)* (pp. 1112–1114). John Wiley & Sons.
- Íñiguez-de-la Torre, A., & Íñiguez, J. (2009). Aerodynamics of a cycling team in a time trial: does the cyclist at the front benefit? *European Journal of Physics*, 30(6), 1365.
- Jones, W. P., & Launder, B. E. (1972). The prediction of laminarization with a two-equation model of turbulence. *International Journal of Heat and Mass Transfer*, 15(2), 301–314. [http://doi.org/10.1016/0017-9310\(72\)90076-2](http://doi.org/10.1016/0017-9310(72)90076-2)
- Menter, F. R. (1994). Two-equation eddy-viscosity turbulence models for engineering applications. *AIAA Journal*, 32(8), 1598–1605. <http://doi.org/10.2514/3.12149>
- Menter, F. R., Langtry, R. B., Likki, S. R., Suzen, Y. B., Huang, P. G., & Völker, S. (2006). A correlation-based transition model using local variables—Part I: model formulation. *Journal of Turbomachinery*, 128(3), 413–422. <http://doi.org/10.1115/1.2184352>
- Shih, T.-H., Liou, W. W., Shabbir, A., Yang, Z., & Zhu, J. (1995). A new k-ε eddy viscosity model for high reynolds number turbulent flows. *Computers Fluids*, 24(3), 227–238.
- Sohankar, A. (2012). A numerical investigation of the flow over a pair of identical square cylinders in a tandem arrangement. *International Journal for Numerical Methods in Fluids*, 70(10), 1244–1257. <http://doi.org/10.1002/flid.2739>
- Spalart, P., & Allmaras, S. (1992). A one-equation turbulence model for aerodynamic flows. In *30th*

- Aerospace Sciences Meeting and Exhibit*. American Institute of Aeronautics and Astronautics.
<http://doi.org/http://doi.org/doi:10.2514/6.1992-439>
- Tominaga, Y., Mochida, A., Yoshie, R., Kataoka, H., Nozu, T., Yoshikawa, M., & Shirasawa, T. (2008). AIJ guidelines for practical applications of CFD to pedestrian wind environment around buildings. *Journal of Wind Engineering and Industrial Aerodynamics*, 96(10–11), 1749–1761. <http://doi.org/10.1016/j.jweia.2008.02.058>
- Tucker, P., & Mosquera, A. (2001). NAFEMS Introduction to grid & mesh generation for CFD. *NAFEMS CFD Work Group*. <http://doi.org/10.1017/CBO9781107415324.004>
- UCI. (2017). Cycling Regulations, Part 16 Para-Cycling, version on 01/02/2017. Union Cycliste Internationale. Retrieved from
http://www.uci.ch/mm/Document/News/Rulesandregulation/16/26/73/16-PAR-20170201-E_English.PDF
- Walters, D. K., & Cokljat, D. (2008). A three-equation eddy-viscosity model for Reynolds-Averaged Navier–Stokes simulations of transitional flow. *Journal of Fluids Engineering*, 130(12), 121401. <http://doi.org/10.1115/1.2979230>
- Wolfshtein, M. (1969). The velocity and temperature distribution in one-dimensional flow with turbulence augmentation and pressure gradient. *International Journal of Heat and Mass Transfer*, 12, 301–318. [http://doi.org/10.1016/0017-9310\(69\)90012-X](http://doi.org/10.1016/0017-9310(69)90012-X)

On the effects of crosswinds in tandem aerodynamics: an experimental and computational study

This chapter builds on the turbulence model sensitivity studies from Chapter 3 to expand the guideline to include crosswinds. Novel wind tunnel experiments are used to provide aerodynamic force information of both the pilot and stoker athletes at all yaw angles tested, to validate the numerical simulations. Further numerical analysis is conducted on the aerodynamics of full-scale tandem cycling under crosswind conditions using new guidelines for crosswind investigations of tandem cycling.

This chapter has been published in the international peer-reviewed journal *European Journal of Mechanics – B/Fluids*:

Mannion, P., Toparlar, Y., Clifford, E., Hajdukiewicz, M., Andrienne, T., & Blocken, B. (2018). On the effects of crosswinds in tandem aerodynamics: an experimental and computational study. *74*, 68-80. <https://doi.org/10.1016/j.euromechflu.2018.11.001>

Abstract: Aerodynamics has been an important research aspect in cycling science, with aerodynamic apparel and equipment, athlete postures, and race strategies all taking advantage of scientific aerodynamics knowledge. Crosswinds occur when cyclists travel at a non-zero angle to the direction of the wind. Research into crosswinds has yielded race strategies for able-bodied cyclists such as staggered drafting, and wind conditions are recognised as a key factor to consider for cyclist safety. The impact of crosswinds on tandem para-cyclists is less understood. Within the tandem para-cycling discipline, two athletes compete as a team on a single bicycle with a high degree of flow interaction between both athletes. Wind tunnel experiments and computational fluid dynamics were utilised in this research to investigate the drag and lateral forces at yaw angles between 0°-20°. No single turbulence model was found superior for all yaw angles investigated, with the SST $k-\omega$ and $k-kl-\omega$ turbulence models providing good results for separate yaw ranges. The individual drag and lateral forces experienced by both athletes and the tandem bicycle were investigated to provide further clarity on the distribution of wind loads for each yaw angle tested, and to aid in identifying potential locations for aerodynamic optimisation. 15° yaw was found to be the critical yaw angle where the maximum

drag area of 0.337 m^2 was experienced. The lateral force exceeded the drag force by 52.8% at a yaw angle of 20° .

4.1 Introduction

Research on para-cycling aerodynamics is an emerging field in the world of cycling aerodynamics. The importance of aerodynamics at elite levels of cycling is evident by its persuasive reach across the sport from riding position, leg motion and race tactics over equipment and apparel design to the effects of in-race vehicles (Blocken et al., 2013; 2016; 2018; Fintelman et al. 2014a; 2014b; 2015a; 2015b; Blocken & Toparlar, 2015; Crouch et al, 2017; Crouch et al., 2016). Evaluating the effect of crosswinds is an important aspect for cycling and para-cycling aerodynamics research. Athletes at outdoor cycling events are commonly, if not always, cycling in crosswind conditions if any wind conditions are present. Tandem cycling is a Paralympics classified sport that holds some similarities to solo cycling, but lacks a substantial research backing in the literature, with only two known publications on the topic by Mannion et al. (2018a, 2018b). Given the bluff body aerodynamics interaction between two tandem athletes, the influence of crosswinds is expected to be a more complex consideration than for solo cycling. The distribution of the forces acting on a tandem setup is of interest from both a safety and an aerodynamics optimisation point of view.

Lukes et al. (2005) termed “the effect of wind” as a key component of cycling aerodynamics that needs to be addressed. By far, most experimental and numerical studies on cycling aerodynamics, even very recent ones, did not consider crosswind conditions (e.g. Barry et al. 2015a; 2015b; Blocken et al., 2013, 2016; Crouch et al., 2016; Defraeye et al., 2010a, 2010b; Mannion et al., 2018a, 2018b). An exception are the studies by Fintelman et al. (2014a; 2015a). Fintelman et al. (2014a) studied crosswind effects on solo cyclists using full-scale wind tunnel experiments, with a focus on cyclist safety by investigating cycling stability under adverse crosswind conditions. Crosswind angles in increments of 15° from 0° to 90° were investigated, using a mannequin to represent a rider. Several torso angles were tested, along with two bicycle types. The study concluded that the bicycle type had a larger impact on the lateral force coefficient than the torso angle of the rider. Measured lateral force coefficients were up to 34% larger for a TT bike with a rear disk wheel, in comparison to a road bicycle with two standard spoked wheels. Fintelman et al. (2015a) studied crosswind effects using numerical simulation with computational fluid dynamics (CFD) on a cycling setup for road race events. Both steady-state Reynolds-Averaged Navier-Stokes (RANS) and transient Detached-Eddy Simulations (DES) and Large-Eddy Simulations (LES) were utilised. Yaw angles from 0° to 90° were

investigated in 15° increments using steady RANS, and the angle of 15° was simulated using DES and LES. Discrepancies between experimental data and simulation results were apparent, with DES deviating from experimental data by up to 17% at 15° yaw. LES provided the best overall result at 15° yaw with a drag coefficient error of 5%. However, the RANS method provided a good agreement with the experimental data for all yaw angles tested, with the standard $k-\epsilon$ (Jones & Launder, 1972) turbulence model proving superior to the SST $k-\omega$ (Menter, 1994) turbulence model for force predictions where wall functions based on the log law were used to solve the near-wall flow. At 15°, drag was under-predicted by 7% when using the standard $k-\epsilon$ model, but was under-predicted by 12% when using the SST $k-\omega$ model.

Tandem aerodynamics were investigated by Mannion et al. (2018a) using wind tunnel experiments and CFD analysis, where both methods provided individual drag data for the pilot and the stoker. A variety of challenges were observed to obtain accurate numerical results, with a large dependence found for the boundary layer resolution and choice of turbulence models. The SST $k-\omega$ (Menter, 1994) turbulence model and an average y^* resolution of 1 provided the most accurate drag predictions with a drag deviation of 4.0% and 4.2% from the measurements, calculated for both the pilot and stoker respectively. Mannion et al. (2018b) investigated four tandem setups at 0° yaw using CFD; upright, dropped, time-trial and frame-clench setups. The frame-clench setup was a variation of the time-trial setup that resulted in the lowest C_{DA} of the four setups tested, at 0.286 m².

By considering simplified geometries for the tandem athletes such as cylinders, some parallels can also be drawn between tandem athletes and two inline cylinders where two cylinders can be considered as simplified forms of the tandem athletes' torsos. Cylinders have been used as simplified representation of cyclists in a team time-trial by Íñiguez-de-la Torre & Íñiguez, (2009) who found that the cyclist in front benefits by 5% from the trailing riders. Staggered cylinder configurations in effect simulate non-zero incidence angles for the oncoming flow. Depending on the spacing of two staggered cylinders, they can experience proximity interference effects and wake interference effects with interaction from separated free shear layers and von Kármán vortices (Sumner, 2010). Similar complexity can be expected for tandem Para-cycling in crosswind conditions.

The importance and relevance of understanding the drag and lateral forces of each athlete under crosswind conditions is made apparent by the directions taken by athletes and cycling teams to gain aerodynamic improvements. Limitations are placed on the design of tandem bicycles by the Union Cycliste Internationale (UCI) to promote fairness and safety in race events (UCI, 2017). As a result, athletes' postures and positioning have become the focus of aerodynamic refinements in modern day cycling. Understanding how the tandem athletes' drag and lateral forces react

individually in crosswind conditions could provide insights into where and how aerodynamic refinements can be obtained.

There is a gap in knowledge regarding the performance of tandem cyclists in crosswind conditions, with no known prior studies investigating crosswind aerodynamics for tandem cycling, to the best of the authors' knowledge. This research aims to close this gap using wind tunnel experiments and CFD simulations. In this study, various turbulence models are evaluated over a range of yaw angles to determine if the sensitivity to turbulence modelling demonstrated by Mannion et al. (2018a) at 0° also applies to other yaw angles. Yaw angles between 0°-20° were identified as the range that tandem cyclists most commonly experience in crosswinds. 5° increments were chosen to explore this yaw range. A tandem cycling setup resembling an outdoor road race scenario was chosen to provide the geometrical model for this research. Wind tunnel experiments were conducted with quarter-scale geometries at high velocities for Reynolds number matching, where the aerodynamic forces on both athletes could also be measured simultaneously.

4.2 Wind tunnel experiments

4.2.1 Experimental setup

The tandem geometry was subjected to analysis for five different yaw angles (α), namely 0°, 5°, 10°, 15° and 20°. The analysis was conducted with wind tunnel experiments in the aeronautical test section of the wind tunnel in the University of Liège, Belgium (Figure 4.1a). The experiments were designed to extract drag and lateral force data from both athletes separately under crosswind conditions. As such, quarter-scale models of a tandem bicycle and athletes were manufactured, and a system of two force transducers that collected force data independently and simultaneously was devised. Geometrical information for the tandem model was acquired via 3D scanning using an Eva structured light scanner (Artec Europe, 2017). Written consent of the scanned cyclist was obtained. The geometry of the same single athlete was used to represent both the pilot and the stoker to remove any inferred drag bias from having different anthropometric characteristics for the two athletes. An aggressive drops posture was adopted by the scanned athlete which was representative of a posture adopted by both the pilot and stoker in a road race scenario. The quarter-scale tandem model was divided into four components to separate the pilot and stoker geometries from the tandem bicycle geometry. Figure 4.1b illustrates, via colour, the separation of these geometries. The tandem bicycle was split in the middle to allow for complete disassembly of the model. Tight fitting sleeves joined the frame tubes at their separation point to provide a complete joint and to remove vibrations during

testing. The tandem handlebars were included with the athlete components, and were not attached to the bicycle frame.

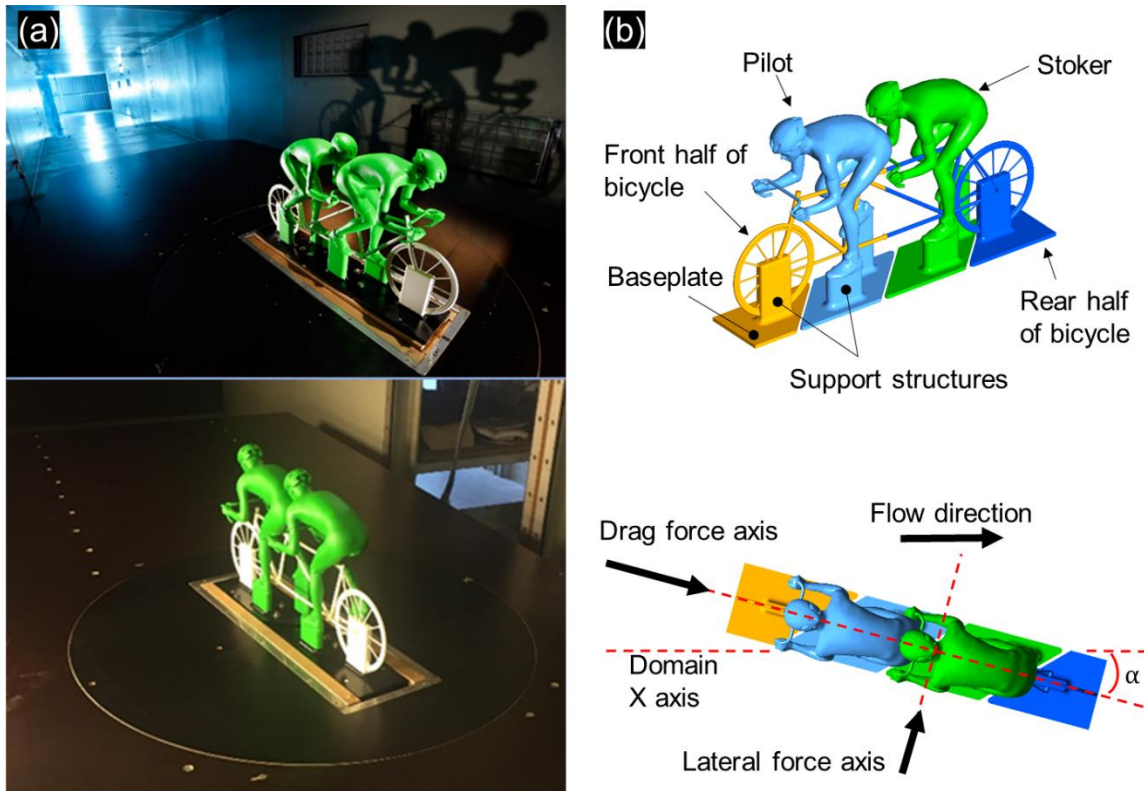


Figure 4.1. (a) Photos of the quarter-scale tandem setup in the wind tunnel of the University of Liège, showing the rotational plate used to vary the yaw angle of the tandem model. (b) Tandem geometry representative of the quarter-scale wind tunnel experiments and of the corresponding CFD simulations. Axis directions are defined and geometry components are labelled.

Each of the four components, the pilot, stoker, and the front and rear tandem bicycle halves were manufactured separately from blocks of acrylonitrile butadiene styrene (ABS) plastic using CNC milling. The resulting surfaces were considered to be smooth. Each of the four components had a baseplate (labelled in Figure 4.1b) included in the manufacturing process to allow for the two athlete geometries to be attached to the force transducers, and for the tandem bicycle components to be secured. Two Delta model six axis force transducers were used from ATI Industrial Automation (ATI, 2018). Both force transducers were aligned with the centres of gravity of the individual athletes. Additional support structures were required for each component to prevent vibrations from occurring under wind loads. These support structures included vertical supports connecting the athletes to their respective baseplates, and rectangular supports encompassing the wheel hubs to securely connect the bicycle components to their respective baseplates. This is displayed in the corresponding computational geometry for the tandem athletes and bicycle in Figure 4.1b. A rotational plate with a

diameter of 1 m was built into the centre of the platform on to which the tandem model was placed. The platform and rotational plate raised the tandem geometry by 0.3 m from the boundary layer at the floor of the test section of the wind tunnel to reduce the boundary-layer height of the flow approaching the model. The platform was sharp-edged to minimise flow disturbance upstream of the test model. The measured boundary layer height at the location of the tandem geometry was 0.06 m, which is below the feet of the cyclists. Above this height of 0.06 m, the approach-flow turbulence intensity in the test section of the wind tunnel was 0.2%.

The desired full-scale flow velocity for tandem athletes was 15 m/s. As such, a velocity of 60 m/s was used for the quarter-scale tandem models to match the Reynolds number of a full-scale tandem. The two force transducers were zeroed before each experiment commenced under zero velocity conditions. Force data was sampled every 0.1 seconds and averaged over a period of 180 seconds. Before the data was sampled, the testing velocity of 60 m/s was held for 30 s in the wind tunnel to provide a settling period for the force transducers. The force transducers maximum error estimate was 1.24 N at a 95% confidence interval. The error estimate was obtained from the calibration of the two transducers; 0.75% of the maximum loads for drag and lateral forces. Stream-wise air velocity was measured using a pitot tube in the wind tunnel test section along with the air temperature for each experiment. Thus, the force data acquired were corrected for any deviations from the measured 60 m/s. The velocity of 60 m/s was measured using a Pitot tube located at a height of 1 m above the ground of the floor of the test section of the wind tunnel, i.e. 0.7 m above the raised platform. The probe was located 0.5 m upstream of the centre of the turn table in the platform. The recorded force data was also corrected for air density at 1.225 kg/m^3 using temperature measurements and local atmospheric pressure. The approach-flow turbulence intensity in the test section of the wind tunnel was 0.2% above the thin boundary layer (0.06 m).

4.2.2 Results from the wind tunnel experiments

The recorded forces in the wind tunnel demonstrate different drag trends for the pilot and stoker as the yaw angle increased (Figure 4.2a). The pilot experienced a steady decline in drag force with increasing yaw angle, a total difference of -12.6% between 0° and 20° yaw. In contrast, the stoker experienced an increase in drag force from 0° - 10° by 19.7%. With increasing yaw angle from 0° - 10° , the stoker benefited less from the drafting effect behind the pilot and experienced a larger drag force from the oncoming flow. However, the stoker began to experience the same reductions in drag as the pilot experienced, as the yaw angle increased beyond 10° , and a reduction in drag of -12.2% was found between 10° - 15° . The drag experienced by the stoker continued to decrease as the yaw angle

increased to 20°. At 20°, the drag experienced by the stoker was lower than the initial drag experienced at 0° by 4.6%. Large lateral forces were experienced by the pilot and stoker as the yaw angle increased, by comparison to the drag forces (Figure 4.2b). The lateral force experienced by the pilot at 20° was 96.4% larger than the drag force at the same angle, while that by the stoker at 20° was 166.9% larger. The largest lateral force experienced by the pilot and the stoker was at 20° yaw. Compared to the pilot, the stoker experienced a smaller lateral force for all yaw angles tested. However, it is expected that the support structures for the athletes located at their feet (Figure 4.1b) impacted the lateral force to a greater degree than the drag force due to the larger side area exposed to the oncoming flow.

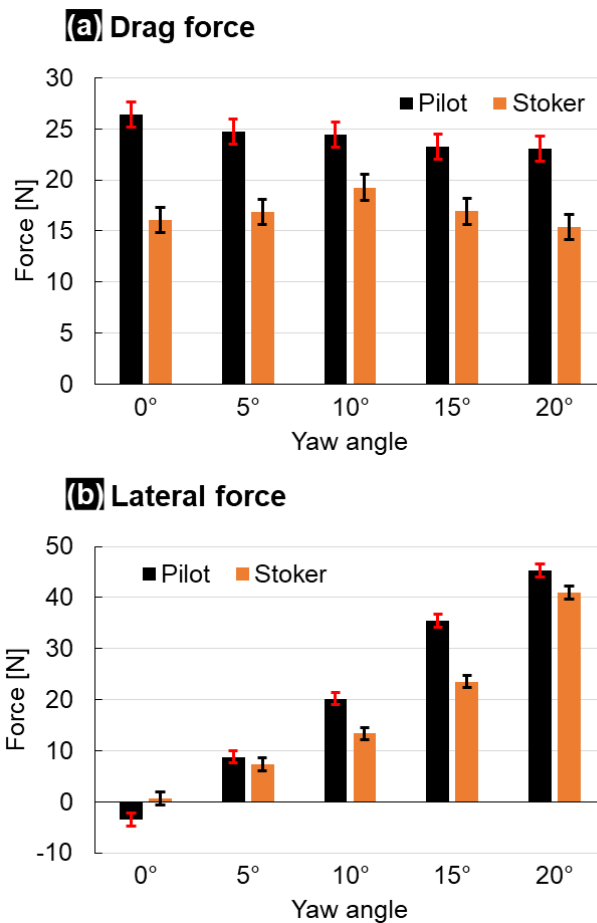


Figure 4.2. (a) Drag and (b) lateral force results from wind tunnel experiments. The error bars represent the conservative error range of ± 1.24 N.

4.3 CFD simulations: Validation study

4.3.1 Computational grid and boundary conditions

CFD simulations were performed to replicate the wind tunnel environment presented in section 2. The aeronautical test section of the wind tunnel laboratory in the University of Liège had a cross sectional area of $2 \times 1.5 \text{ m}^2$, presenting a Blockage Ratio (BR) of 2.2% when the tandem geometry was at 0° yaw, and a BR of 3.3% when at 20° yaw. The platform and supporting structures were included in the BR calculation. The BR was determined as small enough ($\approx 3\%$) to prevent any severe effects (Franke et al., 2007; Tominaga et al., 2008), but large enough to be taken into consideration to provide accurate validation data for CFD simulations. No solid blockage corrections were applied to the force data acquired in the wind tunnel experiments. Instead, CFD simulations were performed that matched the wind tunnel dimensions (Figure 4.3) and thus capture any solid blockage effects, allowing for the resulting drag and lateral forces to be compared directly. All support structures and geometry simplifications necessary for the wind tunnel experiments were included in these CFD models, as illustrated in Figure 4.1b and Figure 4.3. Furthermore, the raised platform from the wind tunnel experiments was also included in the numerical simulation. A no-slip wall with zero roughness was specified to represent the tandem geometry, support structures, platform geometry and the walls of the wind tunnel. A velocity of 60 m/s was set at the velocity-inlet boundary, and a zero static gauge pressure was imposed at the outlet boundary. An inlet turbulence intensity of 0.2% and a hydraulic diameter of 1 m were used, where the turbulence intensity matched that of the wind tunnel experiment. Also in the wind tunnel test, the mean velocity approaching the cyclist model was uniform except for a thin boundary layer that was present at the platform surface and that reached a height of 0.06 m at the position of the cyclists. For the validation study, the geometry of the wind tunnel test section and test set-up including the raised platform and support structures were included in the computational domain to allow similar boundary layer development over the platform as in the wind tunnel experiments. The air was specified to have a density of 1.225 kg/m^3 and a dynamic viscosity of $1.789\text{e-}5 \text{ kg/m.s}$. A cylindrical interface was used to allow for the rotation of the tandem geometry and the closed container below the rotational plate (Figure 4.3) which held the two force transducers.

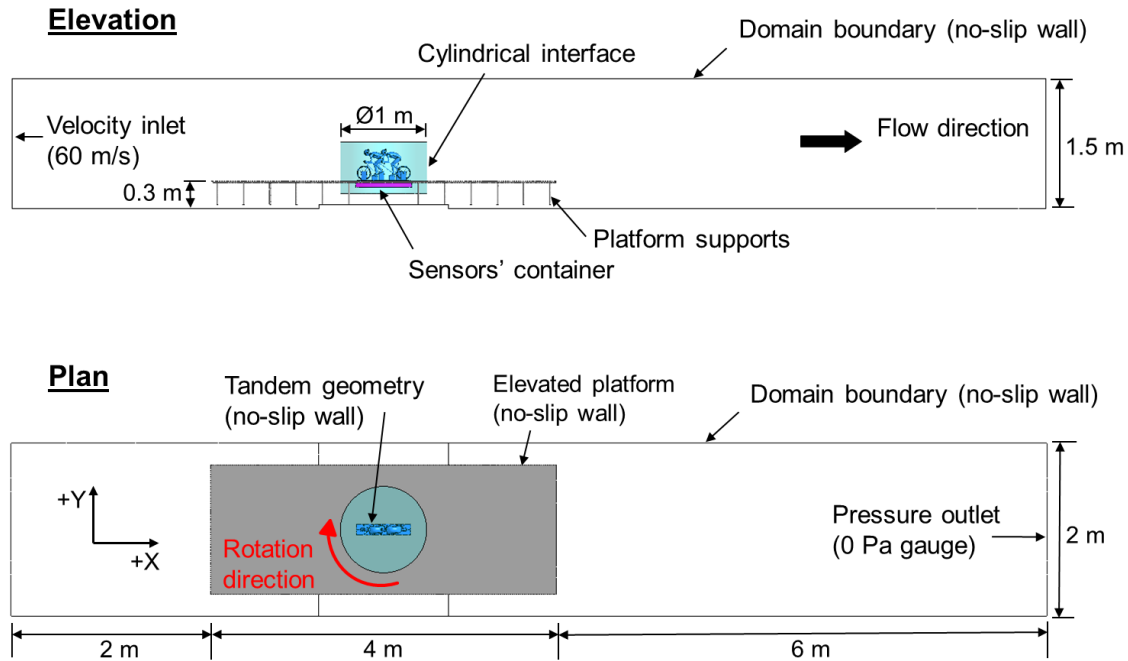


Figure 4.3. Elevation and plan view of the computational domain for the quarter-scale tandem geometry. The tandem geometry and dimensions of the flow domain are representative of the wind tunnel experimental setup.

Polyhedral cells were used to discretise the fluid domain, with surface face sizes and cell volume sizes based on the grid sensitivity studies conducted by Mannion et al. (2018a). As recommended by Mannion et al. (2018a), inflation layers were used to capture wall bounded flow, and to yield an average y^* value of 0.8. The y_P value for the first cells at the surface of the scaled tandem geometry was $5 \mu\text{m}$. The total number of computational cells was 18,981,392. Figure 4.4a illustrates the grid on a section plane through the centre of the fluid domain. Figure 4.4b-c illustrate grid densities on part of the athlete geometry and on part of the bicycle geometry, respectively. Figure 4.4d-e illustrate the inflation layers from the athlete geometry and the tandem bicycle wheel geometry.

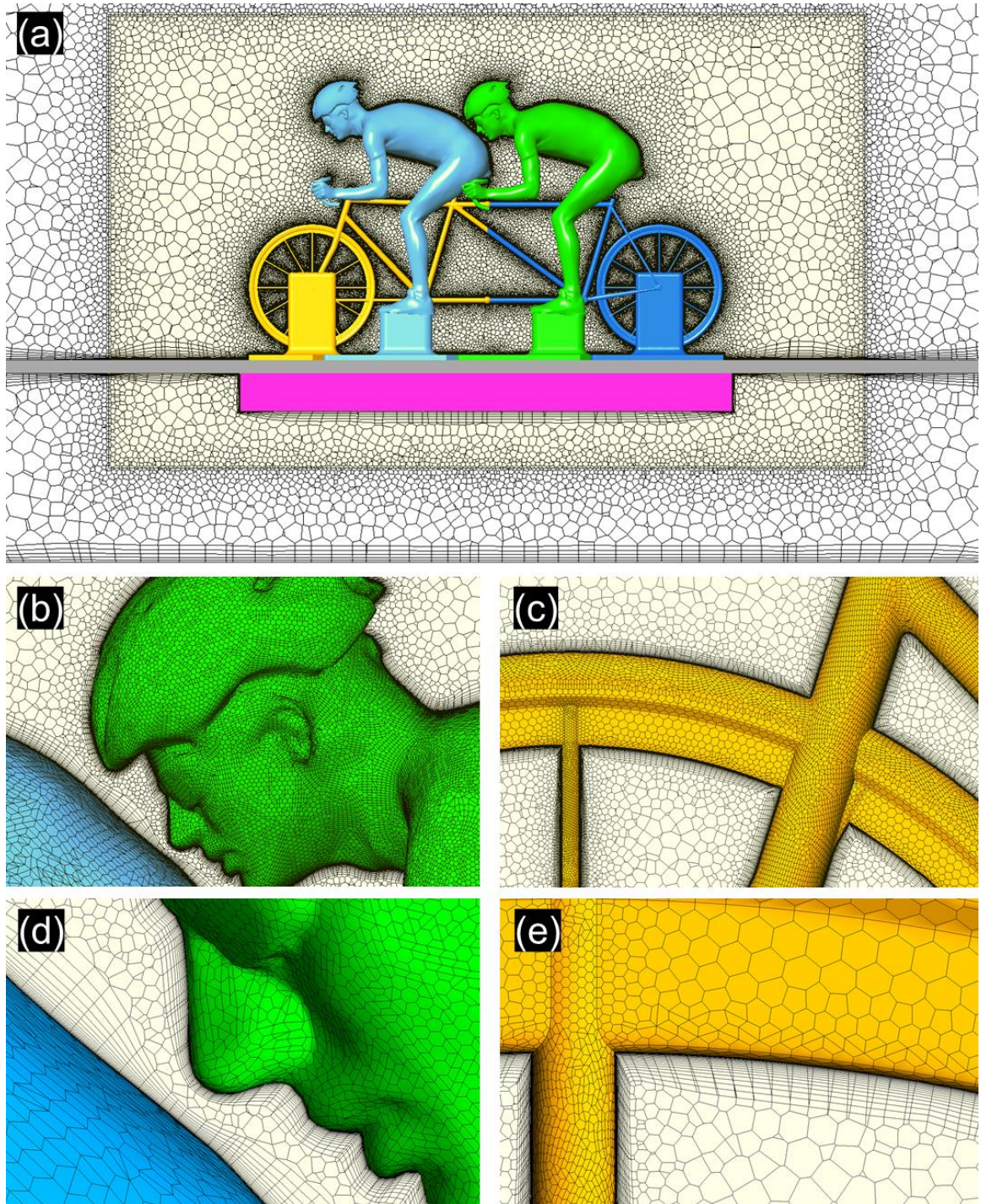


Figure 4.4. (a) Parts of the computational grid: (a) in a plane through the centre of the fluid domain, (b) the athlete geometry, (c) the tandem front wheel, (d) inflation layers on the athlete geometry, (e) inflation layers on the tandem wheel geometry. 18,981,392 polyhedral cells exist in the grid.

4.3.2 Solver settings

ANSYS Fluent 16 (ANSYS Fluent, 2015) was used to perform the RANS simulations. The choice of turbulence model for closure was based on a sensitivity analysis, described in the following subsection. Second-order discretisation schemes were used, with second-order pressure interpolation, the Coupled algorithm for pressure velocity coupling, and the Least Squares Cell Based method to compute gradients. Tandem cycling aerodynamics is inherently unsteady due to the bluff body aerodynamics and the proximity of the pilot and stoker athletes. Hence, the pseudo transient solver was used, because conventional steady-state proved unsuitable to attain acceptable convergence, and force values were averaged over 4000 iterations after a stable oscillatory phase had been achieved, with a pseudo-transient time-step of 0.000625 s. The averaging time period of 2.5 s (4000 steps) was determined through comparisons with drag and lateral forces for the pilot and stoker, averaged over progressively larger time scales as illustrated in Figure 4.5.

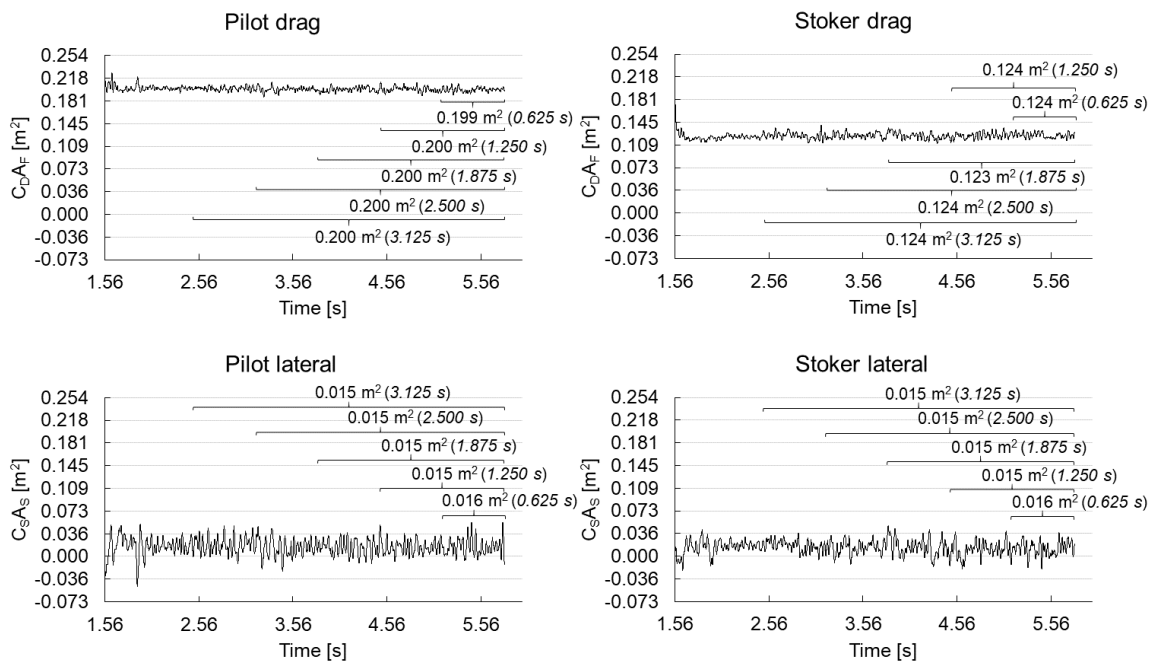


Figure 4.5: Drag and lateral areas over time for the pilot and stoker, at 0° yaw using the SST k- ω turbulence model.

4.3.3 Turbulence model study

A turbulence model sensitivity analysis was conducted considering 20° yaw to gauge the sensitivity of turbulence modelling to the yaw angle. Based on the findings by Mannion et al. (2018a),

four turbulence models were used in the sensitivity analysis; the 1-equation Spalart-Allmaras (S-A) turbulence model (Spalart and Allmaras, 1992), the 2-equation SST $k-\omega$ model (Menter, 1994), the 3-equation $k-kl-\omega$ model (Walters & Cokljat, 2008), and the 4-equation T-SST turbulence model (Menter et al., 2006). Figure 4.6a-b presents a comparison of forces predicted by each turbulence model on the pilot and stoker respectively, against the wind tunnel findings for 20° yaw. A wide spread of force predictions was found, with the $k-kl-\omega$ turbulence model providing the most accurate results. The $k-kl-\omega$ predicted the drag and lateral forces on the pilot within -12.0% and 10.8% respectively to the wind tunnel results for 20° yaw. The drag on the stoker was predicted to be within 1.7%, and the lateral force to be within -11.1%. The SST $k-\omega$ and T-SST turbulence models under-predicted the lateral force on the pilot and stoker in excess of -20%. The drag predictions for the pilot and stoker using the T-SST and SST $k-\omega$ models were over-predicted; exceeding 20%. The S-A provided a reasonable drag prediction for the pilot with a deviation of 7.4%, but the drag for the stoker deviated by 18.3%. Lateral force predictions for the S-A model for both the pilot and stoker exceeded 20%. The $k-kl-\omega$ turbulence model was chosen for further study across all yaw angles based on the results of this study. Mannion et al. (2018a) found that the SST $k-\omega$ model provided good predictions for tandem cycling aerodynamics at 0° yaw (drag deviations < 5%) from a wide selection of turbulence models. Thus, this turbulence model was also chosen for further evaluation across a range of yaw angles, detailed in subsection 4.3.4.

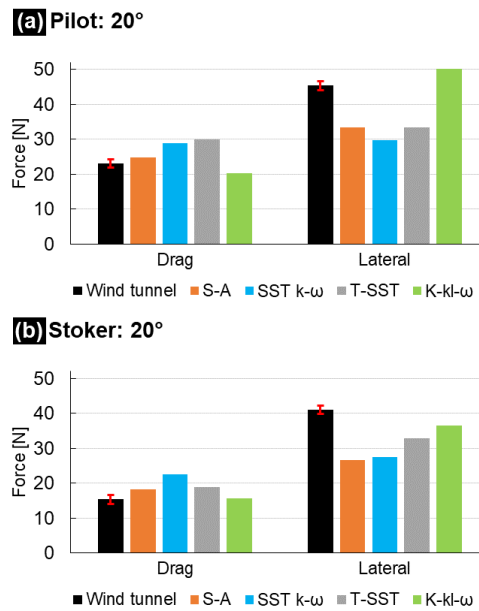


Figure 4.6. Comparison of experimental and numerical of drag and lateral forces on the (a) pilot, and (b) stoker, at 20° yaw.

4.3.4 Validation study

In addition to the individual force component comparisons, the combination of the drag and lateral forces via the force magnitude calculation was also used as an indicator for the agreement between the wind tunnel and CFD results, and the percentage deviation of the CFD results was calculated by:

$$\%_{dev} = \frac{\sqrt{F_{D_CFD}^2 + F_{S_CFD}^2} - \sqrt{F_{D_WT}^2 + F_{S_WT}^2}}{\sqrt{F_{D_WT}^2 + F_{S_WT}^2}} \quad (4.1)$$

where F_{D_CFD} is the drag force predicted by CFD, F_{S_WT} is the lateral force predicted by CFD, F_{D_WT} is the drag force predicted in wind tunnel experiments, and F_{S_WT} is the lateral force predicted in wind tunnel experiments.

The $k\text{-}kl\text{-}\omega$ and SST $k\text{-}\omega$ turbulence models were used in the validation study across all the yaw angles investigated in the wind tunnel experiments (0° , 5° , 10° , 15° and 20°). Figure 4.7a-b compare the drag and lateral force data for the pilot and the stoker, respectively. The SST $k\text{-}\omega$ model provided more accurate aerodynamic force predictions than the $k\text{-}kl\text{-}\omega$ model for both the pilot and stoker at 0° and 5° , with deviations (equation 4.1) of 3.6% and 8.5% for the pilot, and 6.5% and -5.4% for the stoker at both yaw angles respectively. However, the $k\text{-}kl\text{-}\omega$ model provided more accurate drag and lateral predictions for the yaw range of 10° to 20° . The predictions for the force magnitude on the pilot and stoker using the $k\text{-}kl\text{-}\omega$ turbulence model for 10° , 15° and 20° yaw were all within the 10% deviation from the results of the wind tunnel experiments (Figure 4.7c), outperforming the predictions from the SST $k\text{-}\omega$ turbulence model. The $k\text{-}kl\text{-}\omega$ predictions of the force magnitude for the pilot deviated by 1.4%, 2.0% and 6.5% for 10° , 15° and 20° respectively. Fairly good force magnitude predictions were also found for the stoker with deviations of 8.8%, 5.3% and -9.5% for 10° , 15° and 20° respectively (Figure 4.7c). Between 10° - 20° yaw, the SST $k\text{-}\omega$ model under-predicted the lateral force on the pilot and over-predicted the drag force. Deviations (equation 4.1) were in excess of 10% for 10° - 20° yaw for the SST $k\text{-}\omega$ model. The $k\text{-}kl\text{-}\omega$ model over-predicted drag forces on the pilot and stoker at 0° and 5° yaw, but provided more reliable force predictions at higher yaw angles (10° - 15°), most notably where the SST $k\text{-}\omega$ under-predicted the lateral forces on the pilot and stoker at 20° yaw.

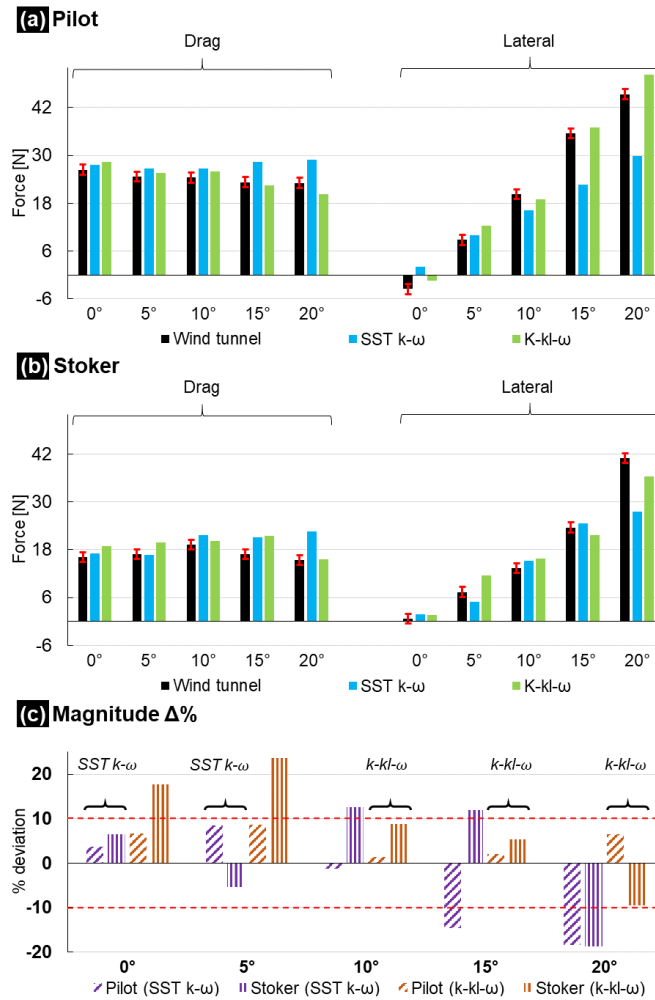


Figure 4.7. Drag and lateral force comparison on (a) the pilot and (b) the stoker for the wind tunnel and CFD simulation results. (c) The difference between the force magnitude predictions (%) of the wind tunnel experiments and CFD simulations for the pilot and stoker. The brackets indicate the chosen turbulence model specific to a yaw angle which was used for the remainder of the study.

Differences in the flow predictions between the k-kl- ω and SST k- ω turbulence models are presented in Figure 4.8a-b for 20° yaw. The SST k- ω turbulence model was found to generate larger under-pressure zones and smaller over-pressure zones than the k-kl- ω model. Flow separation was delayed when using the k-kl- ω model by comparison to the SST k- ω , resulting in improved pressure recovery from the separation occurring farther to the rear of the tandem athlete geometry. The difference in the predictions of the flow separation locations is thought to impact the drag and lateral force predictions by determining the location of the maximum and minimum pressure differentials on the torso of the athlete. Figure 4.9a-b illustrates the difference in flow separation locations between the k-kl- ω and SST k- ω models respectively on the backs of the pilot and the stoker at 20° yaw, where the SST k- ω was found to predict flow separation at locations upstream to those predicted by the k-

kl- ω model. Compared to the wind-tunnel results, the k-kl- ω correctly predicted the decreasing drag forces on the pilot and stoker between 10°-20° yaw, and the corresponding high increase in lateral forces at the same yaw angles; 166.2% increase in lateral force for the pilot using the k-kl- ω model by comparison to 82.6% by the SST k- ω model. The difference in flow separation locations predicted by the two turbulence models, further impacted vortex locations and their directions. Figure 4.8 demonstrates the difference in normalised vorticity predictions between the k-kl- ω and SST k- ω models in a horizontal plane at 20° yaw. The interactions of the vortices from the pilot on the stoker downstream further impact the difference in flow predictions between both turbulence models. The correct prediction of flow separation locations by the k-kl- ω model at higher yaw angles may also be partly due to the laminar-turbulent transition calculation enabled by this turbulence model. It is noted that the Transition SST (T-SST) k- ω turbulence model (Menter et al., 2006) also enables a laminar-turbulent transition to be resolved in the boundary layer, but this model did not provide benefits over the SST k- ω model at 20° yaw for the pilot. However, more accurate lateral force predictions were provided for the stoker using the T-SST model, indicating that the laminar-turbulent transition may be important in tandem aerodynamics modelling in crosswind conditions. The k-kl- ω turbulence model drag predictions for the pilot and stoker were less accurate than the SST k- ω model at 0° and 5°. However, although the SST k- ω provided more accurate drag force predictions at 0° and 5° yaw, it did not correctly predict the drag and lateral force trends as the yaw angles increases to 10°, 15° and 20° (Figure 4.7). Thus, it is recommended that the turbulence model employed should consider the yaw angle of interest. The SST k- ω turbulence model was chosen for further study for 0° and 5° only, while the k-kl- ω was used for the yaw angles of 10°, 15° and 20°, as highlighted in Figure 4.7c where the better performing turbulence model is highlighted using brackets for each respective yaw angle.

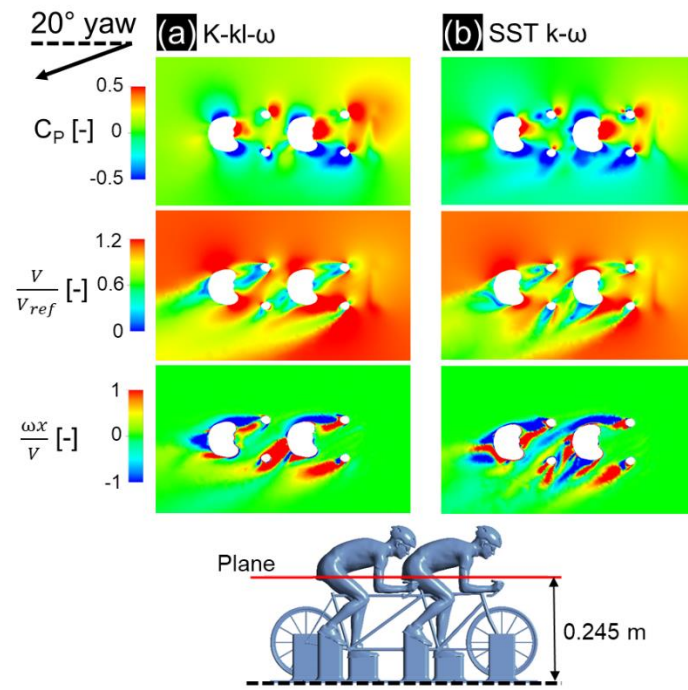


Figure 4.8. Comparison of pressure coefficient, normalised velocity, and normalised vorticity at 20° yaw for (a) the k-kl- ω , and (b) the SST k- ω turbulence model.

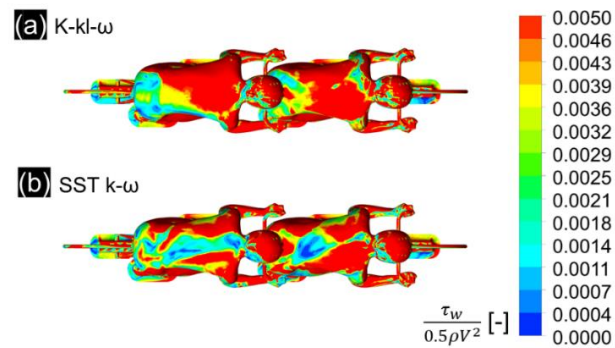


Figure 4.9. Comparison of normalised shear stress on the quarter-scale tandem simulations at 20° yaw using (a) the k-kl- ω , and (b) the SST k- ω turbulence models.

4.4 CFD simulations: Aerodynamic analysis of crosswind conditions

4.4.1 Computational settings

The geometrical model of the tandem and the athletes used in this section were obtained by removing the structural support/stiffness elements present in the quarter-scale wind tunnel model. In

addition to removing the supporting structures attached to the wheels and athlete legs, the tandem was raised 0.02 m from the ground surface to prevent highly skewed cells at the contact patch between the tyres and road surface. Accurate representations of the front forks, chain stays, wheel hubs, pedals, cranks and handlebars were included in the simulations (Figure 4.10). However, some elements of the tandem bicycle were neglected from the geometrical model that were considered small enough not to influence the characteristic flow around the tandem. These included the chains, sprockets, and also brake and gear cables and mechanisms. The projected frontal area of the tandem geometry was 0.399 m², and the projected side area was 1.364 m².

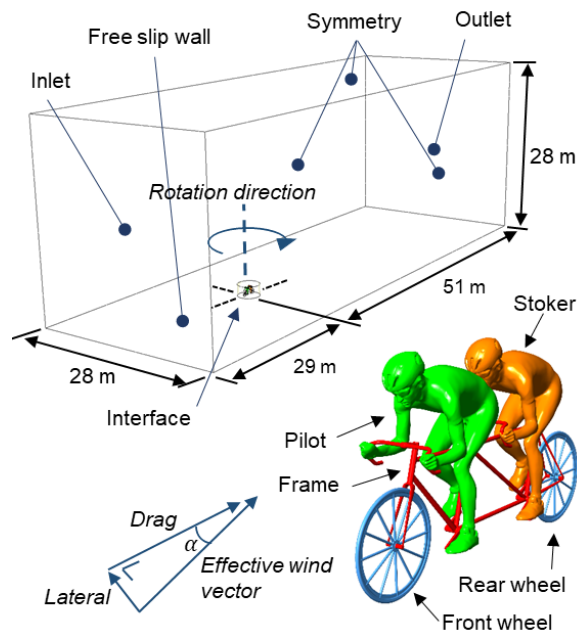


Figure 4.10. Isometric view of the computational domain used for the aerodynamic analysis and the full-scale tandem geometry.

The computational domain was represented by a cuboid with dimensions of 80x28x28 m³ (Figure 4.10). The resulting maximum blockage ratio at 20° yaw was 0.1% to negate any blockage effects. A maximum blockage ratio of 3% is recommended by (Franke et al., 2007; Tominaga et al., 2008). Figure 4.10 depicts the boundary conditions implemented for the computational domain. An inlet velocity of 15 m/s was used, which is representative of the high velocities that tandem athletes can achieve. All surfaces of the tandem bicycle and the athletes were represented using a smooth no-slip wall with zero roughness. A symmetry boundary condition with a zero-normal gradient for all variables was imposed on the outer boundaries of the domain. A pressure-outlet condition with 0 Pa static gauge pressure was imposed on the outlet boundary. An interface was used to facilitate a cylindrical volume around the tandem's geometry which could be rotated to specific yaw angles (Figure 4.10). A pseudo-time-step of 0.01 s was used for the simulations, which was scaled from the

quarter-scale simulations using the Courant-Friedrichs-Lewy (CFL) condition described in equation 4.2, to ensure the time-step size was representative of the geometrical scale and fluid velocity. The numerical methodology described in section 4.3.2 was followed to set up the full-scale simulations. In addition, the grid sizes used for the full-scale simulations were scaled directly from the quarter-scale simulations described in section 4.3.1. The average y^* for the full-scale simulation was below 1 as per the quarter-scale simulations. The y_P value for the first cells at the surface of the athletes and tandem bicycle was $10\ \mu\text{m}$. Figure 4.11 illustrates the y^* distribution at 0° yaw for the quarter-scale and full-scale simulations for comparison. The SST $k-\omega$ turbulence model was used for the 0° and 5° yaw angles, while the $k-kl-\omega$ turbulence model was used for the 10° , 15° and 20° yaw angles following the findings outlined in subsection 4.3.4.

$$C = \frac{U \Delta t}{x} \quad (4.2)$$

C is the Courant number [-], U is the velocity [m/s], Δt is the time-step size [s], and x is the length scale [m].

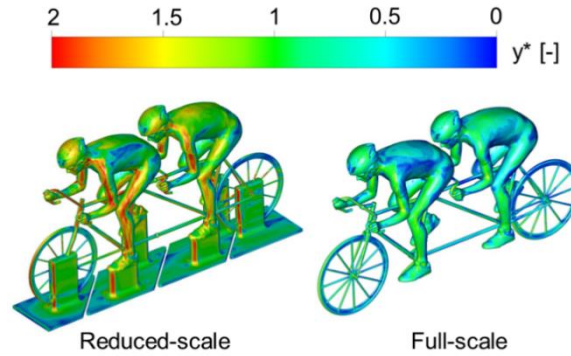


Figure 4.11. Comparison of y^* at 0° yaw for the full-scale and reduced-scale simulations.

4.4.2 Crosswind force predictions

The drag area ($C_D A_F$) and the lateral force area ($C_S A_S$) were used to describe and compare the forces on tandem cycling in crosswind conditions:

$$C_D A_F = \frac{F_D}{0.5\rho V^2} \quad (4.3)$$

$$C_S A_S = \frac{F_S}{0.5\rho V^2} \quad (4.4)$$

where F_D is the drag force [N], V is the crosswind velocity [m/s] (free-stream velocity in the computational domain), ρ is the density [kg/m^3], A_F is the frontal area [m^2], and F_S is the lateral force [N] where the sub-script letter ‘S’ represents the side (lateral) force, 90° to the drag axis (Figure 4.10).

A_S is the projected side area [m^2] of the tandem, C_D is the drag force coefficient and C_S is the lateral force coefficient.

The results are provided in Figure 4.12. The C_{DAF} was found to increase with increasing yaw angle up to 15° . It reached its maximum value at 15° with an increase of 8.4% from 0° . The drag at 20° dropped by 9.5% from its value at 15° ; slightly lower than the drag originally experienced at 0° . The C_{SA_S} increased steadily with yaw angle, providing a near match to the drag force at 15° (3.9% difference). At 20° , the C_{SA_S} was larger than the C_{DAF} by 52.8%.

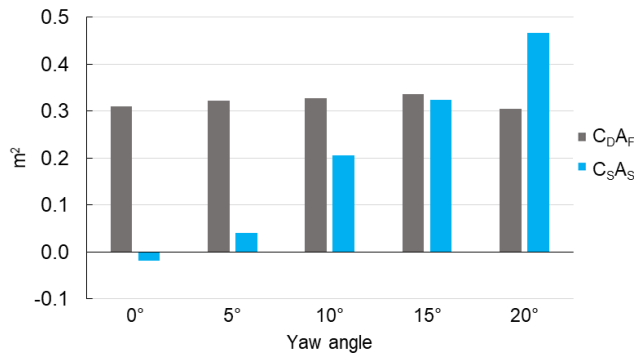


Figure 4.12. A comparison of drag area (C_{DAF}), and the lateral force area (C_{SA_S}) for the full tandem geometry (pilot, stoker and bicycle) as obtained from the full-scale CFD simulations.

Figure 4.13a presents the drag forces on the pilot, stoker and tandem bicycle. The inclusion of data on the tandem bicycle lends clarity to the distribution of the drag forces, and their impact on the C_{DAF} displayed in Figure 4.13. The pilot experienced a maximum drag at 0° and a reduction thereafter with increasing yaw angle. The stoker experienced a maximum drag at 15° . The bicycle experienced a steady increase in drag with increasing yaw angle. This elucidates the increase in drag area (Figure 4.12) with increasing yaw angle from 0° - 15° , where the drag increase experienced by the bicycle and the stoker offsets the drag reduction experienced by the pilot. However, between 15° - 20° , the stoker experienced a reduction in drag. This drag reduction experienced by the stoker in addition to the reduction experienced by the pilot resulted in a net reduction for the total drag, providing a C_{DAF} slightly less even than the value predicted for 0° . The bicycle experienced an equivalent drag force to the stoker at 20° yaw, and contributed 31.6% to the total drag force, in comparison to a 21.1% contribution at 0° yaw, illustrating the extent to which the drag increased on the bicycle as the yaw angle increased.

The lateral forces experienced by the pilot and stoker are presented in Figure 4.13b. The tandem bicycle was also found to follow a comparable trend to the athletes, with larger lateral forces with increasing yaw angle. The bicycle experienced lateral forces comparable to the pilot, and the

stoker experienced a lesser lateral force than the pilot at yaw angles between 5°-20°. At 5°, the stoker experienced a near-zero lateral force of 0.11 N, which is not visible in Figure 4.13b.

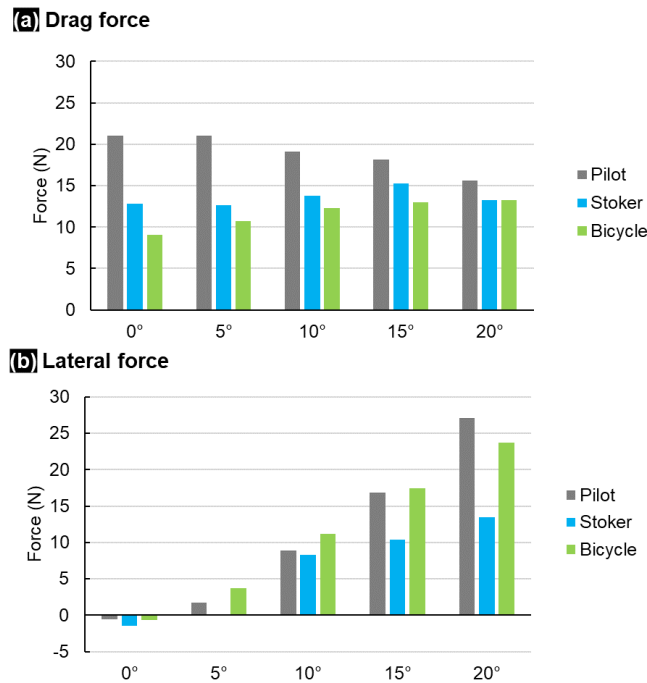


Figure 4.13. Drag (a) and lateral (b) forces experienced by the pilot, stoker and the tandem bicycle through the investigated yaw angles as obtained from the full-scale CFD simulations.

4.5 Discussion

The range of deviations between wind tunnel and numerical studies at different yaw angles found in this study are comparable to those found by Fintelman et al. (2015a) using RANS methods, who reported typical deviations of 9% for drag forces, and 21% for lateral forces. Deviations in excess of 10% for lateral forces were also found by Fintelman et al. (2015a) for 15° using LES and DES methods. The best performing turbulence model for each yaw range yielded aerodynamic force deviations (equation 4.1) < 10% in the present study; the SST $k-\omega$ model for 0°-5° yaw and the $k-kl-\omega$ model for 10°-15° yaw. Deviations outside of this selection were in excess of 20% for some turbulence models. Maximum C_{DAF} values were found at 15° yaw by Fintelman et al. (2015a) for a solo cyclist, and also for tandem cycling in the present study.

This study found that the drag of a tandem (pilot, stoker and tandem bicycle) rises by up to 8.4% with increasing yaw angles from 0°-15° deg. However, at 20°, a reduction in drag was found, with the resulting drag force 1.9% less than the force experienced at 0°. The C_{SA} s was found to be

52.8% greater than the drag force at 20° yaw, whereas at 15° yaw, the lateral force was 3.9% less than the drag force. The athletes contended with a higher lateral force than the drag force at 20° yaw, which could have implications for cyclist stability. Figure 4.14 details pressure coefficient contour plots on the model surfaces for each yaw angle tested. An extensive low-pressure region developed on the sides of the athletes' legs and arms leeward to the stream-wise flow direction. The pilot experienced larger pressure gradients than the stoker at lower yaw angles at equivalent locations, as the stoker was shielded from the oncoming flow by the pilot. However, at a yaw angle of 20°, the stoker experienced a comparable under-pressure region on his legs and helmet, along with a similar over-pressure region on the front of his right arm, right leg and helmet (Figure 4.14). The drafting effect experienced by the stoker was reduced as the yaw angle increased and the stoker was partially removed from the wake of the pilot. However, at 20°, the drag benefit from the crosswind outweighed the drag losses from being removed from the wake of the pilot. This finding for the stoker experiencing a reduction in drag at 20° was similar to the pilot's reduction in drag at the same yaw angle (13.1% and 14.2% respectively).

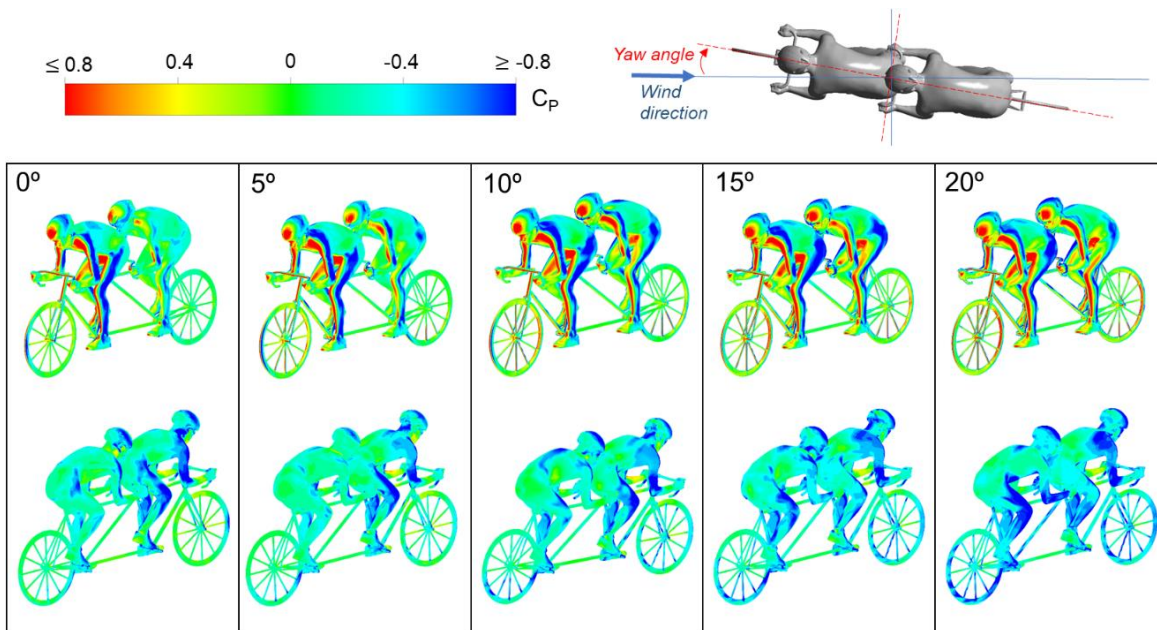


Figure 4.14. Pressure coefficient contours plotted on the tandem surfaces for each yaw angle investigated.

The combinations of various flow phenomena contributed to the trends in aerodynamic forces, including flow separation and reattachment locations, pressure recovery on the bodies of the pilot and stoker athletes, the interaction of the wake flow from the pilot with the stoker, and the subsonic upstream disturbance from the stoker on the pilot. A noticeable trend in the drag forces of the pilot and stoker athletes was that the difference between the drag of both athletes was reduced with increasing yaw angle. At yaw angles of 15° and 20°, the drag difference between the pilot and

stoker was just 16.2% and 15.1% respectively. The stoker was partially removed from the wake of the pilot at these yaw angles (Figures 4.14 and 4.15), however, Figure 4.15a₂-b₂ shows a local acceleration in the flow in Plane B between the pilot and stoker, which resulted in higher velocity gradients on the right side of the stoker torso (athletes perspective) similar to that of the pilot. This local acceleration effectively separated the low velocity wake field from the pilot and the approach flow for the stoker to some extent. An over-pressure region on the surface of the stoker and in the flow field ahead of the torso formed, similar to that of the pilot; excluding the stoker's right arm which is firmly in the wake of the pilot at 15° and 20° yaw. This flow phenomenon induced flow fields around the stoker similar to that of the pilot, and may also be attributed to the stoker experiencing a reduction in drag between 15°-20° yaw similar to the pilot. Furthermore, the pressure coefficient fields around the legs of the stoker at 20° (Figure 4.15a₁-b₁) resembled that of the pilot. The right leg of the pilot was also impacted from the wake flow of the front wheel and tandem frame which may have aided in the similarities between the two pressure-fields at this yaw angle.

The drag reduction found for both the pilot and stoker athletes between 15°-20° was due in part to the shifting locations of maximum and minimum pressure differentials around the body of the athlete, which resulted in larger lateral forces. However, the drag of an isolated cyclist (Fintelman et al., 2015a), and indeed even of a hand-cyclist (Mannion et al., 2018c), has been shown to increase between 0°-15° yaw before reducing at subsequent higher yaw angles. This phenomenon was not found for the pilot in this study, likely due to the upstream impact of the stoker. The upstream disturbance from the stoker likely reduced the absolute under-pressure on the back and left side of the pilot's torso as the yaw angle increased, improving pressure recovery and delaying flow separation by comparison to what might occur with a solo cyclist; possibly contributing to the acceleration of the flow between both athletes at yaw angles of 15° and 20°. Similar instances of upstream disturbance from a trailing athlete have been reported in the literature for two drafting cyclists (Blocken et al., 2013) and also for tandem cyclists at 0° yaw (Mannion et al., 2015b). However, when evaluating the total drag of the pilot, stoker and tandem bicycle combined, it is interesting to note that the maximum drag also occurs at 15°, as per the findings of Fintelman et al. (2015) and Mannion et al. (2018c) for a solo able-bodied cyclist and a hand-cyclist respectively.

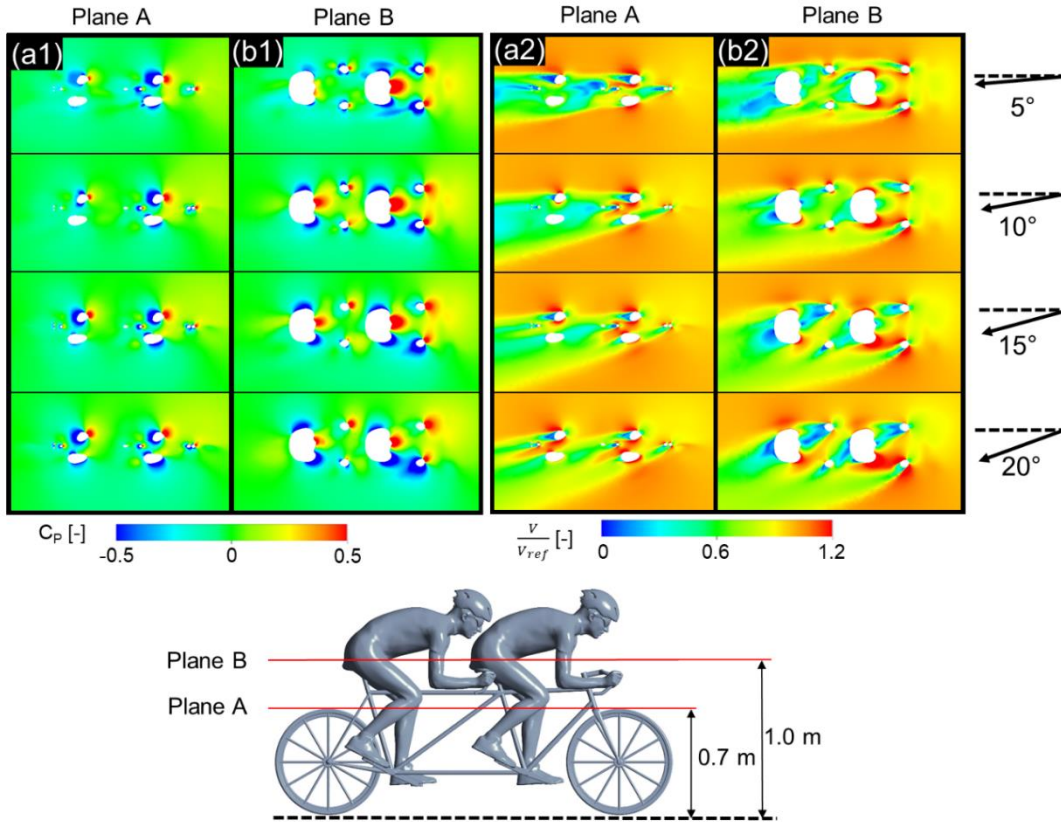


Figure 4.15. Pressure coefficient and normalised velocity on (a) plane A, and (b) plane B, respectively.

Among the yaw angles tested, the largest drag force experienced by the pilot was at 0° , and the stoker at 15° . It is recommended that tandem bicycles should also be a focus of drag optimisation in the design phase to ensure good overall aerodynamic performance of a tandem. It should be noted that the critical angle to a single degree increment where the dominant aerodynamic force switches from drag to lateral, is not quantified in this study, and is expected to be dependent on individual and unique athlete anthropometrics. It is also noted that the findings of this study may not hold for all tandem athlete posture/positioning combinations, and that further research is required in this area.

The accessibility and computational cost of the RANS approach makes it an effective choice for tandem cycling aerodynamics, provided that the simulation results adhere to best practice guidelines (e.g. Casey and Wintergerste 2000, Franke et al. 2007, Tominaga et al. 2008) and are validated. However, methods such as Large Eddy Simulation (LES) may provide accurate solutions with less dependency on turbulence modelling. Furthermore, methods such as Detached Eddy Simulation (DES) (or sub-variants thereof) and Scale Adaptive Simulation (SAS) may also provide accurate solutions. If validated, the potential benefit of such methods would be the provision of a single method with a higher accuracy than RANS (Blocken, 2018), applicable for all tandem cycling

simulations and reducing uncertainty on which turbulence model to use for any given investigation. However, the cost benefit of RANS in both time and computing resources currently makes it a more accessible method than LES.

There were several simplifications made in this experimental and numerical research of tandem cycling. Firstly, the wheels were modelled as static. In reality, they would be rotating at a velocity dependent on the linear speed at which the cyclist would be travelling. Secondly, the full-scale wheel spokes were simplified to twelve 0.012 m diameter spokes. The quarter-scale tandem models manufactured for the wind tunnel experiment had a diameter limitation of 3 mm for manufacturing purposes, and the spokes for the computational model matched in scale. The full-scale tandem computational model contained additional geometrical complexity than the quarter-scale wind tunnel geometry. However, there were still geometrical simplifications present such as neglected cables, chain, sprockets, brake mechanisms and gearing mechanisms. The added computational effort to accurately capture the flow around these small components was deemed too prohibitive given the small influence they would likely have on the flow characteristics in tandem cycling. In addition, all surfaces were modelled as smooth surfaces with zero roughness, when in reality there may be varying roughness on surfaces such as the rider's skinsuit, or bicycle tyres. The impact of roughness on skin-suits for tandem cycling is an open field for future research.

4.6 Conclusions

Wind tunnel experiments and CFD simulations were conducted to assess the accuracy of CFD simulations for modelling tandem cycling aerodynamics in yaw conditions. CFD simulations were designed to match the physical parameters of the wind tunnel with a high degree of detail for validation purposes. A second set of full scale simulations were created to mimic tandem cycling in free air conditions. Flow velocities were representative of those experienced by tandem athletes at outdoor race events. It was found that a single turbulence model does not provide reliable results for all yaw angles tested. The SST $k-\omega$ turbulence model was found to be most accurate at 0° and 5° yaw angles for predicting drag and lateral forces, but less accurate at higher yaw angles. However, at these higher yaw angles the $k-kl-\omega$ turbulence model followed the trends set in the wind tunnel, and yielded more accurate force predictions at 10°, 15° and 20° yaw.

For the whole tandem system (pilot, stoker and bicycle), a C_{DAF} of 0.311 m² was found for 0° yaw using full-scale CFD, which increased to 0.337 m² at 15°. However, a reduction in drag was found at 20° with a C_{DAF} of 0.305 m². The pilot was found to experience decreasing drag with increasing yaw angle. The stoker experienced increasing drag from 0° to 15° and a drag reduction

between 15° to 20°. The tandem bicycle was found to experience larger drag forces with increasing yaw angles, and contributed to 31.6% of the net drag at 20° yaw, in comparison to 21.1% at 0° yaw.

The maximum C_{SA_S} was recorded at 20° yaw. The C_{SA_S} recorded at 20° yaw was 52.8% greater than the C_{DA_F} at the same angle. A significant C_{SA_S} was also recorded at 15°, only 3.9% less than the C_{DA_F} recorded at the same angle. The distribution of lateral forces was 42.1%, 21.0%, and 36.9% between the pilot, stoker and tandem bicycle respectively at 20° yaw.

For future work, it is recommended that tandem crosswind scenarios are modelled with additional yaw angle resolution, and with different athlete postures/positioning combinations, to provide greater understanding of the response of tandem cycling to crosswind effects. For practice it is recommended that athlete posture and apparel drag optimisation studies be conducted under crosswind conditions, with at least 0° and 15° recommended as key yaw angles from this research.

4.7 References

- ANSYS Fluent. (2015). ANSYS Fluent theory guide. *Release 16.1 Documentation*. ANSYS Inc.
- Artec Europe. (2017). Artec Eva, 3D Scanners. Retrieved May 22, 2017, from <https://www.artec3d.com/3d-scanner/artec-eva>
- ATI Industrial Automation, (2018). F/T Sensor Delta. Retrieved April 4, 2018, from www.atia.com/app_content/Documents/9230-05-1330.auto.pdf
- Barry, N., Burton, D., Sheridan, J., Thompson, M., & Brown, N. A. T. (2015a). Aerodynamic drag interactions between cyclists in a team pursuit. *Sports Engineering*, 18, 93–103. <https://doi.org/10.1007/s12283-015-0172-8>
- Barry, N., Burton, D., Sheridan, J., Thompson, M., & Brown, N. A. T. (2015b). Aerodynamic performance and riding posture in road cycling and triathlon. *Proceedings of the Institution of Mechanical Engineers, Part P: Journal of Sports Engineering and Technology*, 229(1), 28–38. <https://doi.org/10.1177/1754337114549876>
- Blocken, B., Defraeye, T., Koninckx, E., Carmeliet, J., & Hespel, P. (2013). CFD simulations of the aerodynamic drag of two drafting cyclists. *Computers & Fluids*, 71, 435–445. <https://doi.org/10.1016/j.compfluid.2012.11.012>
- Blocken, B., & Toparlar, Y. (2015). A following car influences cyclist drag: CFD simulations and wind tunnel measurements. *Journal of Wind Engineering and Industrial Aerodynamics*, 145(0),

178–186. <https://doi.org/10.1016/j.jweia.2015.06.015>

- Blocken, B., Toparlar, Y., & Andrienne, T. (2016). Aerodynamic benefit for a cyclist by a following motorcycle. *Journal of Wind Engineering and Industrial Aerodynamics*, 155, 1–10. <https://doi.org/https://doi.org/10.1016/j.jweia.2016.04.008>
- Blocken B., van Druenen, T., Toparlar Y., Malizia F., Mannion P., Andrienne T., Marchal T., Maas GJ., Diepens J. (2018). Aerodynamic drag in cycling pelotons: new insights by CFD simulation and wind tunnel testing. *Journal of Wind Engineering and Industrial Aerodynamics*. *Accepted for publication*.
- Blocken, B. (2018). LES over RANS in building simulation for outdoor and indoor applications: A foregone conclusion? *Building Simulation*, 11(5), 821-870 <https://doi.org/10.1007/s12273-018-0459-3>
- Crouch, T. N., Burton, D., LaBry, Z. A., & Blair, K. B. (2017). Riding against the wind: a review of competition cycling aerodynamics. *Sports Engineering*, 20(2), 81–110. <https://doi.org/10.1007/s12283-017-0234-1>
- Crouch, T. N., Burton, D., Thompson, M. C., Brown, N. A. T., & Sheridan, J. (2016). Dynamic leg-motion and its effect on the aerodynamic performance of cyclists. *Journal of Fluids and Structures*, 65, 121–137. <https://doi.org/10.1016/j.jfluidstructs.2016.05.007>
- Defraeye, T., Blocken, B., Koninckx, E., Hespel, P., & Carmeliet, J. (2010a). Aerodynamic study of different cyclist positions: CFD analysis and full-scale wind tunnel tests. *Journal of Biomechanics*, 43(7), 1262–1268. <https://doi.org/10.1016/j.jbiomech.2010.01.025>
- Defraeye, T., Blocken, B., Koninckx, E., Hespel, P., & Carmeliet, J. (2010b). Computational fluid dynamics analysis of cyclist aerodynamics: Performance of different turbulence-modelling and boundary-layer modelling approaches. *Journal of Biomechanics*, 43(12), 2281–2287. <https://doi.org/10.1016/j.jbiomech.2010.04.038>
- Fintelman, D. M., Sterling, M., Hemida, H., & Li, F.-X. (2014a). The effect of crosswinds on cyclists: an experimental study. In *The 2014 conference of the International Sports Engineering Association, Procedia Eng.* (Vol. 72, pp. 720–725). <https://doi.org/10.1016/j.proeng.2014.06.122>
- Fintelman, D. M., Sterling, M., Hemida, H., & Li, F.-X. (2014b). Optimal cycling time trial position models: Aerodynamics versus power output and metabolic energy. *Journal of Biomechanics* 47(8): 1894-1898. <https://doi.org/10.1016/j.jbiomech.2014.02.029>

- Fintelman, D. M., Hemida, H., Sterling, M., & Li, F.-X. (2015a). CFD simulations of the flow around a cyclist subjected to crosswinds. *Journal of Wind Engineering and Industrial Aerodynamics*, *144*, 31–41. <https://doi.org/10.1016/j.jweia.2015.05.009>
- Fintelman, D. M., Hemida, H., Sterling, M., & Li, F.-X. (2015b). The effect of time trial cycling position on physiological and aerodynamic variables. *Journal of Sports Sciences* *33*(16): 1730–1737. <https://doi.org/10.1080/02640414.2015.1009936>
- Franke, J., Hellsten, A., Schlünzen, H., & Carissimo, B. (2007). Best practice guideline for the CFD simulation of flows in the urban environment. *COST Action 732: Quality Assurance and Improvement of Microscale Meteorological Models*. Hamburg Germany.
- Íñiguez-de-la Torre, A., & Íñiguez, J. (2009). Aerodynamics of a cycling team in a time trial: does the cyclist at the front benefit? *European Journal of Physics*, *30*(6), 1365.
- Jones, W. P., & Launder, B. E. (1972). The prediction of laminarization with a two-equation model of turbulence. *International Journal of Heat and Mass Transfer*, *15*(2), 301–314. [https://doi.org/10.1016/0017-9310\(72\)90076-2](https://doi.org/10.1016/0017-9310(72)90076-2)
- Lukes, R. a, Chin, S. B., & Haake, S. J. (2005). The understanding and development of cycling aerodynamics. *Sports Engineering*, *8*, 59–74. <https://doi.org/10.1007/BF02844004>
- Mannion, P., Toparlar, Y., Blocken, B., Hajdukiewicz, M., Andrianne, T., & Clifford, E. (2018a). Improving CFD prediction of drag on Paralympic tandem athletes: Influence of grid resolution and turbulence model. *Sports Engineering*, *21*(2) 123-135. <https://doi.org/10.1007/s12283-017-0258-6>
- Mannion, P., Toparlar, Y., Blocken, B., Clifford, E., Andrianne, T., & Hajdukiewicz, M. (2018b). Aerodynamic drag in competitive tandem para-cycling: road race versus time-trial positions. *Journal of Wind Engineering & Industrial Aerodynamics*, *179*, 92–101. <https://doi.org/10.1016/j.jweia.2018.05.011>
- Mannion, P., Toparlar, Y., Blocken, B., Clifford, E., Andrianne, T., & Hajdukiewicz, M. (2018c). Analysis of crosswind aerodynamics for competitive hand-cycling. *Journal of Wind Engineering and Industrial Aerodynamics*, *180*(August), 182–190. <https://doi.org/10.1016/j.jweia.2018.08.002>
- Menter, F. R. (1994). Two-equation eddy-viscosity turbulence models for engineering applications. *AIAA Journal*, *32*(8), 1598–1605. <https://doi.org/10.2514/3.12149>
- Menter, F. R., Langtry, R. B., Likki, S. R., Suzen, Y. B., Huang, P. G., & Völker, S. (2006). A

- correlation-based transition model using local variables—Part I: model formulation. *Journal of Turbomachinery*, 128(3), 413–422. <https://doi.org/10.1115/1.2184352>
- Spalart, P., & Allmaras, S. (1992). A one-equation turbulence model for aerodynamic flows. In *30th Aerospace Sciences Meeting and Exhibit*. American Institute of Aeronautics and Astronautics. <https://doi.org/http://doi.org/doi:10.2514/6.1992-439>
- Sumner, D. (2010). Two circular cylinders in cross-flow : A review. *Journal of Fluids and Structures*, 26(6), 849–899. <https://doi.org/10.1016/j.jfluidstructs.2010.07.001>
- Tominaga, Y., Mochida, A., Yoshie, R., Kataoka, H., Nozu, T., Yoshikawa, M., & Shirasawa, T. (2008). AIJ guidelines for practical applications of CFD to pedestrian wind environment around buildings. *Journal of Wind Engineering and Industrial Aerodynamics*, 96(10–11), 1749–1761. <https://doi.org/10.1016/j.jweia.2008.02.058>
- UCI. (2017). Cycling Regulations, Part 1 General Organisation of Cycling as a Sport, version on 26/07/2017. Union Cycliste Internationale. Retrieved from http://www.uci.ch/mm/Document/News/Rulesandregulation/18/30/80/1-GEN-20170726-EN_English.PDF
- Walters, D. K., & Cokljat, D. (2008). A three-equation eddy-viscosity model for Reynolds-Averaged Navier–Stokes simulations of transitional flow. *Journal of Fluids Engineering*, 130(12), 121401. <https://doi.org/10.1115/1.2979230>

Aerodynamic drag in competitive tandem para-cycling: road race versus time-trial positions

Chapter 5 uses the grid and turbulence model sensitivity studies from Chapter 3 to inform the initial parameters of a wider study that investigates the aerodynamic drag from different tandem setups; focused at both road and track race events. Numerical simulations for solo cyclists are also used to aid in further understanding the aerodynamic interaction between the pilot and stoker athletes in tandem cycling.

This chapter has been published in the international peer-reviewed *Journal of Wind Engineering and Industrial Aerodynamics*:

Mannion, P., Toparlar, Y., Blocken, B., Clifford, E., Andrienne, T., & Hajdukiewicz, M. (2018). Aerodynamic drag in competitive tandem para-cycling: road race versus time-trial positions. *Journal of Wind Engineering & Industrial Aerodynamics*, 179, 92–101. <https://doi.org/10.1016/j.jweia.2018.05.011>

Abstract: An athlete's riding posture is a key element for aerodynamic drag in cycling. Tandem cycling has the complication of having two athletes in close proximity to each other on a single tandem bicycle. The complex flow-field between the pilot and stoker in tandem cycling presents new challenges for aerodynamic optimisation. Aerodynamic drag acting on two tandem road race setups and two track time-trial setups were analysed with computational fluid dynamics (CFD) simulations. For validation purposes, wind tunnel measurements were designed providing drag measurements from both tandem athletes simultaneously using a quarter-scale model. A max drag force deviation of 4.9% was found between the wind tunnel experiments and CFD simulations of the quarter-scale geometry. Full-scale CFD simulations of upright, crouched, time-trial and frame-clench tandem setups were performed. The drag force experienced by individual athletes in all investigated tandem setups was compared to that of solo riders to enhance understanding of the aerodynamic interaction between both tandem athletes. The most aerodynamic tandem setup was found to be the frame-clench setup which is unique to tandem cycling and had a C_{DA} of 0.286 m², and could provide an advantage of 8.1 s over a standard time-trial setup for a 10 km time-trial event.

5.1 Introduction

Tandem cycling is a sports branch governed by the International Cycling Union (UCI). Athletes who are visually impaired can compete in this discipline as the stoker, the rear athlete on the tandem bicycle. The lead athlete, denoted as the pilot, has full visual capabilities. The UCI has rules and restrictions over the suitability of an athlete to perform as a pilot, most notably, that members of a UCI professional team cannot perform as a tandem pilot, although it is allowed for former professional riders to do so (UCI, 2017).

Becoming faster by improving their aerodynamic profile is becoming a coveted prize for both elite and amateur cyclists. This is especially common within the core of elite cycling institutions across the world both for able-bodied and para disciplines. Aerodynamic enhancements in elite able-bodied solo cycling have often traversed over to tandem cycling; in the form of aerodynamic wheel and frame designs, athlete apparel, and athlete posture refinements. However, little is known about the fundamentals of tandem aerodynamics and how the air flow interacts with the pilot and the stoker. Thus, there are likely opportunities for aerodynamic refinements specific to tandem cycling with alternative posture combinations, athlete apparel, and equipment design. Typical tandem postures for individual tandem athletes are often similar to postures adopted by solo athletes (Figure 5.1). These include upright, dropped, crouched and various time-trial (TT) postures. Postures can be athlete specific depending on the anthropometrics and flexibility of the riders. Postures can also exist specific to tandem cycling, such as the frame-clench stoker posture (Figure 5.1b); used particularly in timed events. Here, the stoker grasps the top tube of the frame (just behind or under the pilot's saddle) instead of holding the handlebars in a track event, in an effort to 'hide' behind the pilot to a greater degree. The UCI has specific restrictions limiting the movement of the handlebars and the saddle, which are used for athlete posture adjustments. Additional rules limit the dimensions of the tandem frame tubes, and aerodynamic devices or attachments are not permitted (UCI, 2017). These rules apply to both tandem and solo competitive cyclists, and are intended to keep the competition both fair and safe for all athletes participating.

CFD simulations and wind tunnel testing have been widely used in sports engineering in general and in cycling aerodynamics studies in particular (Blocken, 2014; Crouch et al., 2017). To the best of our knowledge, only Mannion et al. (2018) published a CFD and wind tunnel investigation on tandem cycling aerodynamics. Mannion et al. (2018) presented new guidelines for the modelling of tandem aerodynamics using CFD, and determined that the accurate prediction of flow separation is crucial for the appropriate assessment of tandem aerodynamics using CFD. Hence, a low average y^* value less than 1 was recommended when generating a grid for a tandem cycling case study.

Counter-intuitive and incorrect drag occurrences between the pilot and the stoker were observed when this guideline was not followed, with the stoker experiencing a larger drag force than the pilot. Mannion et al. (2018) also highlighted the impact of selecting a suitable turbulence model for tandem cycling aerodynamics, with the SST $k-\omega$ model (Menter, 1994) recommended for tandem cycling aerodynamics research. This is in agreement with the findings of Defraeye et al. (2010b) who also determined that the SST $k-\omega$ turbulence model provided the best overall predictions for solo cyclist aerodynamics, through obtaining detailed validation data from wind tunnel experiments with pressure measurements in addition to force and moment measurements.

Within the remaining literature, tandem cycling bears a close resemblance to a two-rider drafting formation; where two athletes cycle in close proximity and in-line with each other in order to provide a drag reduction primarily for the trailing cyclist. However, Blocken et al. (2013) determined through CFD simulations that the leading cyclist in a two-rider drafting formation can experience a reduction in drag by up to 2.6%. The benefit that a leading cyclist can gain was found to be enhanced if, instead of a trailing cyclist, a motorbike or a car was behind the cyclist (Blocken & Toparlar, 2015; Blocken et al., 2016). Indeed, a cyclist was found to experience drag reductions of up to 8.7% from a single following motorbike. The flow structures around two reduced scale in-line cyclists were analysed experimentally by Barry et al. (2016), who observed that the wake flow of the trailing cyclist was characteristic of that from a solo cyclist. Full scale wind tunnel experiments on two drafting cyclists were conducted by Barry et al. (2014), who found that the leading and trailing cyclists experienced maximum drag reductions up to 5% and 49% respectively.

Competitive solo cyclist postures and cycling positions have been widely researched in the literature, for both optimal power output and aerodynamics (Gnehm et al., 1997; Oggiano et al., 2008; Defraeye et al. 2010a; Underwood & Jermy, 2010; Chabroux et al., 2012; Fintelman et al., 2014a, 2015) where both computational and experimental methods have been successfully utilised to determine optimal postures for athletes. Defraeye et al. (2010a) conducted CFD analyses of solo cycling postures; upright, dropped and TT, and results from full-scale wind tunnel experiments were used to validate the computational results; C_{DA} values of 0.270 m², 0.243 m² and 0.211 m² were obtained for the upright, dropped and TT postures respectively from the wind tunnel experiments. Fintelman et al. (2014a) concluded that athletes should balance power output with aerodynamics, but determined that aerodynamic losses exceeded physical power losses at a velocity of 46 km/h, indicating that the importance of aerodynamics may outweigh the importance of power delivery at high speeds. Barry et al. (2015b) conducted wind tunnel experiments using solo cyclists to determine the influence of various athlete postures on aerodynamic drag. It was found that an optimal aerodynamic solution was for the athlete to bring his arms inside the silhouette of his torso and hips. It was also found that for an athlete in a dropped posture for a road race setup, the power requirement

to maintain the same velocity can drop by 7% by lowering the head and torso to a crouched posture with horizontal forearms.

To the best knowledge of the authors, there has been no research on tandem posture variations conducted in the literature, and with no appearance in relevant review papers (Crouch et al., 2017; Lukes et al., 2005). Given the number of aerodynamic posture refinements that are applicable for a solo cyclist, there is an extensive scope of research for tandem athletes yet to be conducted. Readers are referred to Defraeye et al. (2010a) for a comparative summary of drag data for various solo cycling postures in the early cycling aerodynamics literature (1980's – 2000's).

The research presented here addresses the predominant gap in the literature regarding typical tandem athlete posture combinations. CFD simulations are performed by solving the 3D Reynolds-averaged Navier-Stokes (RANS) equations to explore the aerodynamics of two typical tandem road setups, and two tandem track TT setups. Figure 5.1 shows two examples of competitive tandem cyclists with athlete posture combinations for a road race and outdoor TT event. Wind tunnel experiments are used to provide validation data for the CFD simulations.

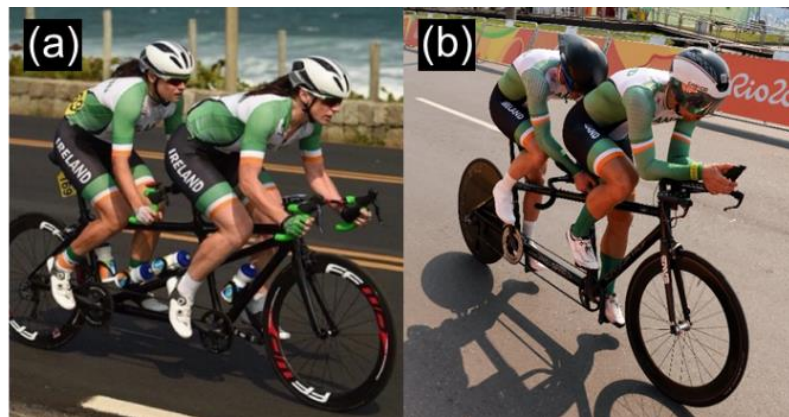


Figure 5.1. (a) Irish female tandem team competing in a road race event, (b) Irish male tandem team competing in an outdoors TT event. The athletes in these photos were not involved in this research. (© Sportfile, Cycling Ireland and Paralympics Ireland, reproduced with permission).

5.2 Wind tunnel experiments

Wind tunnel experiments were devised to provide drag data on both the pilot and the stoker individually. Wind tunnel experiments were carried out in the aeronautical test section of the wind tunnel laboratory in the University of Liège, Belgium. A single athlete was 3D scanned using an Eva structured light scanner (Artec Europe, 2017) in a crouched posture, relevant to both pilot and stoker positions. By using the same geometrical athlete model for both the pilot and stoker positions, any

inferred drag bias raised due to anthropometrical differences between two different athletes was removed. Quarter-scale 3D models were manufactured for the pilot, stoker and tandem bicycle by CSC cutting (Figure 5.2). Similar to the set-up in Blocken et al. (2016), the model was raised 0.3 m from the bed of the test section by a sharp edged horizontal platform to limit the boundary layer development upstream of the test geometries. The resulting blockage in the 2 m x 1.5 m test chamber with zero yaw was 2.2%. The tandem bicycle was simplified, with restrictions on the size of components capable of being manufactured at quarter-scale by CSC cutting. Components smaller than 3 mm could not be accurately manufactured. Thus, smaller components such as sprockets, the chain, derailleur, and cables were neglected. Furthermore, the front and rear wheel required large rectangular supports that encompassed the wheel hub to ensure the stiffness of wheels and frame to avoid vibrations throughout testing. A single cylindrical tube represented the front forks. Twelve spokes were modelled in the wheel geometries, with a spoke diameter of 3 mm in the quarter-scale model.

Instead of attaching a single force transducer to the complete tandem setup to provide total drag measurements, the pilot and stoker geometries were kept separated from the tandem bicycle with individual force transducers attached to both athletes to provide forces on each separate athlete. The vertical axis of each sensor was positioned at the centre of gravity of both athlete geometries. The tandem bicycle was split into front and rear halves as per Figure 5.2, to allow for model disassembly.

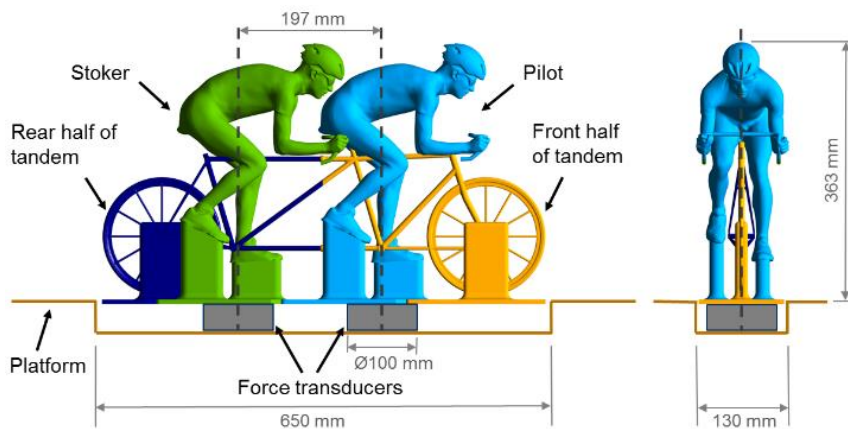


Figure 5.2. Quarter-scale tandem geometry used for the wind tunnel experiments with the two force transducers.

A full-scale velocity of 15 m/s was chosen for the tandem setup, resulting in a 60 m/s velocity in the wind tunnel to obtain Reynolds number similarity. Both force transducers were zeroed prior to experimentation. The sampling rate for the recorded drag data was 10 Hz. The recording period was 180 s in total. A settling period of 30 s was allocated for the transducers at a test velocity of 60 m/s prior to recording force data. A pitot tube provided flow velocity recordings. Temperature

measurements were taken to correct the drag data to 15°C, to align with the air density of 1.225 kg/m³ that was used for the CFD simulations. The drag data were also corrected for atmospheric pressure to a standard atmosphere of 101325 Pa, which was the value used in the CFD simulations. The variation of atmospheric pressure in Liège on the test day was obtained from local meteorological data and was limited: 6 am (102500 Pa) 12pm noon (102500 Pa) and 6pm eve (102700 Pa). These variations were not taken into account in correcting the drag data.

Only a single tandem geometrical model was manufactured, representing a single athlete posture combination. In addition to 0° yaw, a yaw angle of 5° was also considered in the experiments to provide a second data set in the absence of being able to test various postures. A rotational plate built into the elevated platform in the wind tunnel allowed for the alignment of 0° and 5° yaw angles. The resulting drag forces for the tandem at 0° and 5° yaw are discussed in section 5.3.4 alongside the CFD results for comparison.

5.3 Validation study

5.3.1 Computational domain and boundary conditions

The problems in applying solid blockage corrections to tandem cyclists and the related inaccuracy were presented by Mannion et al. (2018). Thus, for validation purposes, a CFD fluid domain that replicated the geometry of the wind tunnel with a quarter-scale tandem model was developed for validation purposes, allowing for direct comparison with the drag recorded on the pilot and stoker in the wind tunnel experiments without any solid blockage correction being required (Figure 5.3). The tandem geometry matched the geometry used in the wind tunnel experiment, with all support structures and simplifications. Features in the wind tunnel with a frontal area smaller than 0.02 m² (e.g. screw heads) were neglected from the computational domain. The surfaces of the tandem geometry, platform surface and supports, and outer domain surfaces which represented the walls of the wind tunnel, were modelled using a no-slip wall with zero roughness (Figure 5.3). A velocity inlet condition was used to impose a uniform velocity of 60 m/s for the quarter-scale validation simulation, with a 0.2% turbulence intensity and a hydraulic diameter of 1 m. The fluid was specified as air with a viscosity of 1.789×10^{-5} kg/m.s and a density of 1.225 kg/m³ (air at 15°C). A pressure outlet condition was applied at the outlet plane, with a 0 Pa static gauge pressure. An interface zone (Figure 5.3) was used to allow the tandem geometry to be rotated clockwise from 0° to 5° in the same location as the wind tunnel experiment. A second interface zone was positioned underneath the upper platform

surface to capture the rotation of the casing box that encompasses the force transducers in the wind tunnel setup. The location of the interface zone is also visible in Figure 5.4 via the grid sizes imposed on the interface boundary condition.

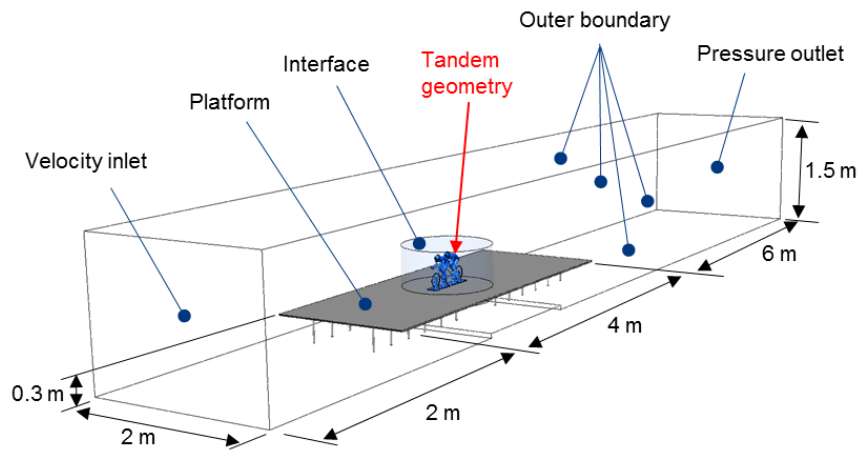


Figure 5.3. Geometrical replica of the wind tunnel test section used for the validation of the CFD simulations.

5.3.2 Computational grid

The grids generated in this study were based on the grid convergence studies described by Mannion et al. (2018). Prism layers were grown from no-slip wall surfaces in the fluid domain. For the tandem geometry, a total of 26 layers were used with a growth ratio of 1.2. A wall-adjacent cell centre normal height restriction of $5 \mu\text{m}$ was applied to the tandem athlete and bicycle surfaces, resulting in average and maximum y^+ values of 0.8 and 3.0 respectively. To model the boundary layer flow on the platform surfaces and on the outer walls of the wind tunnel geometry, 10 prism layers with a first aspect ratio of 20 were imposed. Two bodies of influence (BOI's) were used to envelope the tandem geometry with cells limited to specific sizes, to accurately capture wake flow features: 1) A $0.5 \times 0.15 \times 0.375 \text{ m}^3$ BOI with a maximum cell volume of $6.25 \times 10^{-8} \text{ m}^3$ was placed around the tandem geometry, and 2) A BOI with dimensions of $1.25 \times 0.45 \times 0.5 \text{ m}^3$, extended further into the wake region with a maximum cell volume of $3 \times 10^{-6} \text{ m}^3$. Figure 5.4a depicts the surface grid on the athletes, with the prism layers growing from the wall surfaces visible via a centre-plane. The volume grid density surrounding the interface zone, platform surface, and outer domain surface is illustrated in Figure 5.4c. The maximum cell face size on the rotational interface surface was 6 mm. The maximum cell face size in the complete fluid domain was 80 mm on the outer walls of the domain. The total number of computational cells was 46,167,727.

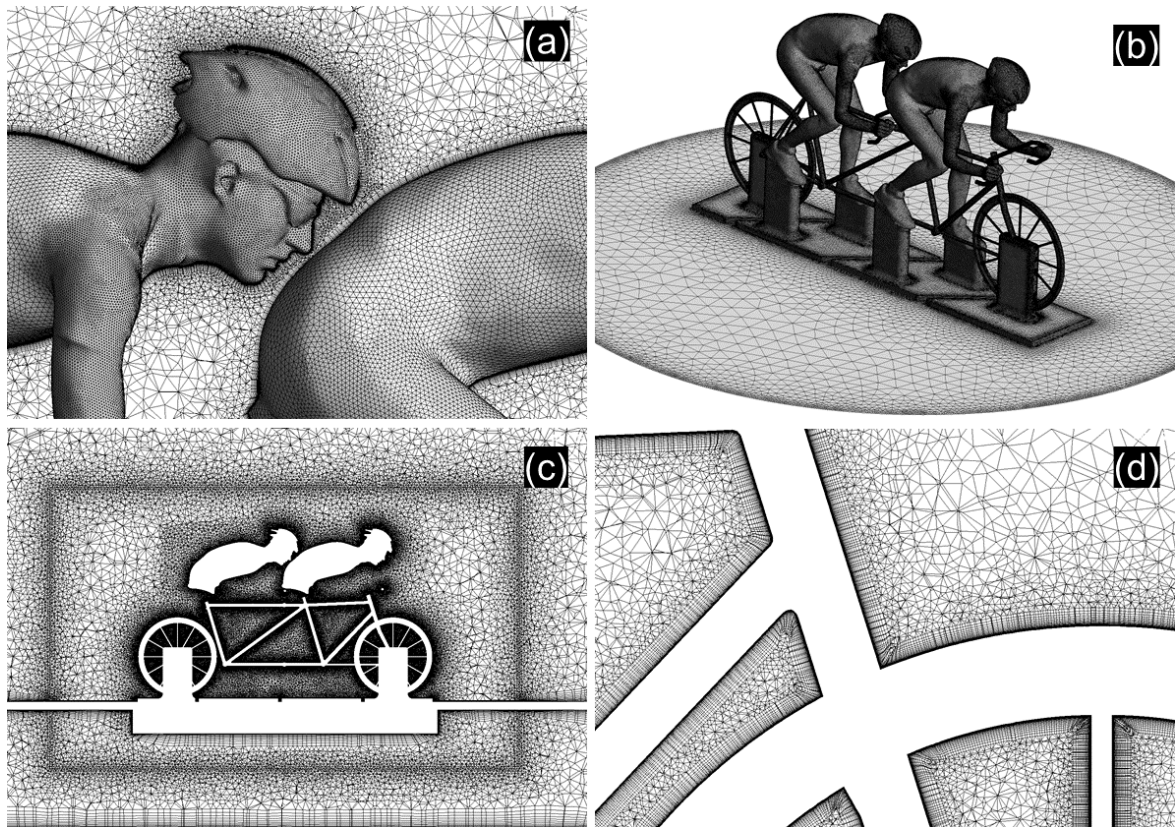


Figure 5.4. (a) Part of the surface grid on the tandem athletes, (b) part of the surface grid on the platform and tandem geometry (c) part of the volume grid in a vertical plane for the tandem geometry in the modelled wind tunnel environment (d) part of the volume grid around the front wheel rim, spokes, and front frame tube members (number of cells: 46,167,727).

5.3.3 Governing equations & solver settings

The commercial CFD solver ANSYS Fluent 16 (ANSYS Fluent, 2015) was used for all the simulations which utilises the control volume discretisation method. The 3D steady RANS equations were solved, using the shear stress transport (SST) $k-\omega$ 2-equation turbulence model (Menter, 1994) to achieve closure. Pressure-velocity coupling was handled with the Coupled algorithm. Gradients were computed using the Least-squares Cell-Based method (ANSYS Fluent, 2015). Pseudo-transient calculations were utilised with a pseudo time-step size of 0.000625 s. Second order discretisation schemes were used for turbulent kinetic energy, specific dissipation rate, and momentum, in addition to second order pressure interpolation. The following minima in scaled residuals were observed for the converged solutions: 5×10^{-6} for momentum, 1×10^{-3} for continuity, 7×10^{-4} for specific turbulence dissipation rate and 4×10^{-4} for turbulent kinetic energy. Drag forces were averaged over the final 4000 iterations from a total of 9000, which allowed for a stationary oscillatory period to emerge prior to averaging.

5.3.4 Comparison of results with wind tunnel experiments

As shown in the colour coded Figure 5.2, the drag measurements for both the pilot and the stoker included their respective handlebars and foot supports. The drag experienced by the bicycle was not recorded in the wind tunnel experiment, and hence is not discussed for the validation of the CFD simulations. The resulting drag forces on the pilot and the stoker at both yaw angles tested are displayed in Figure 5.5, for both the wind tunnel experiments and CFD simulations. The drag predictions were representative of the x-axis of the force transducers which were yawed along with the tandem model, and not held in the stream-wise flow direction. Thus, the transducers x-axis remained aligned with the tandem geometry. At 0° yaw, the CFD simulations drag predictions deviated by 4.7% for the pilot, and by -3.4% for the stoker. At 5° yaw, further good agreement between the CFD and wind tunnel experiments was observed for the pilot with a deviation of 4.9%. The CFD drag prediction for the stoker at 5° yaw deviated again by -3.4% from the wind tunnel result. The absolute difference between the CFD and wind tunnel experiments for all drag measurements was within the 1.24 N error range of the force transducers used in the experiments.

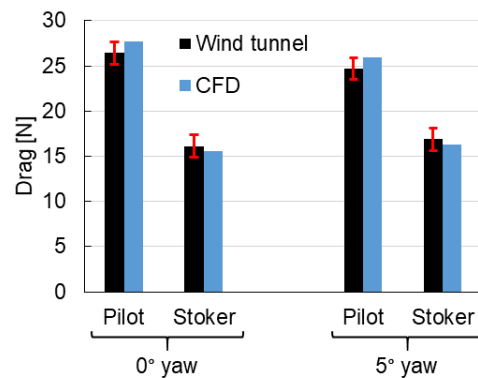


Figure 5.5. Comparison of drag forces from wind tunnel experiments and CFD simulations at yaw angles of 0° and 5°. The error lines denote the margin of errors due to the measurement equipment.

Good agreement and consistency was found between the wind tunnel experiments and CFD simulations (< 5% drag deviation). Thus, the settings and parameters used for the CFD simulations were considered suitable for the analysis of variations of the tandem geometry, i.e. road and TT event setups. The same athlete and the same basic bicycle geometry were used for all further studies, with the position of the legs identical for all posture variations investigated.

5.4 Comparison of tandem setup variations

5.4.1 Geometrical models

Four tandem geometries were developed for aerodynamic analysis using CFD as shown in Figure 5.6; upright, crouched, time-trial (TT) and frame-clench (FC). Due to varying athlete anthropometrics, there is a wide variety of possible tandem athlete positions, some unique to the individual pairs of athletes. Thus, this study uses the same rider for both pilot and stoker positions to provide non-biased results. The upright setup is not commonly adopted in competitive cycling events and it is most commonly used for casual non-competitive tandem cycling, or for warming up or relaxing at the beginning or the end of a competitive event. However, it provides an interesting comparison to other tandem postures. In this setup, both athletes wore a road helmet and spoked wheels were fitted to the bicycle geometry. The athletes had their hands on the upper part of a standard handlebar with outstretched arms. The crouched setup featured both the pilot and stoker in an aggressive drops posture with bent elbows, forearms parallel to the road, wearing road helmets, and with spoked wheels fitted to the bicycle geometry. The stoker in the TT setup adopted a crouched posture, wearing a TT helmet. The pilot in the TT and FC setups adopted a typical solo TT posture with their arms resting on elbow pads. The stoker in the FC setup (used in time-trial events), exhibited a torso angle similar to that of the crouched posture, but did not use the handlebars. Instead, the stoker grasped the top tube of the tandem bicycle in the vicinity underneath the pilot's saddle. The exact location of grasping the frame can vary depending on individual rider preferences. For this study, the stoker grasped the intersection of the top tube and seat tube below the pilot's saddle. The stoker's head was tilted towards the ground to a larger degree than that of the crouched posture, which can be typical of a stoker athlete when grasping the frame over the handlebars (Figure 5.1b). Both the TT and FC setups were representative of track TT events, with two disk wheels fitted to the bicycle, while the riders wore teardrop shaped TT helmets. The location of the legs within the 360° crank cycle in each tandem setup was identical. During scanning of the actual athlete body, a wooden pedal stopper was used to ensure uniformity in the location of the legs between 3D scans of different postures, where the left crank (athlete perspective) was positioned at an angle of 20° anticlockwise to the horizontal plane.

Three solo geometries were created, representative of an upright, crouched and TT setup (Figure 5.6). These solo geometries used the same athlete's geometrical model as their respective tandem counterparts. By modelling these athlete postures in a solo scenario, it was possible to gain further understanding on the flow interaction between the pilot and stoker, determining the effect

each athlete has on the flow-field around the other. The same grid parameters for the tandem geometries were applied to the solo geometry for equivalent geometrical features, using the sizing's discussed in section 5.3.2 scaled to the full-scale geometry.

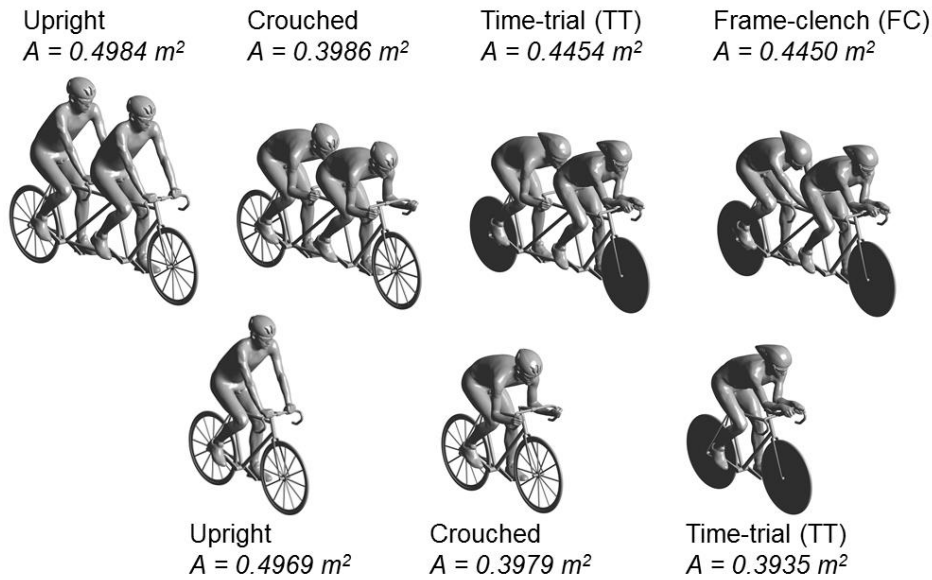


Figure 5.6. Tandem and solo setups with frontal area comparisons.

For both tandem and solo setups, the bicycle geometry was simplified to keep the computational grid from exceeding the capability of the available computational resources. Items such as the chain and sprocket, derailleurs, brake mechanisms and handles were neglected. The spoked wheels were also simplified as per the 3D model for the wind tunnel experiment; twelve spokes with diameters of 0.012 m. Some geometric detail was added, in comparison to the validated case study (section 5.3), including frame forks, cranks, pedals, and frame members that previously, in the experimental setup, were removed or simplified. Each tandem setup was raised 0.02 m from the ground surface to prevent skewed cells forming at the location where the ground surface would be tangent to the wheels. All wheels and athletes' geometries were considered as static within the simulations.

5.4.2 Simulation settings and parameters

The computational domain used for the full-scale tandem and solo cyclists was described by an $80 \times 28 \times 28 \text{ m}^3$ cuboid, which kept the maximum blockage ratio below the recommended by Blocken, (2015), Franke et al. (2007), and Tominaga et al. (2008). The tandem geometry was located

28 m from the inlet boundary condition and centred laterally in the domain. The surfaces of the athletes and bicycle geometries were modelled using a no-slip wall with zero roughness. A uniform velocity of 15 m/s with a 0.2% turbulence intensity was used for the inlet condition, and a 0 Pa static gauge pressure was imposed for the outlet condition. A symmetry condition with zero-normal gradients was applied to the side surfaces of the domain. A pseudo time-step size of 0.01 s was used for these full-scale simulations. The grids for the full-scale tandem geometries were scaled up from the quarter-scale simulations discussed in section 5.3.2. The solo cyclist geometries received identical grid sizing as the tandem simulations on respective athlete and bicycle surfaces to ensure good comparability. Grid sizes are provided in Figure 5.7. All other numerical simulations in this section utilised the same CFD solver parameters as outlined in section 5.3.3.

Target parameters included the drag area [m^2] and pressure coefficient [-]. The drag area is given by:

$$C_D A = \frac{F_D}{0.5 \rho V^2} \quad (5.1)$$

where F_D is the drag force [N], A is the frontal area [m^2], ρ is the density [kg/m^3], and V is the free-stream velocity [m/s]. The pressure coefficient is defined as:

$$C_P = \frac{\Delta P}{0.5 \rho V^2} \quad (5.2)$$

where ΔP [Pa] is the pressure difference between the location of interest and the reference pressure.

5.4.3 Aerodynamic analysis of different setups

The CFD simulations for the different tandem setups showed that the upright setup produced the highest $C_D A$ of 0.413 m^2 , while the crouched tandem setup produced a lower $C_D A$ of 0.314 m^2 . The TT and FC tandem setups yielded similar aerodynamic performance to each other with only 2.4% difference between their $C_D A$ predictions. The FC setup was the more aerodynamic of the two with a $C_D A$ of 0.286 m^2 , against 0.293 m^2 predicted for the TT setup. The solo cyclists experienced $C_D A$ values of 0.327 m^2 , 0.233 m^2 and 0.213 m^2 for the upright, crouched and TT setups respectively. Figure 5.7 compares A , C_D , and $C_D A$ values.

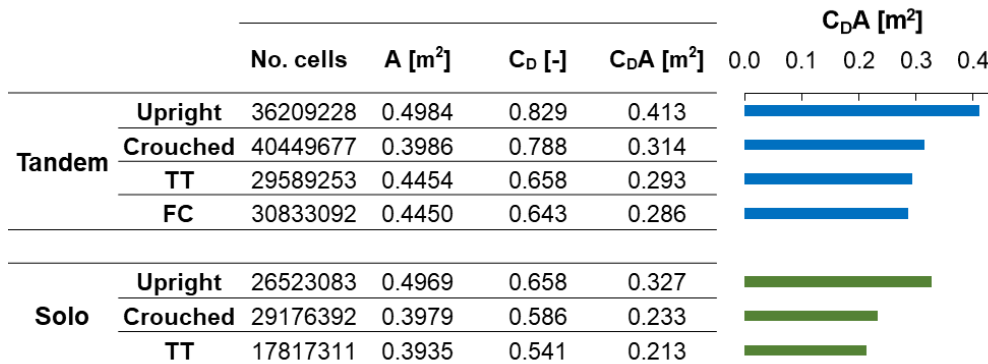


Figure 5.7. Comparison of C_D [-] and C_DA [m²] values as predicted by the CFD simulations for the tandem and solo geometries, with the number of cells per simulation and the projected frontal areas [m²].

The drag experienced by the tandem athletes for each posture combination, and for the solo geometries is plotted in Figure 5.8 without the bicycles included in the drag summations. The pilot and stoker contributed 54.7% and 29.2% respectively to the total drag when adopting upright postures. Respective contributions were 52.4% and 27.0% when crouched postures were adopted. A comparison of the drag interaction between the pilot and stoker for the TT and FC setups presented interesting results relevant to attaining optimisations for tandem athletes. The TT posture the pilot adopted was identical for both the TT and FC tandem setups. For the FC setup, the stoker clenched the frame rather than the handlebars, and tilted his head slightly towards the ground. The stoker in the standard TT setup adopted a crouched posture identical to that of the crouched setup, and experienced 3.8% more drag than the stoker of the FC setup as a result. The pilot of the FC setup also benefited from the posture adopted by the stoker, and experienced 5.1% less drag than the pilot in the standard TT setup, despite the geometrical models of both the TT and FC pilots being the same. This indicates that adjusting the stoker's posture not only provided less drag to the stoker, but also helped to reduce the drag of the pilot. The percentage contributions of the TT and FC athletes to their total drag was similar to the crouched setup, with contributions of 54.6% and 25.1%, and 53.3% and 24.7% for the pilots and stokers respectively. By comparison, the solo TT athlete contributed to 79.2% of their total drag with the bicycle experiencing the remaining 20.8%. Note that despite the differences in bicycle geometry, the sum of the drag contributions of the TT and FC athletes is the equivalent sum of the solo athlete drag contribution ($\approx 79\%$).

Both athletes on all tandem setups received an aerodynamic benefit from the other athlete, pilot or stoker. In the following, a comparison is provided of the drag of the isolated tandem athletes relative to the drag experienced by a solo rider in an equivalent posture. The upright and crouched setup geometries had identical athlete geometry for their respective tandem and solo athletes. Thus,

reasonable comparisons can be made between the athletes with the drag isolated from the bicycles. Compared to their solo cyclist equivalent, the upright tandem pilot experienced a drag reduction of 15.1% by the presence of the stoker, who experienced a drag reduction of 54.6% by the presence of the pilot. The drag reductions for the crouched and TT pilots and stokers by comparison to their solo cyclist counterparts were 7.3% and 52.2%, and 5.4% and 56.6% respectively. The FC tandem setup was the most aerodynamically efficient tandem setup. By comparison to the TT solo cyclist, the pilot saved 9.9% in drag force due to the presence of the stoker, and the stoker in the FC setup experienced a 58.2% reduction in drag. The arms of the stoker in the FC setup were in close proximity to the pilot, which assisted in the drag reduction of both the pilot and the stoker by reducing the under-pressure on the back of the pilot and the over-pressure on the arms of the stoker. It is noted that this is a generalised comparison for the TT setups; the solo TT athlete and tandem TT and FC stokers do not share identical geometries, where the stoker athletes grasp the handlebars and frame respectively. In addition, there are differences between the tandem and solo bicycle geometry (additional frame tubes, handlebars etc.) whose interference flow affects all solo and tandem athlete comparisons. However, the comparisons to the solo riders remain useful to generate further understanding of tandem aerodynamics.

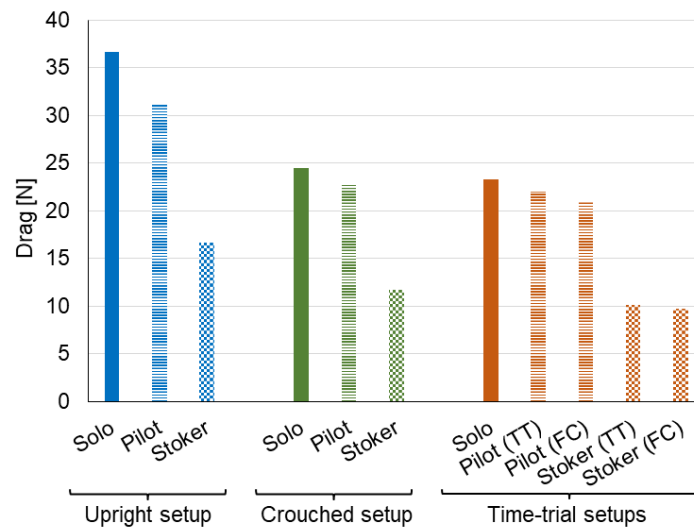


Figure 5.8. Comparison of drag forces experienced by the athletes with different postures for solo and tandem setups.

Pressure coefficient contours on the surfaces of the two road and two TT setups in tandem cycling are plotted in Figure 5.9 and Figure 5.10 respectively. Pressure coefficient contours for the three comparison solo geometries are also plotted in Figure 5.9 and Figure 5.10 alongside the tandem geometries for comparison purposes. These contours provide insights into the flow interaction between the pilot and stoker. The difference in pressure coefficient on the torsos of both the pilot and stoker is apparent for all posture combinations (Figure 5.9-Figure 5.10). In comparison to equivalent

solo athletes, all stoker athletes experienced a reduced maximum pressure on their frontal areas due to the presence of the pilot, while the pressure distribution on the front of the tandem pilots was comparable to that of the solo equivalent solo athlete.

The pressure coefficient contours for the solo setups (Figure 5.9-Figure 5.10) highlight the importance of the flow interaction between the pilots and stokers. The subsonic upstream pressure (Blocken et al., 2013) imparted from the stoker in all tandem setups decreased the absolute value of the pressure coefficient on the back of the pilot, and reduced the severity of the pressure gradient on the outer sides of the pilot's torso and legs (by comparison to equivalent solo athletes). A general comparison of all pilots to their stokers revealed notable differences in pressure gradients from the upper arms, on the side of the torsos, and on the legs. While the pressure gradients were located at similar positions on the stoker as the pilot, the pressure gradients were not as large over the stoker as they were over the pilot.

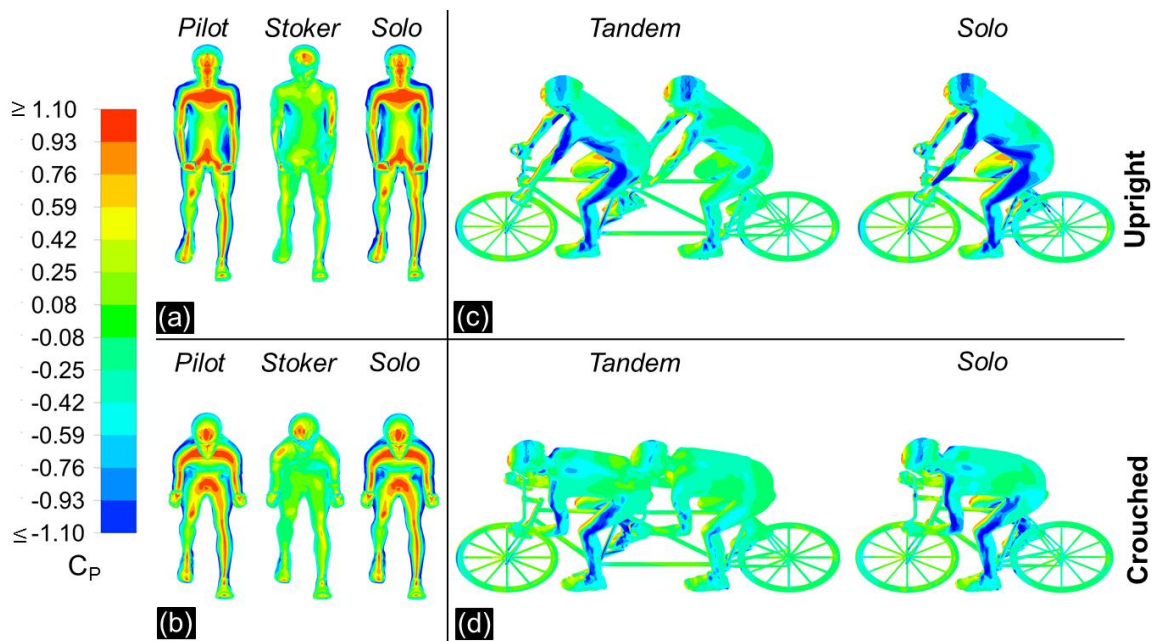


Figure 5.9. Pressure coefficient contours on the projected frontal areas of the pilot, stoker and solo athletes for (a) an upright setup, and (b) a crouched setup. Pressure coefficient contours are presented on a complete tandem and solo geometries for a (c) upright, and (d) crouched setups.

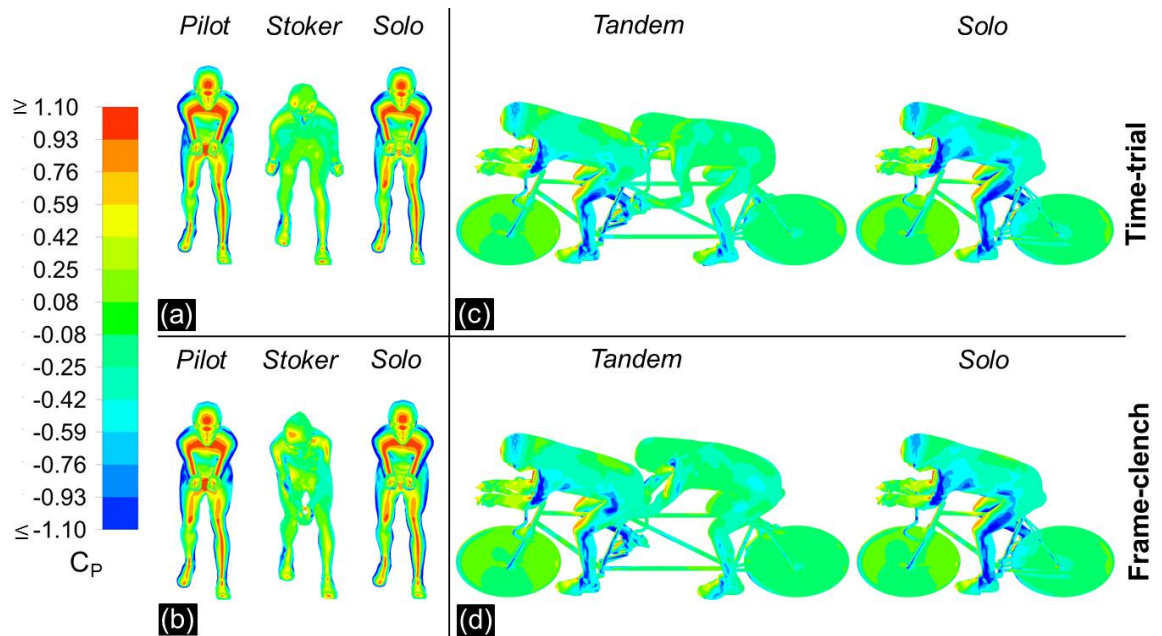


Figure 5.10. Pressure coefficient contours on the projected frontal areas of the pilot, stoker and solo athletes for (a) a time-trial setup, and (b) a frame-clench setup. Pressure coefficient contours are presented on the complete tandem and solo geometries for a (c) time-trial, and (d) frame-clench setups.

5.5 Discussion

5.5.1 Evaluation of the numerical findings

The tandem FC setup proved to be the most aerodynamic setup analysed with a C_{DA} of 0.286 m^2 , and experienced air resistance 2.4% lower than the standard TT tandem setup. The tandem crouched setup produced a C_{DA} of 0.314 m^2 , 7.2% larger than the tandem TT setup, which experienced a C_{DA} of 0.293 m^2 . The solo crouched setup was found to experience 9.4% more drag than the solo TT setup, with C_{DA} values of 0.233 m^2 and 0.213 m^2 respectively. The low torso angle and horizontal forearms of the crouched postures contributed to their good aerodynamic performance by comparison to the TT postures, with drag differences less than 10% found for both the tandem and solo setups between their respective crouched and TT setups. The upright tandem setup experienced 31.3% more drag than the crouched tandem setup for comparison.

The difference in aerodynamics between the tandem setups can be converted into time differences over a racing distance of 10 km, assuming that all tandem setups deliver a power output

equal to that required for the FC setup to travel at 15 m/s. In this scenario the crouched tandem setup would travel 1.83 m/s faster than the upright setup and would theoretically finish the 10 km race 102.6 s earlier. Under the same conditions, the FC tandem would finish 8.1 s before the TT tandem, travelling 0.18 m/s faster. It is also interesting to compare a tandem and solo setup, albeit under idealised conditions and considering aerodynamic variables only. If we consider the crouched solo rider, and the two tandem athletes in crouched postures from this study, and further consider that each athlete outputs the same power of 300 W; the tandem would have a velocity 14.1% higher than the solo bicycle, completing a distance of 10 km 96.3 s before the solo rider. Furthermore, if the tandem travelled at the same velocity as the solo rider, each tandem athlete would consume only 67.4% of the energy that the solo rider expends to overcome aerodynamics.

5.5.2 Comparison with prior research

5.5.2.1 Tandem cycling

Since prior studies on tandem cycling are limited, a useful comparison of percentage drag reductions can be made to the published material on drafting in the literature. In a drafting scenario, a cyclist takes advantage of energy saved by being in the wake of an upstream cyclist. The work by Blocken et al. (2013) holds many comparable aspects to the present research. It was found that the over-pressure at the front and the under-pressure on the back of the trailing cyclist were reduced by the presence of the leading cyclist, who in turn received a benefit from the over-pressure in front of the trailing cyclist. Static CFD simulations were considered for the two inline cyclist geometries. The bicycle was neglected from the cyclist geometries; however, this allows for more direct comparison to the drag experienced by the athletes in the present research when isolated from the tandem bicycle. Upright, dropped and TT athlete postures were tested. The maximum benefit found for the lead rider of a two-formation drafting scenario was 2.6%. The benefit was acquired from the presence of the trailing rider, who experienced a maximum drag reduction of 27.1%. These maximum benefits were measured for a minimum wheel to wheel distance of 0.01 m. The percentage benefit to both the leading and trailing riders were found to be dependent on the posture adopted by the athlete, and the spacing between them. The maximum drag saving recorded in the tandem studies in the present paper was 15.1% and 58.2% for the pilot and stoker of the upright and FC setups respectively. These findings were in excess of the maximum savings recorded by Blocken et al. (2013) as expected due to the closer proximity of the tandem athletes on the tandem bicycle. Barry et al. (2014) conducted wind tunnel experiments of two full-scale drafting cyclists, and confirmed the earlier findings by Blocken et al. (2013) that the leading cyclist in a drafting formation benefitted aerodynamically from

the trailing cyclist. At the minimum inline wheel to wheel separation distance (≈ 0 m), drag reductions of 5% and 49% were recorded for the leading and trailing cyclists (athlete and bicycle) respectively.

5.5.2.2 Solo cycling

The solo upright, crouched and TT postures produced C_{DA} values of 0.327 m^2 , 0.233 m^2 and 0.213 m^2 respectively. The validity of the results for each solo setup was ensured via literature comparisons with full-scale wind tunnel experiments for each respective geometry. Comparisons were limited to experiments that used static cyclists as per the CFD simulations (no wheel rotation or pedalling), and that provided photographic or descriptive evidence that the postures adopted by the athletes provided a close match to the present research (Table 5.1). Details on the wind tunnel experiments were extracted where possible to provide further insight into the C_{DA} values reported in the literature. The blockage ratio (BR) is defined as the ratio of the frontal area of the cyclist to the area of the test section of a closed test section tunnel or nozzle exit area for an open test section tunnel.

Table 5.1. C_{DA} values from the literature, where full-scale wind tunnel experiments were conducted on static solo cyclists and their bicycles, whose postures were a close match to those used in the present research with photographic or descriptive evidence. BR = blockage ratio. TI = turbulence intensity. Open/Closed refers to the test section type of the wind tunnel.

Author	C_{DA} [m^2]			Wind tunnel operating parameters		
	Upright	Crouched	Time-trial	Open/Closed	BR (%)	TI (%)
Fintelman et al. (2014b)	0.330 ^{a,g}			Open	12.5 ^j	0.67
Defraeye et al. (2010a)	0.270 ^b			Closed	6	0.02
Fintelman et al. (2014b)		0.300 ^{c,g}		Open	12.5 ^j	0.67
Kyle and Burke, (1984)		0.249 ^d		Closed	6 ⁱ	-
Griffith et al. (2014)			0.201 ^e	Open	4	1.6
Defraeye et al. (2010a)			0.211	Closed	5	0.02
García-López et al. (2008)			0.260 ^f	Closed	6 ⁱ	-
Present research (numerical)	0.327	0.233	0.213	-	0.06 ^k	0.2 ^k

^a From Figure 4 Fintelman et al. (2014b).

^b Disk wheels and a time-trial helmet were used in contrast to spoked wheels and a standard road helmet in the present research.

^c Dropped posture with torso angle of 16° , not as aggressive as a crouched posture but a useful comparison.

^d From Figure 1 by Kyle and Burke, (1984).

^e From Figure 3 by Griffith et al. (2014) at a crank angle of 15° , similar to the angle adopted in the present research.

^f Spoked wheels were used in contrast to disk wheels used in the present research.

[§] Blockage corrections by Mercker & Wiedemann, (1996) applied

ⁱ Assuming a frontal area of 0.4 m²

^j Assuming a frontal area of 0.5 m²

^k Values from CFD boundary conditions

Comparisons can be drawn for the upright and crouched setups, with wind tunnel experiments conducted by Kyle & Burke, (1984) and Defraeye et al. (2010a), respectively. There was a 21.1% difference in C_{DA} between the upright solo cyclist in the present study, and the full-scale experimental predictions of Defraeye et al. (2010a). However, the lower C_{DA} predicted by Defraeye et al. (2010a) can at least partly be attributed to the use of disk wheel and a TT helmet in the experiments, which would have lowered the drag considerably in comparison to the spoked wheels and standard road helmet used in the present research. A smaller difference of 0.9% was calculated between the C_{DA} measurements of Fintelman et al. (2014b) and the present research for the upright posture, with more closely matching bicycle and wheel geometries between both studies. A difference in C_{DA} of 6.4% was obtained between the solo crouched postures of the present research and the wind tunnel experiment of Kyle & Burke, (1984). The crouched posture adopted in the present research yielded a low C_{DA} value only 9.4% greater than the prediction for the solo TT cyclist. However, this is due to the low torso angle and horizontal forearms. Underwood et al. (2011) and Barry et al. (2015b) both conducted studies relating aerodynamic performance to athlete posture and found trends for drag reductions with lower torso angles.

The wind tunnel experiments by Defraeye et al. (2010a) on a TT cyclist closely represented the solo TT posture adopted by the athlete used in this research. Both studies utilised static disk wheels and tear drop TT helmets. A difference in C_{DA} of only 0.9% was found between the drag results of both studies. García-López et al. (2008) conducted wind tunnel experiments considering a TT cyclist who adopted a comparable posture to the one used in the present research. A C_{DA} of 0.260 m² was found, 18.1% higher than the value found for the present research. However, standard spoked wheels were used by García-López et al. (2008) opposed to the disk wheels used in this research, which the larger drag predictions can be attributed to. Griffith et al. (2014) reported a C_{DA} range between 0.20-0.24 m² for a range of crank positions with a TT cyclist using static wind tunnel experiments; spoked wheels were also used for this study by Griffith et al. (2014), in contrast to the disk wheels used in the present research.

In addition to the different wind tunnel operating conditions outlined in Table 5.1, there were further differences between the previous experimental tests (Table 5.1) and the present research, such as the presence of a bicycle stand in experimental studies to maintain rider and bicycle stability. The surface geometries in the present numerical study experienced some smoothing and small

components were neglected for meshing purposes as per section 5.4.1. Anthropometric differences also existed between the athletes used in this research and the literature. However, the overall agreement between the literature and this numerical study is considered good with the correct drag trend between different postures predicted.

5.5.3 Limitations and future perspectives

Variations in torso angle may provide tangible information for athletes on how their posture influences the total drag in a tandem setup. Additional studies investigating variations in head positions, and arm positions, may yield further trends for tandem athletes for optimising the overall system. As per Barry et al. (2015b), reducing a cyclist's silhouette to improve aerodynamics through a lower frontal area might be translatable to tandem cycling; for example, for the stoker to be fully hidden behind the frontal silhouette of the pilot. Further aerodynamic improvements may be acquired through individualised posture-specific skin suits for the pilot and stoker. Existing postures adopted by athletes could potentially be adjusted to yield greater drag reductions for both the pilot and stoker, such as the FC setup providing improvements over the TT setup in this study. Fintelman et al. (2015) investigated the effect of time-trial cycling postures on physiological and aerodynamic variables, determining that trade-offs between aerodynamic drag and physiological functioning were available. The similarity of a single tandem athlete's position to that of a regular cyclist, with the added complexity of the second tandem athlete in close proximity, implies that the application of this research to tandem cycling is both relevant and may yield aerodynamic and physiological trade-offs unique to tandem cycling.

The same athlete was used for the pilot, stoker and solo athlete geometries in this study, to provide good comparison between drag predictions. However, it is recommended that individual tandem athletes with differing anthropometrics are considered for future research, to determine the influence of different anthropometric characteristics on the drag of both tandem athletes. This is emphasised by the findings from Barry et al. (2015a), who observed strong aerodynamic interactions between the drafting riders, which were attributed to be functions of individual athlete anthropometrics. Furthermore, Barry et al. (2015a) found that general trends were not consistent across tests conducted and suggested that in order to fully optimise athletes in a team, the actual athletes would be required for the analysis.

There were several limitations to this study: All the geometries considered in the CFD simulations were static, with no rotation of the wheels and no movement of the athlete's limbs. All athlete and bicycle surfaces were modelled as smooth walls, with no varying roughness of athletes' apparel and skin accounted for. All athlete surfaces were smoothed for meshing purposes. Future

studies should include unique individual athletes, of different anthropometric dimensions, to provide conclusions whether particular anthropometrics are favourable for the pilot or stoker. It is noted that these findings are for numerical differences and that practical applications may differ.

5.6 Conclusions

CFD simulations were conducted to compare and provide insight into the aerodynamic performance of four tandem setups and three solo cyclist setups. Wind tunnel experiments were conducted on a single tandem setup to provide validation data, where the largest drag deviation between CFD simulations and measurements was 4.9%. A non-biased comparison based on athlete anthropometrics was conducted for each tandem setup, by using a singular athlete for both the pilot and the stoker geometries in all tandem setups, and also for the solo rider geometries.

Two road setups and two TT setups for tandem cycling were analysed using CFD. The crouched posture combination experienced a lower aerodynamic drag than the upright posture combination as expected, with C_{DA} values of 0.314 m^2 and 0.413 m^2 measured for both setups respectively. A smaller difference in drag was recorded between the numerical results for the two TT setups, a standard TT setup and a variation termed as the frame-clench (FC) setup; where the stoker grasped the frame instead of the handlebars while the pilots retained the same position in both setups. The FC setup proved to be more favourable aerodynamically than the standard TT setup, as both the pilot and stoker experienced a lower drag than their counterparts on the standard TT setup. According to the numerical results, a C_{DA} of 0.286 m^2 was measured for the FC setup, 2.4% less than the TT setup, which can be translated as a gain of 8.1 s over a 10 km time-trial race. It was found that the stoker impacted the drag experienced by the pilot for this setup, providing a reduction of 9.9% for the pilot by comparison to a solo rider holding an equivalent posture, while the stoker experienced a maximum drag reduction of 58.2% in the wake of the pilot.

The benefits of providing detailed information on the aerodynamics in tandem cycling are applicable to a wide audience of athletes, coaches, manufacturers, cycling institutions and fellow researchers. By providing a non-biased baseline level of knowledge regarding tandem aerodynamics, with respect to the same identical athlete geometry being used for the pilot and the stoker, one can derive the effect of athlete anthropometrics for both respective positions. Furthermore, with greater understanding of the fundamentals of tandem aerodynamics, the potential for performance gains can be made specific to individual athletes and teams, within the rules set by the International Cycling Union (UCI).

5.7 References

- ANSYS Fluent. (2015). ANSYS Fluent theory guide. *Release 16.1 Documentation*. ANSYS Inc.
- Artec Europe. (2017). Artec Eva, 3D Scanners. Retrieved May 22, 2017, from <https://www.artec3d.com/3d-scanner/artec-eva>
- Barry, N., Burton, D., Sheridan, J., Thompson, M., & Brown, N. A. T. (2016). Flow field interactions between two tandem cyclists. *Experiments in Fluids*, 57(12), 1–14. <https://doi.org/10.1007/s00348-016-2273-y>
- Barry, N., Burton, D., Sheridan, J., Thompson, M., & Brown, N. A. T. (2015a). Aerodynamic drag interactions between cyclists in a team pursuit. *Sports Engineering*, 18, 93–103. <https://doi.org/10.1007/s12283-015-0172-8>
- Barry, N., Burton, D., Sheridan, J., Thompson, M., & Brown, N. A. T. (2015b). Aerodynamic performance and riding posture in road cycling and triathlon. *Proceedings of the Institution of Mechanical Engineers, Part P: Journal of Sports Engineering and Technology*, 229(1), 28–38. <https://doi.org/10.1177/1754337114549876>
- Barry, N., Sheridan, J., Burton, D., & Brown, N. A. T. (2014). The effect of spatial position on the aerodynamic interactions between cyclists. In *Proceedings of the 2014 conference of the International Sports Engineering Association, Procedia Eng.* (Vol. 72, pp. 774–779). Elsevier B.V. <https://doi.org/10.1016/j.proeng.2014.06.131>
- Blocken, B. (2015). Computational Fluid Dynamics for urban physics: Importance, scales, possibilities, limitations and ten tips and tricks towards accurate and reliable simulations. *Building and Environment*, 91, 219–245. <https://doi.org/10.1016/j.buildenv.2015.02.015>
- Blocken, B. (2014). 50 years of Computational Wind Engineering: Past, present and future. *Journal of Wind Engineering and Industrial Aerodynamics*, 129, 69–102. <https://doi.org/https://doi.org/10.1016/j.jweia.2014.03.008>
- Blocken, B., Defraeye, T., Koninckx, E., Carmeliet, J., & Hespel, P. (2013). CFD simulations of the aerodynamic drag of two drafting cyclists. *Computers & Fluids*, 71, 435–445. <https://doi.org/10.1016/j.compfluid.2012.11.012>
- Blocken, B., Toparlar, Y., & Andrienne, T. (2016). Aerodynamic benefit for a cyclist by a following motorcycle. *Journal of Wind Engineering and Industrial Aerodynamics*, 155, 1–10. <https://doi.org/https://doi.org/10.1016/j.jweia.2016.04.008>
- Blocken, B., & Toparlar, Y. (2015). A following car influences cyclist drag: CFD simulations and wind tunnel measurements. *Journal of Wind Engineering and Industrial Aerodynamics*, 145(0), 178–186. <https://doi.org/10.1016/j.jweia.2015.06.015>

- Chabroux, V., Barelle, C., & Favier, D. (2012). Aerodynamics of cyclist posture, bicycle and helmet characteristics in time trial stage. *Journal of Applied Biomechanics*, 28, 317–323. [https://doi.org/10.1016/S0765-1597\(01\)00049-1](https://doi.org/10.1016/S0765-1597(01)00049-1)
- Crouch, T. N., Burton, D., LaBry, Z. A., & Blair, K. B. (2017). Riding against the wind: a review of competition cycling aerodynamics. *Sports Engineering*, 20(2), 81–110. <https://doi.org/10.1007/s12283-017-0234-1>
- Defraeye, T., Blocken, B., Koninckx, E., Hespel, P., & Carmeliet, J. (2010a). Aerodynamic study of different cyclist positions: CFD analysis and full-scale wind tunnel tests. *Journal of Biomechanics*, 43(7), 1262–1268. <https://doi.org/10.1016/j.jbiomech.2010.01.025>
- Defraeye, T., Blocken, B., Koninckx, E., Hespel, P., & Carmeliet, J. (2010b). Computational fluid dynamics analysis of cyclist aerodynamics: Performance of different turbulence-modelling and boundary-layer modelling approaches. *Journal of Biomechanics*, 43(12), 2281–2287. <https://doi.org/10.1016/j.jbiomech.2010.04.038>
- Fintelman, D. M., Sterling, M., Hemida, H., & Li, F.-X. (2015). The effect of time trial cycling position on physiological and aerodynamic variables. *Journal of Sports Sciences*, 414(April 2015), 1–8. <https://doi.org/10.1080/02640414.2015.1009936>
- Fintelman, D. M., Sterling, M., Hemida, H., & Li, F.-X. (2014a). Optimal cycling time trial position models: Aerodynamics versus power output and metabolic energy. *Journal of Biomechanics*, 47(8), 1894–1898. <https://doi.org/10.1016/j.jbiomech.2014.02.029>
- Fintelman, D. M., Sterling, M., Hemida, H., & Li, F.-X. (2014b). The effect of crosswinds on cyclists: an experimental study. In *The 2014 conference of the International Sports Engineering Association, Procedia Eng.* (Vol. 72, pp. 720–725). <https://doi.org/10.1016/j.proeng.2014.06.122>
- Franke, J., Hellsten, A., Schlünzen, H., & Carissimo, B. (2007). Best practice guideline for the CFD simulation of flows in the urban environment. *COST Action 732: Quality Assurance and Improvement of Microscale Meteorological Models*. Hamburg Germany.
- García-López, J., Rodríguez-Marroyo, J. A., Juneau, C.-E., Peleteiro, J., Martínez, A. C., & Villa, J. G. (2008). Reference values and improvement of aerodynamic drag in professional cyclists. *Journal of Sports Sciences*, 26(3), 277–286. <https://doi.org/10.1080/02640410701501697>
- Gnehm, P., Reichenbach, S., Altpeter, E., Widmer, H., & Hoppeler, H. (1997). Influence of different racing positions on metabolic cost in elite cyclists. *Medicine and Science in Sports and Exercise*, 29(6), 818–23. <https://doi.org/10.1097/00005768-199706000-00013>
- Griffith, M. D., Crouch, T., Thompson, M. C., Burton, D., & Sheridan, J. (2014). Computational fluid dynamics study of the effect of leg Position on cyclist aerodynamic drag. *The American Society*

- of *Mechanical Engineers, Journal of Fluids Engineering*, 136.
<https://doi.org/10.1115/1.4027428>
- Kyle, C. R., & Burke, E. R. (1984). Improving the racing bicycle. *Mechanical Engineering*, 106(9), 34–45.
- Lukes, R. a, Chin, S. B., & Haake, S. J. (2005). The understanding and development of cycling aerodynamics. *Sports Engineering*, 8, 59–74. <https://doi.org/10.1007/BF02844004>
- Mannion, P., Toparlar, Y., Blocken, B., Hajdukiewicz, M., Andrienne, T., & Clifford, E. (2018). Improving CFD prediction of drag on Paralympic tandem athletes: Influence of grid resolution and turbulence model. *Sports Engineering*, 21(2), 123–135. <http://doi.org/10.1007/s12283-017-0258-6>
- Menter, F. R. (1994). Two-equation eddy-viscosity turbulence models for engineering applications. *AIAA Journal*, 32(8), 1598–1605. <https://doi.org/10.2514/3.12149>
- Mercker, E., & Wiedemann, J. (1996). On the Correction of Interference Effects in Open Jet Wind Tunnels. *SAE International*. <https://doi.org/10.4271/960671>
- Oggiano, L., Leirdal, S., Sætran, L., & Ettema, G. (2008). Aerodynamic Optimization and Energy Saving of Cycling Postures for International Elite Level Cyclists. *The Engineering of Sport* 7, 1(2), 597–604. https://doi.org/10.1007/978-2-287-09411-8_70
- Tominaga, Y., Mochida, A., Yoshie, R., Kataoka, H., Nozu, T., Yoshikawa, M., & Shirasawa, T. (2008). AIJ guidelines for practical applications of CFD to pedestrian wind environment around buildings. *Journal of Wind Engineering and Industrial Aerodynamics*, 96(10–11), 1749–1761. <https://doi.org/10.1016/j.jweia.2008.02.058>
- UCI. (2017). Cycling Regulations, Part 16 Para-Cycling, version on 01/02/2017. Union Cycliste Internationale. Retrieved from http://www.uci.ch/mm/Document/News/Rulesandregulation/16/26/73/16-PAR-20170201-E_English.PDF
- Underwood, L., Schumacher, J., Burette-Pommay, J., & Jermy, M. (2011). Aerodynamic drag and biomechanical power of a track cyclist as a function of shoulder and torso angles. *Sports Engineering*, 14(2–4), 147–154. <https://doi.org/10.1007/s12283-011-0078-z>
- Underwood, L., & Jermy, M. (2010). Optimal hand position for individual pursuit athletes. *Procedia Engineering*, 2(2), 2425–2429. <https://doi.org/10.1016/j.proeng.2010.04.010>

Impact of pilot and stoker torso angles in tandem para-cycling aerodynamics

This chapter investigates the aerodynamic interaction of the pilot and stoker with respect to their torso angles. Grid and turbulence model sensitivity studies from Chapter 3 informed the initial parameters of this study that is focused at road race events. Twenty-three torso angle combinations of the pilot and stoker athletes are investigated to further understand the aerodynamic interaction between both athletes, and to find an optimal aerodynamic solution.

This chapter has been published in the international peer-reviewed journal *Sports Engineering*:

Mannion, P., Toparlar, Y., Blocken, B., Hajdukiewicz, M., Andrianne, T., & Clifford, E. (2019). Impact of pilot and stoker torso angles in tandem para-cycling aerodynamics. *Sports Engineering*. <https://doi.org/10.1007/s12283-019-0301-x>

Abstract: The torso angle of a cyclist is a key element to consider when attaining aerodynamic postures. For athletes competing in the tandem para-cycling category as the pilot or stoker, the torso angles are similar to those adopted by able-bodied athletes. However, their aerodynamic interaction is not yet fully understood. To date, there has been no study to identify aerodynamically advantageous torso angles for tandem athletes. In this study, numerical simulations with Computational Fluid Dynamics and reduced-scale wind tunnel experiments were used to study the aerodynamics of tandem cyclists considering 23 different torso angle combinations. The sagittal torso angle combination of the pilot and stoker that yielded the lowest overall drag area of 0.308 m² (combined pilot, stoker and bicycle) was 25° for the pilot coupled with 20° for the stoker. The results suggest that higher torso angles for the pilot have a lower impact on the overall drag area than equivalent torso angles for the stoker. This study suggests that a slight relaxation of pilot torso angle (which may help increase power output) may not penalise aerodynamics, in low (< 25°) sagittal torso angle ranges.

6.1 Introduction

Tandem para-cycling is a Paralympic sport branch that features high speeds and unique aerodynamic considerations; two athletes in close proximity on a single tandem bicycle. Aerodynamic optimisation has become a key element of competitive cycling in recent years (Haake, 2009). Numerous studies have been conducted to quantify and understand aerodynamic drag in cycling (Barry et al., 2016; Blocken et al., 2016; 2018; Blocken & Toparlar, 2015; Crouch et al., 2017; 2014; Defraeye et al., 2010b; Fintelman et al., 2015a; Griffith et al., 2014; Lukes et al., 2005; Oggiano et al., 2008, García-López et al., 2008). It has been shown for a competitive able-bodied cyclist that drag reductions in the order of 20% with respect to a traditional athlete's posture can be obtained through refinements and adjustments of cycling positions/postures, while remaining within the boundaries of the rules set by the Union Cycliste Internationale (UCI) (Gibertini et al., 2008). The balance between power output and aerodynamics has become an important aspect of competitive cycling that can be unique to each athlete (Fintelman et al., 2015b; 2016; Grappe et al., 1997; Heil et al., 1997; Underwood & Jermy, 2013). Two tandem athletes together contribute to the total power output, and both athletes along with the tandem bicycle experience aerodynamic drag forces. The aerodynamics of both athletes, the pilot and the stoker, need to be optimised both individually and simultaneously for a collective drag reduction, while keeping the power output at an optimal level. Recent research has shown that the aerodynamics of each tandem athlete is highly dependent on the other athlete (Mannion et al., 2018a, 2018b). A supposed aerodynamic improvement to the pilot could have a negative effect on the stoker downstream and thus a balance is required.

Competitive tandem para-cycling has received little attention in the literature by comparison to its able-bodied counterparts and tandem aerodynamics have only recently been investigated numerically and experimentally (Mannion et al., 2018a, 2018b). Mannion et al. (2018a) demonstrated reliable numerical modelling of tandem aerodynamics requires careful grid generation and turbulence modelling. Mannion et al. (2018b) investigated four tandem setups along with the tandem athletes on solo bicycles to aid in understanding the aerodynamic interaction between the pilot and the stoker. The pilot was found to benefit aerodynamically by the presence of the stoker by up to 15.1%, while the stoker experienced up to 58.2% less drag than a solo cyclist. The unique frame-clench tandem setup (Mannion et al., 2018b) was found to yield the lowest drag area (C_{DA}) from four setups tested.

Underwood et al. (2011) investigated if a cyclist's drag could be minimised with changes in torso and shoulder angles. Wind tunnel experiments at 40 km/hr were conducted with three competitive track cyclists, using a custom handlebar setup for repeatability and measurability. The optimum torso angle for each athlete varied from 1.6° to 8.6° to the horizontal plane. Barry et al.

(2015) performed wind tunnel tests to investigate the effect of variations in body posture on aerodynamic performance. The torso angle of the athlete was also investigated in dropped positions. It was determined that the wake field behind the cyclist could be reduced by lowering the head and torso angle of a cyclist, resulting in a reduction of aerodynamic drag.

Computational fluid dynamics (CFD) has also been used to evaluate cyclist posture. Defraeye et al. (2010a) used both Reynolds-averaged Navier-Stokes (RANS) and large eddy simulation (LES). The lesser computational expense of the RANS method was deemed attractive over LES for the purpose of cycling posture analysis, with deviations from wind tunnel experiments of 11% and 7% respectively. CFD has also been used to further the understanding of the underlying physics behind cycling aerodynamics. Two cyclists drafting in close proximity bears some resemblance to tandem cycling aerodynamics, and Blocken et al. (2013) used CFD to find that the aerodynamics of the leading cyclist were significantly influenced by the trailing cyclist due to the subsonic upstream disturbance effect by the trailing cyclist. In this study, CFD simulations were performed considering 23 torso angle combinations for a tandem setup, to investigate their impact on aerodynamic drag.

6.2 Numerical methodology

6.2.1 Tandem geometrical models

The tandem geometry used in this study was based on the ‘dropped’ road race geometry utilised by Mannion et al. (2018a, 2018b). This geometry used the same 3D scanned athlete for the pilot (front athlete) and stoker (rear athlete) to remove anthropometrical biases in the aerodynamic comparison between both athletes (Figure 6.1). Sagittal torso angles are highlighted in red in Figure 6.1, while the forearm angle (α), elbow angle (β), shoulder angle (γ), hip angle (δ), and knee angle (φ) are in blue. Subscripts for the angles denoted with Greek letters indicate the torso angle at which the anthropometric angle is achieved. For example, β_{25° indicates the elbow angle when a torso angle of 25° is adopted. The sagittal torso angles (θ) of the pilot and stoker were set to 20° , 25° , 30° , 40° and 50° from the horizontal plane (Figure 6.1). The torso angle was adjusted at the hip pivot point. No movement was allowed at the neck as the torso angle was adjusted. The forearms were hinged at the elbow locations and at the point of contact with the handlebars, and the shoulder joints were held static. Thus, the shoulder angle (γ) and knee angle (φ), as presented in Figure 6.1, remained constant throughout all torso angles at 60° and 57° respectively. 23 viable torso angle combinations for the

tandem setup were obtained, with sagittal torso angles of 20°, 25°, 30°, 40° and 50° for the pilot and stoker. Two particular torso angle combinations of 40° and 50° for the pilot, coupled with 20° for the stoker, were not viable due to intersecting geometries. In addition, more aggressive dropped postures with a lower torso angle than the baseline torso angle of 20° (Figure 6.1b) were not viable due to geometry intersections, and would not have resulted in positions possible to attain on the tandem bicycle.

The torso angle combinations are described as “*Pilot angle-stoker angle*” throughout the remainder of the manuscript. For example, the tandem setup with a pilot and stoker adopting angles of 40° and 30° respectively would be denoted as “40°-30°”.

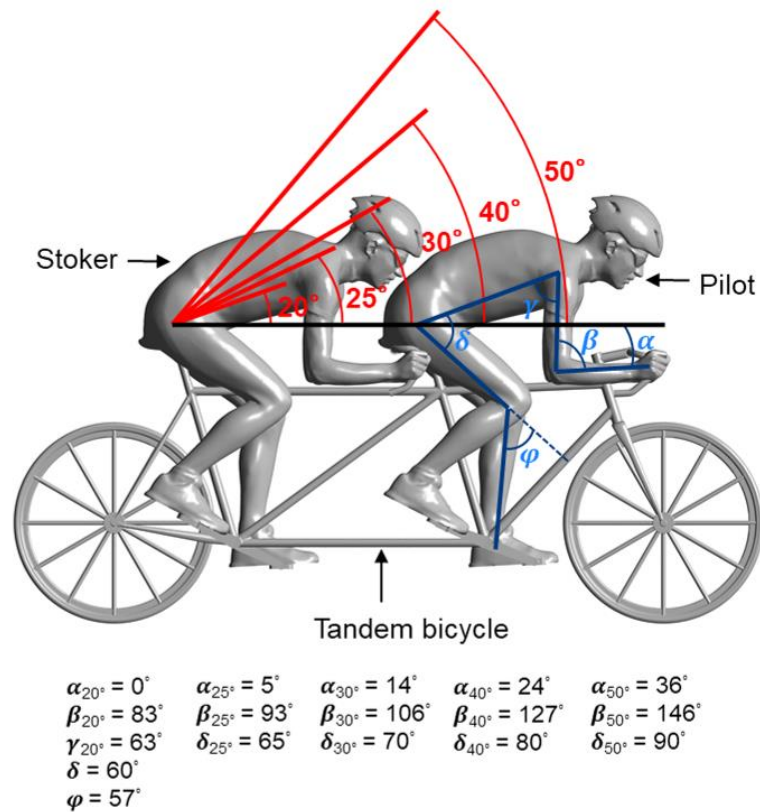


Figure 6.1. Side profile of the dropped tandem setup with the pilot and stoker at 20° sagittal torso angles respectively, with the (α) forearm angle, (β) elbow angle, (γ) shoulder angle, (δ) hip angle, and (φ) knee angle for the five positions.

6.2.2 Validation studies

The numerical simulations corresponding to the tandem setup with both the pilot and stoker at the baseline torso angle 20°-20° were validated with results from wind tunnel experiments as reported by Mannion et al. (2018a, 2018b). The drag was measured individually and simultaneously on the

pilot and the stoker whose geometry matched the corresponding CFD simulations. Drag force deviations between CFD and wind tunnel of 4.7% and 4.9% were reported for the pilot at 0° and 5° yaw respectively (Mannion et al., 2018b). Deviations of -3.4% and -3.4% were reported for the stoker at the same two yaw angles (Mannion et al., 2018b). These experiments were also used for the grid sensitivity study and turbulence model evaluation as reported by Mannion et al. (2018a). The SST $k-\omega$ turbulence model (Menter, 1994) was recommended, coupled with a grid sufficiently refined to yield an average y^* (the non-dimensional wall distance) less than 1 at no-slip walls. The CFD simulations performed in the present study utilise the recommended, best-performing numerical settings as documented by Mannion et al. (2018a, 2018b), discussed briefly in sections 6.2.4 and 6.2.5.

6.2.3 Boundary conditions

The fluid domain created for this study was developed according to guidelines by Franke et al. (2007), Tominaga et al. (2008) and Blocken (2015). The domain size was 28x28x80 m³, with the tandem geometry centred laterally and the midpoint of the geometry located 29 m from the inlet boundary (Figure 6.2a). The maximum blockage ratio was 0.06%, occurring when a 50° torso angle was simulated by either the pilot or stoker, which was below the 3% maximum recommendation (Blocken, 2015; Franke et al. 2007; Tominaga et al., 2008). The tandem geometry was raised 0.02 m from the ground surface to ensure high grid quality where the wheel tyre would otherwise be tangent to the road surface. A free-slip wall was used for the ground surface. The tandem geometry was simulated using a no-slip wall with zero roughness. Symmetry conditions were applied to the side and top surfaces of the fluid domain. A velocity of 15 m/s (54 km/hr) was applied to the inlet boundary with 0.2% turbulence intensity and a hydraulic diameter of 1 m. Zero static gauge pressure was applied to the outlet boundary condition.

6.2.4 Numerical parameters

The commercial CFD solver ANSYS Fluent (ANSYS, 2015) was used for the simulations, which utilises the control volume method. The SST $k-\omega$ (Menter, 1994) turbulence model was used to achieve closure in the 3D Reynolds-Averaged Navier-Stokes (RANS) simulations. Second order pressure and second order discretisation schemes were used, along with the Least-Squares Cell-Based method to compute gradients. The Coupled algorithm was used for the pressure-velocity coupling

with the pseudo-transient solver. A pseudo time-step of 0.01 s was used and the aerodynamic drag was averaged over 4000 steps after an initialisation period of 5000 steps. The typical standard deviation measured for the total C_{DA} (pilot, stoker and bicycle combined) was 0.005 m².

6.2.5 Numerical grid

The grids generated in this study utilised the best-performing grid settings specified by the grid sensitivity study Mannion et al. (2018a), which were determined from systematic sensitivity studies. The first cell height was 2×10^{-5} m at the surfaces of the tandem geometry. 26 prism layers were used with a growth ratio of 1.2. The average y^* was below 1. Additional volume grid refinements were placed between the athletes, where larger torso angles increased the separation distance between the stoker's head and the pilot's torso. Figure 6.2b₁ illustrates the volume grid density between the pilot and stoker. The density of the prism layers on the athletes is illustrated in Figure 6.2b₂. The surface and volume grid density of the front wheel and forks of the tandem bicycle is highlighted in Figure 6.2b₃.

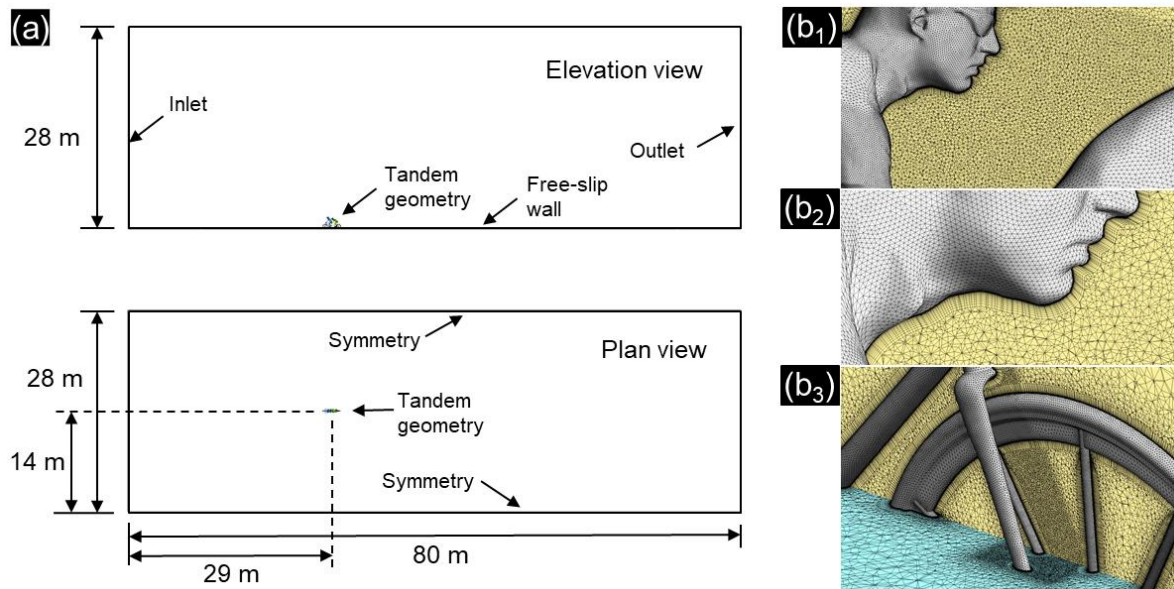


Figure 6.2. (a) Domain size and shape for the tandem simulations (elevation and plan views). (b₁) Volume and surface grid density between pilot and stoker at torso angles of 5°-20° in a vertical centre-plane. (b₂) The prism layer grid (composed of 26 layers) on part of stoker geometry in a vertical centre-plane. (b₃) Volume and surface grid density for the front wheel and forks in a vertical centre-plane and in a horizontal plane

6.3 Results

The drag area ($C_D A$) was used to describe and compare the aerodynamic drag as:

$$C_D A = \frac{F_D}{0.5\rho U_{ref}^2} \quad (6.1) \quad C_{D:P} A = \frac{F_{D:P}}{0.5\rho U_{ref}^2} \quad (6.2) \quad C_{D:S} A = \frac{F_{D:S}}{0.5\rho U_{ref}^2} \quad (6.3)$$

where C_D is the drag coefficient for the pilot, stoker and bicycle combined [-], $C_{D:P}$ the drag coefficient for the pilot only [-], $C_{D:S}$ the drag coefficient for the stoker only [-], A is the frontal area of the pilot, stoker and bicycle combined [m^2], F_D the total drag force [N], $F_{D:P}$ the pilot drag force [N], $F_{D:S}$ the stoker drag force [N], ρ the air density [kg/m^3], and U_{ref} the reference velocity of 15 m/s.

The $C_D A$ ranged between a minimum of $0.308 m^2$ (for the $25^\circ-20^\circ$ setup) and a maximum of $0.399 m^2$ (for the $20^\circ-50^\circ$, $25^\circ-50^\circ$ and $50^\circ-50^\circ$ setup). Figure 6.3a shows the distribution of $C_D A$ over the range of torso angle combinations. The general trend was for $C_D A$ to increase as the torso angle of either the pilot or the stoker increased. However, there were a few exceptions. From $20^\circ-20^\circ$ to $25^\circ-20^\circ$, the $C_D A$ decreased reaching its minimum at $25^\circ-20^\circ$, suggesting that at this torso angle combination, it might be more favourable for the pilot to have a larger torso angle than the stoker as it can provide better aerodynamic shielding of the stoker. In the torso angle range from $20^\circ-50^\circ$ to $50^\circ-50^\circ$, the $C_D A$ was reduced with increasing torso angle for the pilot from 20° to 40° , with a minimum $C_D A$ of $0.383 m^2$ at $40^\circ-50^\circ$. This was opposite to the trends found at alternative stoker torso angles (Figure 6.3a), and was attributed to the drafting benefit to the stoker from the pilot adopting a larger torso angle, which reduced the net drag until $40^\circ-50^\circ$, after which the large drag experienced by the pilot resulted in an increase in $C_D A$ at $50^\circ-50^\circ$.

The maximum drag for the pilot and the minimum drag for the stoker shared the same torso angle combination, at $50^\circ-25^\circ$ (Figure 6.3b and Figure 6.3c). $C_{D:P} A$ and $C_{D:S} A$ values of $0.230 m^2$ and $0.054 m^2$ were recorded for the pilot and the stoker respectively at $50^\circ-25^\circ$; 65.4% and 15.3% of the total drag force respectively. It was observed that the pilot and stoker both experienced larger drag forces as they increased their torso angle. However, for any set torso angle for the stoker, the stoker experienced a smaller drag force as the torso angle of the pilot increased (Figure 6.3c). Notably, the same was often found to be true for the opposite case with the pilot. For any particular torso angle for the pilot, the pilot typically experienced less drag as the torso angle of the stoker increased (Figure 6.3b), albeit on a smaller scale compared to the drag savings the stoker experienced from larger pilot torso angles. The maximum drag reduction found for the pilot as a result of changes to the stoker's torso angle occurred between torso angle combinations of $20^\circ-20^\circ$ and $20^\circ-50^\circ$, with a drag reduction

of 5.5%. By comparison, the stoker experienced a 36.2% drag reduction between 20°-50° and 50°-50°.



Figure 6.3. $C_{D,A}$ values for (a) the pilot, stoker and tandem bicycle combined, (b) the pilot individually, and (c) the stoker individually.

*Torso angle combinations of 40° and 50° for the pilot, coupled with 20° for the stoker, were not viable due to intersecting geometries.

At 20°-50°, the stoker experienced a larger drag force than the pilot. $C_{D:PA}$ and $C_{D:SA}$ values of 0.156 m² and 0.177 m² were recorded for the pilot and stoker respectively at 20°-50°; 39.1% and 44.4% of the total drag force at that torso angle combination. The same drag trend was also found at 25°-50°, with a $C_{D:PA}$ of 0.162 m² and a $C_{D:SA}$ of 0.172 m². At these torso angle combinations, it is indicated in Figure 6.4a that the stoker experienced a large over-pressure region near the head and lower torso in addition to a large under-pressure region near the back. The pilot by comparison did not experience a large under-pressure region on the back at both 20°-50° and 25°-50° due to the subsonic upstream effect imparted by the stoker.

Higher torso angles for the stoker were found to have a larger detrimental effect to the C_{DA} than higher torso angles for the pilot. For comparative purposes, the torso angle combination 25°-25° was used as a baseline and torso angle combinations with 20° are not compared as the 40°-20° and 50°-20° positions were invalid due to geometry intersections. Thus, with 25°-25° as the baseline case, the 25°-50° combination increased drag by 23.9% (from a C_{DA} of 0.322 m² to 0.399 m²). However, a 9.3% increase from the 25°-25° torso angle combination was found for the 50°-25° torso angle combination by comparison, with C_{DA} values of 0.322 m² and 0.352 m² respectively. Figure 6.4a contributes evidence as to why the drag for the 25°-50° case was higher than the 50°-25° case. Figure 6.4a depicts the static pressure coefficient in the vertical centre-plane in the fluid domain. At the 25°-50° torso angle positions, both the pilot and the stoker were found to exhibit large over-pressure regions, whereas in the 50°-25° torso angle positions, only the pilot exhibits an over-pressure region. Figure 6.4b illustrates that the stoker was completely engulfed in the wake of the pilot for the 50°-25° torso angle combination. However, the stoker was partially removed from the wake of the pilot for the 25°-50° torso angle combination (Figure 6.4b).

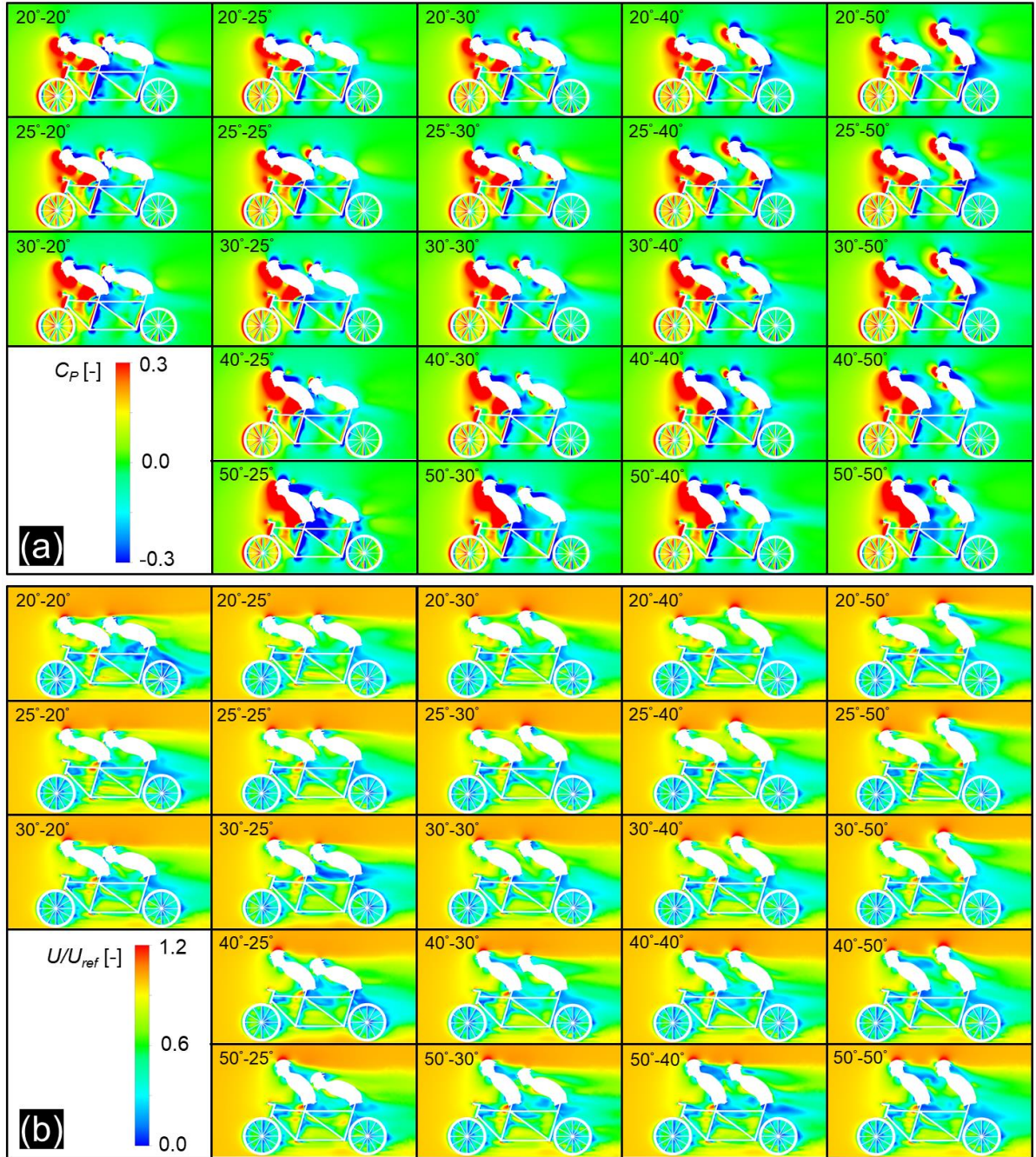


Figure 6.4. (a) Static pressure coefficient (C_p) contours in a vertical centre-plane. (b) Normalised velocity (U/U_{ref}) contours in a vertical centre-plane.

6.4 Discussion

A range of athlete torso angles were investigated for the pilot and stoker in tandem para-cycling with regards to aerodynamics. The sagittal torso angles investigated were 20°, 25°, 30°, 40° and 50° (Figure 6.1), where the same athlete's geometry was used for both the pilot and stoker in numerical simulation to remove anthropometric bias. This study found that torso angles within 20° to 25° resulted in the lowest range of C_{DA} values, with 0.322 m² at 25°-25° and 0.308 m² at 25°-20°, and 0.314 m² at 20°-25° and 20°-20°. The pilot in this study could thus potentially benefit from a slightly more relaxed position at a torso angle of 25°, potentially affording greater power output, but crucially optimising the aerodynamic interaction between the pilot and stoker (if the stoker remained at 20°) to attain the lowest overall C_{DA} . It is noted that the sagittal torso angles investigated in this study were discrete angles, and that the absolute optimum torso angle combination for the pilot and stoker may be between these discrete angles. Fintelman et al. (2014) discussed that adopting extreme low torso angles may not benefit an athlete by compromising power output, and that a balance could be found between aerodynamics and power output. In able-bodied solo cycling, athletes are capable of attaining torso angles lower than the minimum of 20° from the horizontal plane investigated in this study, with torso angles as low as 0° (Fintelman et al., 2014, 2015b). However, that case study was for a time-trial setup with elbow pads and aerobars, and similar low torso angles would be difficult to maintain on dropped handlebars in a road race setup. In addition, the optimal torso angle to balance power output and aerodynamics is often athlete-dependent, as demonstrated by Underwood et al. (2011).

The proximity of the pilot and stoker can limit the torso angle range available to both athletes, with restrictions placed by the UCI on the dimensions of the tandem frame. The individual anthropometrics of the athletes also play a role in the torso angle range available. The relationship between power output and torso angle for a solo able-bodied athlete has some resemblance to the pilot of a tandem, who has a similar cockpit to that of a solo cyclist. However, the same relationship for the stoker is not well understood or investigated in the literature. The results from this research suggest that the stoker needs to maintain a torso angle equal to or less than the pilot for aerodynamic purposes, which might have a yet unknown negative impact on the power output of the stoker. Increasing torso angle for the stoker had a more detrimental effect on the total C_{DA} than increasing torso angle on the pilot (Figure 6.3). A C_{DA} of 0.329 m² was found for the torso angle combination of 20°-30°, higher by 1.9% than 0.323 m² found at 30°-20°, and 0.9% higher than 0.326 m² found at 30°-25°. The 20°-25° torso angle combination resulted in the same C_{DA} of 0.314 m² found for 20°-20°, but was 1.9% higher than 0.308 m² found at 25°-20°. The difference in power to maintain a velocity of 15 m/s between 25°-20° and 20°-20° was estimated at 12.4 W. Alternatively in another

perspective, the 25°-20° torso angle combination could save 6.5 s over a 10 km race, compared to 20°-20°. The difference was greater between 25°-20° and 25°-25°, at 28.9 W and 15.0 s for both power and time comparisons respectively. These calculations on time difference are conducted considering continuous power output throughout the course of the race distance. Furthermore, the clear aerodynamic advantage of lower torso angles for both the pilot and the stoker, suggests that the design of the tandem frame should accommodate the lowest possible athlete torso angles while remaining within the limits set by the UCI. A torso angle combination of 25°-20° was the optimum value found within this research for non-biased athletes; however, the result may be athlete dependant to some degree. A study that standardises athlete anthropometrics may yield further information to the preferable athlete anthropometric proportions for the pilot and stoker positioning for aerodynamics purposes. The UCI rules determine the dimensions for the tandem bicycle, which in turn, limit the positioning options for the athletes to some degree. The present study considers athletes placed on a road bicycle within the regulations; however, some athletes may prefer positions farther back or farther forwards on the saddle. Such individual and unique positioning may further expand or detract from the range of torso angles available to the stoker athlete. Furthermore, the anthropometrics of both athletes and in particular the vertical height of the stoker, have large impacts on the torso angle combinations achievable by the team. Athletes should consider where possible to adjust the tandem bicycle (saddle, seat tube, and handlebars) to allow for the lower torso angle combinations. For example, for particular tandem teams, it may be possible to achieve torso angles lower than those achieved in this study, and a new range of optimal torso angle combinations may be possible.

The individual drag trends of the pilot and stoker increased and decreased as the other athlete adopted smaller or larger torso angles, respectively (Figure 6.3b-c), excluding the torso angle combination of 25°-20°. The drag experienced by the stoker followed the same trend for each fixed pilot torso angle and resulting variations in stoker's torso angle (Figure 6.3c). Higher drag forces were found on the stoker for increasing torso angle. As the pilot's torso angle increased for fixed stokers' torso angles, the typical trend across all fixed stoker torso angles was for the drag to decrease (Figure 6.3c). However, the drag experienced by the stoker increased by 1.9% from 20°-30° to 25°-30°, and by 1.4% from 20°-40° to 25°-40°. The drag on the pilot increased with his increasing torso angle (Figure 6.3b). The typical trend with increasing stoker's torso angle was for the drag on the pilot to decrease. However, at fixed pilots' torso angles of 20° and 40° there were variations to this trend, with the drag of the pilot increasing between torso angle combinations of 30°-30° to 30°-40°, and between 40°-30° and 40°-40°. These outliers from the general trends are associated with subtle aerodynamic interactions between the pilot and stoker. The C_{DA} (Figure 6.3a) broke from its typical trend of increasing with larger pilot torso angles when the torso angle of the stoker was fixed at 50°.

Maximum C_{DA} values of 0.399 m^2 were measured for $20^\circ\text{-}50^\circ$, $25^\circ\text{-}50^\circ$ and $50^\circ\text{-}50^\circ$, with the minimum C_{DA} value of 0.383 m^2 at this fixed stoker torso angle occurring at $40^\circ\text{-}50^\circ$.

Tandem cyclists are exposed to atmospheric wind conditions in outdoor events. The properties of the atmospheric wind conditions may impact the aerodynamics of the tandem cyclists and the optimal torso angle combination may not be applicable to all wind conditions. Mannion et al. (2019) demonstrated that crosswinds can impact the drag distribution of the pilot and stoker. It was found that the drag of the pilot reduced from a 0° yaw angle to 15° yaw. In contrast, the drag of the stoker increased between the same yaw angles. This infers that a singular torso angle combination optimised for 0° yaw conditions, may not be the optimum choice in crosswind conditions. This holds greater significance in outdoor competitive events than indoor velodrome events, as crosswinds may be more prevalent in the former. Moreover, this study considered still air with a low turbulence intensity with no headwind, tailwind or crosswind. It is likely that in reality, turbulence intensity may be higher due to wind conditions which may impact the flow separation locations on the athletes, further impacting their aerodynamic drag.

There were several limitations and simplifications with this study. Firstly, the study considered static geometries with no leg or wheel rotation. It is possible that the movement of the athletes' legs may transfer some movement to the torso of the athlete. This may impact the aerodynamics and thus, the optimum torso angle combination. Secondly, all surfaces of the athletes and bicycle geometries were considered as smooth, with zero roughness. The roughness would vary from the skin to the skin suits, bicycle frame, tyres and other components in actual cycling conditions. The roughness of the athletes' skinsuits coupled with the torso angle adopted by the athletes could impact the locations of flow separation on the torso surfaces of the athletes. This in turn could positively or negatively impact the drag of the athletes. Thirdly, the head angle relative to the torso angle was not changed between torso angle variations. The head and helmet of the athlete were rotated with the torso for each increment. Athletes typically adjust their head angle to maintain forward visibility and for relaxation/comfort. The head angle would impact the orientation of the helmet which, typically, has aerodynamic considerations in its design. There may be an optimum head angle to minimise aerodynamic drag and this angle may be specific to unique helmet designs. Thus, further torso angle combination optimisation for tandem athletes should consider this variable within their analyses.

Future research could couple CFD and wind tunnel experiments, by utilising articulated mannequins in the wind tunnel to allow for precise adjustments of torso angles, while maintaining repeatability and preventing a bias between the anthropometrics of the pilot and the stoker. However, the effect of differing anthropometrics between the pilot and stoker is also of interest for future

research. A pilot that is larger than the stoker may provide good aerodynamic shielding at a greater range of torso angles, allowing for more relaxed positions for the stoker to increase power output without negatively impacting the overall aerodynamics. Furthermore, the optimal choice of helmets and skin suits for tandem athletes may have a dependency on the postures adopted by the athletes. Finally, an investigation should be conducted to optimise the balance between power output and aerodynamics for the pilot and stoker in tandem para-cycling, with additional focus on the stoker.

6.5 Conclusions

Tandem para-cycling aerodynamics were investigated with respect to the pilot and stoker torso angles. The athletes' sagittal torso angles were altered from 20° to 25°, 30°, 40° and 50° leading to a total of 23 viable torso angle combinations. CFD simulations were performed using computational settings based on prior solution verification and validation studies. Increasing the torso angle in excess of 25° for either athlete caused detrimental effects on the C_{DA} of the tandem setup. However, it was found that a 5° increment from 20° to 25° for the pilot or stoker had only small effects on the C_{DA} within a range of 1.9% to 4.5% (C_{DA} range between 0.308 m² and 0.322 m²). Within this range, it might be possible that athletes can adopt a slightly more relaxed position if it gives greater power output than the aerodynamic losses from increased torso angles. It was found that larger adjustments to the torso angle of the stoker had more severe implications for the C_{DA} than the equivalent torso angle adjustments for the pilot, indicating that there should be additional impetus on optimising the stoker's posture in order to minimise the C_{DA} .

The minimum C_{DA} value were recorded at a torso angle combination of 25°-20° at 0.308 m². The pilot experienced maximum and minimum aerodynamic drag at the torso angle combinations of 50°-25° and 20°-50° respectively, and the stoker at 20°-50° and 50°-25° respectively. The drag of the pilot increased with increasing torso angle, but decreased with increasing torso angle of the stoker. The drag of the stoker decreased with increasing torso angle of the pilot, and increased with his (stoker's) increasing torso angle.

6.6 References

- ANSYS Fluent. (2015). ANSYS Fluent theory guide. *Release 16.1 Documentation*. ANSYS Inc.
- Barry, N., Burton, D., Sheridan, J., Thompson, M., & Brown, N. A. T. (2015). Aerodynamic performance and riding posture in road cycling and triathlon. *Proceedings of the Institution of Mechanical Engineers, Part P: Journal of Sports Engineering and Technology*, 229(1), 28–38. <https://doi.org/10.1177/1754337114549876>
- Barry, N., Burton, D., Sheridan, J., Thompson, M., & Brown, N. A. T. (2016). Flow field interactions between two tandem cyclists. *Experiments in Fluids*, 57(12), 1–14. <https://doi.org/10.1007/s00348-016-2273-y>
- Blocken, B. (2015). Computational Fluid Dynamics for urban physics: Importance, scales, possibilities, limitations and ten tips and tricks towards accurate and reliable simulations. *Building and Environment*, 91, 219–245. <https://doi.org/10.1016/j.buildenv.2015.02.015>
- Blocken, B., Defraeye, T., Koninckx, E., Carmeliet, J., & Hespel, P. (2013). CFD simulations of the aerodynamic drag of two drafting cyclists. *Computers & Fluids*, 71, 435–445. <https://doi.org/10.1016/j.compfluid.2012.11.012>
- Blocken, B., & Toparlar, Y. (2015). A following car influences cyclist drag: CFD simulations and wind tunnel measurements. *Journal of Wind Engineering and Industrial Aerodynamics*, 145(0), 178–186. <https://doi.org/10.1016/j.jweia.2015.06.015>
- Blocken, B., Toparlar, Y., & Andrienne, T. (2016). Aerodynamic benefit for a cyclist by a following motorcycle. *Journal of Wind Engineering and Industrial Aerodynamics*, 155, 1–10. <https://doi.org/https://doi.org/10.1016/j.jweia.2016.04.008>
- Blocken, B., van Druenen, T., Toparlar, Y., Malizia, F., Mannion, P., Andrienne, T., Marchal, T., Maas, G.J., Diepens, J. (2018). Aerodynamic drag in cycling pelotons: New insights by CFD simulation and wind tunnel testing. *Journal of Wind Engineering and Industrial Aerodynamics*, 179(May), 319–337. <https://doi.org/10.1016/J.JWEIA.2018.06.011>
- Crouch, T. N., Burton, D., Brown, N. a. T., Thompson, M. C., & Sheridan, J. (2014). Flow topology in the wake of a cyclist and its effect on aerodynamic drag. *Journal of Fluid Mechanics*, 748, 5–35. <https://doi.org/10.1017/jfm.2013.678>
- Crouch, T. N., Burton, D., LaBry, Z. A., & Blair, K. B. (2017). Riding against the wind: a review of competition cycling aerodynamics. *Sports Engineering*, 20(2), 81–110.

<https://doi.org/10.1007/s12283-017-0234-1>

- Defraeye, T., Blocken, B., Koninckx, E., Hespel, P., & Carmeliet, J. (2010a). Aerodynamic study of different cyclist positions: CFD analysis and full-scale wind-tunnel tests. *Journal of Biomechanics*, *43*(7), 1262–1268. <https://doi.org/10.1016/j.jbiomech.2010.01.025>
- Defraeye, T., Blocken, B., Koninckx, E., Hespel, P., & Carmeliet, J. (2010b). Computational fluid dynamics analysis of cyclist aerodynamics: Performance of different turbulence-modelling and boundary-layer modelling approaches. *Journal of Biomechanics*, *43*(12), 2281–2287. <https://doi.org/10.1016/j.jbiomech.2010.04.038>
- Fintelman, D. M., Sterling, M., Hemida, H., & Li, F.-X. (2014). Optimal cycling time trial position models: Aerodynamics versus power output and metabolic energy. *Journal of Biomechanics*, *47*(8), 1894–1898. <https://doi.org/10.1016/j.jbiomech.2014.02.029>
- Fintelman, D. M., Hemida, H., Sterling, M., & Li, F.-X. (2015a). CFD simulations of the flow around a cyclist subjected to crosswinds. *Journal of Wind Engineering and Industrial Aerodynamics*, *144*, 31–41. <https://doi.org/10.1016/j.jweia.2015.05.009>
- Fintelman, D. M., Sterling, M., Hemida, H., & Li, F.-X. (2015b). The effect of time trial cycling position on physiological and aerodynamic variables. *Journal of Sports Sciences*, *0414*(April 2015), 1–8. <https://doi.org/10.1080/02640414.2015.1009936>
- Fintelman, D. M., Sterling, M., Hemida, H., & Li, F. X. (2016). Effect of different aerodynamic time trial cycling positions on muscle activation and crank torque. *Scandinavian Journal of Medicine and Science in Sports*, *26*(5), 528–534. <https://doi.org/10.1111/sms.12479>
- Franke, J., Hellsten, A., Schlünzen, H., & Carissimo, B. (2007). Best practice guideline for the CFD simulation of flows in the urban environment. *COST Action 732: Quality Assurance and Improvement of Microscale Meteorological Models*. Hamburg Germany.
- García-López, J., Rodríguez-Marroyo, J. A., Juneau, C.-E., Peleteiro, J., Martínez, A. C., & Villa, J. G. (2008). Reference values and improvement of aerodynamic drag in professional cyclists. *Journal of Sports Sciences*, *26*(3), 277–286. <https://doi.org/10.1080/02640410701501697>
- Gibertini, G., Campanardi, G., Grassi, D., & Macchi, C. (2008). Aerodynamics of Biker Position. In *BBA VI International Colloquium on: Bluff Bodies Aerodynamics & Applications*. Milano, Italy.
- Grappe, F., Candau, R., Belli, A., & Rouillon, J. D. (1997). Aerodynamic drag in field cycling with special reference to the Obree's position. *Ergonomics*, *40*(12), 1299–1311.

<https://doi.org/10.1080/001401397187388>

- Griffith, M. D., Crouch, T., Thompson, M. C., Burton, D., & Sheridan, J. (2014). Computational fluid dynamics study of the effect of leg Position on cyclist aerodynamic drag. *The American Society of Mechanical Engineers, Journal of Fluids Engineering*, 136.
<https://doi.org/10.1115/1.4027428>
- Haake, S. J. (2009). The impact of technology on sporting performance in Olympic sports. *Journal of Sports Sciences*, 27(13), 1421–1431. <https://doi.org/10.1080/02640410903062019>
- Heil, D. P., Derrick, T. R., & Whittlesey, S. (1997). The relationship between preferred and optimal positioning during submaximal cycle ergometry. *European Journal of Applied Physiology and Occupational Physiology*, 75(2), 160–165. <https://doi.org/10.1007/s004210050141>
- Lukes, R. a, Chin, S. B., & Haake, S. J. (2005). The understanding and development of cycling aerodynamics. *Sports Engineering*, 8, 59–74. <https://doi.org/10.1007/BF02844004>
- Mannion, P., Toparlar, Y., Blocken, B., Clifford, E., Andrianne, T., & Hajdukiewicz, M. (2018a). Aerodynamic drag in competitive tandem para-cycling: road race versus time-trial positions. *Journal of Wind Engineering & Industrial Aerodynamics*, 179, 92–101.
<https://doi.org/10.1016/j.jweia.2018.05.011>
- Mannion, P., Toparlar, Y., Blocken, B., Hajdukiewicz, M., Andrianne, T., & Clifford, E. (2018b). Improving CFD prediction of drag on Paralympic tandem athletes: Influence of grid resolution and turbulence model. *Sports Engineering*, 21(2), 123–135. <https://doi.org/10.1007/s12283-017-0258-6>
- Mannion, P., Toparlar, Y., Clifford, E., Hajdukiewicz, M., Blocken, B. (2019) On the effects of crosswinds in tandem aerodynamics: An experimental and computational study. *European Journal of Mechanics / B Fluids* 74 (2019) 68–80. doi:10.1016/j.euromechflu.2018.11.001.
- Menter, F. R. (1994). Two-equation eddy-viscosity turbulence models for engineering applications. *AIAA Journal*, 32(8), 1598–1605. <https://doi.org/10.2514/3.12149>
- Oggiano, L., Leirdal, S., Sætran, L., & Ettema, G. (2008). Aerodynamic Optimization and Energy Saving of Cycling Postures for International Elite Level Cyclists. *The Engineering of Sport* 7, 1(2), 597–604. https://doi.org/10.1007/978-2-287-09411-8_70
- Tominaga, Y., Mochida, A., Yoshie, R., Kataoka, H., Nozu, T., Yoshikawa, M., & Shirasawa, T. (2008). AIJ guidelines for practical applications of CFD to pedestrian wind environment around buildings. *Journal of Wind Engineering and Industrial Aerodynamics*, 96(10–11),

1749–1761. <https://doi.org/10.1016/j.jweia.2008.02.058>

Underwood, L., & Jermy, M. (2013). Optimal handlebar position for track cyclists. *Sports Engineering*, *16*(2), 81–90. <https://doi.org/10.1007/s12283-013-0111-5>

Underwood, L., Schumacher, J., Burette-Pommay, J., & Jermy, M. (2011). Aerodynamic drag and biomechanical power of a track cyclist as a function of shoulder and torso angles. *Sports Engineering*, *14*(2–4), 147–154. <https://doi.org/10.1007/s12283-011-0078-z>

Part II: Hand-cycling

CFD analysis of hand-cycle aerodynamics: turbulence model and grid sensitivity analyses and the impact of wheel selection

Chapter 7 is the first chapter of four in Part II of this thesis, which focuses on hand-cycling. This chapter focuses on grid and turbulence model sensitivity analyses with wind tunnel experimental data providing validation data. In addition, this chapter explores the impact of wheel selection through numerical simulations using static simplified wheel geometries (disk and spoked). The impact of wheel diameters on hand-cycling aerodynamics is also investigated, with different combinations of wheel diameters on the front and rear axle tested.

This chapter has been submitted to an international peer-reviewed as:

Mannion, P., Toparlar, Y., Blocken, B., Hajdukiewicz, M., Andrianne, T., & Clifford, E. (2019). CFD analysis of hand-cycle aerodynamics: turbulence model and grid sensitivity analyses and the impact of wheel selection. *Under review*.

Abstract: Aerodynamics research in cycling has underpinned innovative bicycle design, new refined riding positions and optimised rider apparel. There has been a rise in the level of aerodynamics research focused on cycling since the turn of the millennium, enabled by significant increases in computational power and the availability of software/hardware. However, cycling research has not yet fully embraced para-cycling, with limited studies conducted on the aerodynamic performance of hand-cyclists and other para-cyclists. Wind tunnel experiments and Computational Fluid Dynamics (CFD) simulations were conducted in this research for the analysis of hand-cycling aerodynamics, focused on competitive H1-H4 category hand-cyclists. A quarter-scale representative geometry of a hand-cyclist was used in high-speed wind tunnel experiments. The accuracy of the simulations performed with the 3D Reynolds-Averaged Navier-Stokes equations was found to be dependent on the turbulence model choice and near-wall grid resolution. CFD simulations predicted the magnitude of the drag and lateral forces to an accuracy of 2.5% using the SST $k-\omega$ turbulence model. This study also presents the impact of wheel diameter and disk wheels on hand-cycling aerodynamics via CFD simulations, providing a deeper understanding of the aerodynamic characteristics unique to the hand-cycling discipline in the sport of competitive cycling. Drag reductions of up to 8.9% were found when utilising 20-inch diameter spoked wheels, opposed to the 26-inch wheels. Variations in wheel

diameter between the front and rear wheels were found to have a significant impact on the C_{DA} in part through altering the pitch angle of the hand-cycle.

7.1 Introduction

Hand-cycling is a para-cycling sport regulated by the International Cycling Union (UCI) and is composed of five categories; H1-H5. The H5 category is a kneeling position, where athletes can use their arms and trunk when cycling (UCI, 2017). In categories H1-H4, athletes adopt a reclined position with different levels of lower limb mobility (UCI, 2017). E.g. athletes from the H1 category experience a complete loss of trunk and leg function and have limited arm function, while athletes in the H4 class have good arm and trunk function, but limited leg function (UCI, 2017). Thanks to major sporting events like the Olympics, Paralympics and international racing (e.g. Le Tour de France), competitive cycling technologies and designs have experienced continuing development (Hart, 2006; Keogh, 2011).

The importance of aerodynamic efficiency in cycling is widely recognised, with a large number of publications in relation to cycling aerodynamics in recent years (Blocken et al., 2018; Blocken, Toparlar, & Andrienne, 2016; Blocken & Toparlar, 2015; Crouch et al., 2017; Crouch et al., 2016; Fintelman et al., 2014; Griffith et al., 2014; Lukes et al., 2005). However, there have been limited studies conducted on para-cyclists, and in particular on hand-cyclists, with only a single known publication focusing on the aerodynamics of hand-cyclists using wind tunnel experiments (Belloli et al., 2014). Despite the lack of leg power, hand-cyclists are capable of achieving high speeds, in some cases higher than those achieved by able-bodied traditional cyclists (e.g. while descending hills) due to their lower frontal area than able-bodied cyclists. New research could lend further visibility to hand-cycling, in addition to providing further advances in understanding the aerodynamics of competitive hand-cyclists.

Wheels play an important role in cycling aerodynamics and are expected to be influential also in hand-cycling aerodynamics, where three wheels contribute to the drag of the hand-cycle (one front and two rear). A range of wheel types have been explored using both computational and experimental methods in the literature. Tew & Sayers, (1999) conducted wind tunnel experiments for rotating wheels that accommodated for several designs isolated from a bicycle frame; from disk and tri-spoke to spoked wheels with various rim depths. The standard 32-spoked wheel was found to generate the largest drag force and the disk wheel produced the lowest drag at 0° yaw. Numerical simulations were performed by Godo et al. (2009) on a rotating spoked wheel. Unique observations were made possible through the use of CFD, such as the finding that pressure drag was the dominant cause of aerodynamic

drag, with viscous drag contributing only up to 3%. Furthermore, the spokes of a standard wheel were observed to generate a drag comparable to the wheel hub. However, the wheel rims and tyres generated the majority of the drag. This provided a good insight into the potential for simplifying wheel geometries for complex CFD simulations with computationally expensive grids. Geometric modelling of the rims, tyres and wheel hub with no spokes would reduce the computational effort considerably. Six commercial bicycle wheels of similar types to those studied by Tew & Sayers, (1999) were analysed by Godo et al. (2010) using numerical methods, where a range of yaw angles were tested using steady-state and transient methods; the accuracy of the numerical results was determined via qualitative analysis which produced similar trends to experimental data. In addition, numerical studies by Pogni et al. (2015) further confirmed the capabilities of steady RANS calculations to correctly describe the aerodynamic characteristics of bicycle wheels. Additional experiments on wheel aerodynamics were conducted by Barry et al. (2012) on several wheel types, with a dynamic mannequin mounted on a bicycle to provide realistic flow-field effects. It was found that wheel drag trends were influenced by the presence of the mannequin on the bicycle. It was recommended that wheel aerodynamic performance should not be assessed through isolated experiments, but through experiments where the wheel is included in a bicycle-rider system.

Belloli et al. (2014) investigated recumbent H1-H4 category hand-cyclist and upright H5 category hand-cyclist aerodynamics. It should be noted that the H4 position analysed and discussed by Belloli et al. (2014) in fact represents the H5 class according to the current mobility classifications (UCI, 2017). Wind tunnel experiments were used to determine that in a hill descent position termed as an 'aerodynamic stage' with static arms, an upright category H5 hand-cyclist yielded lower aerodynamic drag than a recumbent H1-H4 category hand-cyclist, with a drag area ($C_D A$) of 0.13 m^2 and 0.20 m^2 respectively. However, the recumbent hand-cycle position proved to yield a slightly lower aerodynamic drag than an upright hand-cyclist when actively cycling, with $C_D A$ values of 0.21 m^2 and 0.22 m^2 respectively. With regards to other para-cycling aerodynamics research, Dyer (2015) evaluated the ability of outdoor velodrome aerodynamics tests for testing and evaluating small-scale changes made to prosthetic limb components. A difference of 0.01 m^2 in $C_D A$ was found between the baseline experiment with a wooden dowel attached to the athlete's bicycle and the change condition of adding a sphere to the end of the dowel. It was concluded that the aerodynamic optimisation of prosthetic limb components could yield decisive improvements for para-athletes. Accurate CFD simulations for the analysis of hand-cycling aerodynamics could be useful in testing different design and posture alternatives. However, CFD simulations have not yet been utilised for the purposes of analysing and accurately predicting hand-cycling aerodynamics. This paper aims to focus on this research gap.

The research presented in this paper addresses competitive hand-cycling aerodynamics, relevant to UCI's categories of H1-H4 (UCI, 2017) (Figure 7.1). This work utilised wind tunnel experiments (a scaled 3D geometry of a hand-cyclist, as shown in Figure 7.1) validating CFD simulations in order to provide a better understanding of hand-cycle aerodynamics. Grid and turbulence model sensitivity analyses were conducted to determine their impact on CFD predictions. Generic wheel geometries for hand-cycling were analysed and compared to give insight into the role they play in hand-cycling aerodynamics.

7.2 Wind tunnel experiments

A quarter-scale geometric model of a hand-cyclist was manufactured from ABS (acrylonitrile butadiene styrene) material with smooth surfaces and it was used for the wind tunnel experiments in the aeronautical test section of the wind tunnel laboratory in the University of Liège, Belgium (Figure 7.1). The combined geometry of the hand-cycle and the athlete was obtained via structured light 3D scanning, using an Eva (Artec, 2017) scanner. The spoked wheels were modelled independently using Computer Aided Design (CAD) tools, and integrated with the scanned cyclist geometry. Small geometric details such as the chain and cables were neglected due to their size being below the 3 mm minimum size tolerance for manufacturing at quarter-scale. For this reason, the diameter of the spokes was limited to 3 mm on the quarter scale model, which also served the function to stabilise and secure the wheel rims/tyres when under wind load. The air velocity in the test section was 60 m/s, to match the Reynolds number of a full-scale hand-cyclist travelling at 15 m/s, representative of velocities achieved by hand-cyclists during hill descents. A single force transducer was attached to the hand-cycle model, via the baseplate (Figure 7.1a), positioned in vertical alignment with the model's centre of gravity. The hand-cycle model was mounted on a sharp edged horizontal platform, elevated 0.3 m from the floor of the test section. This platform limited boundary layer development upstream of the hand-cycle model. The frontal areas of the hand-cycle model, the platform and supporting structures were calculated to have a blockage ratio of 1.85% in the test chamber (which had a cross sectional area of $2 \times 1.5 \text{ m}^2$). 3D solid blockage corrections to the measured velocity were applied based on Barlow et al. (1999) using a value of 0.96 for the body shape form factor. These corrections are applicable between the blockage ratios of 1-10% (Barlow et al., 1999).

Air velocity in the stream-wise direction was measured using a pitot tube. Temperature measurements were recorded to correct drag measurements for density deviations between the experiments and CFD simulations, where an air density of 1.225 kg/m^3 at 15°C was used. Atmospheric pressure was obtained from local meteorological data and the drag data were corrected

to the value used in the CFD simulations; 101325 Pa. The force transducer was zeroed in the wind tunnel under zero wind load conditions before commencing the experiment. A 30 second settling period for the transducer was allowed after the wind tunnel air velocity had reached full speed. The force recordings from the settling period were not included in the final experimental data. The force data acquired after the settling period was sampled at 10 Hz for 180 seconds. A conservative maximum error estimate of 1.25 N at a 95% confidence interval was reported via private communication by the manufacturer of the force transducer. No turbulence intensity measurements were conducted during the experiment in the test section of the wind tunnel. However, the turbulence intensity was expected to be below 0.2%, as reported by Blocken et al. (2016) for similar experiments conducted at the same velocity in the wind tunnel of the University of Liège.

The hand-cycle geometry in the wind tunnel experienced a drag force of 23.94 ± 0.70 N, and a lateral force of 0.86 ± 0.65 N. A single standard deviation is provided for each component force result. The measured lateral force was small by comparison to the drag force due to the near symmetry of the hand-cycle geometry.

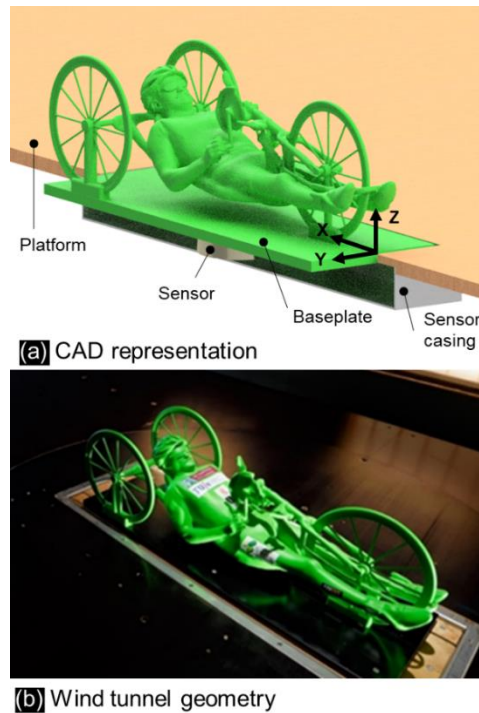


Figure 7.1. (a) Computer aided design (CAD) representation of the wind tunnel setup, with the platform and sensor casing cut through the centre to reveal the sensor within. (b) Photo of the quarter-scale geometry in the wind tunnel.

7.3 CFD simulations: validation study and sensitivity analysis

7.3.1 Geometry and boundary conditions

The CFD simulations for the validation study and sensitivity analysis were performed on full-scale hand-cycle geometry that included the baseplate and wheel supports used in the wind tunnel experiments (Figure 7.2). The $4 \times 1.5 \text{ m}^2$ platform that raised the hand-cycle geometry from the bed of the test chamber was included in the full-scale CFD simulation (Figure 7.2), to include the boundary layer that developed on the platform (which would interact with the hand-cycle geometry). The platform surface was modelled as a no-slip wall with zero roughness.

The computational domain was created as a cuboid with dimensions of $70 \times 28 \times 20 \text{ m}^3$ and a blockage ratio of 0.05% to prevent any blockage effects (Figure 7.2). The platform and the hand-cycle geometry were centred laterally, with the hand-cycle geometry also centred longitudinally on the platform (Figure 7.2).

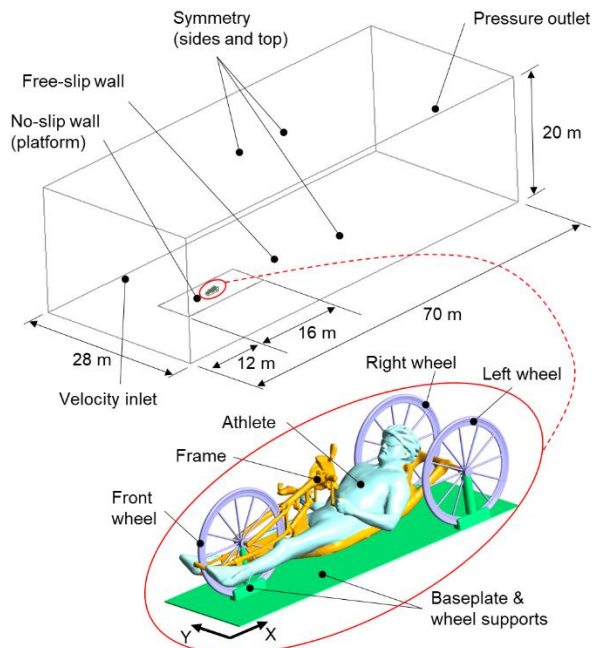


Figure 7.2. A schematic representation of the computational domain. The axis direction indicates the positive force directions in accordance with the wind tunnel force transducers.

The hand-cycle surfaces, along with the baseplate, wheel supports, and platform surfaces were modelled using a no-slip wall condition with zero roughness. The lower horizontal domain boundary was modelled using a free-slip wall (Figure 7.2) to prevent boundary layer development prior to the platform surface, providing further similarity to the wind tunnel experiment. The fluid

was specified as air with a dynamic viscosity of $1.789\text{e-}5$ kg/m.s and a density of 1.225 kg/m³. A uniform velocity of 15 m/s was applied at the inlet, with 0.2% turbulent intensity and a hydraulic diameter of 1 m. An external static gauge pressure of 0 Pa was applied to the outlet boundary. Symmetry conditions were imposed on both lateral boundaries and the top boundary of the domain, where zero normal gradients were assumed for all the variables. The computational grid was established based on a grid sensitivity analysis, which is described in sub-section 7.3.3.

7.3.2 Computational settings

ANSYS Fluent 16 (ANSYS, 2015) was utilised for numerical simulations, using the control volume discretisation method. The 3D Reynolds-Averaged Navier-Stokes (RANS) equations were solved, with several turbulence models tested for closure (section 7.3.4). The Least Squares Cell Based method (ANSYS, 2015) was applied to compute the gradients, and the Coupled algorithm was used for pressure-velocity coupling to allow for pseudo-transient simulations, averaging force values over 4000 pseudo-timesteps with a timestep size of 0.01 s. Second-order pressure interpolation was used, along with the second-order discretisation schemes for momentum, turbulent kinetic energy, turbulence dissipation rate and all other spatial terms relevant to individual turbulence models. The simulations concluded with typical maximum values for the scaled residuals of: $1\text{x}10^{-7}$ for momentum, $1\text{x}10^{-5}$ for continuity, $1\text{x}10^{-6}$ for turbulent eddy viscosity, $1\text{x}10^{-4}$ for kinetic energy, and $1\text{x}10^{-4}$ for dissipation rate.

7.3.3 Computational grid and grid convergence study

A high resolution computational grid (Figure 7.3a) was created, informed by a sensitivity study that followed the best practice guidelines (Casey & Wintergerste, 2000; Franke et al., 2007; Tominaga et al., 2008). This grid was denoted as grid A, and examples of the surface and volume grid density for grid A are illustrated in Figure 7.3b-d. Twenty prism layers were grown from the athlete, hand-cycle, wheel supports and baseplate surfaces (Figure 7.3). Five prism layers were grown from the platform surface. Three body of influences (BOI's) were used to resolve wake flow features and pressure gradients. The first BOI, $0.20\text{x}0.27\text{x}0.20$ m³, encompassed the rear of the athlete's helmet with a maximum cell volume of $2\text{x}10^{-9}$ m³. The second BOI, encompassed the complete hand-cycle geometry, with dimensions of $2.0\text{x}0.8\text{x}0.7$ m³, and a max cell volume of $1\text{x}10^{-6}$ m³. The final and largest BOI was $12\text{x}2\text{x}5$ m³, with a max cell volume of $8\text{x}10^{-4}$ m³, resolving the wake flow behind the hand-cyclist and the upstream pressure effect ahead of the hand-cyclist. The resulting grid (grid A) contained 25.7 million cells.

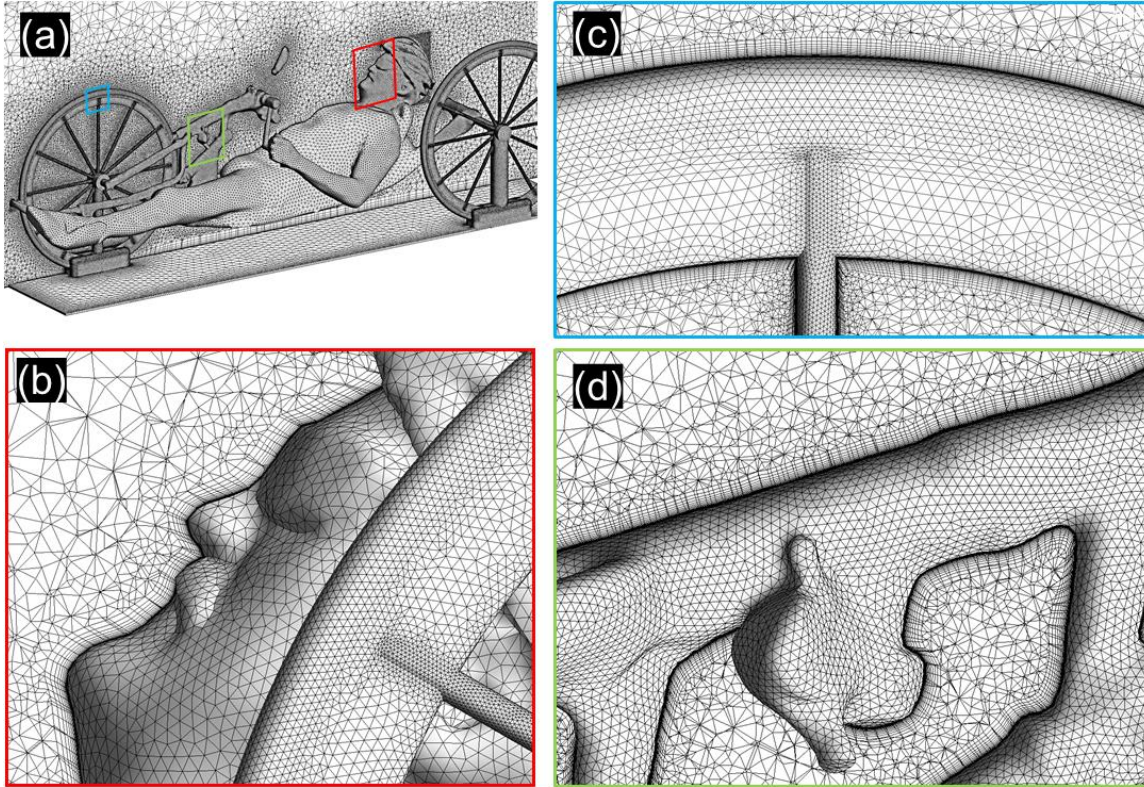


Figure 7.3. Part of surface and volume grid for grid A indicated for (a) the hand-cyclist geometry (25.7 million cells), (b) the athlete's head, (c) the front wheel, and (d) the hand-cycle frame.

The dimensionless wall unit y^* was used for grid descriptions further in this section. y^* is defined as:

$$y^* = \frac{u^* y_p}{\nu} \quad (7.1)$$

where y_p (m) is the normal height of the wall-adjacent cell centre point P from the wall surface, ν [m^2/s] is the kinematic viscosity and u^* [m/s] the friction velocity, defined as:

$$u^* = C_\mu^{\frac{1}{4}} k_p^{\frac{1}{2}} \quad (7.2)$$

where C_μ [-] is a model constant (0.09), and k_p [m^2/s^2] is the turbulent kinetic energy at point P.

The drag area [m^2] was used as a target parameter:

$$C_D A = \frac{F_D}{0.5 \rho V^2} \quad (7.3)$$

where F_D is the drag force [N], V the velocity [m/s], and ρ the density [kg/m^3].

A y^* sensitivity study was conducted with grid A as the baseline grid. For this grid, the wall-adjacent cell centre for all cells across the hand-cycle, wheel supports and baseplate was $12.5 \mu\text{m}$ in height, normal to the wall surfaces. The average y^* value for grid 4a was 0.8 and the maximum y^*

was 2.9. Four additional grids, named grids B-E, were created by adjusting y_p , with the coarsest grid (grid E) yielding an average y^* in excess of 40. The SST $k-\omega$ turbulence model (Menter, 1994) was used for closure, which can be integrated through the viscous sublayers in wall-bounded flows. Compared to the wind tunnel measurements, CFD simulations using grid A underestimated the drag by -1.4%. The underestimation of drag was found to be dependent on y^* resolution, where the deviations increased with increasing y^* for grids B-E (Figure 7.4a). Thus, grid A was chosen for further research (denoted by a red 'X' on Figure 7.4a), with its y^* distribution on the modelled geometry displayed in Figure 7.4b.

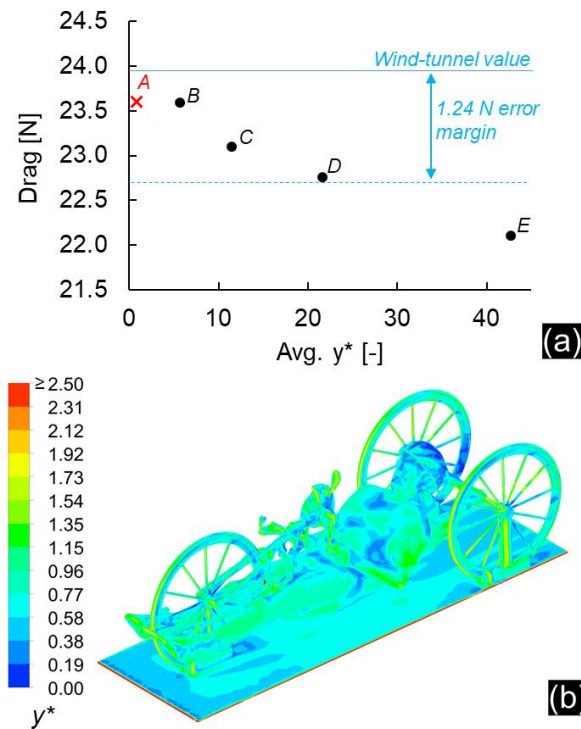


Figure 7.4. (a) The average y^* resolution on the hand-cyclist geometry plotted against the resulting drag coefficient for grids A-E. (b) A contour plot of the y^* distribution corresponding to grid A marked with a red 'X' in (a).

7.3.4 Turbulence model sensitivity

Grid A was used for a turbulence model sensitivity study with six turbulence models: the 4-equation transition SST (T-SST) (Menter et al., 2004), the 3-equation $k-kl-\omega$ (Walters & Cokljat, 2008), the 2-equation SST (Shear Stress Transport) $k-\omega$ (Menter, 1994), the standard $k-\epsilon$ (Jones & Launder, 1972), the Re-Normalisation Group (RNG) $k-\epsilon$ (Choudhury, 1993), and the 1-equation Spalart-Allmaras (Spalart & Allmaras, 1992) model. The 1-equation model by Wolfshtein

(Wolfshtein, 1969) was used with the standard $k-\varepsilon$ and RNG $k-\varepsilon$ turbulence models for low-Reynolds number modelling.

Figure 7.5 shows the resulting drag and lateral forces. The predictions by the $k-kl-\omega$, T-SST, $k-kl-\omega$, and Spalart-Allmaras models all fall within the error range from the wind tunnel experiments for both the drag and lateral forces. The $k-kl-\omega$ provided the most accurate drag predictions, deviating by 0.1% from the wind tunnel data. The lateral force predicted by the wind tunnel experiment and CFD simulations was small due to the near-symmetry of the hand-cyclist, and the predictions using the $k-kl-\omega$, T-SST, SST $k-\omega$ and Spalart-Allmaras all fell within the error range of the transducers. The T-SST and SST $k-\omega$ models followed closely behind the $k-kl-\omega$ as the 2nd and 3rd best performing turbulence models for drag predictions, with deviations still within the error range of the force transducers, at -0.7% and -1.4% respectively. The Spalart-Allmaras model also provided good predictions of the drag despite being the cheapest in terms of computational requirements, with a deviation of -3.7%. The RNG $k-\varepsilon$ and standard $k-\varepsilon$ models provided the least accurate drag predictions from the selection of turbulence models tested, with deviations of -8.6% and -14.3% respectively. With several turbulence models providing close results to the wind tunnel data, the SST $k-\omega$ model was chosen for further research for its acceptable accuracy, with drag and lateral force deviations of -1.4% and 9.6% respectively, and absolute deviations of -0.33 N and 0.08 N respectively. The SST $k-\omega$ model has also been reported as successful in the literature for the accurate prediction of aerodynamic forces in cycling and Para-cycling (Defraeye et al., 2010; Mannion et al., 2018a, 2018b)

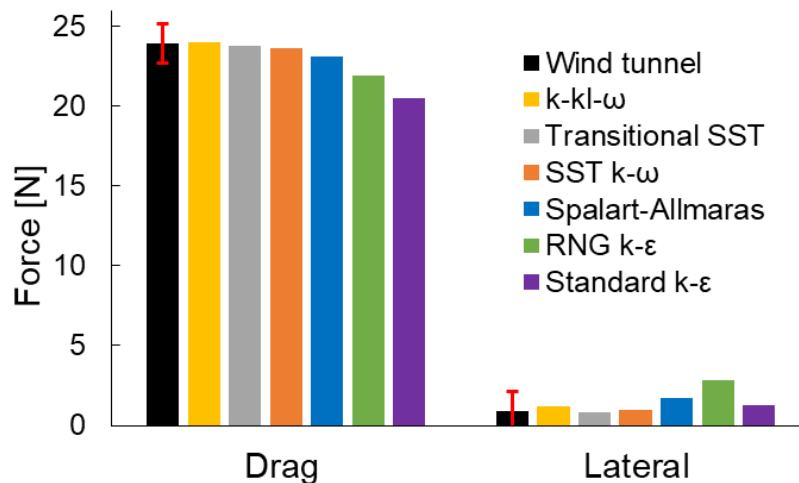


Figure 7.5. The drag and lateral forces from the turbulence model sensitivity study are plotted with the results from the wind tunnel experiments. ± 1.24 N error bars are included with the wind tunnel data.

7.4 CFD simulations: analysis of hand-cycle aerodynamics

7.4.1 Wheel geometries

The aerodynamic influences of wheels for competitive hand-cycling were investigated. Wheel sizes are discussed in inches throughout this paper as per the convention in the cycling industry. The athlete and hand-cycle frame both reside within the vertical coordinate of a standard 26-inch diameter wheel (660.4 mm), and three wheels are used for a hand-cycle in comparison to the two used in conventional cycling. The wheelbase length was 1.525 m, and the rear wheel spacing was 0.650 m. Two variations of spoked wheel geometries were analysed, representative of the simplified wheel geometries used in the wind tunnel experiments. The first was a direct representation of the spoked wheels used in the wind tunnel experiments with twelve spokes, each 0.012 m in diameter for the full-scale geometry (Figure 7.6). The profile of the rims with dimensions are provided in Figure 7.6. The wheel hub was a 0.06 m diameter cylinder, 0.07 m in length. This geometry is denoted as ‘spoked wheel’ geometry for the remainder of this paper to provide clarity for comparison purposes. The second variation of the spoked wheel geometry neglected the spokes from the geometrical model, leaving only the tyres, rims and wheel hubs (Figure 7.6). This provided the means to determine the influence of the simplified 0.012 m diameter spokes on the aerodynamics of the hand-cycle. This geometry is denoted as ‘rims-only’ for the duration of this paper (Figure 7.7a). A third hand-cycle geometry with representations of disc wheels based on no specific commercial design was also simulated. The disk wheels had the same diameter and tyre dimensions as the spoked wheel geometry, 0.05 m wide at the hub, and tapered between the hub and the rims. This geometry is denoted as the ‘disk wheel’ geometry (Figure 7.7a).

To provide an accurate representation of hand-cycle aerodynamics, the wheel support structures, baseplate and platform surface from the validation case study were removed from the geometrical model used for the CFD simulations. Grid parameters for grid A (section 7.3.3), were followed for each geometry. The ground surface was modelled as a no-slip wall, with a linear velocity of 15 m/s. This represented a hand-cycle travelling at this velocity, with the inlet velocity set to the same value. The hand-cycle geometry was raised 0.01 m from the ground surface to prevent highly skewed grid cells forming at the tangent meeting location of the wheels and ground surface. The wheel geometries remained static for all simulations.

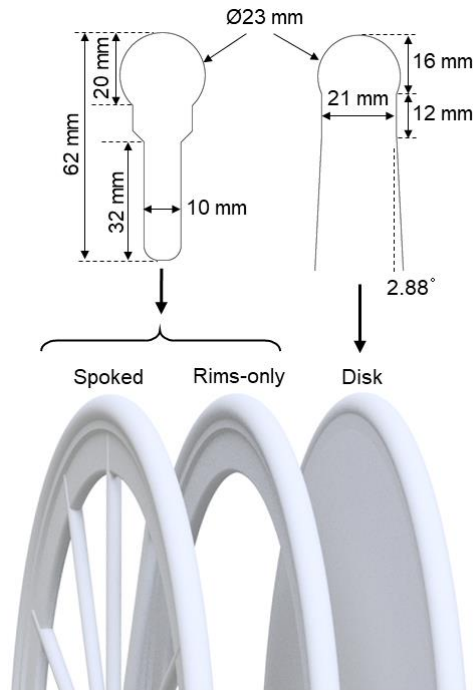


Figure 7.6. Rim profiles for the three wheel geometries with dimensions.

7.4.2 Aerodynamics investigations

In addition to the drag area comparison, the pressure coefficient was also used in the analysis of hand-cycling aerodynamics as a target parameter:

$$C_P = \frac{\Delta P}{0.5\rho V^2} \quad (7.4)$$

where ΔP is the difference of pressure [Pa] between the undisturbed flow at the inlet and at the point of interest in the fluid domain.

Figure 7.7b shows that the hand-cycle with disk wheels provided the most aerodynamic geometry overall, with a C_{DA} of 0.135 m^2 . The drag are experienced by the hand-cycles with rims-only and spoked wheel geometries were 0.141 m^2 and 0.158 m^2 , respectively.

The drag break-down in Figure 7.7c shows that the hand-cycle frame experienced a larger drag force than the athlete for all three wheel configurations (Figure 7.7c). However, the athlete and hand-cycle frame together experienced a larger drag force when using disk wheels than the spoked and rims-only wheel geometries, even though the configuration with the disk wheels produces the lowest overall drag. Further investigation revealed that the left and right disk wheels attached to the rear of the hand-cycle produced an under-pressure region in-between the wheels, generating

additional suction drag on the frame components and athlete in proximity to this region. Figure 7.8a-b illustrates the pressure coefficient contours in a vertical plane normal to the flow direction for the hand-cycle geometries with spoked and disk wheels. The vertical plane was located 1.4 m from the axis of the front wheel (Figure 7.8c); 0.125 m from the axis of the rear wheel. Note that the hand-cycle geometry is not symmetric, due to gear and brake levers, a non-symmetric gear cowl (protective covering), and a non-symmetric athlete position on the hand-cycle. A larger under-pressure region was found between the disk wheels, than the spoked wheels (Figure 7.8b). The differences between utilising the spoked and disk wheel geometries are also highlighted by pressure coefficient contours on the surface of the hand-cycle geometry, where again, an extensive under-pressure region was found on the on the hand-cycle frame and athlete arms when disk wheels were used.

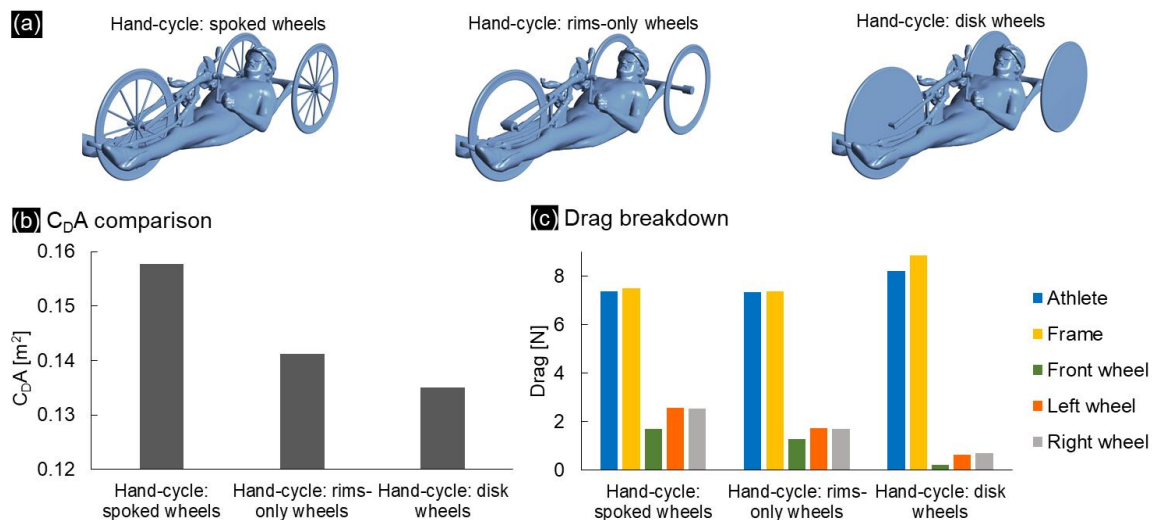


Figure 7.7. (a) Hand-cycle geometries with the wheel variations tested in this study. (b) A comparison of $C_D A$ predictions from the CFD simulations, (c) a breakdown of the drag forces from the CFD simulations.

The pressure coefficient at point P (Figure 7.8a-b) for the spoked (P_1) and disk (P_2) wheel setups respectively were used to determine the differences in pressure coefficient values in the wake of the hand-cyclist. The pressure coefficients at P_1 and P_2 were -0.18 and -0.25, respectively, with P_2 experiencing a pressure coefficient 38.8% higher than P_1 . The difference between the pressure coefficient contours in Figures 7.8a and 7.8b are illustrated in Figure 7.8c. In addition, the volume flow rate was measured through the boundary between the rear wheels of the spoked wheel and disk wheel setups, as illustrated in Figure 7.8c. A flow rate of $3.39 \text{ m}^3/\text{s}$ was found for the spoked wheel setup, and a flow rate of $3.61 \text{ m}^3/\text{s}$ for the disk wheel setup, indicating a channelling effect of the flow between the two rear disk wheels. These differences in the under-pressure region behind the hand-cyclist, coupled with the difference in volume flow rate for the rear wheels, and the drag increase

found on the athlete and hand-cycle frame, indicate that using the disk wheel type for the left and right rear wheels of a hand-cycle can negatively impact the drag of the hand-cycle frame and the athlete. However, the effect is expected to have a dependency on wheel diameter, proximity between the two rear wheels, and perhaps on rotational velocity. In addition, the negative drag effect measured in this study from utilising disk wheels was outweighed by the low drag experienced by the wheels themselves by comparison to spoked wheels.

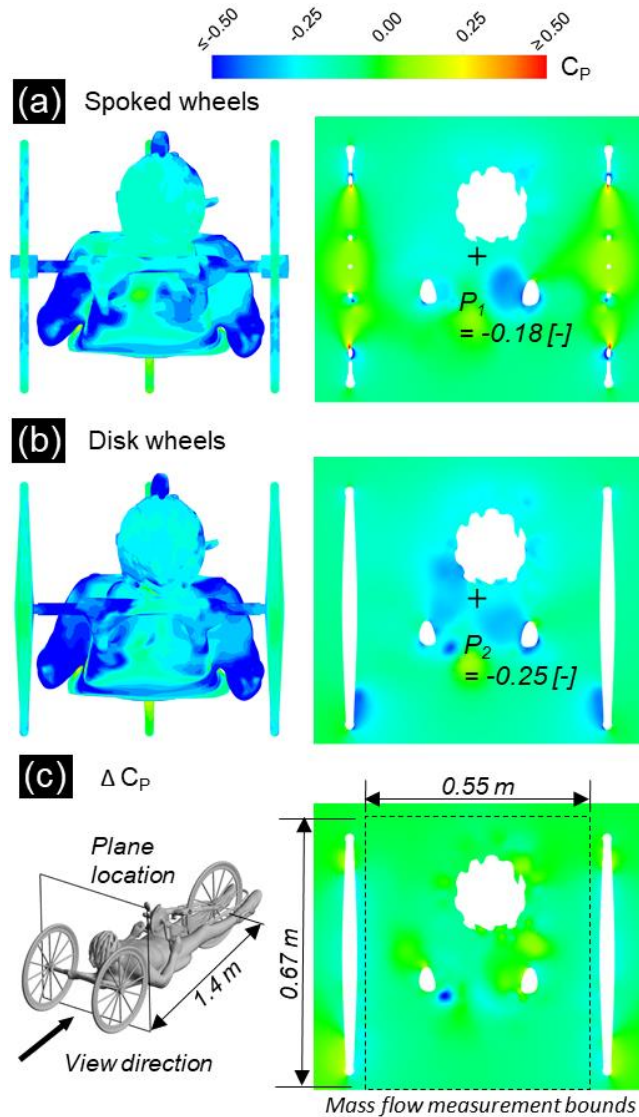


Figure 7.8. Pressure coefficient contours presented in a vertical plane and on the rear of the hand-cycle geometry for a hand-cycle with (a) spoked wheels, and (b) disk wheels. The difference in pressure coefficient contours on the vertical plane is illustrated in part (c). $\Delta C_p < 0$ indicates where the under-pressure for the disk wheel setup has a higher absolute value than the spoked wheel setup.

7.4.3 Impact of wheel diameter

Hand-cycling supports the use of a large variety of wheel sizes. Common wheel diameters include 26-inch (660.4 mm) and 20-inch (508 mm) wheels. Imperial units are used as per the bicycle wheel industry convention. Varying the wheel size on a hand-cycle can have far larger consequences aerodynamically than in conventional cycling. Firstly, there are the aerodynamics of three wheels to consider (as opposed to two), where the two rear wheels are parallel to each other. Cambered rear wheels are also possible, but are not addressed in this study. Furthermore, the variation in wheel diameters impacts the distance between the ground surface and the underside of the hand-cycle geometry. Moreover, it is allowable within the UCI rules for a hand-cycle to have wheels of different diameters on the front and rear axles, which alters the pitch angle of the frame and athlete. This study investigated the impact of two wheel diameter variations on hand-cycle aerodynamics. As a consequence, the effect of adjusting distance between the hand-cycle frame and the ground surface is also investigated along with the pitch angle of the hand-cycle frame and athlete.

Two wheel sizes were included in this study; 26-inch and 20-inch diameter wheels. Both wheel geometries are designed to be closely representative of the wheels from the hand-cycle geometry used in the wind tunnel experiments, with diameter 0.012 m spokes and constant tyre thickness, rim depth and hub size for both wheel sizes. The variation between the wheels sizes was in diameter only. All wheels within this study were static with no rotation modelled. The pitch angle of the hand-cycle frame and athlete was altered by $\pm 2.9^\circ$ from the horizontal plane by combining 20-inch and 26-inch wheels on the front or rear of the hand-cycle, respectively. For naming convention, the combination of wheels on the hand-cycle will be discussed as “front wheel diameter”-“rear wheel diameter” with units of inches, where 26-20 stands for one 26-inch diameter wheel attached to the front axle and two 20-inch diameter wheels to the rear axle. Figure 7.9a displays the four hand-cycle geometry variations with the 26-inch and 20-inch diameter wheels. The resulting C_{DA} for each setup is provided in Figure 7.9b with a contour of the normalised velocity field through a vertical centre plane. The lowest C_{DA} of 0.144 m^2 was found for the 20-20, followed closely by the 26-20 setup at 0.147 m^2 . The highest C_{DA} was found for the 20-26 setup with a value of 0.162 m^2 ; 2.5% higher than the 26-26 setup.

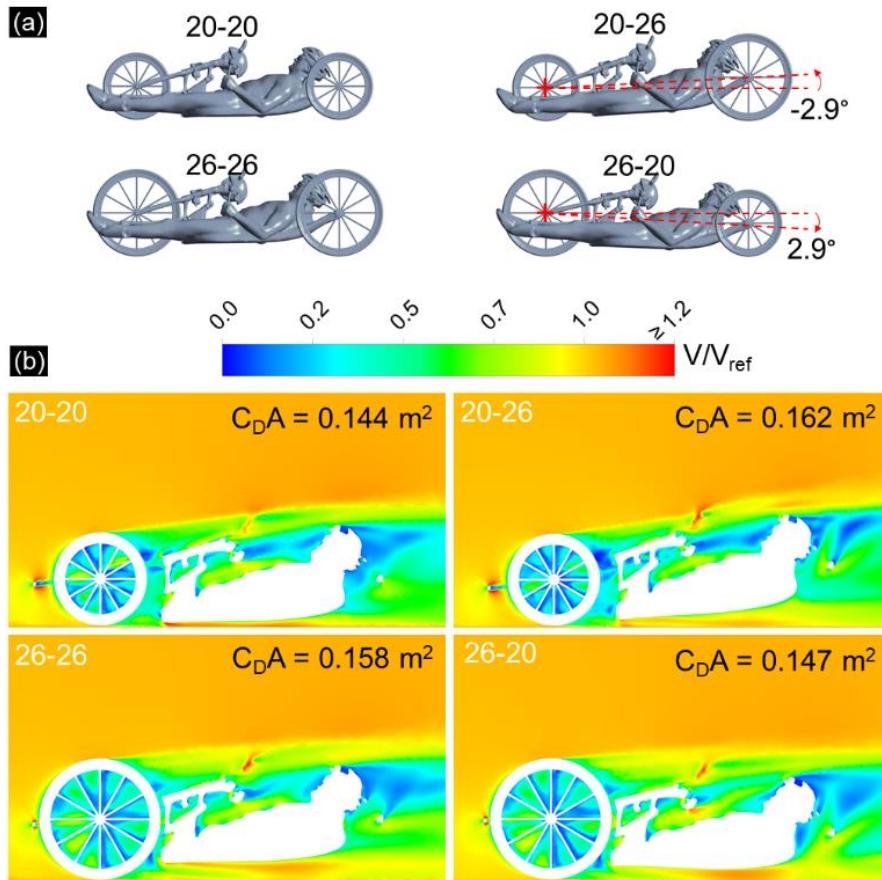


Figure 7.9. (a) Each hand-cycle variation with different wheel diameters, and (b) normalised velocity contours in a vertical centre-plane are presented for each hand-cycle geometry.

The drag force on each of the three wheels played a role in determining the $C_D A$ for each setup. Figure 7.10a illustrates the drag experienced by each wheel for all four setups. The asymmetry of the athlete who was inclined to one side, along with the asymmetry of the gear cowl, and brake levers (among some of the hand-cycle frame parts) contributed to the asymmetry of the drag experienced by the two rear wheels (Figure 7.10a). The cumulative drag of all three wheels (one front and two rear) for each setup followed an intuitive trend from lowest drag to highest as a function of wheel size; 20-20, 26-20, 20-26, and 26-26 (Figure 7.10b). However, the drag experienced by the hand-cycle frame and the athlete was influenced by the pitch angle of the hand-cycle along with the proximity to the ground surface. Figure 7.10b illustrates the drag experienced by the athlete and hand-cycle frame geometries combined. For the 20-20 setup, the resulting drag on the athlete and frame increased by 0.9% in comparison to the drag experienced by the same components for the 26-26 setup, maintaining the same pitch angle. This suggests that the increased proximity to the ground surface could have a limited negative effect on the aerodynamic drag of the athlete and frame. However, the increase in drag force (0.9%) for the athlete and frame surfaces between the 26-26 and

20-20 wheel setups was offset by the reduction in drag experienced by the 20-inch wheels themselves by comparison to the 26-inch wheels (Figure 7.10a).

Large drag differences were found by adjusting the pitch angle from 0° (all wheels of same diameter) to -2.9° for the 20-26 setup. The drag on the athlete and frame combined increased by 7.6% by comparison to the 20-20 setup, and 6.7% by comparison to the 26-26 setup. The alternate wheel combination of having a 26-inch wheel on the front and 20-inch wheels on the rear (26-20 setup) did not have the same effect on the drag of the athlete and frame, with an increase of 0.2% from the 26-26 setup (0° pitch). The benefit of reduced drag experienced by the rear 20-inch wheels for the 26-20 setup outweighed the negative drag effects on the athlete and frame and thus the 26-20 combination produces 7.0% less drag than the 26-26 setup. In contrast, the front wheel of the 20-26 setup did not provide enough of a drag reduction by comparison to an equivalent 26-inch wheel to outweigh the negative drag effects presented by altering the pitch angle of the hand-cycle.

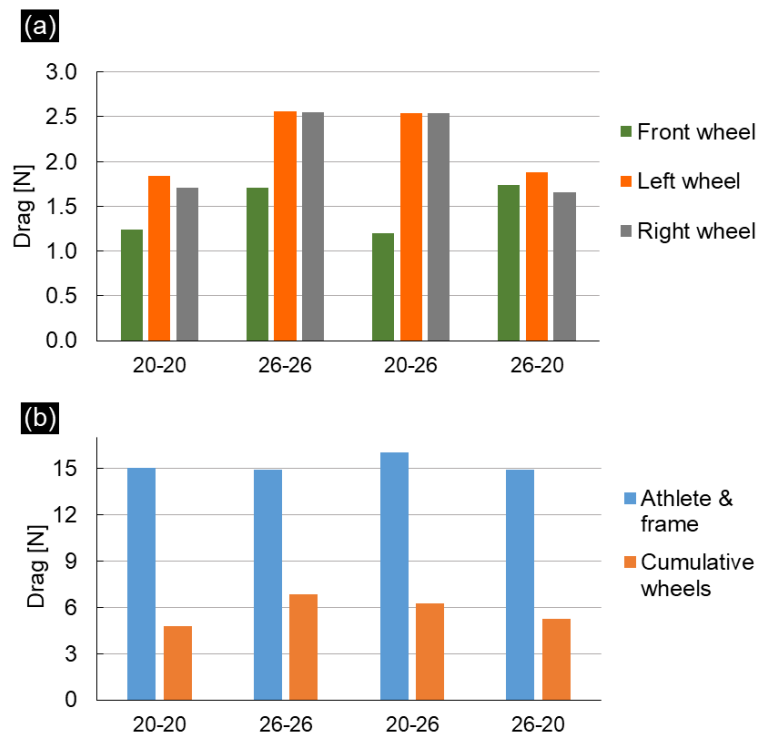


Figure 7.10. (a) Comparison of individual wheel drag forces and, (b) c comparison of drag experienced by the athlete and frame geometries combined, and cumulative drag on all three wheels of the hand-cycle.

7.5 Discussion

Turbulence model sensitivity analysis for the hand-cycle geometry revealed that a range of turbulence models, SST $k-\omega$, T-SST, $k-kl-\omega$ and Spalart-Allmaras, provide fairly accurate results with $< 5\%$ deviation from wind tunnel experiments. A suitable low y^* grid was used for this comparison. The standard $k-\varepsilon$ turbulence model has been found to provide accurate drag predictions in the literature for traditional cyclists (Blocken & Toparlar, 2015; Blocken et al., 2016; Fintelman et al., 2015); however, the ω based turbulence models provided more accurate aerodynamic force predictions for hand-cycling in the present study. Mannion et al. (2018) and Defraeye et al. (2010) also found that the SST $k-\omega$ turbulence model provided good drag predictions for tandem cycling and traditional able-bodied cycling respectively, with drag deviations $< 5\%$. However, it is noted that the hand-cycling geometry did not experience the same sensitivity to turbulence model choice as seen for traditional able-bodied cycling (Defraeye et al., 2010) and Paralympic tandem cycling (Mannion et al., 2018), where deviations in excess of 20% were reported in both studies depending on turbulence model choice.

C_{DA} values of 0.158 m^2 and 0.135 m^2 were found for the spoked wheel and disk wheel hand-cycle geometries respectively, both using 26-inch diameter wheels. An additional simulation was conducted with the simplified spokes removed from the wheel geometry, leaving only the tyre, rims and hub to represent the wheels, denoted as the rims-only geometry, which yielded a C_{DA} of 0.141 m^2 . Disk wheels were found to have a negative impact on the aerodynamics of the athlete and hand-cycle frame, from air channelled between the two parallel rear wheels and a subsequent low-pressure region between the wheels. However, the disk wheels themselves experiencing a lower drag than their spoked counterparts, leading overall lower drag values for the entire setup. The influence of rotating wheels, spoked, disk or otherwise, on the pressure field behind the hand-cyclist is yet unknown. It might be possible that deep rim wheels or tri-spoke wheels attached to the rear of the hand-cycle provide more favourable aerodynamic conditions than disk wheels, or that disk wheels with smaller diameters than those tested in this study may have a reduced impact on the drag of the athlete and hand-cycle frame. Indeed, there is scope for new innovations in wheel designs unique to the sport of hand-cycling. Furthermore, it was found that the hand-cycle frame experienced more drag than the athlete for the spoked wheel, rims-only and disk wheel setups (Figure 7.6c), indicating that the hand-cycle frame may be a key area to focus on for aerodynamics optimisation together with an appropriate wheel selection.

It is recommended that wheel rotation is modelled using sliding grid interfaces in future research regarding hand-cycle aerodynamics with spoked wheel designs. The wind tunnel experiments by Belloli et al. (2014) predicted a C_{DA} range for a H1-H4 hand-cyclist using spoked

wheels in the region of 0.20 m^2 (rotating wheels and static arms – no pedalling) and 0.21 m^2 (rotating wheels and dynamic arms) respectively. It must be noted however that in addition to the rotating wheels and athlete arm movement in the research by Belloli et al. (2014) there were further differences in helmets, hand-cycle design, and the position of the athlete on the hand-cycle, which may have led to higher C_{DA} values compared to the ones reported in the present study.

This study found that attaching smaller diameter wheels (20-20, opposed to 26-26) lowered the C_{DA} of the hand-cyclist, primarily because of the lower drag experienced by the wheels themselves (Figure 7.10a-b). An 8.9% drag reduction was found by switching from the 26-26 setup to the 20-20 setup. The 26-20 wheel selection was found to yield the second lowest C_{DA} (0.147 m^2), outperforming the 26-26 setup (0.158 m^2). However, the 20-26 setup yielded the highest C_{DA} of 0.162 m^2 with the negative pitch angle (Figure 7.9a) adversely affecting the drag of the athlete and hand-cycle frame (Figure 7.10b). It is noted that the rim depth of the wheels, tyre thickness, hub diameter, and the number and thickness of the spokes were kept constant throughout this study. For example, 20-inch spoked wheels with shallow rim depths might not have necessarily yielded any aerodynamic advantage over deep rim depth 26-inch wheels. There remains a large range of wheel types and sizes to be tested to fully understand which wheel selections are preferable for hand-cycle aerodynamics.

7.6 Conclusions

This study investigated the aerodynamics of a H1-H4 category hand-cyclist using CFD simulations and scaled wind tunnel experiments. Turbulence model and grid sensitivity studies alongside the experimental data from wind tunnel testing revealed a low sensitivity with ω based turbulence models, and that a low y^* grid would provide the most accurate predictions of hand-cycle aerodynamics. Validation studies were performed with CFD simulations using the same geometry used in the wind tunnel, and results in drag and lateral forces were found to be within the error range of the force transducers used in the experiments. A difference in drag of -1.4% was found for the magnitude of the drag and lateral force components between the wind tunnel and CFD results, when using the SST $k-\omega$ turbulence model. By comparison, the standard $k-\epsilon$ turbulence model under-predicted the drag force by -14.3%.

A C_{DA} of 0.158 m^2 was calculated for the hand-cycle geometries with 26-inch diameter spoked wheels. The removal of the simplified spokes reduced the C_{DA} to 0.141 m^2 , and a C_{DA} of 0.135 m^2 was calculated for a geometry with disk wheels (26-inch). It was found that wheel selection played a prominent role in the aerodynamics of hand-cycling. This was due to hand-cycles utilising 3 wheels instead of two to the proximity of the left and right wheels attached to the rear of the frame,

and the varying pitch angle of the frame and athlete though the use of differing wheel diameters on the front/rear of the hand-cycle. Utilising a 20-inch wheel on the front axle and 26-inch wheels on the rear (20-26 setup) was found to negatively impact the drag, by comparison to utilising three 26-inch wheels. Utilising a 26-inch wheel on the front axle and 20-inch wheels on the rear (26-20 setup) was found to provide an aerodynamic advantage over using three 26-inch wheels, but using three 20-inch wheels proved to yield the lowest C_{DA} for the spoked wheel combinations tested.

This study shows that there is a scope to modify/optimize existing hand-cycles for improved aerodynamic performance through wheel selection. In addition, it is recommended that a comprehensive analysis of commercial wheels is carried out in relation to hand-cycle aerodynamics, to determine the most suitable combination of wheel types and sizes. For example, disk wheels may not be the most suitable wheel type to be attached to the rear of a hand-cycle, due to the low-pressure region generated between the rear wheels. It was not determined in this research whether spoked wheels would be aerodynamically superior to disk wheels for the rear wheel selections, and this is advised for future research. It is possible that deep rim spoked wheels, bladed spokes, or tri-spoke wheels may be more advantageous aerodynamically than disk wheels for the hand-cycle rear wheel selection. In addition, smaller diameter 20-inch rear wheels may prove advantageous over 26-inch wheels in crosswind conditions. Furthermore, this study hints that there may be scope for new wheel designs that are unique to hand-cycling.

7.7 References

- ANSYS Fluent. (2015). ANSYS Fluent theory guide. *Release 16.1 Documentation*. ANSYS Inc.
- Artec Europe. (2017). Artec Eva, 3D Scanners. Retrieved May 22, 2017, from <https://www.artec3d.com/3d-scanner/artec-eva>
- Barlow, J. B., Rae, W. H., & Pope, A. (1999). *Low-speed Wind Tunnel Testing* (3rd ed.). John Wiley & Sons.
- Barry, N., Burton, D., Crouch, T., Sheridan, J., & Luescher, R. (2012). Effect of crosswinds and wheel selection on the aerodynamic behavior of a cyclist. In *9th Conference of the International Sports Engineering Association, Procedia Eng.* (Vol. 34, pp. 20–25). <http://doi.org/10.1016/j.proeng.2012.04.005>
- Belloli, M., Cheli, F., Bayati, I., Giappino, S., & Robustelli, F. (2014). Handbike aerodynamics: wind tunnel versus track tests. In *The 2014 conference of the International Sports Engineering*

Association, Procedia Eng. (Vol. 72, pp. 750–755). Elsevier B.V.
<http://doi.org/10.1016/j.proeng.2014.06.127>

- Blocken, B., & Toparlar, Y. (2015). A following car influences cyclist drag: CFD simulations and wind tunnel measurements. *Journal of Wind Engineering and Industrial Aerodynamics*, *145*(0), 178–186. <http://doi.org/10.1016/j.jweia.2015.06.015>
- Blocken, B., Toparlar, Y., & Andrienne, T. (2016). Aerodynamic benefit for a cyclist by a following motorcycle. *Journal of Wind Engineering and Industrial Aerodynamics*, *155*, 1–10. <http://doi.org/https://doi.org/10.1016/j.jweia.2016.04.008>
- Blocken, B., van Druenen, T., Toparlar, Y., Malizia, F., Mannion, P., Andrienne, T., Marchal, T., Maas, G.J., Diepens, J. (2018). Aerodynamic drag in cycling pelotons: New insights by CFD simulation and wind tunnel testing. *Journal of Wind Engineering and Industrial Aerodynamics*, *179*(May), 319–337. <http://doi.org/10.1016/J.JWEIA.2018.06.011>
- Casey, M., & Wintergerste, T. (2000). Best Practice Guidelines. *ERCOFTAC Special Interest Group on “Quality and Trust in Industrial CFD.”* ERCOFTAC.
- Choudhury, D. (1993). Introduction to the renormalization group method and turbulence modeling. Fluent Inc. Technical Memorandum TM-107.
- Crouch, T. N., Burton, D., LaBry, Z. A., & Blair, K. B. (2017). Riding against the wind: a review of competition cycling aerodynamics. *Sports Engineering*, *20*(2), 81–110. <http://doi.org/10.1007/s12283-017-0234-1>
- Crouch, T. N., Burton, D., Thompson, M. C., Brown, N. A. T., & Sheridan, J. (2016). Dynamic leg-motion and its effect on the aerodynamic performance of cyclists. *Journal of Fluids and Structures*, *65*, 121–137. <http://doi.org/10.1016/j.jfluidstructs.2016.05.007>
- Defraeye, T., Blocken, B., Koninckx, E., Hespel, P., & Carmeliet, J. (2010). Computational fluid dynamics analysis of cyclist aerodynamics: Performance of different turbulence-modelling and boundary-layer modelling approaches. *Journal of Biomechanics*, *43*(12), 2281–2287. <http://doi.org/10.1016/j.jbiomech.2010.04.038>
- Dyer, B. (2015). The importance of aerodynamics for prosthetic limb design used by competitive cyclists with an amputation: An introduction. *Prosthetics and Orthotics International*, *39* (3), 232–237. <http://doi.org/10.1177/0309364614527121>
- Fintelman, D. M., Hemida, H., Sterling, M., & Li, F.-X. (2015). CFD simulations of the flow around a cyclist subjected to crosswinds. *Journal of Wind Engineering and Industrial*

Aerodynamics, 144, 31–41. <http://doi.org/10.1016/j.jweia.2015.05.009>

- Fintelman, D. M., Sterling, M., Hemida, H., & Li, F.-X. (2014). Optimal cycling time trial position models: Aerodynamics versus power output and metabolic energy. *Journal of Biomechanics*, 47(8), 1894–1898. <http://doi.org/10.1016/j.jbiomech.2014.02.029>
- Franke, J., Hellsten, A., Schlünzen, H., & Carissimo, B. (2007). Best practice guideline for the CFD simulation of flows in the urban environment. *COST Action 732: Quality Assurance and Improvement of Microscale Meteorological Models*. Hamburg Germany.
- Godo, M., Corson, D., & Legensky, S. (2009). An aerodynamic study of bicycle wheel performance using CFD. In *47th AIAA Aerospace Sciences Annual Meeting*. Orlando, Florida: AIAA. <http://doi.org/10.2514/6.2009-322>
- Godo, M., Corson, D., & Legensky, S. (2010). A comparative aerodynamic study of commercial bicycle wheels using CFD. *48th AIAA Aerospace Sciences Meeting*, (2010–1431).
- Griffith, M. D., Crouch, T., Thompson, M. C., Burton, D., & Sheridan, J. (2014). Computational fluid dynamics study of the effect of leg Position on cyclist aerodynamic drag. *The American Society of Mechanical Engineers, Journal of Fluids Engineering*, 136. <http://doi.org/10.1115/1.4027428>
- Hart, J. H. (2006). The use of CFD in the chase of Olympic gold . *Sports Engineering*, 1–11.
- Jones, W. P., & Launder, B. E. (1972). The prediction of laminarization with a two-equation model of turbulence. *International Journal of Heat and Mass Transfer*, 15(2), 301–314. [http://doi.org/10.1016/0017-9310\(72\)90076-2](http://doi.org/10.1016/0017-9310(72)90076-2)
- Keogh, J. W. L. (2011). Paralympic sport: An emerging area for research and consultancy in sports biomechanics. *Sports Biomechanics*, 10(3), 234–253. <http://doi.org/10.1080/14763141.2011.592341>
- Lukes, R. a, Chin, S. B., & Haake, S. J. (2005). The understanding and development of cycling aerodynamics. *Sports Engineering*, 8, 59–74. <http://doi.org/10.1007/BF02844004>
- Mannion, P., Toparlar, Y., Blocken, B., Clifford, E., Andrienne, T., & Hajdukiewicz, M. (2018a). Aerodynamic drag in competitive tandem para-cycling: road race versus time-trial positions. *Journal of Wind Engineering & Industrial Aerodynamics*, 179, 92–101. <http://doi.org/10.1016/j.jweia.2018.05.011>
- Mannion, P., Toparlar, Y., Blocken, B., Hajdukiewicz, M., Andrienne, T., & Clifford, E. (2018b). Improving CFD prediction of drag on Paralympic tandem athletes: Influence of grid resolution

- and turbulence model. *Sports Engineering*, 21(2), 123–135. <http://doi.org/10.1007/s12283-017-0258-6>
- Menter, F. R. (1994). Two-equation eddy-viscosity turbulence models for engineering applications. *AIAA Journal*, 32(8), 1598–1605. <http://doi.org/10.2514/3.12149>
- Menter, F. R., Langtry, R. B., Likki, S. R., Suzen, Y. B., Huang, P. G., & Völker, S. (2004). A correlation-based transition model using local variables—Part I: model formulation. *Journal of Turbomachinery*, 128(3), 413–422. Retrieved from <http://dx.doi.org/10.1115/1.2184352>
- Pogni, M., Petrone, N., Antonello, M., & Gobbato, P. (2015). Comparison of the aerodynamic performance of four racing bicycle wheels by means of CFD calculations. *Procedia Engineering*, 112, 418–423. <http://doi.org/10.1016/j.proeng.2015.07.218>
- Spalart, P., & Allmaras, S. (1992). A one-equation turbulence model for aerodynamic flows. In *30th Aerospace Sciences Meeting and Exhibit*. American Institute of Aeronautics and Astronautics. <http://doi.org/http://doi.org/doi:10.2514/6.1992-439>
- Tew, G. S., & Sayers, a. T. (1999). Aerodynamics of yawed racing cycle wheels. *Journal of Wind Engineering and Industrial Aerodynamics*, 82(1), 209–222. [http://doi.org/10.1016/S0167-6105\(99\)00034-3](http://doi.org/10.1016/S0167-6105(99)00034-3)
- Tominaga, Y., Mochida, A., Yoshie, R., Kataoka, H., Nozu, T., Yoshikawa, M., & Shirasawa, T. (2008). AIJ guidelines for practical applications of CFD to pedestrian wind environment around buildings. *Journal of Wind Engineering and Industrial Aerodynamics*, 96(10–11), 1749–1761. <http://doi.org/10.1016/j.jweia.2008.02.058>
- UCI. (2017). Cycling Regulations, Part 16 Para-Cycling, version on 01/02/2017. Union Cycliste Internationale. Retrieved from http://www.uci.ch/mm/Document/News/Rulesandregulation/16/26/73/16-PAR-20170201-E_English.PDF
- Walters, D. K., & Cokljat, D. (2008). A three-equation eddy-viscosity model for Reynolds-Averaged Navier–Stokes simulations of transitional flow. *Journal of Fluids Engineering*, 130(12), 121401. <http://doi.org/10.1115/1.2979230>
- Wolfshtein, M. (1969). The velocity and temperature distribution in one-dimensional flow with turbulence augmentation and pressure gradient. *International Journal of Heat and Mass Transfer*, 12, 301–318. [http://doi.org/10.1016/0017-9310\(69\)90012-X](http://doi.org/10.1016/0017-9310(69)90012-X)

Analysis of crosswind aerodynamics for competitive hand-cycling

The aim of this chapter was to investigate hand-cycle aerodynamics under crosswind conditions. Grid parameters were based off the results of Chapter 7. Wind tunnel experiments informed validation studies to select a suitable turbulence model for crosswind analyses. Crosswind aerodynamics were explored for two full-scale hand-cycle setups after the validation studies; for TT and road race events.

This study has been published in the international peer-reviewed *Journal of Wind Engineering and Industrial Aerodynamics*:

Mannion, P., Toparlar, Y., Blocken, B., Clifford, E., Andrianne, T., & Hajdukiewicz, M. (2018). Analysis of crosswind aerodynamics for competitive hand-cycling. *Journal of Wind Engineering and Industrial Aerodynamics*. 180, 182–190.
<https://doi.org/10.1016/j.jweia.2018.08.002>

Abstract: Competitive hand-cycling represents a unique case for cycling aerodynamics as the athletes are in a relatively aerodynamic position in comparison to traditional able-bodied cyclists. There are some aerodynamic similarities between both cycling disciplines, including wheel designs and helmets. The lack of research in hand-cycling aerodynamics presents the potential for significant improvements. This research analysed the aerodynamics of competitive hand-cycling under crosswind conditions using wind tunnel experiments and Computational Fluid Dynamics (CFD) simulations. A range of yaw angles from 0°-20° in 5° increments were investigated for two separate hand-cycling setups, a road race and a time-trial setup. A maximum drag increase of 14.1% was found from 0° to 15° yaw, for a hand-cyclist equipped for a road race. The three disk wheels used for the TT setup had a large impact on the lateral forces experienced by the TT hand-cyclist. At just 5° yaw and at 15 m/s, the drag and lateral forces for the TT setup matched closely, while this event did not occur until 15° yaw at the same velocity for the road setup. For 20° yaw, the ratio of the side force to drag force was 1.6 and 5.6 for the road and TT setups respectively.

8.1 Introduction

Crosswinds can be a hindrance for cyclists across all cycling disciplines. Race tactics have been developed to counter crosswind effects, such as riding in staggered formations. In addition to the drag dependence on yaw angle, another important aspect in crosswind conditions is that disk wheels can affect stability and steering (Crouch et al., 2017; Tew and Sayers, 1999). Contrary to aerofoil aerodynamics, the drag experienced by a cyclist is measured in the direction the cyclist is travelling as opposed to the stream-wise flow direction (Barry et al., 2012; Fintelman et al., 2014; 2015a).

Aerodynamic refinement is commonly the subject of scientific investigations for improved performance in cycling (Haake, 2009), with cyclist postures having received significant attention in the literature (Defraeye et al., 2010a; Fintelman et al., 2015b; García-López et al., 2008). However, crosswind analysis of able-bodied traditional cyclists has seen limited attention in the literature, even though cyclists typically experience a crosswind to some degree in all outdoor events. Concerning traditional cycling, Fintelman et al. (2015a) performed Computational Fluid Dynamics (CFD) simulations to analyse solo cycling aerodynamics under crosswind conditions, with validation data acquired from wind tunnel experiments described by Fintelman et al. (2014). It was found that Large-Eddy Simulation (LES), by comparison to the wind tunnel experiments, provided the best performance for drag prediction for 15° yaw with a deviation of 5%. Larger discrepancies were found by Fintelman et al. (2015a) between experimental and numerical results using other methods such as Detached Eddy Simulation (DES), with deviations from the experimental data of up to 17% between the drag forces at yaw angles of 15° .

The majority of the crosswind aerodynamics studies in cycling have focused on isolated wheel geometries (Barry et al., 2012; Godo et al., 2010; Tew and Sayers, 1999). Wind tunnel experiments were conducted by Tew and Sayers (1999) to compare a number of wheel selections over a variety of yaw angles (0° - 30°), wind speeds (30-55 km/h) and rotational velocities (corresponding to 0-55 km/h linear velocities). At 0° yaw, the drag by the disk wheel was 70% lower than for the standard spoked wheel. However, the standard thirty-six shallow rim spoke wheel had significantly lower lateral force coefficients than the other five wheels tested. The disk wheel experienced a reversal in the lateral force direction (perpendicular to the direction of motion) from negative to positive in the region of 0° - 8° yaw for all wind speeds, indicating a shift in the location of boundary layer separation. Godo et al. (2010) considered six isolated wheel geometries over 10 yaw angles at two velocities: 20 mph (32.19 km/h) and 30 mph (48.28 km/h). The disk wheel provided the greatest drag advantage, with the deep-section wheel in second place. However, both wheels experienced lateral forces in excess of all other wheels tested.

Wind tunnel testing and CFD simulations have been used extensively for cycling aerodynamics and other competitive sports topics (Blocken, 2014; Crouch et al., 2017). However, to the best of our knowledge, a detailed analysis of crosswind effects on hand-cycle aerodynamics by either CFD simulations or wind tunnel tests has not yet been published. Crosswinds can be important for performance and safety. This paper analyses the crosswind aerodynamics for a H3 category competitive hand-cyclist in a road race setup (Figure 8.1a,c) and time-trial setup (Figure 8.1b,d), which is relevant for categories H1-H4 due to the athlete positions adopted and the cycling equipment (UCI, 2017).

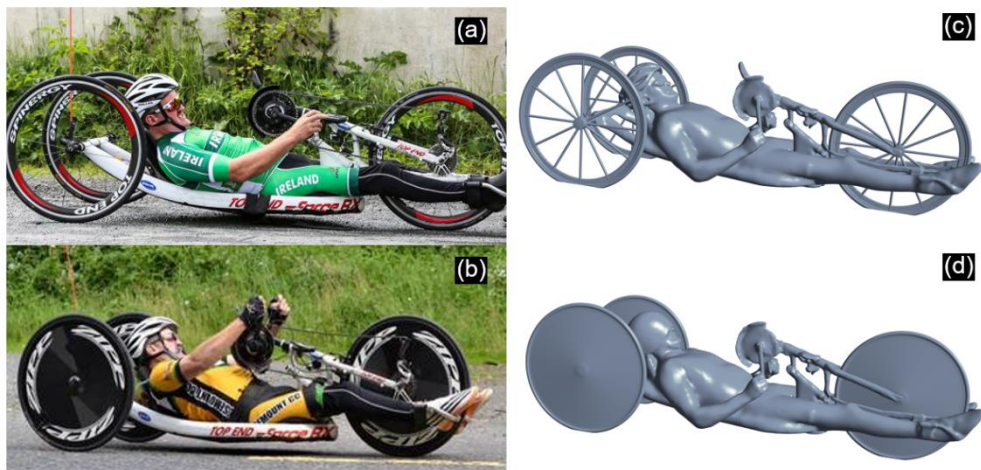


Figure 8.1. Photos of an Irish H3 category hand-cyclist with spoked wheels for a road race, and (b) disk wheels for a TT event. (Photos copyright of Sportfile, Cycling Ireland and Paralympics Ireland, reproduced with permission). Part (c) and (d) illustrate the geometries used for this study to represent (a) and (b) respectively.

8.2 Wind tunnel experiments

Wind tunnel experiments were carried out in the aeronautical test section of the wind tunnel laboratory at the University of Liège, Belgium, in a test chamber with cross-section dimensions 2 x 1.5 m². A H3 competitive hand-cyclist was 3D scanned to provide the geometrical data for manufacturing a quarter-scale model (Figure 8.2a). The blockage ratio reached 2.3% at the maximum yaw angle of 20°. The cyclist model was placed on a smooth horizontal platform with a sharp leading edge and raised 0.3 m from the test chamber floor to reduce the approach-flow boundary layer height (Figure 8.2b). A wind speed of 60 m/s was imposed for Reynolds number similarity with a full-scale hand-cyclist at 15 m/s. 3D solid blockage corrections from (Barlow et al., 1999) applicable for blockage ratios between 1-10% were applied using the short-form equation by Thorn (1943) with a

body shape value (K) of 0.96. A circular plate in the platform allowed yaw angle variation with five crosswind yaw angles investigated (-10° , 5° , 10° , 15° , 20°), in addition to the 0° experiment.

A six-axis Delta model force transducer (ATI, 2018) was attached to the hand-cycle model vertically in line with the model's centre of gravity (Figure 8.2b). The error range was ± 1.24 N at a 95% confidence interval. The error range was calculated from the calibration targets; 0.75% of the full-scale load. Force data were sampled for 180 seconds at a rate of 10 Hz after a 30 seconds settling period. Air temperature measurements inside the test chamber were used to correct force measurements to an air density at 15°C and 101325 Pa, ensuring consistency across all experimental data and CFD simulation results. Local meteorological data was used to correct for the atmospheric pressure at the date of the experiments. A pitot tube was used to measure the stream-wise air velocity, to correct the force measurements to the desired 60 m/s velocity, for all the yaw angles tested. Previous experiments for quarter-scale cyclist models in the same wind tunnel reported an approach-flow turbulence intensity below 0.2% (Blocken et al., 2016).

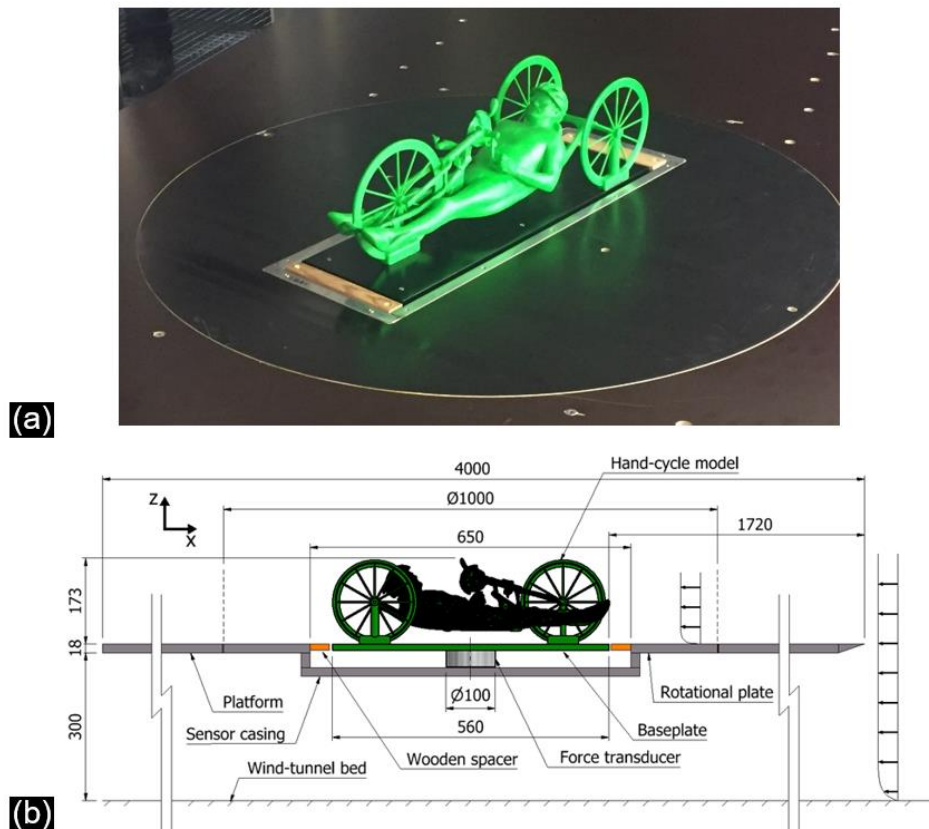


Figure 8.2. (a) Photo of manufactured model at 20° yaw in the wind tunnel. (b) Corresponding schematic of scaled hand-cycle model attached to transducer on rotational plate. Units are in mm.

8.3 CFD simulations

8.3.1 Computational domain and boundary conditions

For the CFD validation, the simulations were performed with the same geometrical model as in the wind tunnel experiments but in full scale, including all hand-cycle wheel supports, baseplate and platform surface in the CFD domain (Figure 8.3). The platform was included as a no-slip wall. This allowed for boundary layer development on the platform as in the wind tunnel experiments. A no-slip wall boundary condition with zero roughness was applied to the hand-cycle, supports, baseplate and platform surfaces. A cylindrical interface was used to rotate the hand-cycle geometry to the selected yaw angles. The computational domain and boundary conditions are shown in Figure 8.3. The max blockage ratio for the domain at 20° was below the 3% maximum recommended (Blocken, 2015; Franke et al., 2010; Tominaga et al., 2008). A velocity of 15 m/s was imposed for all the yaw angles tested. Viscosity was 1.789×10^{-5} kg/ms and density was 1.225 kg/m³. After the validation study, the wheel supports, baseplate and platform surface were removed from the CFD domain for more accurate predictions of hand-cycling aerodynamics, see section 8.4.2.

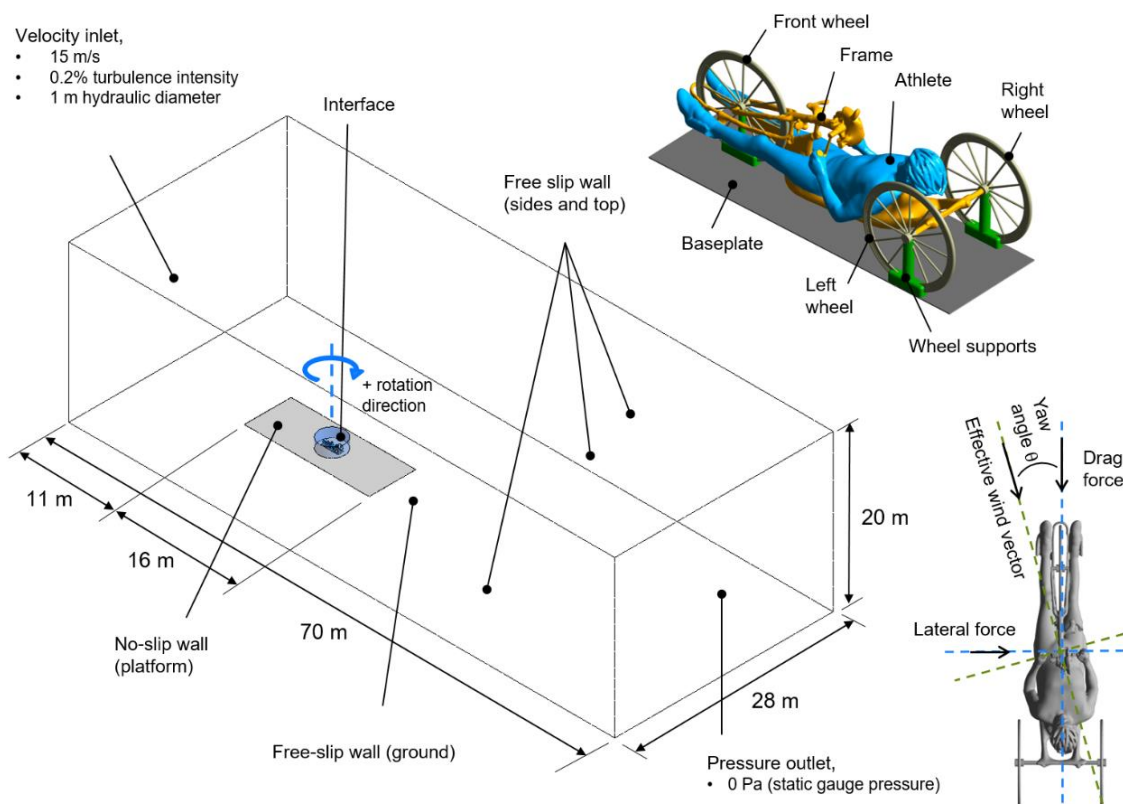


Figure 8.3. Computational domain, boundary conditions and breakdown of primary hand-cycle geometry components.

8.3.2 Solver settings

The commercial CFD code ANSYS Fluent 16 (ANSYS Fluent, 2015) was used to solve the 3D Reynolds-averaged Navier–Stokes (RANS) equations using two turbulence models for closure: the 1-equation Spalart-Allmaras model (Spalart and Allmaras, 1992) and the 2-equation Shear Stress Transport (SST) $k-\omega$ model (Menter, 1994). The pseudo-transient implicit under-relaxation method was used with a time-step of 0.01 s, using the Coupled algorithm for pressure-velocity coupling, and the Least Squares Cell Based method to compute gradients. Aerodynamic forces were averaged at every pseudo-time-step over a period of 4000 steps. Second-order discretisation schemes were used throughout along with second-order pressure interpolation. The maximum values for the scaled residuals were: 1×10^{-5} for continuity, 1×10^{-7} for momentum, 1×10^{-4} for turbulent kinetic energy, 1×10^{-4} for specific dissipation rate and 1×10^{-6} for turbulent eddy viscosity where the Spalart-Allmaras turbulence model was used.

8.3.3 Computational grid

A systematic grid sensitivity analysis of three grids named grids 1-3 (with 77.4, 27.3 and 10.4 million cells) was conducted on the hand-cycle geometry to determine the grid resolution for a fourth grid named grid 4 (25,721,804 cells) which balanced computational effort and accuracy. Grid Convergence Index (GCI) values of 0.29% and 1.29% were obtained for grids 1 and 2 respectively. Grid 4 contained a cylindrical interface to allow for the rotation of the hand-cycle geometry. The cell face size on the cylinder interface surfaces was fixed at 0.02 m, to ensure that interpolation error was kept to a minimum between the two face zones. Twenty prism layers were used in grid 4 with a first layer height of 2.5×10^{-5} m applied to the hand-cycle geometry, wheel supports and baseplate, yielding an average y^* value of 0.8. Five prism layers were applied to the platform surface. Note that y^* was used instead of y^+ , as recommended by Blocken & Toparlar (2015) for grids used in cycling studies. y^+ is defined as follows:

$$y^+ = \frac{u^+ y_P}{\nu} \quad (8.1)$$

where ν is the kinematic viscosity [m^2/s] and y_P [m] is the normal distance from the wall to the centre point P of the first cell. u^+ [m/s] is the friction velocity, defined by:

$$u^+ = \sqrt{\frac{\tau_w}{\rho}} \quad (8.2)$$

where ρ [kg/m³] is the density of the fluid in the wall bounded flow and τ_w [Pa] is the wall shear stress. On the other hand, y^* is defined as:

$$y^* = \frac{u^* y_P}{\nu} \quad (8.3)$$

where the friction velocity u^* [m/s] is defined as:

$$u^* = C_\mu^{\frac{1}{4}} k_P^{\frac{1}{2}} \quad (8.4)$$

where C_μ [-] is a model constant, and k_P [m²/s²] is turbulent kinetic energy at P.

While both definitions will often provide very similar values, y^* is used within this research instead of y^+ . As discussed by Blocken & Toparlak (2015), the formulation for y^* holds an advantage over y^+ for cycling aerodynamics applications. y^* does not go to zero if the shear stress (present in equation 8.2) is zero, such as in locations of flow stagnation and flow reattachment which occur in cycling aerodynamics. Therefore y^* , as opposed to y^+ , can be used to specify the grid requirements in these locations. The y^* distribution on the hand-cyclist is illustrated in Figure 8.4.

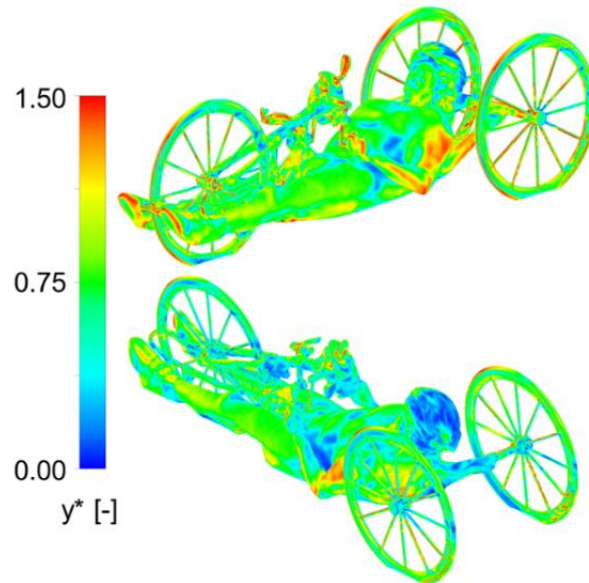


Figure 8.4. y^* distribution on hand-cyclist.

Grid 4 represented the hand-cycle geometry with the wheel support structures, baseplate, and platform surface from the wind tunnel experiments (Figure 8.5a), to provide good comparisons for validation purposes. However, it was desired to investigate the aerodynamics of hand-cycling without the influence of these components. Thus, using the same cell sizings, two additional grids were created, grid 5a and 5b, for a more accurate geometrical representation of hand-cycling without the structural wheel supports, baseplate, and platform surfaces. Grid 5a (28,189,933 cells) represented a

hand-cyclist in a road race setup similar to the geometry used in the wind tunnel experiment (Figure 8.5b). Grid 5b (11,013,008 cells) represented a TT setup, where disk wheels and a TT helmet were used. Fewer computational cells were required for the TT setup due to the replacement of the small geometric details from the three spoked wheels and detailed road helmet with disk wheels and a streamlined TT helmet respectively.

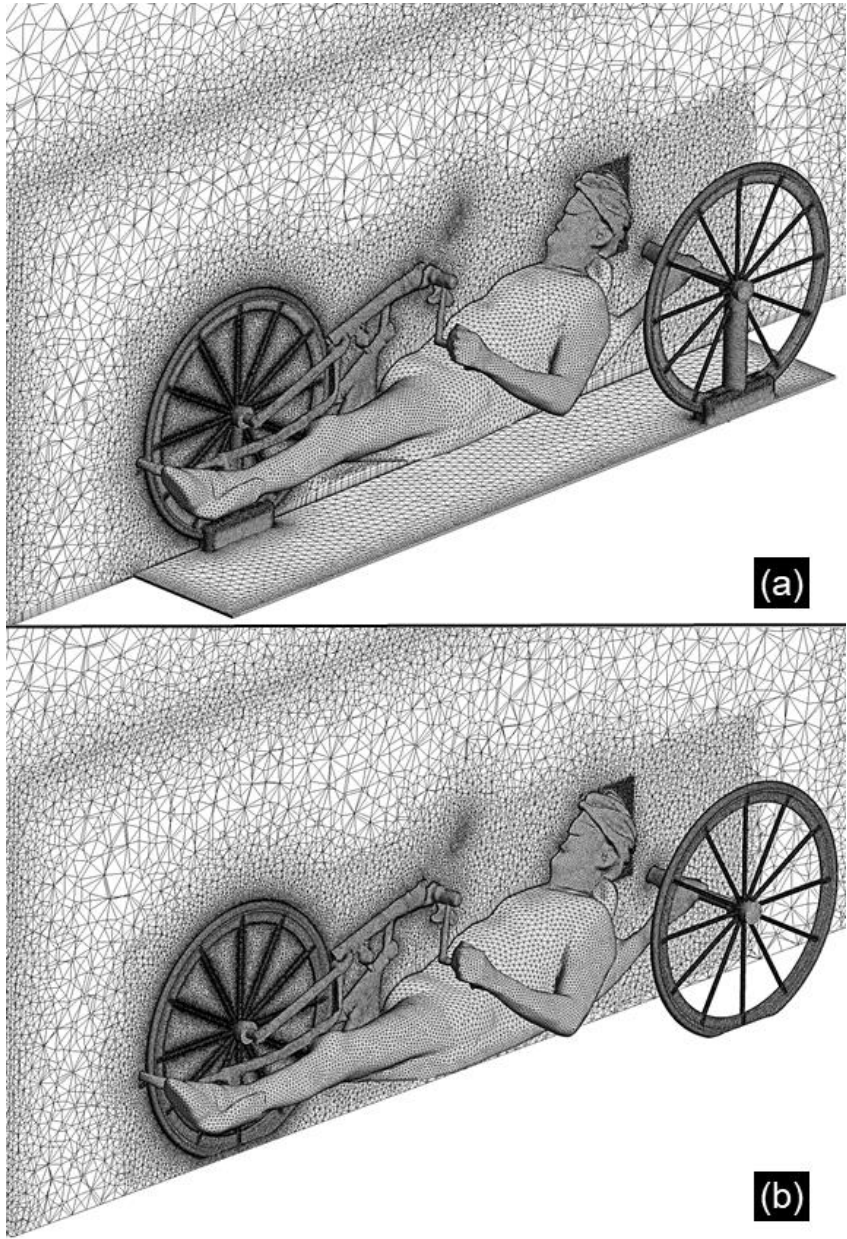


Figure 8.5. Part of the surface and volume grid for (a) grid 4, and (b) grid 5a. Total cell counts are 25,721,804 and 28,189,933, respectively.

8.4 Results

The target parameters were drag area, lateral force area and pressure coefficient. Note that the ‘lateral force area’ was defined as the lateral force normalised by the freestream dynamic pressure in analogy with the definition of the drag area. The frontal area was 0.261 m² for the TT setup and 0.247 m² for the road setup. The projected lateral area was 0.727 m² for the road setup and 0.987 m² for the TT setup. The drag area [m²] and lateral force area [m²] were calculated with the following:

$$C_D A_F = \frac{F_D}{0.5\rho V^2} \quad (8.5)$$

$$C_S A_S = \frac{F_S}{0.5\rho V^2} \quad (8.6)$$

where F_D is the drag force [N], F_S is the lateral force [N] where the letter ‘S’ refers to side or lateral, V is the free-stream velocity [m/s], ρ is the air density [kg/m³], A_F is the frontal area [m²] with reference to the drag axis (Figure 8.3), A_S is the side area [m²] with reference to the lateral force axis of the hand-cycle (Figure 8.3). The lateral force coefficient [-] was defined as:

$$C_S = \frac{F_S}{0.5\rho A_S V^2} \quad (8.7)$$

where it was used to normalise lateral force data in the form of $C_S A_F$. The pressure coefficient [-]:

$$C_P = \frac{\Delta P}{0.5\rho V^2} \quad (8.8)$$

where ΔP is the difference between local static pressure and upstream reference static pressure [Pa].

8.4.1 Validation study

The drag and lateral force data across the yaw angles tested (-10°, 0°, 5°, 10°, 15° and 20°) from the experimental results and numerical results utilising grid 4, are plotted in Figure 8.6a-b. Both the SST $k-\omega$ and Spalart-Allmaras turbulence models provided good agreement with the wind tunnel results. The root-mean-square (RMS) error was used as the performance indicator for both turbulence models against the wind tunnel experiments. The RMS error was calculated by:

$$RMS\ Error = \sqrt{\frac{\sum_{i=1}^n (F_{WT_i} - F_{CFD_i})^2}{n}} \quad (8.9)$$

where F_{WT} is the force [N] measured in the wind tunnel experiments, F_{CFD} is the force [N] prediction from the CFD simulations, and n is the number of yaw angles tested.

RMS errors were calculated separately for both the drag and lateral forces, from the yaw angles of -10°, 0°, 5°, 10°, 15° and 20°. Thus, an indicator was provided for the prediction of the drag and lateral forces individually for both turbulence models. RMS errors of 0.96 N and 1.48 N were

calculated for the predictions of drag and lateral forces for the SST $k-\omega$ model. The Spalart-Allmaras turbulence model drag and lateral force predictions resulted in RMS errors of 1.96 N and 1.56 N respectively. Both turbulence models provided satisfactory predictions. However, the SST $k-\omega$ turbulence model was chosen for further simulations because of its slightly better performance than the Spalart-Allmaras model, and due to its good performance in prior cycling studies reported in literature. Defraeye et al. (2010b) conducted a turbulence model sensitivity analysis for an able-bodied cyclist, and determined that the SST $k-\omega$ model provided the best overall performance, with drag and lift forces predicted within 4% and 11% respectively. A turbulence model sensitivity analysis was also conducted for tandem cycling by Mannion et al. (2018), who determined that the SST $k-\omega$ model was the most suitable for tandem cycling with drag deviations of 4.0% and 4.2% for the front and rear athletes respectively. For comparison, in this study the minimum and maximum drag deviations with the SST $k-\omega$ model were 1.4% and -5.4% at 0° and 10° yaw respectively.

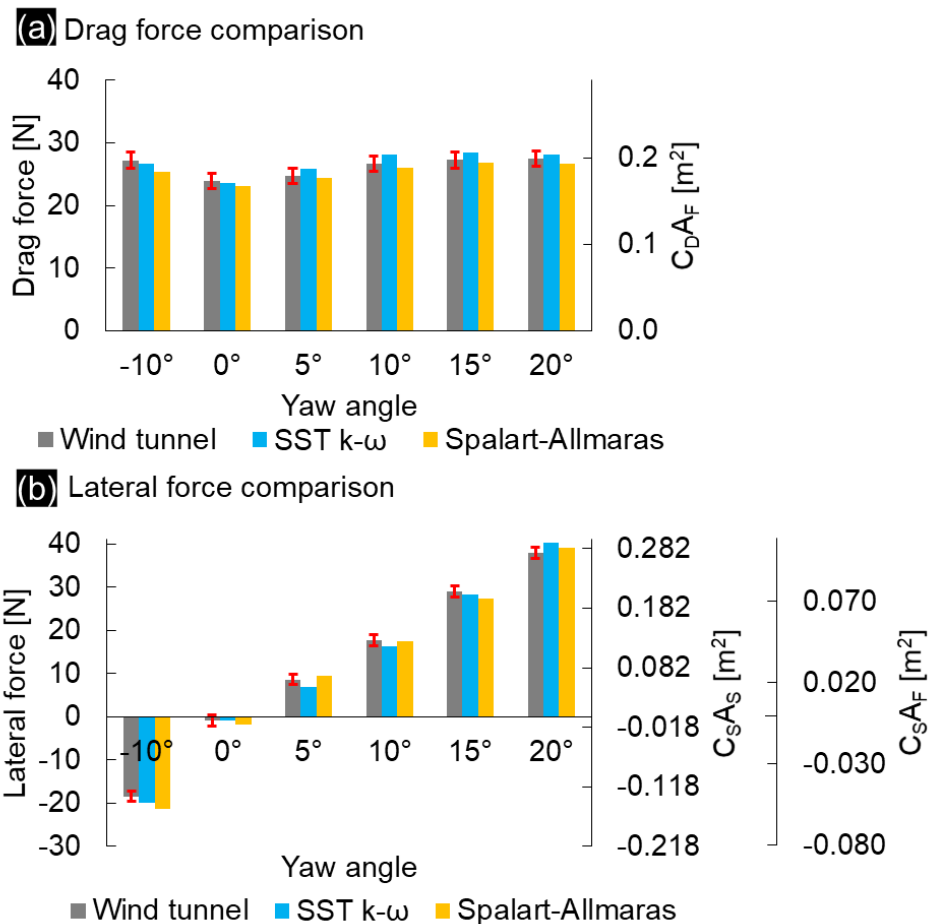


Figure 8.6. Experimental and numerical (a) drag, and (b) lateral forces for the hand-cyclist for investigated yaw angles. Error bars (± 1.24 N) of systematic and random errors combined within a 95% confidence interval are provided for the experimental results. Both force [N] and normalised force in C_{DAF} , C_{SAs} and C_{SAF} terms [m^2] are provided, where C_s [-] is defined in equation 8.7.

8.4.2 Crosswind aerodynamics

Following the validation study, the crosswind aerodynamics were further investigated by removing the supporting structures for the wheels, the baseplate and the platform. The SST $k-\omega$ turbulence model was used for closure as per the validation study in section 8.4.1. Crosswind effects at yaw angles of 0° , 5° , 10° , 15° and 20° were investigated for two hand-cycle setups; a road setup as per the validation study with spoked wheels and a standard helmet for the athlete (grid 5a), and a TT setup with disk wheels and an aero helmet for the athlete (grid 5b). The yaw angle of -10° was not investigated further due to the near symmetry between -10° and 10° (Figure 8.6), with differences of 2.1% between the wind tunnel predictions for the drag forces, and 3.8% for the lateral forces. The wheels were modelled as stationary within the CFD simulation. The resulting C_{DAF} [m^2] and C_{SA_S} [m^2] for both setups are provided in Figure 8.7a-b.

The drag experienced by the hand-cyclist increased with the change in yaw angle from 0° to 15° for the road setup, and from 0° to 5° for the TT setup; by 14.1% and 3.3% respectively. The TT hand-cyclist setup experienced a lesser increase in drag than the road setup counterpart under crosswind conditions. This was expected due to the influence of the disk wheels, as per the findings for disk and spoked wheels by Tew and Sayers (1999) and Godo et al. (2010) under yaw conditions. At 20° yaw, a drag reduction of 4.1% and 6.2% was found for the road and TT setups, compared to 15° yaw. A C_{DAF} of $0.1322 m^2$ was found at 5° and $0.1320 m^2$ at 10° yaw for the TT setup, indicating a stable drag region at this yaw range.

The reduction in drag at 20° compared to 15° found by the CFD simulations for the road setup was not replicated by the wind tunnel experiments, which had resulted in a 0.9% increase in drag between 15° - 20° . However, CFD simulations with the wheel supports, baseplate and platform surfaces included, yielded drag forces within the error range of the sensors used ($\pm 1.24 N$). It is possible that a reversal in drag propagation could have been found at higher yaw angles in the wind tunnel if they had been tested. In addition, the flow interference from the wheel supports might also have been a contributing factor to this finding.

The C_{SA_S} increased monotonically as the yaw angle increased. As the hand-cycle geometry was close to being symmetrical in the lateral plane, low C_{SA_S} values were observed at 0° yaw for the road and TT setups respectively (Figure 8.7b); 3.2% and 3.7% of the drag forces for each setup respectively at the same yaw angle. At 20° yaw, the TT setup experienced a lateral force 134.0% greater than the road setup, indicating potential impact to the stability of the hand-cyclists. This increase was due to the three disk wheels in the TT setup, which were the major geometrical differences between the road and TT setups.

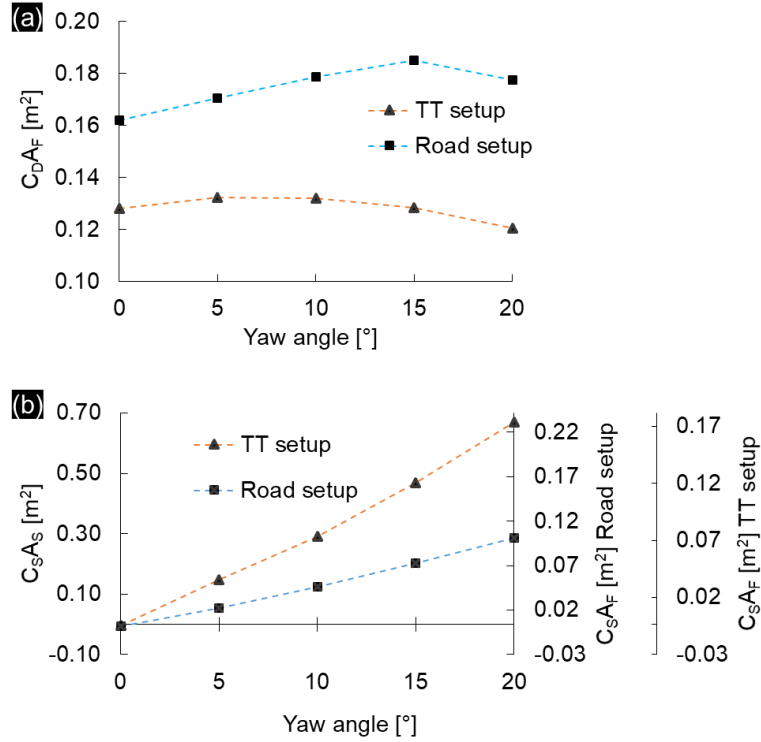


Figure 8.7. (a) Drag areas and (b) lateral force area for both the road and TT hand-cycle setups.

Roll and yaw moments were investigated to further determine the impact of aerodynamics on the stability of a hand-cyclist. The yaw moment was investigated about a vertical axis located at the centre between the front and rear wheels (Figure 8.8a), as defined by Crouch et al. (2017) for cycling applications. The roll moment was investigated about an axis on the ground plane intersecting the theoretical points of contact between the ground plane and the front and right (rear) wheels (Figure 8.8a). The roll and yaw moment coefficients [-] were defined as:

$$C_{M:R} = \frac{M_R}{0.5\rho A_F V^2 L} \quad (8.10)$$

$$C_{M:Y} = \frac{M_Y}{0.5\rho A_F V^2 L} \quad (8.11)$$

where M_R is the roll moment [Nm], M_Y is the yaw moment [Nm], and L is the length [m] between the front and rear wheels in the drag axis (Figure 8.3).

The trend for roll moment coefficient experienced by the road and TT setups (Figure 8.8b) followed the same trend as the lateral forces (Figure 8.7b), throughout the yaw range tested. Similar slopes for were found between the lateral force trends and the roll moment trends between 0°-20° yaw for the road and TT setups respectively, confirming the impact of high lateral forces from disk wheels on the hand-cyclist by comparison to spoked wheels. The variation in yaw moment as the yaw angle increased was smaller than the impact of increasing yaw angle on the roll moment (Figure 8.8b).

Again, the disk wheels for the TT setup contributed to an increase in yaw moment by comparison to the spoked wheels of the road setup. However, the absolute difference between the maximum yaw moment coefficients at 20° for the TT and road setups was less than half the difference in roll moment coefficients at the same yaw angle; differences of 0.172 [-] and 0.351 [-] respectively. It is not expected that that the increase in yaw moment due to the disk wheels would significantly influence the stability or the steering of the hand-cyclist. This is due to the additional friction provided by the two rear wheels of the hand-cycle, and due to the near-horizontal steering axis of the hand-cycle which limits the impact of the aerodynamic yaw moment on the steering of the front wheel by comparison to a traditional bicycle.

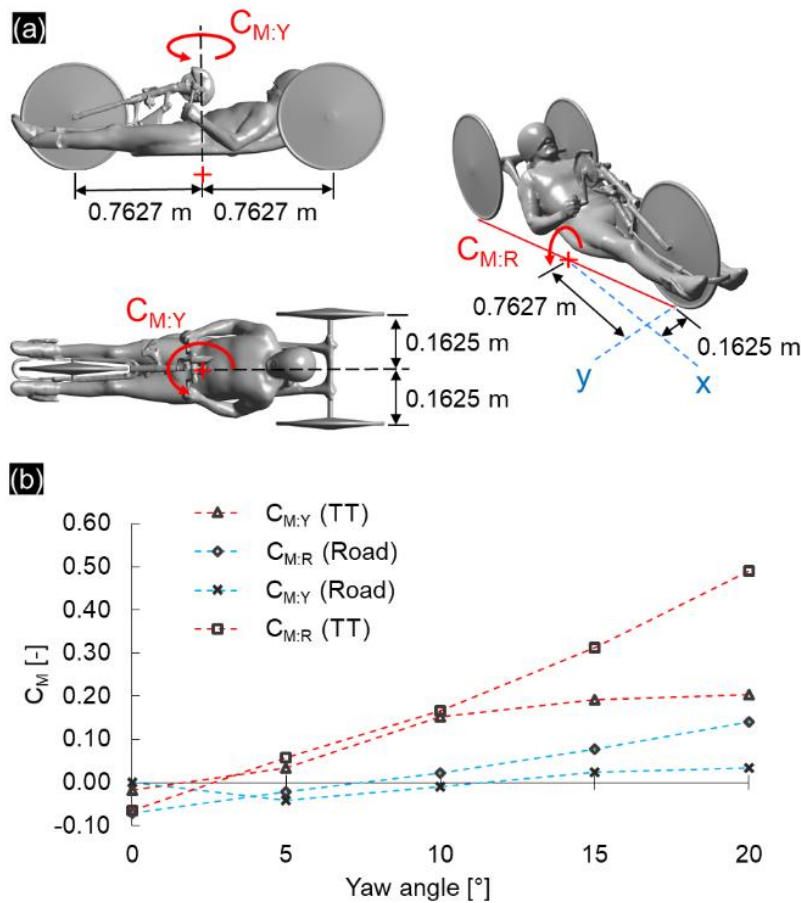


Figure 8.8. (a) Moment axes and locations defined. (b) Roll and yaw moment coefficients for the road and TT hand-cycling setups at different yaw angles.

Figure 8.9 provides further insight into the aerodynamics of the road and TT hand-cycle setups throughout the various yaw angles tested. The flow field is illustrated with streamlines, and with pressure coefficient contours on the surfaces of the athlete and hand-cycle. The impact of the disk wheels on the flow-field over the hand-cyclist is illustrated by the difference in streamlines for

the various yaw angles, which indicate the impact to the flow from the disk wheels (Figure 8.9b). This was not the case with the road setup for the hand-cycle, where the spoked wheels added some additional turbulence, but the direction of the flow was not impacted to the same degree as in the TT setup (Figure 8.9a). A larger pressure coefficient was experienced on the left leg of the athlete in the TT setup at 20° yaw, in comparison to the road setup at the same angle. This was due to the difference in wheel geometries for the road and TT setups. For the TT setup, the disk wheel at the front of the hand-cycle blocked the air from flowing through the open volume that would typically be present with spoked wheels (road setup), creating a larger pressure differential on both sides of the wheel at higher yaw angles, thus impacting the leg geometry at both sides of the wheel.

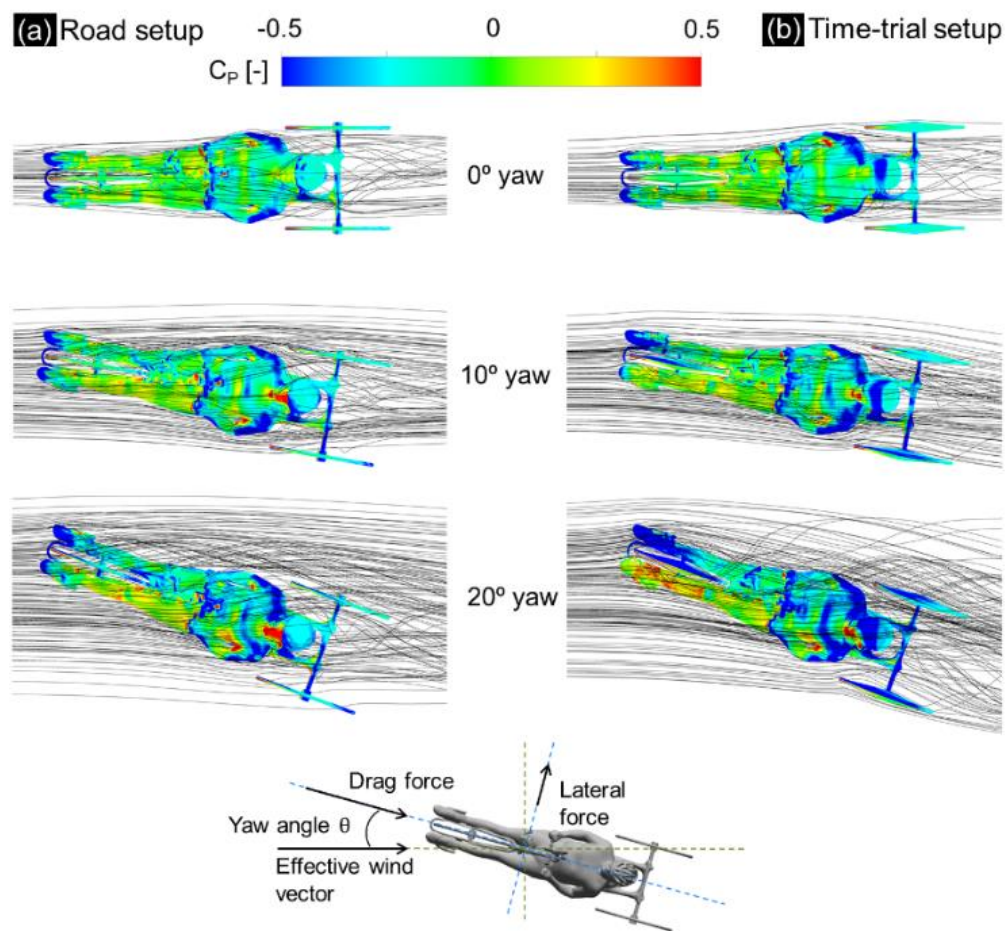


Figure 8.9. Pressure coefficient contours and streamlines at yaw angles of 0°, 10° and 20° for both the road setup and TT setup.

The yaw angle of 20° was investigated further, as illustrated in Figure 8.10a-b, with contours of the static pressure coefficient and the normalised velocity on a horizontal plane. The impact of the wheel geometry is illustrated in this comparison, with the flow passing through the open spoked wheel geometry, but diverted with solid disk wheel geometries. The direction of the wake flow from the TT

setup makes evident the redirection of the flow as a result of the disk wheels. Low pressure regions between the athlete and disk wheels (Figure 8.10a) resulted in high local velocities (Figure 8.10b). These high local velocities induced large suction, both downwind of the front disk wheel and downwind of the wind-exposed rear wheel, and downwind of the athletes' upper body. The pressure distributions on the disk and spoked wheel surfaces at 20° yaw are illustrated in Figure 8.10c. The front wheel and left wheel (both disk and spoked) were found to have the largest variations and peaks in over-pressure and under-pressure of the three hand-cycle wheels, due to the exposure of both wheels to the free-stream velocity under the yaw angles tested. By comparison, the right wheels (disk and spoked) were found to have lower pressure-coefficient variations across its geometry, due to being immersed in the wake of the hand-cyclist.

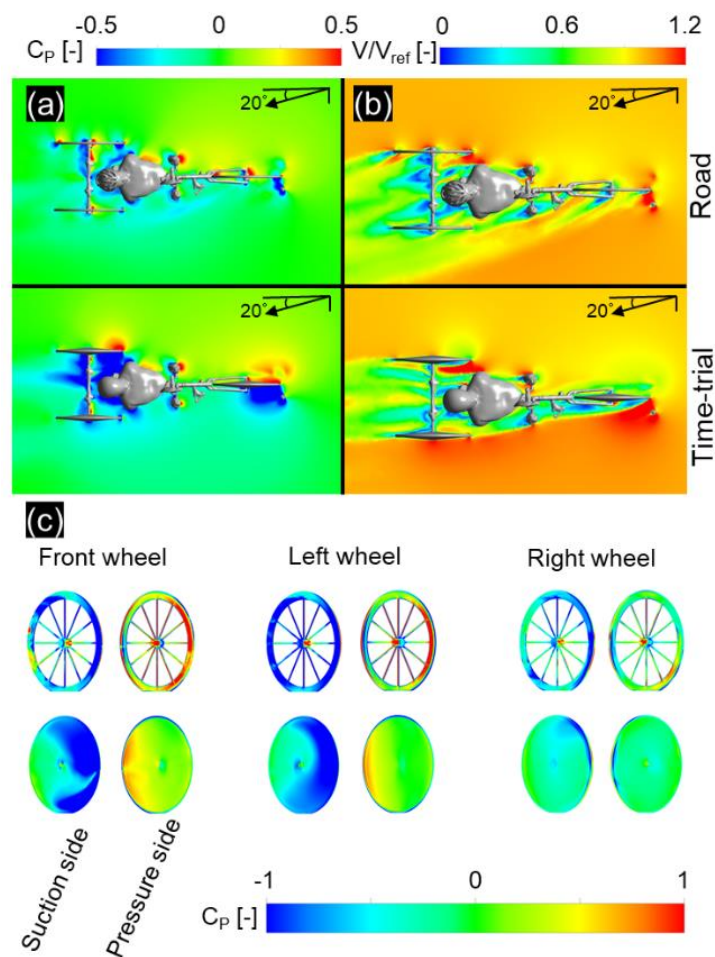


Figure 8.10. Contours in a plane at mid-wheel height at 20° yaw for (a) static pressure coefficient, and (b) normalised velocity, where V_{ref} is the reference velocity of 15 m/s. (c) Pressure coefficient contours on the suction and pressure side of the wheels at 20° yaw.

8.4.3 Breakdown of forces

Figure 8.11a-b compares the drag and lateral forces for the hand-cycle (frame and wheels) and athlete individually for both the road and TT setups, across all yaw angles tested. There was limited variation in the relative contributions of the hand-cycle and the athlete to the total drag across each yaw angle (Figure 8.11a). This suggests that drag optimisations performed for 0° yaw may be valid for all yaw angles. The athlete and hand-cycle contributed to an average of 31.7% and 68.3% to the total drag for the road setup, and 46.0% and 54.0% for the TT setup. There was more variation in athlete and hand-cycle contributions to the total lateral force throughout the yaw range tested (Figure 8.11b). This was partly due to the small lateral forces at 0° yaw. However, a trend emerged between 5° and 20° yaw for both hand-cycle setups with increasing contributions from the athlete to the total lateral force and decreasing contributions from the hand-cycle geometry. At 20°, the athlete contributed 31.1% to the total lateral force for the road setup, and 10.0% for the TT setup.

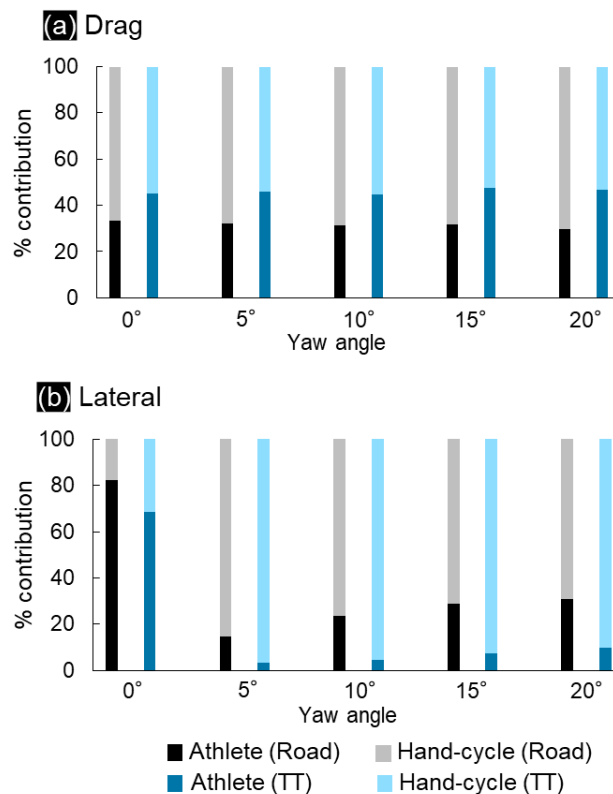


Figure 8.11. Percentage contributions to the drag (a) and lateral (b) force by the hand-cycle and the athlete in the road and TT setups.

8.5 Discussion

This research found that the drag force of a hand-cyclist in a road setup can increase by 14.1%, for increasing yaw angles from 0° to 15°. The TT setup experienced a maximum increase in drag force of 3.3% from 0° to 5° yaw. The drag recorded at 15° returned to the equivalent level of drag at 0° yaw (0.4% difference) for the TT setup, and was reduced by a further 6.2% between 15° and 20°. The road setup also experienced a 4.1% decrease in drag from 15° to 20° yaw. However, the drag force at 20° yaw was 9.5% higher than the 0° yaw prediction for the road setup. Maximum drag values were found at 15° and 5° yaw for the road and TT hand-cycling setups respectively. A similar result was found by Fintelman et al. (2015a) who reported that the drag coefficient for a regular cyclist reaches its max at 15° yaw; spoked wheels were used in this study as per the road hand-cycle setup where 15° was the critical angle for drag.

A large difference was found between the C_{sAs} of the road and TT hand-cycle setups. The lateral force for the road setup at 20° yaw was 1.6 times larger than the drag force. However, the lateral force played a larger role in the aerodynamics of the TT setup, 5.6 times the drag force at 20° yaw. An evaluation of the roll moments revealed that the TT setup was more susceptible to roll than the road setup due to the disk wheels. However, the higher yaw moments resulting from the disk wheels in the TT setup were not expected to have a significant impact on the stability of the hand-cyclist. Hand-cyclists are not as easily influenced by crosswinds in terms of steering-stability as able-bodied traditional riders. This is due to the presence of three wheels in contact with the ground instead of two, combined with a low centre of gravity. Hence, the higher lateral forces might not have a negative effect on the performance of the hand-cyclists, when using disk wheels to attain better drag performance. Further research is required using track measurements or wind tunnel experiments to confirm this.

Fintelman et al. (2014) found up to 60% of the lateral force experienced by an able-bodied cyclist was attributed to the bicycle (road setup) at large yaw angles of up to 90°. This present study showed that for a road hand-cycling setup, the hand-cycle itself can contribute up a minimum of 66.6% at 0°, and a maximum of 70.1% at 20° to the total lateral force (Figure 8.11b), exceeding that of a road bicycle for able-bodied users. Limited variation was found in percentage contributions of athlete/hand-cycle (for the road and TT setups) to the total drag at varying yaw angles (Figure 8.11a). However, the hand-cycle (frame and wheels) contributed significantly more to the lateral forces than the athlete, throughout all the yaw angles tested (excluding 0°). In addition, the hand-cycle contributed more to the drag force than the athlete for all yaw angles, indicating that aerodynamic optimisation of the hand-cycle design and wheel choice instead of the athlete could yield greater benefits.

Simplifications in this study should be taken into account for drag/lateral force comparisons and for future research. The geometries used in the CFD simulations and in the wind tunnel experiments contained static geometries. The surface of the athlete's geometry was smoothed to remove folds in his apparel which would have negatively impacted the grid generation. Small geometric details, such as cables, chain, and the sprocket were neglected. All surfaces in the CFD simulations were assumed to be smooth walls with zero roughness, where in reality, these surfaces would have some degree of roughness.

The arm rotation of the athlete is also expected to have an impact on the drag and lateral forces in different crosswind scenarios. The athletes' arms rotate together symmetrically at the same crank angle, instead of being 180° apart as per a traditional bicycle. The upper torso and head of the athlete along with the left and right rear wheels are located downstream of the hand-cycle cranks, and the interference drag from the rotating arms is expected to vary with the crosswind angle. Despite the legs of a traditional able-bodied cyclist not being upstream of the torso and head like the hand-cycle case, Griffith et al. (2014) found that the leg rotation impacted the drag on the athlete's torso, and thus an equivalent or larger impact could be expected for hand-cyclists.

8.6 Conclusion

This study investigated the aerodynamics of road and TT hand-cycling setups under crosswind conditions. Wind tunnel experiments were used to validate the CFD simulation results for yaw angles of -10°, 0°, 5°, 10°, 15°, and 20°. Two turbulence models were considered, the Spalart-Allmaras and the SST $k-\omega$, and simulations using both models provided good agreement with the wind tunnel results. However, using RMS error as a performance indicator for drag and lateral force predictions over a range of yaw angles, the SST $k-\omega$ turbulence model provided more accurate predictions and is thus recommended for future research.

Following the validation study, additional CFD simulations were performed investigating the crosswind effects on hand-cyclist geometries equipped for road race and TT events. The results demonstrated that the drag of the hand-cyclist in a road setup increased by 14.1% from 0°-15° yaw, but the TT setup experienced a maximum drag increase of only 3.3%, from 0°-5° yaw. Disk wheels were determined as the most influential geometrical factor for both drag and lateral forces between the road (spoked wheels) and TT (disk wheels) hand-cycle setups. The lateral force experienced by the TT hand-cyclist exceeded the drag at 20° yaw by 5.6 times, in comparison to 1.6 times for the road setup at the same yaw angle. Athletes should carefully consider the use of disk wheels if high

wind speeds are present at race events, as despite the drag benefits provided by comparison to spoked wheels, lateral forces in excess of the drag forces can be generated at yaw angles of 5° and higher.

Future research on the topic should include dynamic models with rotating wheels. In addition, a variety of wheel designs should be compared to determine the most suitable designs for drag and lateral force reduction. The three wheels of a hand-cyclist interact aerodynamically with the hand-cycle frame and athlete geometries, and remain a key area for further investigation. There is potential for new innovations in wheel design specific to hand-cycling, with new technologies that are unique to hand-cycling and not derived or borrowed from able-bodied traditional cycling.

8.7 References

- ANSYS Fluent. (2015). ANSYS Fluent theory guide. *Release 16.1 Documentation*. ANSYS Inc.
- ATI Industrial Automation. (2018). F/T Sensor Delta. Retrieved April 04, 2018, from www.atia.com/app_content/Documents/9230-05-1330.auto.pdf
- Barlow, J. B., Rae, W. H., & Pope, A. (1999). *Low-speed Wind Tunnel Testing* (3rd ed.). John Wiley & Sons.
- Barry, N., Burton, D., Crouch, T., Sheridan, J., & Luescher, R. (2012). Effect of crosswinds and wheel selection on the aerodynamic behavior of a cyclist. In *9th Conference of the International Sports Engineering Association, Procedia Eng.* (Vol. 34, pp. 20–25). <https://doi.org/10.1016/j.proeng.2012.04.005>
- Blocken, B. (2014). 50 years of Computational Wind Engineering: Past, present and future. *Journal of Wind Engineering and Industrial Aerodynamics*, *129*, 69–102. <https://doi.org/https://doi.org/10.1016/j.jweia.2014.03.008>
- Blocken, B. (2015). Computational Fluid Dynamics for urban physics: Importance, scales, possibilities, limitations and ten tips and tricks towards accurate and reliable simulations. *Building and Environment*, *91*, 219–245. <https://doi.org/10.1016/j.buildenv.2015.02.015>
- Blocken, B., & Toparlak, Y. (2015). A following car influences cyclist drag: CFD simulations and wind tunnel measurements. *Journal of Wind Engineering and Industrial Aerodynamics*, *145*(0), 178–186. <https://doi.org/10.1016/j.jweia.2015.06.015>
- Blocken, B., Toparlak, Y., & Andrienne, T. (2016). Aerodynamic benefit for a cyclist by a following motorcycle. *Journal of Wind Engineering and Industrial Aerodynamics*, *155*, 1–10.

<https://doi.org/https://doi.org/10.1016/j.jweia.2016.04.008>

- Crouch, T. N., Burton, D., LaBry, Z. A., & Blair, K. B. (2017). Riding against the wind: a review of competition cycling aerodynamics. *Sports Engineering*, 20(2), 81–110.
<https://doi.org/10.1007/s12283-017-0234-1>
- Defraeye, T., Blocken, B., Koninckx, E., Hespel, P., & Carmeliet, J. (2010a). Aerodynamic study of different cyclist positions: CFD analysis and full-scale wind tunnel tests. *Journal of Biomechanics*, 43(7), 1262–1268. <https://doi.org/10.1016/j.jbiomech.2010.01.025>
- Defraeye, T., Blocken, B., Koninckx, E., Hespel, P., & Carmeliet, J. (2010b). Computational fluid dynamics analysis of cyclist aerodynamics: Performance of different turbulence-modelling and boundary-layer modelling approaches. *Journal of Biomechanics*, 43(12), 2281–2287.
<https://doi.org/10.1016/j.jbiomech.2010.04.038>
- Fintelman, D. M., Sterling, M., Hemida, H., & Li, F.-X. (2014). The effect of crosswinds on cyclists: an experimental study. In *The 2014 conference of the International Sports Engineering Association, Procedia Eng.* (Vol. 72, pp. 720–725).
<https://doi.org/10.1016/j.proeng.2014.06.122>
- Fintelman, D. M., Hemida, H., Sterling, M., & Li, F.-X. (2015a). CFD simulations of the flow around a cyclist subjected to crosswinds. *Journal of Wind Engineering and Industrial Aerodynamics*, 144, 31–41. <https://doi.org/10.1016/j.jweia.2015.05.009>
- Fintelman, D. M., Sterling, M., Hemida, H., & Li, F.-X. (2015b). The effect of time trial cycling position on physiological and aerodynamic variables. *Journal of Sports Sciences*, 414(April 2015), 1–8. <https://doi.org/10.1080/02640414.2015.1009936>
- Franke, J., Hellsten, A., Schlünzen, H., & Carissimo, B. (2010). The best practise guideline for the CFD simulation of flows in the urban environment: an outcome of COST 732. *The Fifth International Symposium on Computational Wind Engineering (CWE2010)*, 1–10.
- García-López, J., Rodríguez-Marroyo, J. A., Juneau, C.-E., Peleteiro, J., Martínez, A. C., & Villa, J. G. (2008). Reference values and improvement of aerodynamic drag in professional cyclists. *Journal of Sports Sciences*, 26(3), 277–286. <https://doi.org/10.1080/02640410701501697>
- Godo, M., Corson, D., & Legensky, S. (2010). A comparative aerodynamic study of commercial bicycle wheels using CFD. *American Institute of Aeronautics and Astronautics*. 2010-1431
- Griffith, M. D., Crouch, T., Thompson, M. C., Burton, D., & Sheridan, J. (2014). Computational fluid dynamics study of the effect of leg Position on cyclist aerodynamic drag. *The American*

Society of Mechanical Engineers, Journal of Fluids Engineering, 136.

<https://doi.org/10.1115/1.4027428>

- Haake, S. J. (2009). The impact of technology on sporting performance in Olympic sports. *Journal of Sports Sciences, 27*(13), 1421–1431. <https://doi.org/10.1080/02640410903062019>
- Mannion, P., Toparlar, Y., Blocken, B., Hajdukiewicz, M., Andrienne, T., & Clifford, E. (2017). Improving CFD prediction of drag on Paralympic tandem athletes: Influence of grid resolution and turbulence model. *Sports Engineering*. <https://doi.org/10.1007/s12283-017-0258-6>
- Menter, F. R. (1994). Two-equation eddy-viscosity turbulence models for engineering applications. *AIAA Journal, 32*(8), 1598–1605. <https://doi.org/10.2514/3.12149>
- Roache, P. J. (1997). Quantification of uncertainty in computational fluid dynamics. *Annual Review of Fluid Mechanics, 29*, 123–160. <https://doi.org/10.1146/annurev.fluid.29.1.123>
- Spalart, P., & Allmaras, S. (1992). A one-equation turbulence model for aerodynamic flows. In *30th Aerospace Sciences Meeting and Exhibit*. American Institute of Aeronautics and Astronautics. <https://doi.org/http://doi.org/doi:10.2514/6.1992-439>
- Tew, G. S., & Sayers, a. T. (1999). Aerodynamics of yawed racing cycle wheels. *Journal of Wind Engineering and Industrial Aerodynamics, 82*(1), 209–222. [https://doi.org/10.1016/S0167-6105\(99\)00034-3](https://doi.org/10.1016/S0167-6105(99)00034-3)
- Thorn, A. (1943). Blockage Corrections in a High Speed Wind Tunnel. *ARC R&M 2033*.
- Tominaga, Y., Mochida, A., Yoshie, R., Kataoka, H., Nozu, T., Yoshikawa, M., & Shirasawa, T. (2008). AIJ guidelines for practical applications of CFD to pedestrian wind environment around buildings. *Journal of Wind Engineering and Industrial Aerodynamics, 96*(10–11), 1749–1761. <https://doi.org/10.1016/j.jweia.2008.02.058>
- UCI. (2017). Cycling Regulations, Part 16 Para-Cycling. Internationale Union Cycliste. Retrieved from http://www.uci.ch/mm/Document/News/Rulesandregulation/16/26/73/16han-E_English.PDF

Aerodynamic analysis of wheel configurations in Paralympic hand-cycling: a computational study

This chapter builds on Chapter 8, by investigating a selection of commercially available wheels for the application to hand-cycles for aerodynamic optimisation purposes. Wheel rotation is accounted for, rear wheel spacing, and crosswinds are considered when evaluating new wheel combinations. Numerical simulations of rotating wheels are validated from data available in the literature. The optimal wheel selection is determined, that considered both disk and spoked wheels used together on a single setup. E.g. a front disk wheel with two rear spoked wheels.

This study has been accepted for publication in the international peer-reviewed journal *European Journal of Mechanics – B/Fluids*:

Mannion, P., Toparlar, Y., Clifford, E., Hajdukiewicz, M., Andrienne, T., & Blocken, B. (2019). Aerodynamic analysis of wheel configurations in Paralympic hand-cycling: a computational study. *European Journal of Mechanics – B/Fluids*. *Accepted*.

Abstract: Para-cycling aerodynamics holds additional complexities compared to its able-bodied counterpart. Hand-cycling provides such an example, where three wheels opposed to the two wheels of a traditional bicycle are required. Wheel aerodynamics are therefore even more prevalent in the field of Paralympic hand-cycling. However, there has been little attention devoted to wheel aerodynamics in Paralympic hand-cycling. This study investigates hand-cycling wheel aerodynamics. The optimal wheel selection was investigated from a combination of wheels that represented competitive deep-section spoked wheels and disk wheels. In addition to the various wheel combinations, the spacing between the two rear wheels was varied. A 55 cm rear wheel spacing provided drag reductions of up to 4.7% compared to 70 cm when using rear disk wheels at 0° yaw. Crosswinds were also investigated, and it was shown that a front disk wheel coupled with rear deep-section wheels at 55 cm spacing provided the best aerodynamic drag performance with increasing yaw angle. With this wheel setup, the C_{DA} increased by only 7.7%, between min and max values found at 0° and 15° yaw respectively.

9.1 Introduction

Hand-cycling is a Union Cycliste Internationale (UCI) registered para-cycling sport, with appearances in regional and world para-cycling events and the Paralympics. Athletes compete within 5 classes; H1-H5. The classes of H1-H4 feature a recumbent athlete position on the hand-cycle, with lower levels of athlete impairment from H4 to H1 (UCI, 2017). The H5 class features a kneeling position commonly referred to as an upright position, where the athlete can use his/her arms and torso to provide power, whereas the H1-H4 classes are limited to just arm-provided power. Competitive hand-cycles have three wheels; one front and two rear. The two rear wheels on a competitive hand-cycle are free-rolling, without steering mechanisms. The front wheel is typically centred at the front of the hand-cycle and manages the power application to the ground, braking, gearing and steering. In contrast to traditional cycling, the steering axis is close in orientation to the horizontal ground plane, resulting in the front wheel tilting side to side when steering. Rules set by the UCI restrict the spacing for the rear wheels (UCI, 2017). Maximum and minimum rear wheel spacings are 70 cm and 55 cm respectively, measured from the point of contact of the wheels with the ground. A range of wheel types are allowed to be used for both road race and time-trial events for both the front and rear wheels; including disk and spoked wheels. Also, cambered wheels are allowed and are predominantly featured in the H5 class. Furthermore, a range of wheel diameters as classified by the European Tyre and Rim Technical Organisation (ETRTO) are allowed, from 0.406 m to 0.622 m bead seat diameters. Thus, a wide number of variations are possible for wheel selection in competitive hand-cycling, inferring the possibility for aerodynamics optimisation.

Increasing numbers of publications in the field of elite able-bodied cycling aerodynamics in recent years illustrates the importance of this research field (Blocken et al. 2018a; Crouch et al., 2017; Lukes et al., 2005). Indeed, approximately 90% of the energy expenditure for cyclists at velocities in excess of 54 km/hr is to overcome aerodynamic forces acting on them (Kyle & Burke, 1984; Lukes et al., 2005). Hand-cyclists can have average velocities in the range of 35-40 km/hr on flat terrain with negligible wind conditions, but, can achieve velocities in excess of 54 km/hr in descent phases of race events. Elite able-bodied cycling research has focused on drafting phenomena (Barry et al. 2015a, 2016; Blocken et al., 2018a; Blocken et al., 2013), drag interference effects with cars and motorcycles (Blocken & Toparlak, 2015; Blocken et al., 2016), athlete posture optimisation (Barry et al., 2015b; Blocken et al., 2018b; Defraeye et al., 2010; Oggiano et al., 2008; Underwood & Jermy, 2013; Fintelman et al., 2014, 2015a), and leg rotation effects (Crouch et al., 2012; Griffith et al., 2014). Tandem cycling aerodynamics has been addressed by Mannion et al. (2018a, 2018b, 2019) who used both wind tunnel experiments and computational fluid dynamics (CFD) simulations.

There is little published research in the field of elite hand-cycling aerodynamics. The London 2012 Paralympics initiated the first known hand-cycling aerodynamics research, to the best knowledge of the present authors. Mazzola et al. (2012) investigated athlete ergonomic and aerodynamic variables, and concluded that efforts to improve ergonomics such as raising the inclination of the backseat, negatively affected the aerodynamic performance. Belloli et al. (2014) conducted an experimental study of hand-cycling aerodynamics, using wind tunnel experiments and track tests. Drag area (C_{DA}) values of 0.21 m^2 and 0.20 m^2 were measured in the wind tunnel experiments for a recumbent hand-cyclist (H1-H4 category) in a propulsive (actively applying power) and aerodynamic (static arms) stage respectively. A wider C_{DA} range was found for an upright hand-cyclist (H5 category), with C_{DA} values of 0.22 m^2 and 0.13 m^2 measured for the propulsive and aerodynamic stages respectively. Indeed, the lowest C_{DA} recorded in the wind tunnel campaign was 0.13 m^2 for a H5 class hand-cyclist in an aerodynamic non-propulsive position (Belloli et al., 2014). More recently, Mannion et al. (2018a) conducted an experimental and numerical investigation of hand-cycling aerodynamics. Scaled wind tunnel experiments were used to provide measurement data for the validation of a series of numerical simulations. Yaw angles between 0° - 20° in 5° increments were investigated for a static hand-cyclist geometry, with simplified wheel geometries that represented three spoked wheels for a road race setup, and three disk wheels for a time-trial (TT) setup. Maximum and minimum C_{DA} ranges for the road setup with spoked wheels were 0.1850 m^2 and 0.1621 m^2 at 15° and 0° yaw respectively. The TT setup with three disk wheels yielded lower C_{DA} values, with maximum and minimum values of 0.1322 m^2 and 0.1205 m^2 at 5° and 20° respectively. The roll moment trends were found to match the lateral force trends with increasing yaw angle, where the roll axis was defined on the ground plane between the front wheel and the right rear wheel.

The aerodynamics of bicycle wheels have been a widely researched topic in relation to cycling aerodynamics, and the present study on wheel aerodynamics for hand-cycling applications builds from data available in the literature by Godo et al. (2010). Godo et al. (2010) investigated the performance of several commercial bicycle wheels using CFD. Two velocities of 8.9 m/s (20 mph) and 13.4 m/s (30 mph) were considered over a range of yaw angles (0° , 2° , 5° , 8° , 10° , 12° , 14° , 16° , 18° and 20°), and the results were correlated against available wind tunnel data. Six different wheels were tested, including the Zipp 404, Zipp 808, Zipp 1080, Zipp Sub9, HED TriSpoke and the Rolf Sestriere. The data reported by Godo et al. (2010) concerning numerical and experimental drag coefficients for the Zipp 404 spoked wheel and the Zipp Sub9 disk wheel were utilised in the present research to validate numerical simulations. The numerical results by Godo et al. (2010) for these two wheel types showed good agreement to their experimental data, with the drag coefficients predicted

at 0° yaw within the range of drag coefficients from other sources, and the aerodynamic drag force trends matching their experimental counterparts.

A gap in the literature was identified regarding knowledge of the optimal wheel selection for hand-cycling; considering commercially available wheels instead of simplified wheel geometries. Furthermore, wheel rotation has not been accounted for in numerical studies of hand-cycling aerodynamics. The present study investigated the impact of wheel selection on the aerodynamics of a Paralympic hand-cycling setup using two commercially available wheels used in competitive cycling. Wheel rotation was accounted for along with the impact of crosswinds and the positioning of the rear wheels within the spacing allowable by the UCI. This study used CFD as the primary investigative tool, validated using wind tunnel experiments and experimental data available in the literature. A set of simulations of isolated wheel geometries were conducted for the purpose of validating the numerical method used for modelling wheel aerodynamics. The findings of this study informed a second set of simulations that modelled hand-cycling aerodynamics. Section 9.2 introduces the geometrical models and the CFD parameters used. The validation studies are described in section 9.3, while the results, discussion and conclusions are presented in sections 9.4, 9.5 and 9.6 respectively.

9.2 Simulation setups

9.2.1 Geometrical models

The hand-cyclist's geometry for this study was obtained via 3D scanning using the Artec Eva structured light 3D scanner (Artec, 2017). Informed consent was acquired prior to scanning from the athlete involved. The Zipp Sub9 disk wheel and the Zipp 404 deep-section spoked wheel were selected for this study (Figure 9.1a). The rim and hub profiles for both wheels were obtained from Godo et al. (2009, 2010) and modelled using CAD software. The spokes for the Zipp 404 were elliptical Sapim CX-Ray spokes, 2.2 mm long and 0.9 mm thick (Sapim, 2011). Two wheel diameters were used, 0.695 m and 0.611 m respectively, maintaining the same rim and tyre profiles. Note that the diameter values mentioned are the total diameters of the wheels, for ease of comparative purposes. The 0.695 m diameter wheels were used to validate the numerical method to simulate rotating disk and spoked wheels, by allowing direct comparisons to the wind tunnel experiments and numerical

simulations reported by Godo et al. (2010). The 0.611 m diameter wheels were considered representative of typical sizes used in competitive hand-cycling and were utilised in the CFD simulations. Smooth slick tyres were assumed for all wheels, with no grooves present.

The small geometrical details of the spokes for the Zipp 404 present challenges when generating computational grids, and the resulting high cell count yielded a high computational expense for the simulations in terms of solver time and working memory. Thus, two versions of the Zipp 404 were investigated. The first was fully spoked, and the second had the geometry of the spokes removed, leaving the tyre, rim and hub to represent the wheel geometry (Figure 9.1a). The latter wheel geometry was termed as a ‘free-spoked’ wheel. The focus of this free-spoked wheel geometry without the spokes was to determine if it was necessary to model the spokes in numerical simulations, with the aim of reducing the computational cost of the simulations and enabling a wider comparative study that included several wheel combinations, rear wheel spacings, and yaw angles.

The Zipp Sub9 and free-spoked Zipp 404 wheels were coupled with the hand-cyclist’s geometry to generate a number of geometry variations. Four geometry variations were created based on wheel selection as outlined in Figure 9.1b, all with 55 cm rear wheel spacing. These included I) three Zipp Sub9 wheels, II) three free-spoked Zipp 404 wheels, III) a front free-spoked Zipp 404 wheel and rear Zipp Sub9 wheels, and IV) a front Zipp Sub9 wheel coupled with free-spoked Zipp 404 rear wheels. The impact of rear wheel spacing was investigated on hand-cycles with three Zipp Sub9 wheels (combination I), and front Zipp Sub9 with rear Zipp 404 wheels (combination IV). Four spacings were used for both geometries between the maximum and minimum spacings allowed by the UCI; 55 cm, 60 cm, 65 cm and 70 cm. All hand-cycle and wheel geometries were raised 2 cm from the ground surface, to prevent skewed mesh cells from forming at the wheel-ground intersection point; this method is evident in the literature in the works by (Blocken & Toparlar, 2015; Blocken et al., 2016; Mannion et al., 2018c). The front forks and rear axle were simplified to accommodate the computer aided design (CAD) and grid processes when exchanging the wheel geometries, and their spacing when modelling the rear wheels.

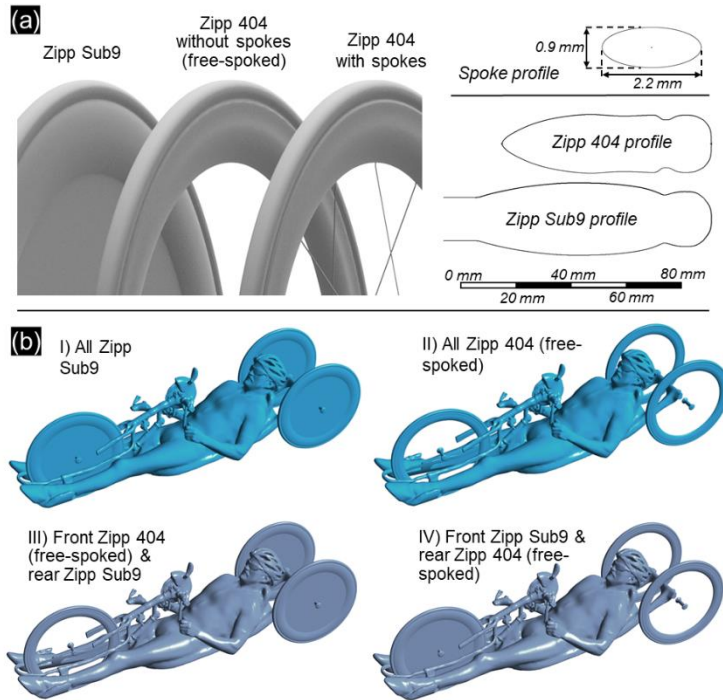


Figure 9.1. (a) Three wheel geometries under study: Zipp Sub9 disk, free-spoked Zipp 404 and Zipp 404 with spokes included. (b) Depiction of hand-cycle geometry with four variants of wheel combination variations.

9.2.2 Boundary conditions and solver settings

Two computational domains were used throughout this work. The first domain was for an isolated wheel, depicted in Figure 9.2a. Best practice guidelines (Blocken, 2015; Casey & Wintergerste, 2000; Franke et al, 2010; Tominaga et al., 2008) were followed to ensure that the wheel geometry was placed at a sufficient distance from the inlet (minimum of 5 times the wheel diameter) and outlet boundaries (minimum of 10 times the wheel diameter) respectively, and that the blockage ratio remained below 3%. Two inlet and two outlet boundary conditions were used to simulate yaw angles, by having the same velocity magnitudes and directions at the inlets. A symmetry condition was used for the top surface of the domain, and a free-slip wall was used for the ground surface. In the case of 0° yaw, the inlet and outlet boundary conditions parallel to the direction of fluid flow were changed to symmetry conditions. A rotational velocity was applied to the wheel geometries corresponding to a 13.4 m/s travelling velocity using the rotating wall boundary condition. A velocity magnitude of 13.4 m/s was maintained for all yaw angles when simulating the isolated wheels, as per the tests by Godo et al. (2010). Yaw angles of 0° , 2° , 5° , 8° , 10° , 12° , 14° , 16° , 18° and 20° were investigated for both the free-spoked Zipp 404 wheel and the Zipp Sub9 disk wheel. The yaw angle

was defined as the incidence angle of the air against the travelling direction of the wheel as per Godo et al. (2010), illustrated in Figure 9.2.

The second computational domain for the geometry of the hand-cyclist resembled in shape the first computational domain used for the isolated wheel (Figure 9.2b). Again, best practice guidelines (Blocken, 2015; Casey & Wintergerste, 2000; Franke et al, 2010; Tominaga et al., 2008) were followed for the domain dimensions. Boundary conditions as per the isolated wheel computational domain previously discussed were also applied. An effective velocity magnitude of 15 m/s with 0.2% turbulence intensity and 1 m hydraulic diameter was maintained for all yaw angles. A 0 Pa ambient zero static gauge pressure outlet was used for all outlet boundaries. Yaw angles of 0°, 5°, 10°, 15° and 20° were simulated. Rotating wall boundary conditions were again used to simulate the wheel rotation in the hand-cycling simulations.

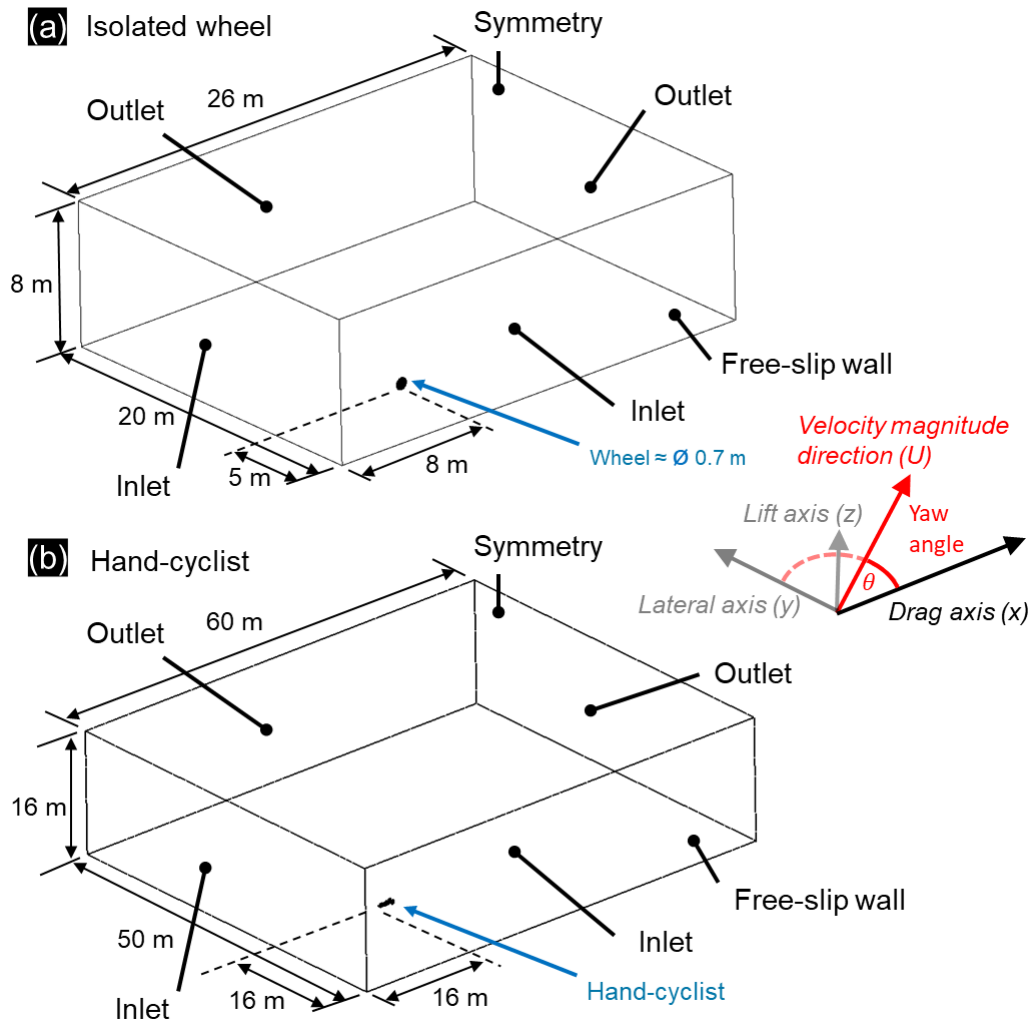


Figure 9.2. Computational domain for (a) the isolated wheels, and (b) the hand-cyclist.

ANSYS Fluent (ANSYS, 2017) was used to solve the Reynolds-averaged Navier–Stokes (RANS) equations, using a 2-equation turbulence model to achieve closure; namely the Shear Stress Transport (SST) $k-\omega$ turbulence model (Menter, 1994). The pseudo-transient solver was used with the Coupled pressure-velocity coupling algorithm and the second-order order discretisation schemes for turbulent kinetic energy and specific dissipation rate. Second-order pressure interpolation was used and gradients were computed using the Least Squares Cell Based method. The pseudo time-step size was 0.01 s, and all force values were averaged over 4000 steps after an initialisation period for statistically steady-state results as per (Mannion et al., 2018a).

9.2.3 Computational grids

9.2.3.1 Wheel computational grids

Separate systematic grid sensitivity studies were conducted for the disk Zipp Sub9 and free-spoked Zipp 404 wheels. Four tetrahedral-prismatic grids were created for the disk wheel, with the cell size at the surface systematically refined for each successive grid. The max y^* for each grid was held below 1 for each of the four grids, with 26 prism layers that maintained a height of 1×10^{-5} m for the wall-adjacent cell and with a growth ratio of 1.2. A growth ratio of 1.1 was used for the volume grid outside of the prism layers. Each of the four grids were tested using a static no-slip wall boundary condition, and a rotating wall boundary condition, to determine the sensitivity of the grid resolution to the static and rotating wheels.

The four grids for the disk wheel were named D1, D2, D3 and D4 with cell counts of 3,945,512, 9,336,891, 23,299,082 and 46,164,126, respectively. The subscript ‘S’ and ‘R’ was added to the grid names in Figure 9.3 to define between static wheels and rotating wheels, respectively. Both the static wheel and rotating wheel simulations were found to exhibit a similar degree of grid convergence. The Grid Convergence Index (GCI) suggested by Roache (1994, 1997) was calculated for both static and rotating simulations using grids D2, D3 and D4. GCIs of 1.04% and 0.26% were calculated for grids $D4_S$ and $D4_R$, respectively using the drag force as the target parameter, indicating acceptable levels of grid convergence. A GCI of 1.33% was calculated for grid $D3_R$.

Grid sensitivity studies were conducted on the static (no rotational modelled) free-spoked Zipp 404 wheel. Four systematically refined tetrahedral-prismatic grids were created for the free-spoked wheel. These grids are denoted as S1, S2, S3 and S4 in Figure 9.3, and had cell counts of 3,646,649, 8,800,024, 22,484,414, and 45,252,126, respectively. 26 prism layers with a first cell height of 1×10^{-5}

⁵ m and a growth ratio of 1.2 were also used on this wheel geometry, to limit any variation to y^* across each of the four grids. A growth ratio of 1.1 was used for the volume grid outside of the prism layers. The grid sensitivity appeared to approach its asymptote after grid S2. A GCI of 1.46% and 1.82% was calculated for grid S4 and S3, indicating an adequate level of grid convergence.

Two grids were created for the spoked Zipp 404 wheel that investigated the sensitivity to the number of cells along the length of the spokes. Mapped quad cells were used to discretise the surface geometry of the spokes. Each spoke contained 32 cells around its circumference to capture the curvature of the elliptical shape. Individual refinement ratios were applied to both ends of the spokes to ensure good transition to the rim and hub. The grid resolution of grid S3 was applied for the wheel rim and hub, and the same volume grid parameters including the 26 prism layers were applied. The two grids contained 220 cells and 320 cells respectively along the length of the spoke, and were named S3₂₂₀ and S3₃₂₀ appropriately. It was noted that a cell count far below the 220 cells across the length of the spokes (such as a count of 120) resulted in stretched cells that compromised the quality of the grid. The sensitivity study of the spokes revealed a low sensitivity between S3₂₂₀ and S3₃₂₀, with a difference of 0.31% between the C_{DA} calculated for both simulations.

Based on the grid sensitivity studies, the grid parameters for grids D3 and S3 were deemed to have sufficient accuracy and were chosen for further study. These results were used for comparison against experimental and numerical data of isolated wheels in the literature, and were applied on the wheels used in the hand-cycle simulations. Grid S3₂₂₀ was used for further comparison in section 9.3.1 for spoked wheels.

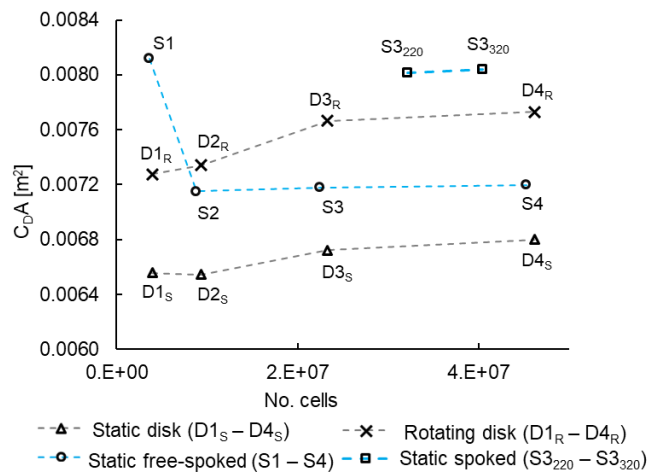


Figure 9.3. Grid convergence for isolated wheels; namely a static Zipp Sub9 disk wheel, a rotating Zipp Sub9 disk wheel, a static Zipp 404 wheel with the spokes removed, and static Zipp 404 wheels with 220 and 320 cells along the length of each spoke. ‘S’ and ‘D’ stand for spoked and disk wheels, respectively. Subscripts ‘S’ and ‘R’ stand for static and rotating, respectively.

9.2.3.2 Hand-cycle computational grids

Three grids were created to test the grid sensitivity for the hand-cycle geometry; a coarse (H1), medium (H2) and fine grid (H3), each systematically refined. Simplified spoked wheels were used in this study instead of the Zipp 404 or Zipp Sub9, that were not based on any commercial design and that contained twelve spokes with diameters of 12 mm. The grid cell counts were 10,404,121, 27,236,409, and 77,363,247 cells for grids H1 – H3, respectively. A GCI of 0.29% was calculated for grid H3, and 1.29% for grid H2. Thus, the parameters for grid H2 were chosen as providing acceptable accuracy for further simulations, and were combined with the grid parameters for the disk and spoked wheels previously analysed. The cell counts for the four wheel combinations (I, II, III, IV) described in Figure 9.1b with 55 cm rear wheel spacing were 51,706,184, 47,778,172, 49,002,622, and 50,445,308, respectively. In addition, a fifth grid was created based on combination IV with a front Zipp Sub9 disk wheel, but with rear Zipp 404 spoked wheels with the geometry of the spokes included. This fifth grid contained 90,998,827 cells.

The grid resolutions are depicted in Figure 9.4, with the volume grid for a hand-cycle setup with a front Zipp Sub9 wheel and rear free-spoked Zipp 404 wheels, combination IV, in the vertical centre-plane in Figure 9.4a. Figures 9.4b and 9.4c illustrate the prism layers used to resolve the boundary layer on the wheels (Figure 9.4b) and the hand-cycle frame (Figure 9.4c). It is noted that the same boundary layer grid parameters were applied to all wall surfaces for each of the hand-cycle grids. The surface grid resolution on the athlete legs, hand-cycle frame, and Zipp Sub9 disk wheel is illustrated in Figure 9.4d. Figure 9.4e depicts the surface grid resolution on the athlete's head and helmet along with the Zipp 404 wheel. Figures 9.4f and 9.4g illustrate the grid density for the spoked wheels, with the quad surface grid for the spokes depicted in Figure 9.4g.

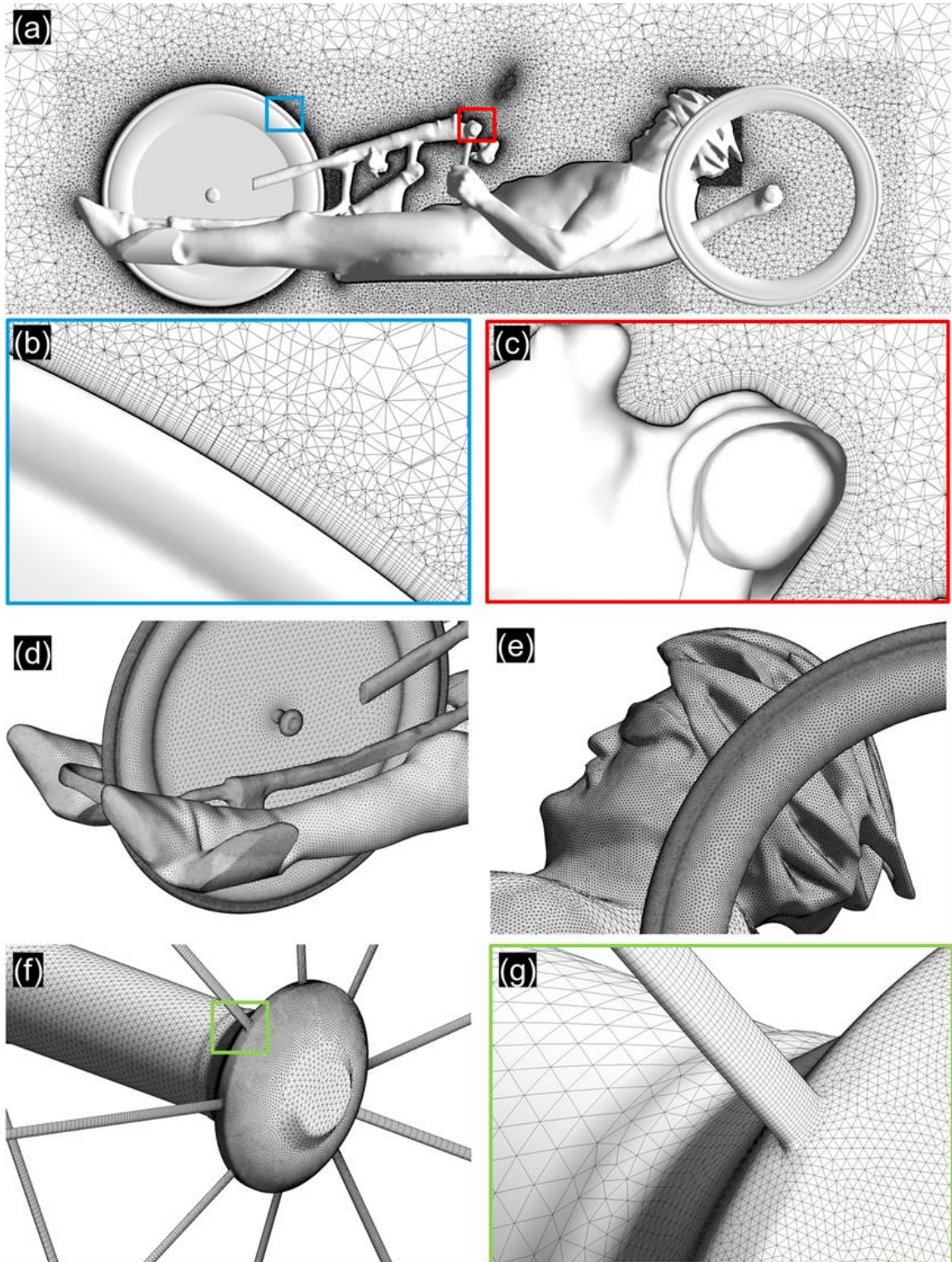


Figure 9.4. (a) Volume grid density in vertical centre-plane. (b) Prism layers resolving boundary layer on the Zipp Sub9 disk wheel. (c) Boundary layer grid around the frame crank. (d) Surface grid density on the athletes' legs, frame and disk wheel. (e) Surface grid density on the athlete's head and helmet and on the Zipp 404 wheel. (f) Surface grid density on the wheel hub. (g) Grid density on the spokes (220 cells along spoke length).

9.3 Validation studies

Two independent validation studies were performed. The first was to validate the method used for modelling the rotating free-spoked Zipp 404 wheels and Zipp Sub9 disk wheels via qualitative comparison to the wind tunnel experiments and numerical simulations reported by Godo et al. (2010); discussed in section 9.3.1. The second validation study, reported by Mannion et al. (2018a), consisted of wind tunnel experiments conducted for a static H1-H4 category hand-cyclist to validate numerical simulations of hand-cycling aerodynamics in yaw conditions, and discussed briefly in section 9.3.2.

The drag area ($C_D A$) was used to describe the drag force data and is described as follows:

$$C_D A = \frac{F_D}{0.5\rho U^2} \quad (9.1)$$

where F_D is the drag force [N], A is the reference area [m^2], U is the velocity magnitude [m/s], and ρ is the air density [kg/m^3].

9.3.1 Isolated rotating wheels

9.3.1.1 Disk wheels

Figure 9.5a compares drag areas calculated for the Zipp Sub9 disk wheel across a range of yaw angles: 0° , 2° , 5° , 8° , 10° , 12° , 14° , 16° , 18° and 20° . Data from wind tunnel experiments conducted by Zipp and reported by Godo et al. (2010) were used in the comparison. In addition, the CFD simulations conducted by Godo et al. (2010) at 13.4 m/s (30 mph) were also compared. The drag trend across the yaw range investigated was found to closely match that reported by Godo et al. (2010), where increases and decreases in drag were found in reaction to the yaw angle. The drag experienced by the wheel was observed to reduce between yaw angles 0° - 8° . The drag then increased between yaw angles 8° - 10° , decreased between yaw angles 10° - 16° , and increased again between yaw angles 16° - 20° . Near matching $C_D A$ values were predicted at yaw angles of 5° , 8° , 10° and 12° with a maximum difference of 0.0006 m^2 . A similar trend was reported from the wind tunnel experiments by Zipp. However, the absolute drag values from the wind tunnel experiments at 0° - 8° were considerably higher than the numerical results of Godo et al. (2010) and the numerical models of the present research; up to 0.0095 m^2 at 0° yaw. In addition, it was reported that the Zipp Sub9 disk wheel experienced a positive thrust force at a yaw angle of 12.5° , which was not predicted by the numerical simulations by Godo et al. (2010) or the present research. It is noted that there is a lack

of knowledge regarding the wind tunnel experiments conducted by Zipp in the publication by Godo et al. (2010), including the shape and size of the wheel supports, how rotation was transferred to the wheel, details of ground boundary or wind tunnel test bed, the approach flow boundary layer, blockage, tyre roughness, turbulence intensity, and sensor uncertainties. However, the overall qualitative agreement between drag trends predicted by Zipp, the numerical studies of Godo et al. (2010) and the present study is considered to be acceptable for the Zipp Sub9 disk wheel. The level of variability between independent investigations of aerodynamic drag is indicated by the numerous drag values reported by Godo et al. (2010) for 0° yaw, from 0.0061 m^2 to 0.0156 m^2 , from various studies with drag data available for the same or similar wheels. A C_{DA} of 0.0061 m^2 was predicted from the present research.

9.3.1.2 Free-spoked wheels

Figure 9.5b compares drag coefficients calculated for the Zipp 404 wheel across yaw angles from 0° - 20° , between the present research and the numerical results of Godo et al. (2010) at 13.4 m/s , and the wind tunnel results from Zipp, as reported by Godo et al. (2010). The Zipp 404 wheels used in this study neglected the geometry of the spokes, and contained only the wheel rim, tyres and hubs. The same drag trends throughout the yaw range investigated were found for the numerical results reported by Godo et al. (2010), the experimental results from Zipp, and the present research. An offset was observed between the drag predictions by the experimental results from Zipp and the numerical results from Godo et al. (2010). In addition, there was a further offset between the numerical results from Godo et al. (2010) and the present study, with an averaged deviation of 33.6%. This can be attributed to the absence of the spokes in the wheel geometry. In addition, any support structures from the wind tunnel experiments by Zipp and the ground contact patch are not replicated in the present study, making meaningful direct quantitative comparisons difficult. A range of drag values were reported by Godo et al. (2010) for 0° yaw, as obtained from other studies. The max and minimum C_{DA} measurements at 0° yaw were 0.0190 m^2 and 0.0064 m^2 respectively, and the value predicted by the present study falls within this range, at 0.0066 m^2 , even without the spokes modelled. The level of agreement between the present results and the numerical reported by Godo et al. (2010) and the wind tunnel data from Zipp are considered fair for the reproduction of the drag trends under yaw conditions, taking into consideration the removal of the spokes from the wheel geometry and that the ground contact patch is not accounted for in the present study. However, as previously mentioned for the Zipp Sub9 disk wheel, there is a lack of knowledge regarding the apparatus and exact settings employed for the wind tunnel experiments conducted by Zipp (Godo et al., 2010). Godo et al. (2010)

also demonstrated a dependency on Reynolds number for both the Zipp 404 spoked wheel and the Zipp Sub9 disk wheel, with the drag trend at 8.9 m/s (20 mph) similar to that at 13.4 m/s (30 mph) but offset in absolute values by a maximum of 9.6%.

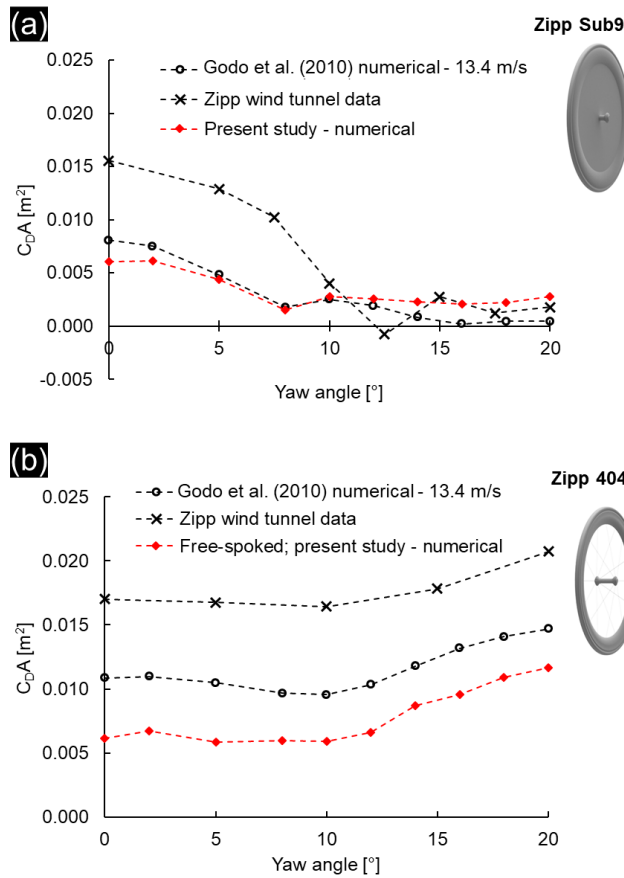


Figure 9.5. Comparison of C_{DA} values of the present study to the wind tunnel data from Zipp and the numerical results from Godo et al. (2010) for (a) the Zipp Sub9, and (b) the (free-spoked) Zipp 404.

The differences between the results of Godo et al. (2010) and the present study could be attributed to several factors. Regarding the Zipp 404 wheel, this included the removal of the spokes from the Zipp 404 wheel geometry. The blockage ratio (defined as the frontal area divided by the fluid domain cross-sectional area) for the present study was lower than that from Godo et al. (2010), where blockage ratio ranged from 1.4% at 0° to up to 9.7% at 20° for the Zip Sub9 disk wheel. This blockage would have resulted in artificial accelerations around the wheel that would impact the drag results. By comparison, the maximum blockage ratio the present study was 0.013%. In addition, the contact patch between the wheel and the ground was modelled differently in the present study and by Godo et al. (2010). The contact patch between a tyre and the ground was measured by Godo et al. (2010) and implemented in the numerical simulation. However, in the absence of this data, the wheels in the

present study were raised 2 cm from the ground surface which prevented skewed cells from forming at the tangent point of contact which would have negatively impacted the discretisation error of the numerical solution.

9.3.1.3 Spoked wheels

To determine the impact of the spokes on the wheel aerodynamics, additional static simulations were performed at 0° yaw of the Zipp 404 wheel with the spokes included. Grid S3₂₂₀ was used as described in section 9.2.3. The total drag of the static wheel was found to increase by 11.7% when the geometry of the spokes was included in the simulation. Furthermore, the drag breakdown of the tyre-rim, hub and spokes was 69.6%, 17.3% and 13.1% respectively. This compares to the values reported by Godo et al. (2009) for the same wheel simulated; 70.7%, 13.1% and 16.2% respectively. The spokes were found to have a comparable drag to the wheel hub, and the majority of the drag was generated by the rim at 70.7%, indicating that removing the geometry of the spokes could be a viable option for simulating wheel aerodynamics. The present study was static and the wheel rotation was accounted for by Godo et al. (2010) and thus the differences between the comparison of static and rotating wheels are noted. The advancing spoke in the rotating wheel would experience a different oncoming flow to its diametrically opposite spoke. However, if the spokes are not considered, the comparisons of the rotating free-spoked Zipp 404 wheel to the wind tunnel data by Zipp and the numerical data by Godo et al. (2010) show that the same drag trends were captured in crosswind conditions.

To conclude the investigation into the necessity of modelling wheel spokes, a static simulation was performed of a hand-cyclist with two fully-spoked Zipp 404 wheels attached to the rear axle (55 cm rear wheel spacing) along with a disk Zipp Sub9 wheel on the front, to test the feasibility of simulating hand-cycling aerodynamics with the geometry of the spokes included. The resulting grid was 90,998,827 cells. This allowed for a direct comparison to a static hand-cycling setup with two free-spoked Zipp 404 wheels on the rear axle, whose grid size was 49,002,622 cells by comparison. A 0.5% increase in total C_{DA} was found by including the geometry of the spokes. Thus, it was determined that the geometry of the spokes for the Zipp 404 wheel could be removed to ensure the computational cost of further simulations remained viable without significantly impacting the drag of the hand-cyclist. It is noted that from this point, all Zipp 404 wheels without the geometry of the spokes are referred to as ‘free-spoked wheels’ and all Zipp Sub9 wheels are referred to as ‘disk wheels’ for efficient reporting and dissemination purposes.

9.3.2 Hand-cycle validation studies

The lateral force area ($C_S A$) was used to describe the lateral force data from the wind tunnel experiments and numerical studies on hand-cycling aerodynamics, and is defined as follows:

$$C_S A = \frac{F_S}{0.5\rho U^2} \quad (9.2)$$

where F_S is the drag force [N].

9.3.2.1 Experimental and numerical setup

High-speed quarter-scale wind tunnel experiments at 60 m/s were conducted in the aeronautical test section of the tunnel in the University of Liège, Belgium, as depicted in Figure 9.6a. These experiments were reported by Mannion et al. (2018a), and are reiterated here for completeness. Reynolds number similarity to a full-scale hand-cyclist at 15 m/s was acquired using a velocity of 60 m/s for the quarter-scale model. The scaled hand-cyclist geometry was solid and manufactured from ABS (acrylonitrile butadiene styrene); its surface was considered smooth. The model was static in nature, with no movement of the arms or wheels. A manufacturing dimension constraint of 3 mm limited the minimum thicknesses to this size, such as the diameter of the spokes. However, this aided in ensuring model stiffness in view of the high-speed experiments. The force sensor used was a commercially available ATI Delta model (ATI, 2018), and was aligned with the centre of gravity of the model. A conservative ± 1.24 N error range was reported for the sensor. The wind tunnel setup is illustrated in Figure 9.6a. A raised sharp-edged platform was used to remove the model from the boundary layer at the bed of the wind tunnel. A rotating plate was built into the platform to allow for yaw angles to be investigated. Blockage corrections by Barlow et al. (1999) were applied, where the maximum blockage ratio was 2.3% at 20° yaw. A Pitot tube was used for velocity measurements, and temperature variations were also measured to correct air density variations. The air density was also corrected to a standard atmospheric pressure of 101325 Pa as per the CFD simulations via local meteorological data. The procedure for the wind tunnel experiments was as follows. After setting up the experiment as per Figure 9.6a, the force sensor was tared under no-wind conditions. The desired velocity was then achieved in the tunnel, and a settling period of 30 s was allowed for the sensor before commencing force measurements. Drag and lateral force data were measured at a rate of 10 Hz for 180 seconds. Each experiment was repeated for yaw angles of 0°, 5°, 10°, 15°, and 20°.

The numerical simulations for the validation study were presented by Mannion et al. (2018a), and the computational domain and boundary conditions are discussed in full detail there. The geometrical model is briefly reiterated here for completeness. The upper surface of the platform and the support structures in the geometrical model of the hand-cyclist were included in the CFD simulations. The geometry of the hand-cyclist was rotated using interface conditions to achieve matching yaw angles to the wind tunnel experiments. The geometry was static with no movement in the arms or wheels as per the wind tunnel experiments. The computational parameters matched those discussed in section 9.2.2.

9.3.2.2 Wind tunnel and CFD comparisons

Both the drag (Figure 9.6b) and the lateral (Figure 9.6c) numerical force predictions followed the same overall trends as their experimental counterparts. The numerical simulations correctly matched the direction of a low lateral force (Figure 9.7, y direction) at 0° yaw, and the increasing lateral force in the opposite direction thereafter (Figure 9.6c). In addition, a low deviation was found in the absolute force values between the numerical and experimental results. The average numerical drag deviation from the experimental results was 3.6% respectively. The average lateral force deviation was 9.1%. It is noted that the geometries used in the CFD simulations for this validation study matched those used in the wind tunnel experiments, including the wheel supports, baseplate, and platform depicted in Figure 9.6a. All aerodynamic force predictions from CFD and wind tunnel experiments were considered to be in good agreement.

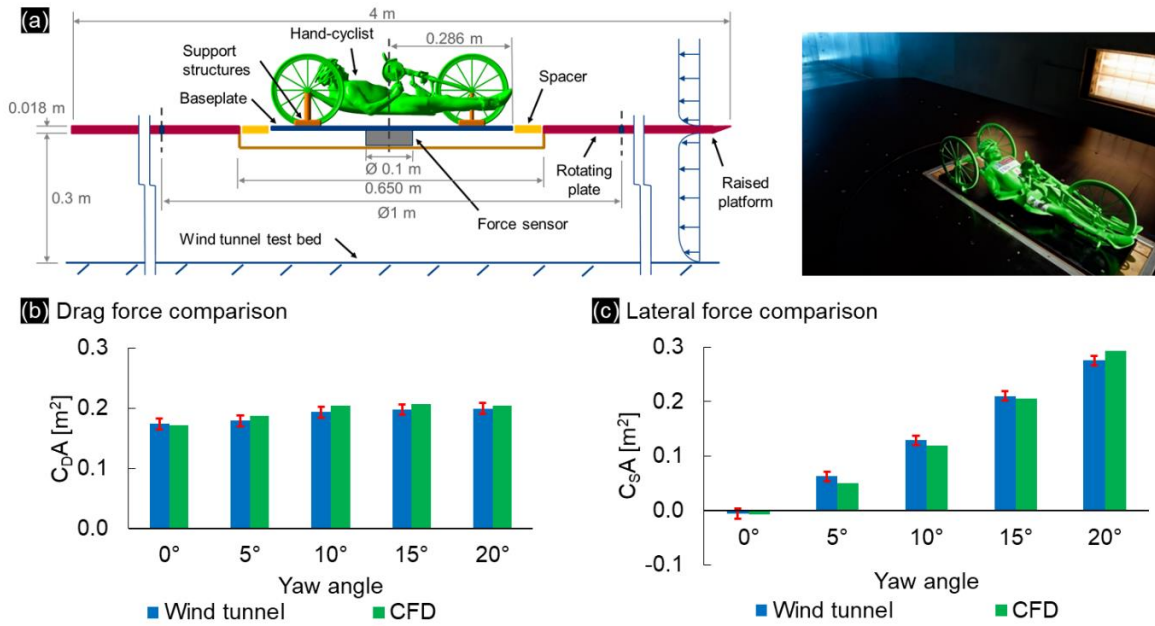


Figure 9.6. (a) Experimental setup. (b,c) Comparison of experimental and numerical (b) drag, and (c) lateral force area predictions.

9.4 Results

The results chapter is divided into two sub sections. The first, section 9.4.1, investigates the aerodynamics associated with the rear wheel spacing. The second, section 9.4.2, investigates the four wheel setups illustrated in Figure 9.1b under crosswind conditions and with the minimum and maximum rear wheel spacings allowed by the UCI (UCI, 2017).

The pressure coefficient (C_p) was used in the analysis of the numerical studies of hand-cycling aerodynamics:

$$C_p = \frac{\Delta P}{0.5\rho U^2} \quad (9.3)$$

where ΔP is the pressure difference between the location of interest and the ambient static pressure [Pa].

9.4.1 Rear wheel spacing

The spacing between the two parallel rear wheels on a competitive hand-cyclist can be adjusted between a minimum of 55 cm and a maximum of 70 cm (Figure 9.7), which represent the inner and outer limits set by the UCI (UCI, 2017). The spacing is measured from the point of contact of the wheel with the ground. This investigation was aimed to determine the optimum spacing for disk and free-spoked wheels on the rear axle of a hand-cycle to optimise aerodynamic drag. Four wheel spacings were simulated; 55 cm, 60 cm, 65 cm and 70 cm, each centred from the front wheel. All wheels were simulated as rotating, and the yaw angle was 0° for this study. All wheels were vertical with no camber.

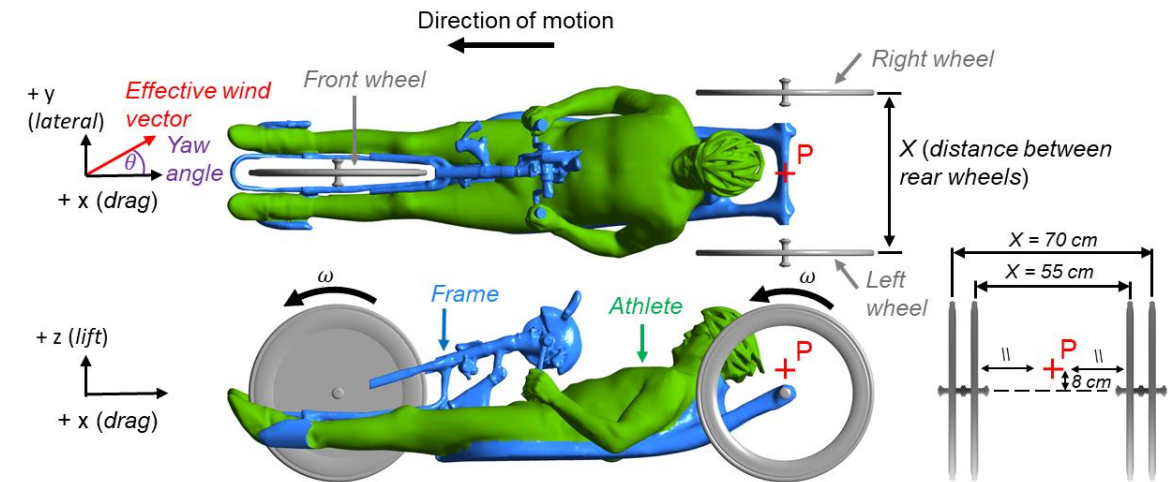


Figure 9.7. Breakdown of hand-cycle components, illustrating the distance ‘X’ between the rear wheels, and the location of point P for pressure coefficient point measurements.

The pressure coefficient was extracted from the simulations at P for all four spacings. Point P was located at the centre between both rear wheels; illustrated in Figure 9.7. Wheel combinations I and IV were used, with disk (I) and free-spoked wheels (IV) on the rear wheel and a disk wheel on the front axle for both combinations. Figure 9.8a compares the pressure coefficient at P for each of the setups. The under-pressure between the two wheels at P was found to decrease with smaller rear wheel spacings. This was found for both free-spoked and disk wheels on the rear axle. For the case of disk wheels, the smaller wheel spacings had a larger impact on the under-pressure than the free-spoked wheels, with a 13.1% reduction in under-pressure between 70 cm and 55 cm, by comparison to 10.1% for the free-spoked wheels. Figure 9.8b shows that the total drag was reduced for smaller rear wheel spacings. This finding was observed for both disk and free-spoked wheels. A net drag

reduction of 4.7% was found for the disk wheels between 70 cm and 55 cm rear wheel spacings, while the drag was reduced by 4.9% using free-spoked wheels between the same spacings.

The channelling of air between the two disk rear wheels may be reduced by the smaller wheel spacings due to the frontal area of the rear wheels being partially hidden behind the torso of hand-cyclist, and experiencing the wake flow from the hand-cyclist opposed to the free-stream flow. This theory was supported by a breakdown of the drag to just the athlete and frame surfaces, as per Figure 9.8c. A reduction in drag of similar proportions to the total C_{DA} was found for the athlete and frame surfaces with reduced spacing between rear disk wheels, which suggests a reduction in the channelling effect. An absolute reduction of 0.0064 m^2 was found for the total C_{DA} between 70 cm and 55 cm with rear disk wheels, and an absolute C_{DA} reduction of 0.0048 m^2 was found for the athlete and frame surfaces combined for the same setup. The free-spoked wheel setups followed a similar trend for the drag experienced by athlete and frame surfaces (Figure 9.8c). However, the minimum drag occurred at 60 cm rear wheel spacing opposed to the minimum spacing of 55 cm. This may be due to interaction between the free-spoked wheels and the wake of the hand-cyclist.

A drag breakdown of the wheels in Figures 9.8d-f provides further insight to the aerodynamic impacts of the rear wheel spacing. Figure 9.8d presents the drag experienced by the front disk wheel for all setups, where a low variability was found. This was attributed to the front wheel being centred far upstream from the rear wheels. Decreasing drag was found for both the left (Figure 9.8e) and right wheel (Figure 9.8f) regardless of wheel type with smaller rear wheel spacings. This was attributed to the frontal area of the wheels exiting the free-stream flow and entering the wake flow of the hand-cyclist. The maximum drag reductions between 70 cm and 55 cm rear wheel spacings were 7.8% and 20.5% for the left and right disk wheels respectively, and 5.4% and 12.0% for the free-spoked wheels. Note that the athlete was not symmetric but leaning slightly to his right. The hand-cycle frame was also not symmetric with brake handles, gear handles, mirror and sprocket cowl (safety cover) located at a single side. These non-symmetric geometric features are responsible for the right wheel experiencing greater drag reductions than the left.

It is noted that contrary to expectation, using disk wheels on the rear axle offered a less aerodynamic setup for the hand-cyclist opposed to free-spoked wheels for all wheel spacing's tested (Figure 9.8b). The disk wheels themselves experienced a lower drag than their free-spoked counterparts, but the negative impact of the disk wheels on the athlete and frame upstream was larger than the benefits to the wheels themselves.

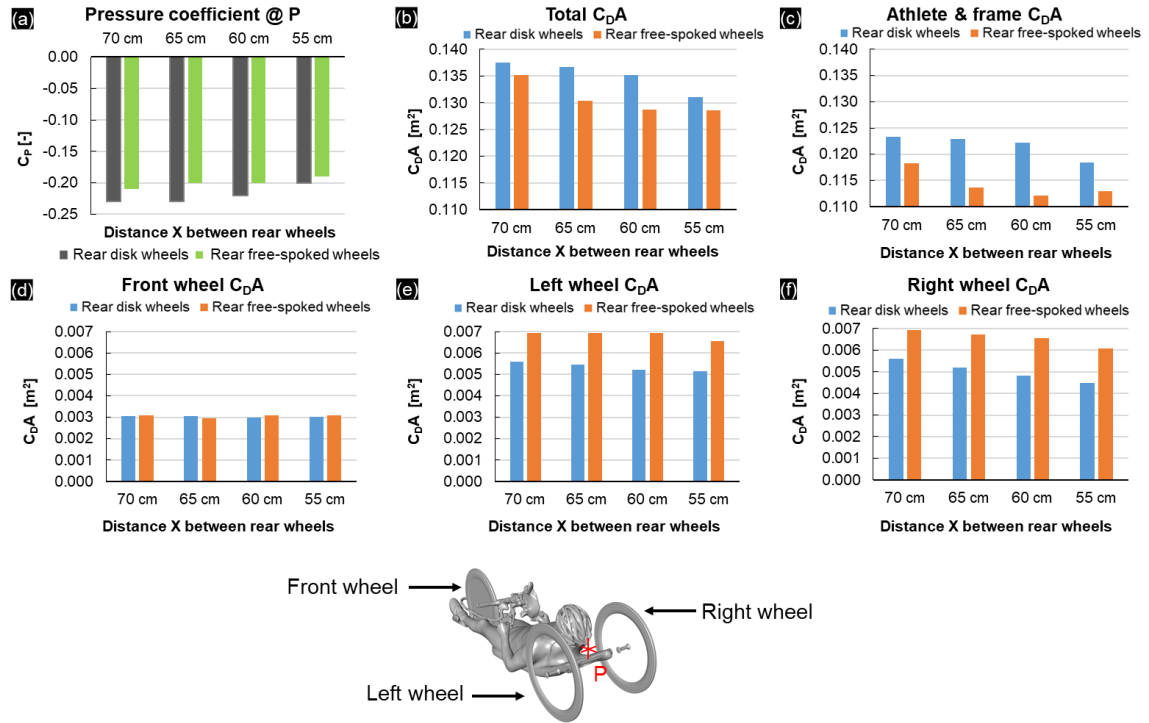


Figure 9.8. Comparisons at different wheel spacing's for (a) pressure coefficient at point P, (b) total C_{DA} , (c) athlete and frame C_{DA} , (d) front wheel C_{DA} , (e) left wheel C_{DA} , and (f) right wheel C_{DA} .

Further investigations were conducted to evaluate the impact of the wheel rotation on the channelling effect between the rear wheels, and the subsequent drag experienced by the hand-cyclist. The smallest rear wheel spacing of 55 cm was chosen for the evaluation of combinations I and IV, where both static and rotating wheels were simulated. The results are presented in Table 9.1. The static disk wheels with combination I were found to have a small impact on the total C_{DA} by comparison to rotating wheels, with a drag difference of 1.4%. The rotating wheels resulted in a drag increase for the hand-cyclist, similar to the drag finding for isolated static and rotating disk wheels (Figure 9.3). A smaller difference was found for the combination IV setup with rear free-spoked wheels, where a C_{DA} difference of 0.6% was recorded. The rotating simulation again experienced a higher drag than the static wheel setup. It was noted that that the larger under-pressure value was recorded for the rotating wheel setups, but the overall impact of the rotating wheels compared to static wheels at 0° yaw was small. Differences of -1.0% and -1.1% were found for the pressure coefficient at point P, for combination I with the rear disk wheels, and combination IV with rear free-spoked wheels, respectively. Modelling the wheels as static or rotating did not seem to have a significant impact on the drag of the hand-cyclist, and it may be possible that modelling wheels as static may be sufficient for some cycling studies depending on the objective. This can be seen elsewhere in the

literature for cycling aerodynamics applications (Blocken et al., 2018a). In addition, the rotation of the wheels did not appear to have a significant impact on the channelling effect between the two rear wheels. However, the geometry of the Zipp 404 wheels in this study did not contain any spokes, and it may be possible that the addition of spokes in a simulation that accounts for wheel rotation (e.g. sliding grid method) may affect the under-pressure between the two rear wheels, and consequently the drag of the hand-cyclist.

Table 9.1. Comparison of C_{DA} and C_P values for static and rotating wheel hand-cycling setups.

		C_{DA} [m ²]	C_P [-] @ P	ΔC_{DA}	ΔC_P
Combination I₅₅: Front disk, rear disk	Static	0.1292	-0.2045	+1.4%	-1.0%
	Rotating	0.1311	-0.2024		
Combination IV₅₅: Front disk, rear free-spoked	Static	0.1278	-0.1944	+0.6%	-1.1%
	Rotating	0.1286	-0.1923		

9.4.2 Crosswinds investigation

Four wheel setups as described in Figure 9.1b (combinations I-IV) were investigated under yaw angles of 0°, 5°, 10°, 15° and 20°. Two rear wheel spacings were analysed for each of the four setups; 70 cm and 55 cm, the maximum and minimum allowable by the UCI (UCI, 2017). This resulted in a total of 40 simulations for this study, with a typical grid size of 50 million cells. For efficient dissemination purposes, the rear wheel spacing dimension is added in subscript to the combination number. For example, combination IV₅₅ is the front disk – rear free-spoked wheel setup with 55 cm rear wheel spacing.

C_{DA} values are presented in Figure 9.9a₁-b₁ for the 70 cm and 55 cm wheel spacings respectively. Small variations ($\leq 5\%$) were found in the total C_{DA} between all setups at 0° yaw, for both wheel spacing's. However, at 0° yaw, all the hand-cycle wheel combinations with 55 cm wheel spacing's experienced a lower drag than their equivalent setups with 70 cm wheel spacing's. The total C_{DA} values were found to disperse with increasing yaw angle. A distinctive trend was found for both rear wheel spacings, with hand-cycle setups that featured a front free-spoked wheel performing worse than the setups that featured a front disk wheel at yaw angles between 10°-20°.

Maximum drag was observed at 15° yaw for all wheel variation setups, and minimum drag at 0°. At a rear wheel spacing of 70 cm and 0° yaw, the hand-cycling setup with three free-spoked wheels (combination II₇₀) provided the lowest C_DA of 0.1305 m², followed by the front disk – rear free-spoked setup at 0.1352 m² (combination IV₇₀), the front free-spoked – rear disk setup at 0.1364 m² (combination III₇₀), and lastly the all disk wheel setup at 0.1375 m² (combination I₇₀). The 55 cm rear wheel setups resulted in a lower total drag for each of the wheel combinations than the 70 cm spacings at 0° yaw. The same trend in the two best performing wheel setups, combinations II and IV, was also found at a 55 cm rear wheel spacing and 0° yaw. Combination II₅₅ yielded a C_DA of 0.1284 m², and combination IV₅₅ yielded a C_DA of 0.1286 m², 0.2% larger. Combination I₅₅ provided the second largest drag for the 55 cm wheel setup at 0° yaw, at 0.1311 m² and 2.1% greater than combination II₅₅, and combination III₅₅ yielded a C_DA of 0.1326 m² which was 3.3% greater than combination II₅₅. However, the best performing wheel setups at 0° did not hold throughout the yaw angles investigated. The combination IV wheel setups provided the second lowest C_DA at 0° yaw for both rear wheel spacings, but provided the lowest C_DA between 5°-20° for the 55 cm rear wheel spacings, and between 10°-20° for the 70 cm rear wheel spacing. The combination III₅₅ setup provided the highest C_DA values from 0°-15°, and the combination III₇₀ setup from 5°-20° yaw.

The drag experienced by each of the wheels across the four setups in crosswind conditions is mapped out in Figure 9.9a_{2,5} for the 70 cm rear wheel spacing, and in Figure 9.9b_{2,5} for the 55 cm rear wheel spacing. Similar drag trends across both rear wheel spacings were observed for each of the hand-cycling wheel combinations. Thrust forces (negative drag) were found opposed to drag forces on disk wheels for several yaw angles. At 10°, 15° and 20° yaw, thrust forces were experienced by the front disk wheel in both the all-disk wheel setup, and the front disk – rear free-spoked wheel setups. Thrust forces were observed on the front disk wheels for both the 70 cm and 55 cm rear wheel spacings. For combination I₇₀, the thrust force experienced by the front wheel at 20° yaw (-0.0023 m²) was similar in magnitude to the drag force experienced by either the left or right rear disk wheels (0.0022 m² and 0.0030 m² respectively, normalised as C_DA). The left disk wheel in the combination I₇₀ and combination III₇₀, also experienced a thrust force at 10°. However, these thrust forces were near-zero with C_DA values of -0.0006 m² and -0.0001 m² respectively. However, the drag trend throughout the range of crosswinds for the left disk wheel for combinations I₇₀, III₇₀, I₅₅, and III₅₅ bore some resemblance to the trend reported from the Zipp wind tunnel experiments (Godo et al., 2010) for an isolated Zipp Sub9 disk wheel. It is noted that the left wheel is the most removed from the wake and interference effects from the frame and athlete geometry of the three wheels on the hand-cycle; the right wheel is submerged in the wake of the hand-cycle as the yaw angle increases. The peak drag force was observed at 0° yaw for the left wheel disk wheel in the aforementioned wheel setups (combinations I₇₀, III₇₀, I₅₅, and III₅₅), and the minimum drag was observed at 10° yaw which

equated to a small thrust force, after which the drag rose to a value at 20° yaw which was less than half of the drag experienced at 0° yaw. The thrust force recorded in the wind tunnel experiments by Zipp was reported to be at 12.5° yaw (Godo et al., 2010). It is noted that the right disk wheel did not experience a thrust force at any yaw angle for any of the wheel combinations or rear wheel spacings, due to being submerged in the wake of the hand-cyclist as the yaw angle increased.

The front free-spoked wheels in combinations II and III, and for both rear wheel spacings, experienced drag trends (Figure 9.9a-b) similar to that of an isolated free-spoked wheel (Figure 9.5b). Maximum drag was recorded at 20° and minimum drag at 10°. The left free-spoked wheel in each of the aforementioned setups also experienced a similar trend, albeit with higher drag forces throughout due to the increased exposure to the free-stream air than the front wheel, which is located between the legs of the athlete. The right free-spoked wheel for all respective setups experienced drag trends similar to that of its disk wheel counterpart, with the drag reducing for increased yaw angles, due to being placed further within the wake of the hand-cyclist.

The lateral forces experienced by the hand-cyclist setups followed intuitive trends throughout the yaw range, based on the area exposed to the free-stream air. The rear wheel spacing had a low impact on the total C_{sA} . Combination II₅₅₋₇₀ provided the lowest C_{sA} values at yaw angles between 5° to 20° (Figure 9.10a-b). This setup was followed by the combinations IV₅₅₋₇₀, and combinations III₅₅₋₇₀ and I₅₅₋₇₀ followed in third and fourth places respectively. At 0° yaw, the wheel choice for the hand-cyclist had a negligible influence on the lateral force, but as the yaw angle increased, the free-spoked wheels experienced lower lateral forces than their disk wheel counterparts, which had a high impact on the total lateral force. The right wheel for all wheel combinations and rear wheel spacings was influenced the least by increasing yaw angle in terms of lateral force. This was due to the wake flow of the hand-cyclist enveloping the right wheel with increasing yaw angle. At yaw angles of 0°, the left and right wheels (both disk and free-spoked) were found to experience near-equal lateral forces in opposite directions due to the low-pressure region generated on one side of the wheel, from the air being channelled between the two wheels. This occurrence was also observed at 5° for some wheel setups, albeit with the left wheel experiencing a higher lateral force than the right wheel due to its increased exposure to the free-stream air.

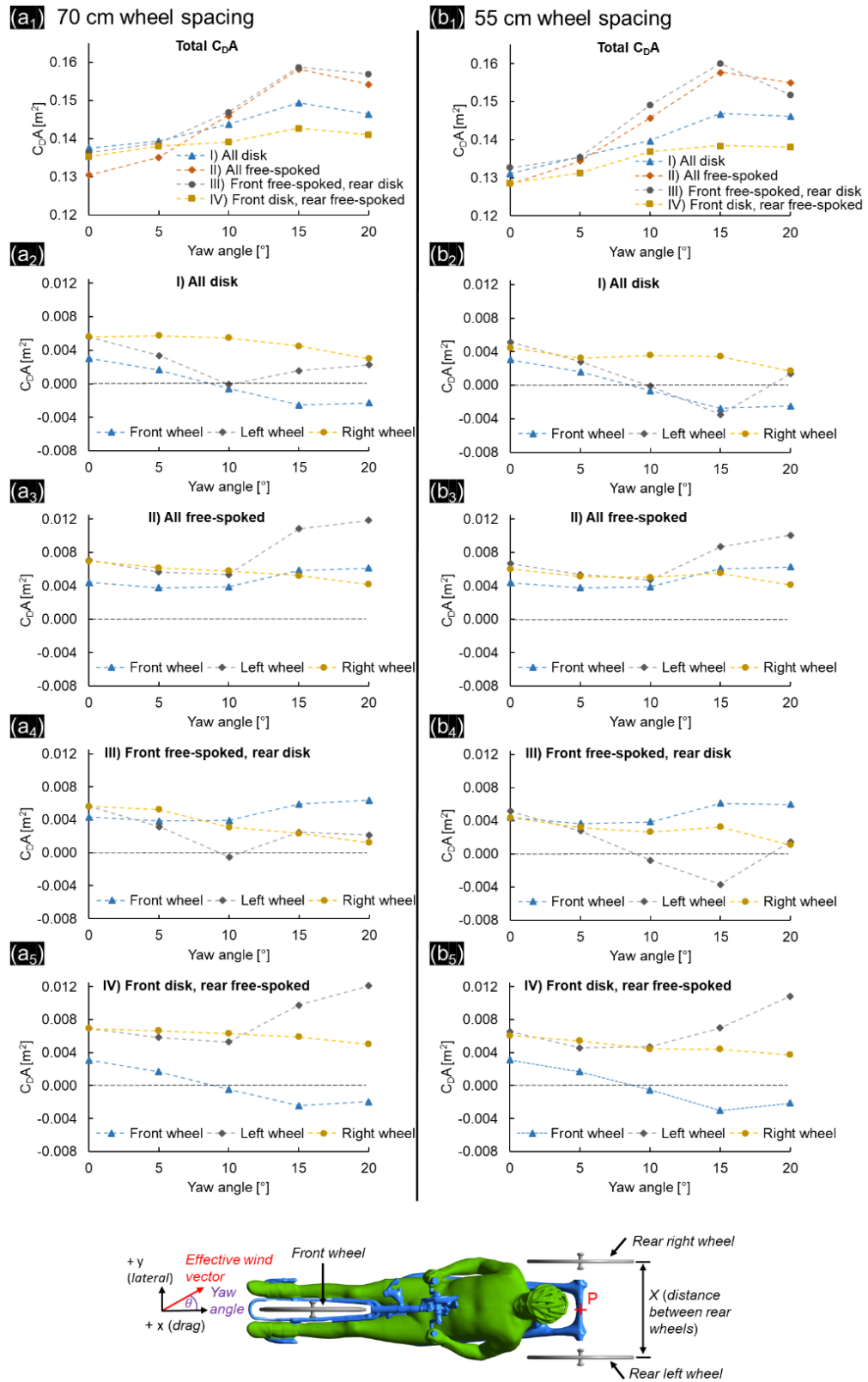


Figure 9.9. Drag area breakdown for each of the four hand-cycling wheel setups under crosswind conditions, for (a) 70 cm rear wheel spacing and (b) 55 cm rear wheel spacing.

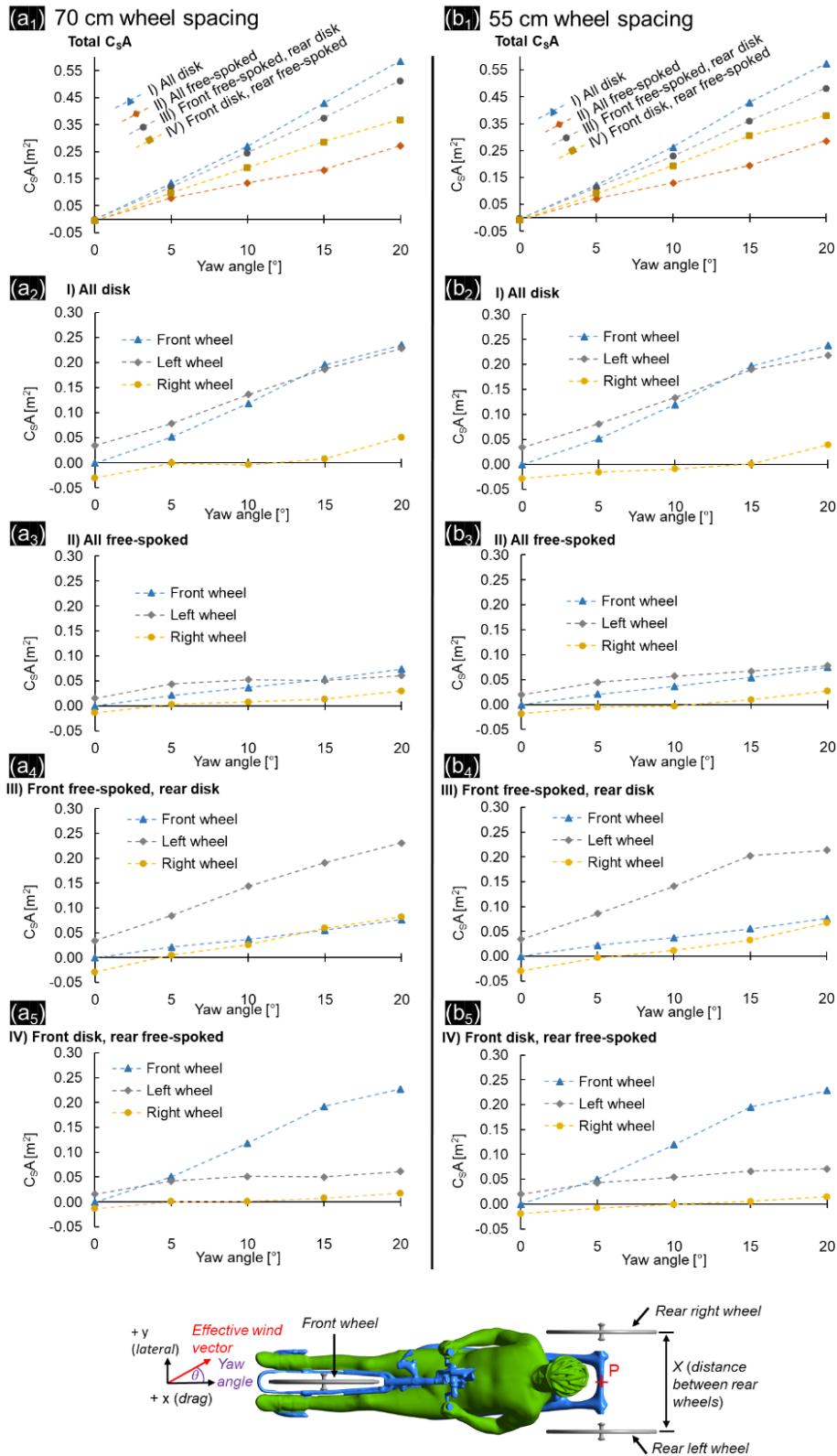


Figure 9.10. Lateral force area breakdown for each of the four hand-cycling wheel setups under crosswind conditions, for (a) 70 cm rear wheel spacing and (b) 55 cm rear wheel spacing.

9.5 Discussion

Two independent validation studies coupled with several grid sensitivity studies were conducted to ensure reliable CFD simulations were used for this research. Several grid sensitivity studies ensured suitable spatial discretisation. Wind tunnel experiments were used to validate the CFD methodology for a static hand-cyclist in crosswind conditions. To confirm that rotating wheels were modelled accurately, isolated rotating Zipp Sub9 disk and free-spoked Zipp 404 wheels were simulated and the results compared to wind tunnel and numerical data available in the literature (Godo et al., 2010). These studies confirmed the reproduction of drag trends in crosswind conditions for both wheels. Furthermore, it was confirmed that the representative drag trend of the free-spoked Zipp 404 wheel could be attained with the geometry of the spokes removed, thus reducing the computational cost of further numerical investigations.

Four rear wheel spacings (for competitive H1-H4 class hand-cyclists) were investigated in this study at 0° yaw. Two wheel setups were used, combinations I and IV (Figure 9.1b) to investigate the impact of the rear wheel spacings when disk wheels or free-spoked wheels were used on the rear axle of the hand-cycle. The four rear wheel spacings consisted of consecutive spacing's in 5 cm increments were tested between a maximum and minimum of 70 cm and 55 cm allowed by the UCI regulations. For smaller rear wheel spacings, the drag on both the rear wheels, the athlete and frame geometries was reduced. This was observed for both disk and free-spoked wheels. Maximum aerodynamic drag reductions of 4.7% were found for disk wheels at a 55 cm rear wheel spacing (opposed to a 70 cm rear wheel spacing), and 4.9% for the free-spoked wheels (at the same spacings). It was noted that the free-spoked wheels contained only the tyres, rim and hub, and that the rotating spokes might have impacted the under-pressure region between the two rear wheels. Furthermore, a 0.1% difference in total drag was found between the 55 cm and 60 cm rear wheel spacings with combination IV (rear free-spoked wheels). 60 cm rear wheel spacing would be preferable to the 55 cm spacing in this case due to the additional stability provided by the larger spacing. The drag benefit for the 55 cm rear wheel spacing was found to hold through 0° to 20° yaw for the all-disk wheel combination (combination I), and the front disk – rear free-spoked wheel combination (IV). Drag benefits at 55 cm rear wheel spacings were also found for the all free-spoked (combination II) and front free-spoked – rear disk wheel combination (combination III), except at 20° for combination II, and at 10° and 15° for combination III.

Peak drag forces for each wheel selection was at 15° yaw, and minimum drag was at 0° yaw. This was in agreement with the finding by Fintelman et al. (2015b), who also determined that the peak drag for a regular able-bodied cyclist occurred at 15° yaw (also using free-spoked wheels). In

contrast, Mannion et al. (2018a) reported maximum drag for a TT hand-cyclist with three disk wheel geometries occurred at 5° yaw. However, static wheels were used in this study, which contained additional geometric simplifications. In addition, the wheel shapes were convex (from the rim to the hub) by comparison to the flat disks used in the present study. It is noted that Fintelman et al. (2015b) investigated yaw angles in 15° increments, and the numerical study in 5° increments, and thus the exact peak yaw angle in 1° increments is not known.

The wheel combination used for competitive hand-cycling, free-spoked, disk or some combination thereof, was found to be key for optimising competitive hand-cyclists aerodynamically. Using IV₅₅ reduced the drag of the hand-cyclist by 3.1% at 0° yaw over combination III₅₅ for example. This reduction was 15.6% at 15° yaw, and averaged at 8.2% over the yaw angles of 0°, 5°, 10°, 15° and 20°. It was found that a disk wheel on the front axle for a hand-cycle positively impacted the drag performance of the hand-cyclist as a whole in yaw conditions, by comparison to a free-spoked wheel. Under yaw conditions, a front disk wheel redirected the air to some extent, positively impacting the drag on the athlete, hand-cycle frame, and rear wheels located downstream of its location. The lowest C_DA in this study was recorded for combination II₅₅; at 0.1284 m² for 0° yaw. Combination IV₅₅ provided the second lowest C_DA measurement at the same yaw angle; at 0.1286 m², however just at 0.2% higher which is considered insignificant given the geometrical simplifications of the free-spoked wheels in this study. However, combination IV₅₅ provided significantly lower C_DA at all other yaw angles investigated (5°, 10°, 15° and 20°) from a minimum of 2.0% at 5° and a maximum of 24.5% at 15°, and thus is considered to provide the best overall aerodynamic solution.

The impact of wheel selection on roll-over can be evaluated from the lateral forces, as indicated by Mannion et al. (2018a). Combination IV would provide the second best overall performance in this regard (Figure 9.10). Smaller rear wheel spacing may impact roll-over stability when cornering at speed, and it is recommended that practitioners consider this outcome when adjusting rear wheel spacing for aerodynamic purposes. Rear disk wheels increase the lateral force experienced by the hand-cyclist (Figure 9.10), further contributing to the potential of rollover when cornering at speed which bears similarity to yawing; and thus are not recommended. The yaw moment resulting from different wheel setups was not expected to influence the stability of the hand-cyclist due to the additional friction from the two rear wheels, opposed to one on a traditional bicycle. Furthermore, the axis around which the steering moment acts for the front wheel is near-parallel to the ground plane, where the wheel tilts to one side to achieve steering. Thus, yaw moments on the front wheel were not expected to impact steering capabilities.

Interesting aerodynamic features found from using disk wheels included thrust forces being generated at specific yaw angles, by the front wheel and the left rear wheel. These wheels were exposed to the free-stream air under the yaw angles analysed. In contrast, the right wheel did not

generate thrust force at any yaw angle; being enveloped in the wake of the hand-cyclist. A disk wheel on the front axle generated thrust forces at 10° , 15° , and 20° yaw. The left disk wheels also generated a thrust force at 10° and 15° yaw for combination I_{55} , and at just 10° yaw for I_{70} . Despite up to two wheels generating a thrust force at some yaw angles, such as the front and left disk wheels at 15° yaw for combination I_{55} , it was not the drag experienced by the wheels themselves that dictated the C_{DA} trends of the total drag in yaw conditions. The net drag of the three wheels for all hand-cycling setups experienced a trend opposite to the total drag, with drag decreasing between 0° - 10° or 0° - 15° , and increasing thereafter, opposed to the total drag of the hand-cyclist increasing between 0° - 15° yaw. Instead, it was the influence the wheel selection had on the flow field, which in turn interacted with the athlete and frame that ultimately determined the total drag trends between wheel selections. A front disk wheel turning the flow at higher angles for the athlete downstream is one such example. However, in contrast to this, the lateral force experienced by the wheels themselves contributed largely to the total C_{SA} , with the wheels on the combination I_{70} contributing between 87.5% to 96.7% of the total lateral force at 20° and 5° yaw respectively. The rear wheel spacing also had a low impact on the total C_{SA} trends for each of the four wheel combinations. A logical trend was observed for the impact on wheel selection and combinations on the C_{SA} throughout all yaw angles investigated; larger forces were observed when disk wheels were used due to the increase in lateral area. Interaction between vortices from the front and rear wheels were also observed under yaw conditions.

There were several limitations to this study that could be addressed with further research. Firstly, the hand-cyclist was static with the arm-crank position at its lowest in its rotational cycle. A dynamic hand-cyclist turning the crank would result in a higher total C_{DA} averaged over several arm-crank cycles (Belloli et al., 2014). Secondly, all surfaces were considered to be smooth, with no roughness accounted for. Thirdly, the spokes were removed from the geometry of the free-spoked wheels. Further research is recommended on this topic, and sliding grids are recommended to evaluate the impact of different spoke counts and spoke shapes for both the front wheel, and the two parallel rear wheels. The wake from the spokes on the front wheel may impact the aerodynamics of the hand-cyclist and two rear wheels downstream of its location. Furthermore, the spokes of the two parallel rear wheels may have an impact on the under-pressure region between the two wheels, which in turn may impact the suction drag experienced by the athlete and hand-cycle frame surfaces in this location. In addition, investigating variations in rim depth for spoked wheels, and aero-spoked wheels such as tri-spoke wheels, could yield further optimisations. Various wheel diameters are also allowed within the UCI rules (UCI, 2017). Thus, there are numerous wheel combinations left to be tested. Finally, the impact of cambered wheels for hand-cycling aerodynamics is yet unknown, which are prominently featured by H5 category hand-cyclists in competitive events.

It was noted that the optimum wheel selection was based on the specific wheels tested in this study, and that other wheel types and designs might have provided different results. For example, standard shallow rim 36 spoke wheels would likely not provide the same aerodynamic performance as the Zipp 404's in this study. In addition, wheels with deeper rim sections such as the Zipp 808 might provide better (or worse) results than the Zipp 404 for hand-cycling aerodynamics. Optimum wheel selection for 0° might also have a dependency on the individual athletes and hand-cycles, where small differences between some wheel selections were observed in this study, in particular when the rear wheel spacing was set to its minimum of 55 cm. Potential differences might also arise between the recumbent H1-H4 category hand-cyclists, and the upright H5 category hand-cyclists. Additional studies using unsteady CFD methods are recommended, that could yield further insights into the peak and fluctuating aerodynamic forces. The pseudo-transient approach followed in the present study does not allow for such transient information to be obtained, and such transient studies could provide further insights for minimising aerodynamic drag.

9.6 Conclusions

Two numerical studies were conducted to investigate the hand-cycling aerodynamics, including the impact of rear wheel spacing, and the crosswind scenarios with different free-spoked and disk wheel combinations. Validation for the numerical simulations was two-fold, with comparisons made to bespoke wind tunnel experiments of a hand-cyclist, and additional comparisons made to wind tunnel and numerical simulations of an isolated free-spoked Zipp 404 wheel and a Zipp Sub9 disk wheel, as reported by Godo et al. (2010).

Smaller rear wheel spacings for H1-H4 category hand-cyclists were deemed to yield lower aerodynamic drag, regardless of whether free-spoked or disk wheels were used. A drag reduction of 4.6% and 4.9% was found between maximum and minimum spacing's of 70 cm and 55 cm at 0° yaw when using disk and free-spoked wheels respectively on the rear axle. However, the rear wheel spacing has smaller impacts on the total drag at higher yaw angles.

An optimum wheel selection was found for competitive hand-cycling that provided the lowest overall drag and acceptable response to lateral forces in crosswind conditions. This selection was a disk wheel in the front, and free-spoked wheels in the rear with a 55 cm spacing between the two rear wheels. Indeed, at 0° yaw, the front disk – rear free-spoked wheel combination (combination IV) with

55 cm rear wheel spacing provided the second lowest C_{DA} recorded in this study; 0.1286 m^2 . The all free-spoked setup (combination II) with 55 cm rear wheel better was marginally better at 0° with a C_{DA} of 0.1284 m^2 ; a marginal difference of 0.2%. However, at all yaw angles between 5° - 20° , the combination IV₅₅ setup provided the lowest C_{DA} . In addition, the spokes in the wheels for the combination II setups were removed, which may increase the drag if included, implying that the combination IV setups might yield lower aerodynamic drag than the combination II setup at 0° in actual cycling conditions, due to spokes being added to the geometry of three wheels compared to just two for the combination IV setup. Combination II provided the lowest sensitivity to crosswinds out of the four wheel combinations tested, with the lowest recorded C_{SA} values throughout the yaw range provided, for both rear wheel spacings. However, combination IV setups provided the second lowest C_{SA} ranges, and is considered an acceptable compromise considering the drag performance for this wheel combination. A low sensitivity to rear wheel spacing was observed for the lateral forces in crosswind conditions.

The results of this study can be used to inform athletes and coaches of the importance and impact of their wheel selection with regards to aerodynamics, and how they may best optimise their aerodynamics for future competitive events.

9.7 References

ANSYS Fluent. (2017). ANSYS Fluent Theory Guide. *Release 18.2 Documentation*.

Artec Europe. (2017). Artec Eva, 3D Scanners. Retrieved May 22, 2017, from <https://www.artec3d.com/3d-scanner/artec-eva>

Automation, A. I. (2018). F/T Sensor Delta. Retrieved April 4, 2018, from www.atia.com/app_content/Documents/9230-05-1330.auto.pdf

Barlow, J. B., Rae, W. H., & Pope, A. (1999). *Low-speed Wind Tunnel Testing* (3rd ed.). John Wiley & Sons.

Barry, N., Burton, D., Sheridan, J., Thompson, M., & Brown, N. A. T. (2015a). Aerodynamic drag interactions between cyclists in a team pursuit. *Sports Engineering*, *18*, 93–103. <https://doi.org/10.1007/s12283-015-0172-8>

Barry, N., Burton, D., Sheridan, J., Thompson, M., & Brown, N. A. T. (2015b). Aerodynamic

performance and riding posture in road cycling and triathlon. *Proceedings of the Institution of Mechanical Engineers, Part P: Journal of Sports Engineering and Technology*, 229(1), 28–38. <https://doi.org/10.1177/1754337114549876>

Barry, N., Burton, D., Sheridan, J., Thompson, M., & Brown, N. A. T. (2016). Flow field interactions between two tandem cyclists. *Experiments in Fluids*, 57(12), 1–14. <https://doi.org/10.1007/s00348-016-2273-y>

Belloli, M., Cheli, F., Bayati, I., Giappino, S., & Robustelli, F. (2014). Handbike aerodynamics: wind tunnel versus track tests. In *The 2014 conference of the International Sports Engineering Association, Procedia Eng.* (Vol. 72, pp. 750–755). Elsevier B.V. <https://doi.org/10.1016/j.proeng.2014.06.127>

Blocken, B. (2015). Computational Fluid Dynamics for urban physics: Importance, scales, possibilities, limitations and ten tips and tricks towards accurate and reliable simulations. *Building and Environment*, 91, 219–245. <https://doi.org/10.1016/j.buildenv.2015.02.015>

Blocken, B., Defraeye, T., Koninckx, E., Carmeliet, J., & Hespel, P. (2013). CFD simulations of the aerodynamic drag of two drafting cyclists. *Computers & Fluids*, 71, 435–445. <https://doi.org/10.1016/j.compfluid.2012.11.012>

Blocken, B., & Toparlar, Y. (2015). A following car influences cyclist drag: CFD simulations and wind tunnel measurements. *Journal of Wind Engineering and Industrial Aerodynamics*, 145(0), 178–186. <https://doi.org/10.1016/j.jweia.2015.06.015>

Blocken, B., Toparlar, Y., & Andrianne, T. (2016). Aerodynamic benefit for a cyclist by a following motorcycle. *Journal of Wind Engineering and Industrial Aerodynamics*, 155, 1–10. <https://doi.org/https://doi.org/10.1016/j.jweia.2016.04.008>

Blocken, B., van Druenen, T., Toparlar, Y., Malizia, F., Mannion, P., Andrianne, T., Marchal, T., Maas, G.J., Diepens, J. (2018a). Aerodynamic drag in cycling pelotons: New insights by CFD simulation and wind tunnel testing. *Journal of Wind Engineering and Industrial Aerodynamics*, 179(May), 319–337. <https://doi.org/10.1016/J.JWEIA.2018.06.011>

Blocken, B., Druenen, T. Van, Toparlar, Y., Andrianne, T., & Marchal, T. (2018b). Numerical analysis of drag of different cyclist positions for hill descent. *Journal of Wind Engineering & Industrial Aerodynamics*, 31(c), 8595. <https://doi.org/10.1016/j.jweia.2018.08.010>

Casey, M., & Wintergerste, T. (2000). Best Practice Guidelines. *ERCOFTAC Special Interest Group on “Quality and Trust in Industrial CFD.”* ERCOFTAC.

- Crouch, T. N., Burton, D., LaBry, Z. A., & Blair, K. B. (2017). Riding against the wind: a review of competition cycling aerodynamics. *Sports Engineering*, 20(2), 81–110.
<https://doi.org/10.1007/s12283-017-0234-1>
- Crouch, T., Sheridan, J., Burton, D., Thompson, M., & Brown, N. A. T. (2012). A quasi-static investigation of the effect of leg position on cyclist aerodynamic drag. *Procedia Engineering*, 34, 3–8. <https://doi.org/10.1016/j.proeng.2012.04.002>
- Defraeye, T., Blocken, B., Koninckx, E., Hespel, P., & Carmeliet, J. (2010). Aerodynamic study of different cyclist positions: CFD analysis and full-scale wind-tunnel tests. *Journal of Biomechanics*, 43(7), 1262–1268. <https://doi.org/10.1016/j.jbiomech.2010.01.025>
- Fintelman, D. M., Sterling, M., Hemida, H., & Li, F.-X. (2014). Optimal cycling time trial position models: Aerodynamics versus power output and metabolic energy. *Journal of Biomechanics*, 47(8), 1894–1898. <https://doi.org/10.1016/j.jbiomech.2014.02.029>
- Fintelman, D. M., Sterling, M., Hemida, H., & Li, F.-X. (2015a). The effect of time trial cycling position on physiological and aerodynamic variables. *Journal of Sports Sciences*, 0414(April 2015), 1–8. <https://doi.org/10.1080/02640414.2015.1009936>
- Fintelman, D. M., Hemida, H., Sterling, M., & Li, F.-X. (2015b). CFD simulations of the flow around a cyclist subjected to crosswinds. *Journal of Wind Engineering and Industrial Aerodynamics*, 144, 31–41. <https://doi.org/10.1016/j.jweia.2015.05.009>
- Franke, J., Hellsten, A., Schlünzen, H., & Carissimo, B. (2010). The best practise guideline for the CFD simulation of flows in the urban environment: an outcome of COST 732. *The Fifth International Symposium on Computational Wind Engineering (CWE2010)*, 1–10.
- Godo, M., Corson, D., & Legensky, S. (2009). An aerodynamic study of bicycle wheel performance using CFD. In *47th AIAA Aerospace Sciences Annual Meeting*. Orlando, Florida: AIAA.
<https://doi.org/10.2514/6.2009-322>
- Godo, M., Corson, D., & Legensky, S. (2010). A comparative aerodynamic study of commercial bicycle wheels using CFD. *48th AIAA Aerospace Sciences Meeting*, (2010–1431).
- Griffith, M. D., Crouch, T., Thompson, M. C., Burton, D., & Sheridan, J. (2014). Computational fluid dynamics study of the effect of leg Position on cyclist aerodynamic drag. *The American Society of Mechanical Engineers, Journal of Fluids Engineering*, 136.
<https://doi.org/10.1115/1.4027428>
- Kyle, C. R., & Burke, E. R. (1984). Improving the racing bicycle. *Mechanical Engineering*, 106(9),

- Lukes, R. a, Chin, S. B., & Haake, S. J. (2005). The understanding and development of cycling aerodynamics. *Sports Engineering*, 8, 59–74. <https://doi.org/10.1007/BF02844004>
- Mannion, P., Toparlar, Y., Blocken, B., Clifford, E., Andrienne, T., & Hajdukiewicz, M. (2018a). Analysis of crosswind aerodynamics for competitive hand-cycling. *Journal of Wind Engineering and Industrial Aerodynamics*, 180(August), 182–190. <https://doi.org/10.1016/j.jweia.2018.08.002>
- Mannion, P., Toparlar, Y., Blocken, B., Hajdukiewicz, M., Andrienne, T., & Clifford, E. (2018b). Improving CFD prediction of drag on Paralympic tandem athletes: Influence of grid resolution and turbulence model. *Sports Engineering*, 21(2), 123–135. <https://doi.org/10.1007/s12283-017-0258-6>
- Mannion, P., Toparlar, Y., Blocken, B., Clifford, E., Andrienne, T., & Hajdukiewicz, M. (2018c). Aerodynamic drag in competitive tandem para-cycling: road race versus time-trial positions. *Journal of Wind Engineering & Industrial Aerodynamics*, 179, 92–101. <https://doi.org/10.1016/j.jweia.2018.05.011>
- Mannion, P., Toparlar, Y., Clifford, E., Hajdukiewicz, M., Andrienne, T., Blocken, B. On the effects of crosswinds in tandem aerodynamics: An experimental and computational study, *Eur. J. Mech. B/Fluids*. 74 (2019) 68–80. doi:10.1016/j.euromechflu.2018.11.001.
- Mazzola, M., Andreoni, G., Campanardi, G., Costa, F., Gibertini, G., Grassi, D., & Romero, M. (2012). Effects of seat and handgrips adjustments on a Hand Bike vehicle. An ergonomic and aerodynamic study for a quantitative assessment of Paralympics athletes's performance. *Advances in Usability Evaluation Part I*, (November 2017), 7167–7174.
- Menter, F. R. (1994). Two-equation eddy-viscosity turbulence models for engineering applications. *AIAA Journal*, 32(8), 1598–1605. <https://doi.org/10.2514/3.12149>
- Oggiano, L., Leirdal, S., Sætran, L., & Ettema, G. (2008). Aerodynamic Optimization and Energy Saving of Cycling Postures for International Elite Level Cyclists. *The Engineering of Sport* 7, 1(2), 597–604. https://doi.org/10.1007/978-2-287-09411-8_70
- Roache, P. J. (1994). Perspective: A method for uniform reporting of grid refinement studies. *Journal of Fluids Engineering*, 116(3), 405–413.
- Roache, P. J. (1997). Quantification of uncertainty in computational fluid dynamics. *Annual Review of Fluid Mechanics*, 29, 123–160. <https://doi.org/10.1146/annurev.fluid.29.1.123>

Sapim. (2011). CX-RAY | Sapim. Retrieved July 23, 2018, from
<http://www.sapim.be/spokes/aero/cx-ray>

Tominaga, Y., Mochida, A., Yoshie, R., Kataoka, H., Nozu, T., Yoshikawa, M., & Shirasawa, T. (2008). AIJ guidelines for practical applications of CFD to pedestrian wind environment around buildings. *Journal of Wind Engineering and Industrial Aerodynamics*, 96(10–11), 1749–1761. <https://doi.org/10.1016/j.jweia.2008.02.058>

UCI. (2017). Cycling Regulations, Part 16 Para-Cycling, version on 01/02/2017. Union Cycliste Internationale. Retrieved from
http://www.uci.ch/mm/Document/News/Rulesandregulation/16/26/73/16-PAR-20170201-E_English.PDF

Underwood, L., & Jermy, M. (2013). Optimal handlebar position for track cyclists. *Sports Engineering*, 16(2), 81–90. <https://doi.org/10.1007/s12283-013-0111-5>

The impact of arm-crank position on the drag of a Paralympic hand-cyclist

This chapter builds on Chapter 7 and 8, using the best performing grid parameters and turbulence model choice to investigate the aerodynamics arm-crank positions for hand-cycling. Four arm-crank positions were investigated, and the results applied to a descent scenario in a road race event. Crosswinds were considered in the analyses. Recommendations are made for tactics in competitive race events.

This study has been accepted for publication in the international peer-reviewed journal *Computer Methods in Biomechanics and Biomedical Engineering*:

Mannion, P., Toparlar, Y., Clifford, E., Hajdukiewicz, M., Andrienne, T., & Blocken, B. (2019). The impact of arm-crank position on the drag of a Paralympic hand-cyclist. *Computer Methods in Biomechanics and Biomedical Engineering*. In Press.
DOI: 10.1080/10255842.2018.1558217

Abstract: The aerodynamic features associated with the rotation of a cyclist's legs have long been a research topic for sport scientists and engineers, with studies in recent years shedding new light on the flow structures and drag trends. While the arm-crank rotation cycle of a hand-cyclist bears some resemblance to the leg rotation of a traditional cyclist, the aerodynamics around the athlete are fundamentally different due to the proximity and position of the athlete's torso with respect to their arms, especially since both arm-cranks move in phase with each other. This research investigates the impact of arm-crank position on the drag acting on a hand-cyclist and is applied to a hill descent position where the athlete is not pedalling. Four primary arm-crank positions, namely 3, 6, 9 and 12 o'clock of a Paralympic hand-cyclist were investigated with CFD for five yaw angles, namely 0°, 5°, 10°, 15° and 20°. The results demonstrated that the 3 and 12 o'clock positions (when observed from the left side of the hand-cyclist) yielded the highest drag area at 0° yaw, while the 9 o'clock position yielded the lowest drag area for all yaw angles. This is in contrast to the 6 o'clock position traditionally held by hand-cyclists during a descent to reduce aerodynamic drag.

10.1 Introduction

Recumbent hand-cycling (Figure 10.1) is a Paralympic sport with four categories, H1-H4 (UCI, 2017). The athletes power the hand-cycle with their arms, as opposed to legs as in traditional able-bodied cycling. The athlete's head, torso and legs remain largely static throughout the motion of cycling. The arms rotate a crank, which powers the front wheel via a chain. Little is known regarding the aerodynamics of the arm-crank rotation cycle. Traditionally, hand-cyclists adopt an arm-crank position at its lowest vertical position when descending in a race. If clock time positions are applied to the arm-crank positions, referenced from the left side of the hand-cyclist, this aerodynamic arm-crank position would be at 6 o'clock (Figure 10.1). This arm-crank position can be perceived to minimise the projected frontal area of the hand-cyclist, which in turn is associated with reducing aerodynamic drag (Debraux et al., 2011). In addition, this 6 o'clock position would be a resting position for the athlete's arms.

Positioning is a popular topic in traditional able-bodied cycling where the leg positioning can play an important role in the aerodynamic drag. Wind tunnel experiments on the leg positions of an able-bodied traditional cyclist have been conducted by Crouch et al. (2014), using a mannequin to ensure precise 15° increments in the leg positioning. It was found that both the wake flow regime and the drag experienced by the cyclist changed significantly throughout the rotation of the legs. A near symmetric wake flow was found for the lowest drag scenario when the pedals were aligned on a near horizontal plane, with a firmly asymmetric flow regime for the highest drag scenario (pedals aligned on a near vertical plane). The drag coefficient was found to vary by up to 15% throughout the leg rotation cycle. Fintelman et al. (2015) used a mannequin to conduct repeatable wind tunnel experiments and CFD simulations of a traditional able-bodied cyclist in crosswind conditions. Yaw angles from 0°-90° were investigated in 15° increments. Variations of 9% were found between the experimental and numerical predictions for the drag force, with larger variations of 21% in the lateral force predictions. Crouch et al. (2016) further investigated the relationship between the motion of an athlete's legs and aerodynamic drag. The wake flow behind both static and pedalling cyclists was analysed and quantified. It was suggested that limited aerodynamic gains would be available by adjusting a cyclist's cadence through non-uniform, or non-circular, pedal strokes.

Focusing specifically on hand-cyclists, Belloli et al. (2014) conducted wind tunnel experiments on the 6 o'clock arm-crank position, called the "aerodynamic stage" (Belloli et al., 2014), yielding a C_{DA} of 0.20 m². A dynamic wind tunnel experiment was also conducted by Belloli et al. (2014), with the athlete rotating the hand-cycle's crank. Data was sampled at 500 Hz over 20 seconds with an RPM (revolutions per minute) of 70. A slightly higher average C_{DA} of 0.21 m² was found. Track tests on the London 2012 Brand Hatch circuit by Belloli et al. (2014) provided further evidence

for an increased C_{DA} experienced by hand-cyclists during propulsive stages of racing (the athlete provides power by rotating the crank), where a C_{DA} of 0.204 m^2 was found for the aerodynamic stage (at a 6 o'clock arm-crank position), and C_{DA} of 0.245 m^2 was found for the propulsive-dynamic stage. This 20.1% increase in the C_{DA} from aerodynamic stage to propulsive stage for the outdoor track tests is in contrast to the 5.0% increase found for the same experiment replicated in the wind tunnel. The outdoor environment could be a large factor contributing to this difference, with the potential for crosswinds and turbulence contributing to an increased drag at different arm-crank positions through the dynamic cycle. In addition, the ratio between cycling speed (wheel rotational velocity) and cadence could be a contributing factor to this difference, where the cycling speed and cadence was held steady in the wind tunnel experiment, but would vary naturally due to the slopes present on the track tests. Further differences could have been present with the posture or apparel of the athlete between both testing methods.

Further knowledge into the arm-crank position of hand-cyclists could yield novel information to aid with both aerodynamic optimisation (skin-suit development, arm-crank positions for descents, etc.) and further understanding of the aerodynamic characteristics of hand-cyclists. For this purpose, in the present study, CFD simulations validated by wind tunnel experiments were conducted to provide further insight into the aerodynamics of hand-cyclists' changing arm-crank positions. A single arm-crank position was analysed using wind tunnel experiments, and, following the validation study, four arm-crank positions, namely 3, 6, 9 and 12 o'clock (Figure 10.1) were chosen for analysis using CFD.

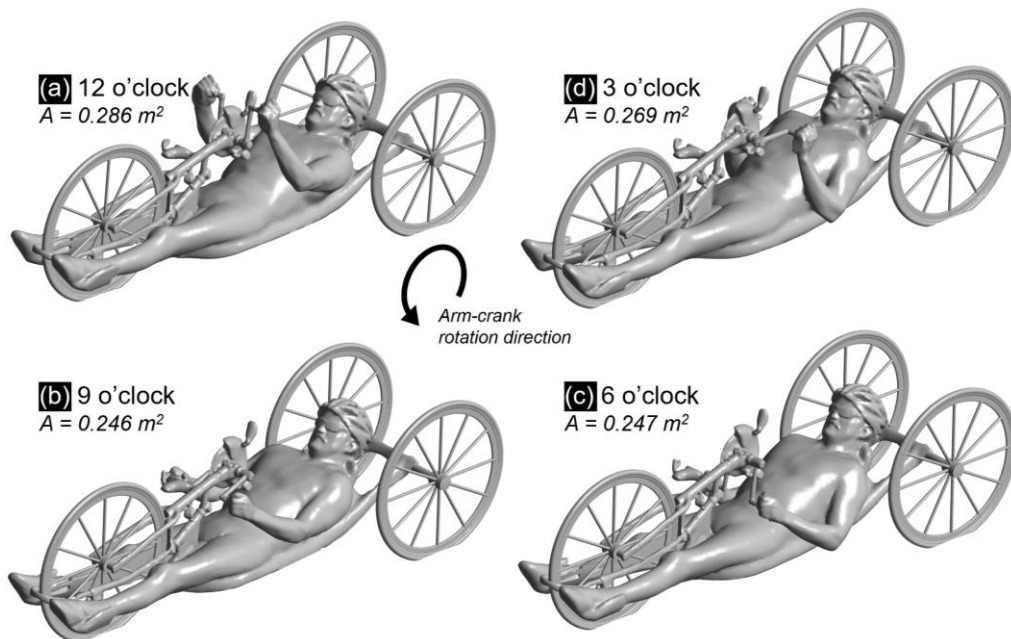


Figure 10.1. Four arm-crank positions of interest, denoted as (a) 12, (b) 9, (c) 6 and (d) 3 o'clock. The projected frontal areas corresponding to each arm-position are included for comparison.

10.2 Validation of CFD simulations with wind tunnel data

10.2.1 CFD simulations: Settings and parameters

A hand-cyclist was 3D scanned (Artec Europe, 2017) in the four arm-crank positions to build the corresponding geometries for the CFD simulations. Informed consent was received from the athlete prior to 3D scanning. The size and shape of the computational domain and the boundary conditions are depicted in Figure 10.2, and followed recommendations by Franke et al., (2007), Tominaga et al., (2008) and (Blocken, 2015) to ensure a low blockage ratio. A uniform inlet velocity of 15 m/s was used with 0.2% turbulence intensity and a 1 m hydraulic diameter. A free-slip wall boundary condition was applied to the lower horizontal surface of the computational domain to prevent boundary layer development upstream of the test geometry, and symmetry condition was applied to both sides and the top surfaces. Zero static gauge pressure was imposed at the outlet. The hand-cyclist surface was modelled as a smooth no-slip wall with zero roughness. Two domain variations were used. The first contained the platform geometry and hand-cyclist support structures from the wind tunnel experiments (Figure 10.2a). The validation simulations that utilised this domain were compared directly to the wind tunnel experiments in section 10.2.2. The second domain (Figure 10.2b) did not contain the platform surface and support structures, and was used for the full-scale simulations discussed in section 10.3.

The 3D RANS equations were solved, in line with previous CFD studies in cycling aerodynamics (Blocken, 2014; Crouch et al., 2017), using ANSYS Fluent 16 (ANSYS Fluent, 2015) and the SST $k-\omega$ (Menter, 1994) turbulence model for closure, which has also been found to be suitable for solo cycling (Defraeye et al., 2010) and tandem cycling (Mannion et al., 2018a, 2018b) aerodynamics. Gradients were computed using the Least Squares Cell Based method (ANSYS Fluent, 2015), and the Coupled algorithm was used for pressure-velocity coupling, with the use of the pseudo-transient solver implicit under-relaxation method; a pseudo time-step size of 0.01 s used, and drag values were averaged over 4000 pseudo-timesteps. Second order pressure interpolation and second order discretisation schemes for momentum, turbulent kinetic energy, and dissipation rate were used.

A grid convergence study was conducted based on three systematically refined tetrahedral grids (coarse, medium, fine). The cell counts for the coarse, medium and fine grids were 10.4, 27.2 and 77.4 million cells, respectively. The Grid Convergence Index (GCI) suggested by Roache (1994, 1997) was calculated for the grids. GCI values of 0.3% and 1.3% were obtained for the fine grid and medium grids respectively.

A second grid independence study was conducted to determine the aerodynamic drag sensitivity to y^* resolution. y^* is defined in equation 10.1. Three prismatic-tetrahedral grids were

created with average y^* values of 0.8, 11 and 43. Deviations of 1.4%, 3.5% and 7.7% in drag were obtained between the CFD results on these grids and the wind-tunnel experiment, indicating that a y^* resolution of 1 or less was required for these hand-cycling simulations. This is in agreement with the findings by Mannion et al. (2018a), who determined that similar grid requirements were required for tandem para-cycling aerodynamics simulation. The formulation for y^* is used opposed to y^+ , due to the advantages of y^* for cycling aerodynamics applications as discussed by Blocken & Toparlar, (2015).

$$y^* = \frac{u^* y_P}{\nu} \quad (10.1)$$

where u^* is the friction velocity [m/s], ν is the kinematic viscosity [m²/s], and y_P is the normal distance from the wall to the centre point P of the first wall-adjacent cell [m].

A final grid was created with 25.7 million cells that balanced the computational effort and accuracy of the medium and coarse grids and attained an average y^* of 0.8. Twenty boundary layers were imposed on the hand-cycle geometry in the tetrahedral-prismatic grid with a first layer cell height of 25 μm and a growth ratio of 1.2, yielding a max y^* value of 2.9, to resolve the thin laminar sublayer at the surface. The surface grid is illustrated in Figure 10.3 for a 12 o'clock arm-crank position, with a focus on the arms (Figure 10.3a), the helmet (Figure 10.3b) and the front wheel surface grids (Figure 10.3c). To provide an accurate comparison to the wind tunnel experiments, the support structures attached to the wheels (required for the wind tunnel experiments) and the plate attached to the scaled model were included in the CFD simulations performed for validation purposes only (section 10.2.2). These support structures were not included in the simulations discussed in the results in section 10.3. A no-slip wall boundary condition was applied to the support structures and plate attached to the hand-cyclist geometry, which were considered smooth with zero roughness. All drag measurements were defined in the axis of the hand-cycle (Figure 10.2) as per the wind tunnel experiments and not with the stream-wise flow direction, where the force transducer was rotated with the hand-cycle geometry for each yaw angle.

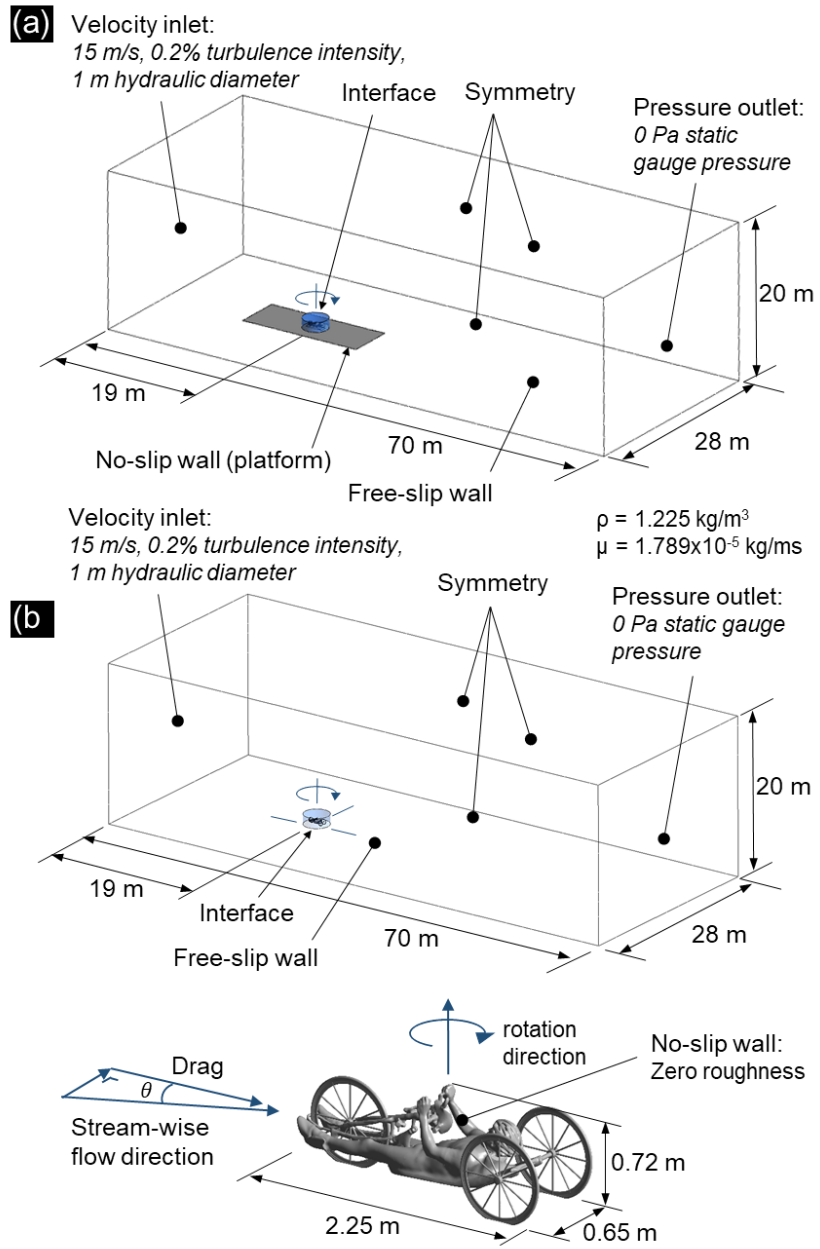


Figure 10.2. The computational domain dimensions, boundary conditions, and general dimensions of the hand-cyclist geometry (full-scale) with (a) the platform and hand-cyclist support structures for comparison to the wind tunnel experiments, and (b) without the platform and support structures. ρ is density and μ is viscosity.

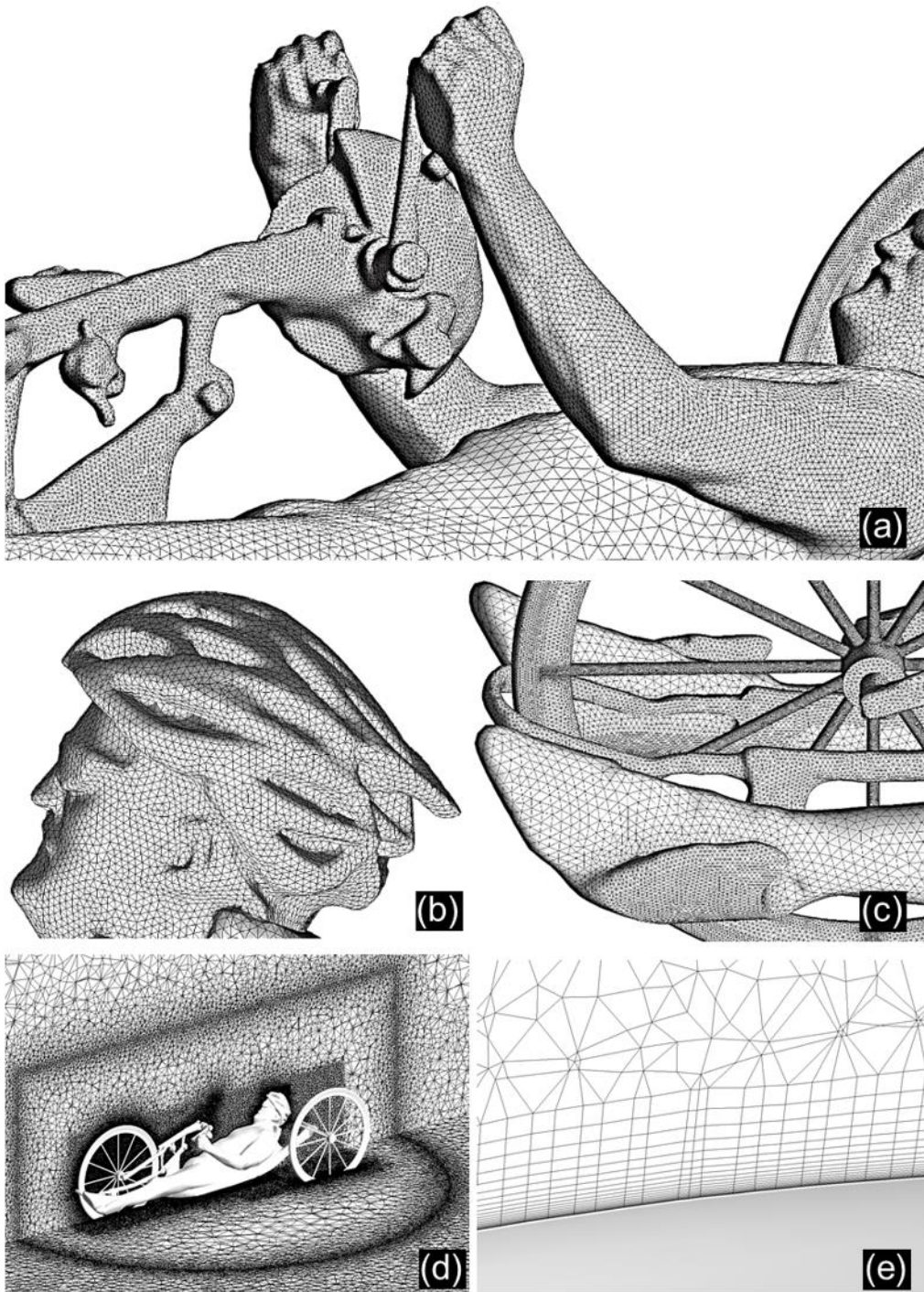


Figure 10.3. Illustration of the surface grid on (a) the athlete's arms (12 o'clock position), (b) head and helmet, and (c) the front wheel (without support structures). (d) The volume grid in vertical and horizontal planes, and (e) the prismatic boundary layer grid. Total number of cells was 28,940,036.

10.2.2 Wind tunnel experiments and comparison with CFD results

Wind tunnel experiments were conducted in the closed-loop aeronautical test section of the wind tunnel laboratory in the University of Liège for yaw angles ranging between 0° and 20° in 5° increments so that the influence of crosswinds could be investigated. The quarter-scale model manufactured based on the 3D scan (with arm-crank position at 6 o'clock) was subjected to a wind tunnel velocity of 60 m/s to provide Reynolds number similarity to the full-scale geometry at 15 m/s in the CFD simulations. The reduced scale model was manufactured from ABS (acrylonitrile butadiene styrene) via CNC (computer numerical control) milling. The physical model was an exact 1:4 scale replica of the digital model and the resulting surface was considered smooth.

A single force transducer was positioned in vertical alignment with the hand-cycle model's centre of gravity for force measurements (Figure 10.4a). A rectangular baseplate (0.56 x 0.16 m) below the hand-cycle geometry acted as the connecting geometry to which the force transducer was attached. The location of the vertical axis of the transducer with respect to the baseplate was 0.285 m from its leading edge and centred laterally. The force transducer used was a six-axis Delta model (ATI, 2018). The force transducer was calibrated prior to testing and had a linear response. In addition, the transducer was certified as compliant with the ISO 9001 standard to ensure performance within stated specifications. The transducer was zeroed in the wind tunnel setup prior to imparting any wind load, and a settling time of 30 s was also provided at full wind load before force measurements were recorded (at 10 Hz for 180 s). The manufacturers of the force transducers reported a conservative maximum error estimate of 1.24 N at a 95% confidence interval, including both random and systematic errors. Additional corrections (via temperature measurements and accounting for atmospheric pressure) were made to the drag measurements to account for the difference in air density between the wind tunnel experiments and the air density (1.225 kg/m^3) used in the CFD simulations. The turbulence intensity of the flow in the wind tunnel was below 0.2% (Blocken et al., 2016).

The quarter-scale hand-cycle model was mounted on a sharp edged horizontal platform, which was elevated 0.3 m from the bottom surface of the wind tunnel test chamber for the purpose of removing the model from the boundary layer at the bed of the wind tunnel and reducing the approach-flow boundary layer height. The platform below the hand-cyclist model was static and its surface was smooth. The approach-flow mean velocity profile above the elevated platform was measured, which revealed a boundary layer of 60 mm above which the profile was constant. The turbulence intensity in the free-stream air was 0.2%. A circular plate was built into the platform flush with the top and bottom surfaces to allow the model to be rotated for crosswind experiments (Figure 10.4a-b). A blockage ratio of 1.8% was calculated for the $2 \times 1.5 \text{ m}^2$ test chamber at 0° , and 2.3% at 20° . Although

the blockage remained relatively low (< 3%), 3D solid blockage corrections from Barlow et al. (1999) were applied to the measured velocity which are applicable for blockage ratios between 1-10%.

For the yaw angles between 0° and 20°, an average deviation in drag force of 3.6% and a maximum deviation of 5.4% (at 10° yaw) was found between the CFD simulation results and wind tunnel experiments. Figure 10.4c compares the CFD and wind tunnel results along with the absolute percentage deviation. The CFD drag forces were within the ±1.24 N error range of the force transducers in the wind tunnel experiment except for 10° yaw, and were considered validated to continue the study with CFD. The Root-Mean-Error (RMS) was used as a statistical indicator to evaluate the differences between the wind tunnel and CFD drag predictions. The following equation was used to calculate the RMS error:

$$\text{RMS Error} = \sqrt{\frac{\sum_{i=1}^x (F_{\text{exp}_i} - F_{\text{sim}_i})^2}{x}} \quad (10.2)$$

where F_{sim} is the force prediction from the simulations, F_{exp} is the force measured from the experiments, and x is the number of yaw angles. An RMS error of 1.0 N was calculated for the CFD drag predictions for the five yaw angles. This indicates the spread of the CFD drag predictions from the experimental data, at an acceptable 4.2% deviation if referenced from the experimental drag at 0° yaw, or 3.6% if referenced from 20° yaw. A trend was found for yaw angles of 5° to 20° where the CFD consistently over-predicted the drag force. At 0° the drag was under-predicted by 1.4%.

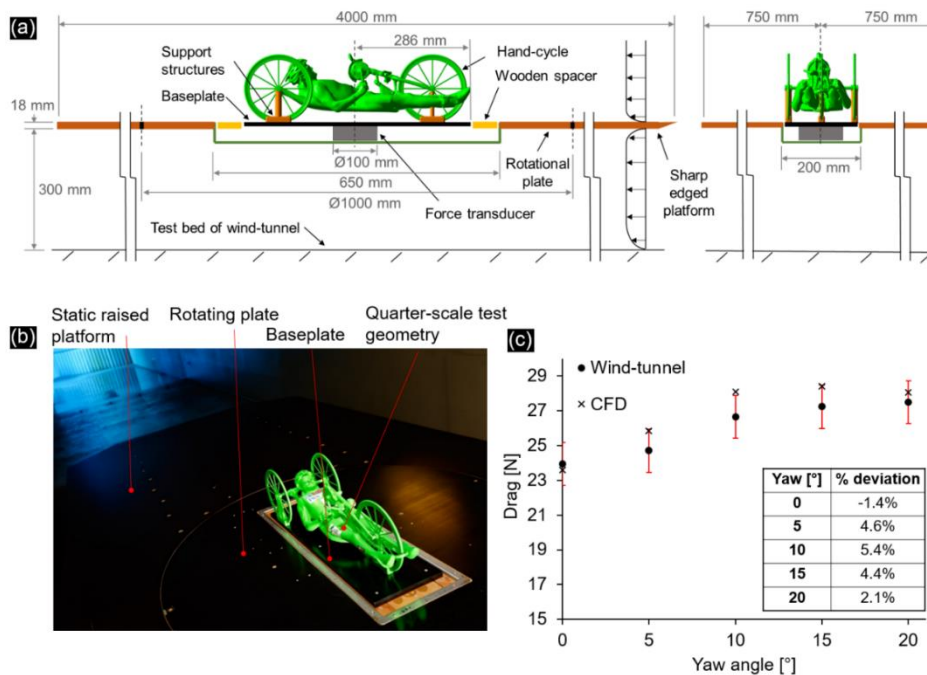


Figure 10.4. (a) Schematic of wind tunnel experiment. (b) Photo of the test geometry in the wind tunnel. (c) Comparison of wind tunnel and CFD drag predictions, at crosswinds ranging from 0°-20° in 5° increments, for a hand-cyclist with arm-crank position at 6 o'clock. The error margin of the wind tunnel measurements (±1.24 N) is indicated with the red error bars.

10.3 Results

The target parameters were the drag area [m²] and the pressure coefficient [-] defined as:

$$C_{DA} = \frac{F_D}{0.5\rho V^2} \quad (10.3)$$

$$C_P = \frac{\Delta P}{0.5\rho V^2} \quad (10.4)$$

where F_D is the drag force [N], ρ the air density [kg/m³], V the freestream velocity [m/s], A the frontal area [m²], and ΔP the difference in local surface pressure with respect to the ambient static pressure [Pa]. The values of A are given in Figure 10.1. All drag predictions were relative to the drag axis of the hand-cycle, and thus, the frontal area remains constant throughout yaw calculations for C_{DA} predictions. The frontal area was acquired from the numerical surface grid of the 3D geometry within the CFD software ANSYS Fluent, to a minimum feature size resolution of 0.00001 m.

Four arm-crank positions, namely 3, 6, 9 and 12 o'clock, were analysed using CFD. The support structures required for the wind tunnel experiments were removed from the computational geometries to provide results more representative of actual hand-cycling aerodynamics. All arm-crank positions followed similar drag area trends throughout the range of yaw angles, with increasing drag between 0°-15° yaw, and decreasing drag between 15°-20° yaw (Figure 10.5). The 9 o'clock position provided the lowest frontal area (Figure 10.1) and also the lowest drag for all yaw angles with a C_{DA} range of 0.155 m² to 0.177 m², (Figure 10.5) and is thus recommended over the other three positions tested during hill descents, to yield the largest aerodynamic advantage. In this position, the forearms were inclined with respect to the oncoming flow at an angle $\alpha = 148^\circ$ relative to the horizontal axis (Figure 10.6e) while the upper-arms (biceps-triceps) were almost parallel to the ground surface. Figure 10. 6a-d illustrates the differences in pressure on the athlete's arms as a result of their orientation. The aerodynamically worst arm-crank positions at 0° yaw were the 3 and 12 o'clock positions, with matching C_{DA} 's of 0.173 m². This was despite the fact that the 3 o'clock position featured a reduced frontal area (0.017 m² lower) when compared to the 12 o'clock position (Figure 10.1). The cause of the drag for the 3 o'clock position was the drag interference between the arms and torso (Figure 10.6b), where high pressure regions were found on the torso in close proximity to the arms. Similar to the 12 o'clock position ($\alpha = 107^\circ$), a large pressure gradient was found over the forearms in the 3 o'clock position ($\alpha = 99^\circ$) in comparison to 6 ($\alpha = 141^\circ$) and 9 o'clock ($\alpha = 148^\circ$) due to their angle α to the horizontal axis (Figures 10.6a, b and e). The forearms of the 12 and 3 o'clock arm-crank positions were increasingly normal to the horizontal axis in comparison to the 6 and 9 o'clock arm-crank positions.

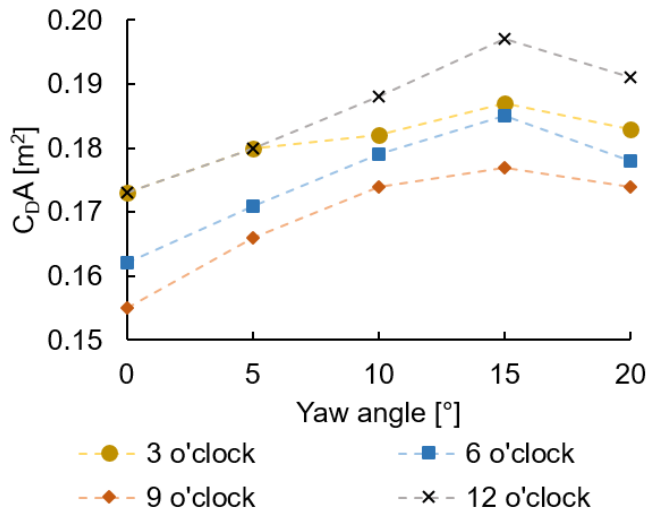


Figure 10.5. Drag area versus yaw angle for each arm-crank position tested.

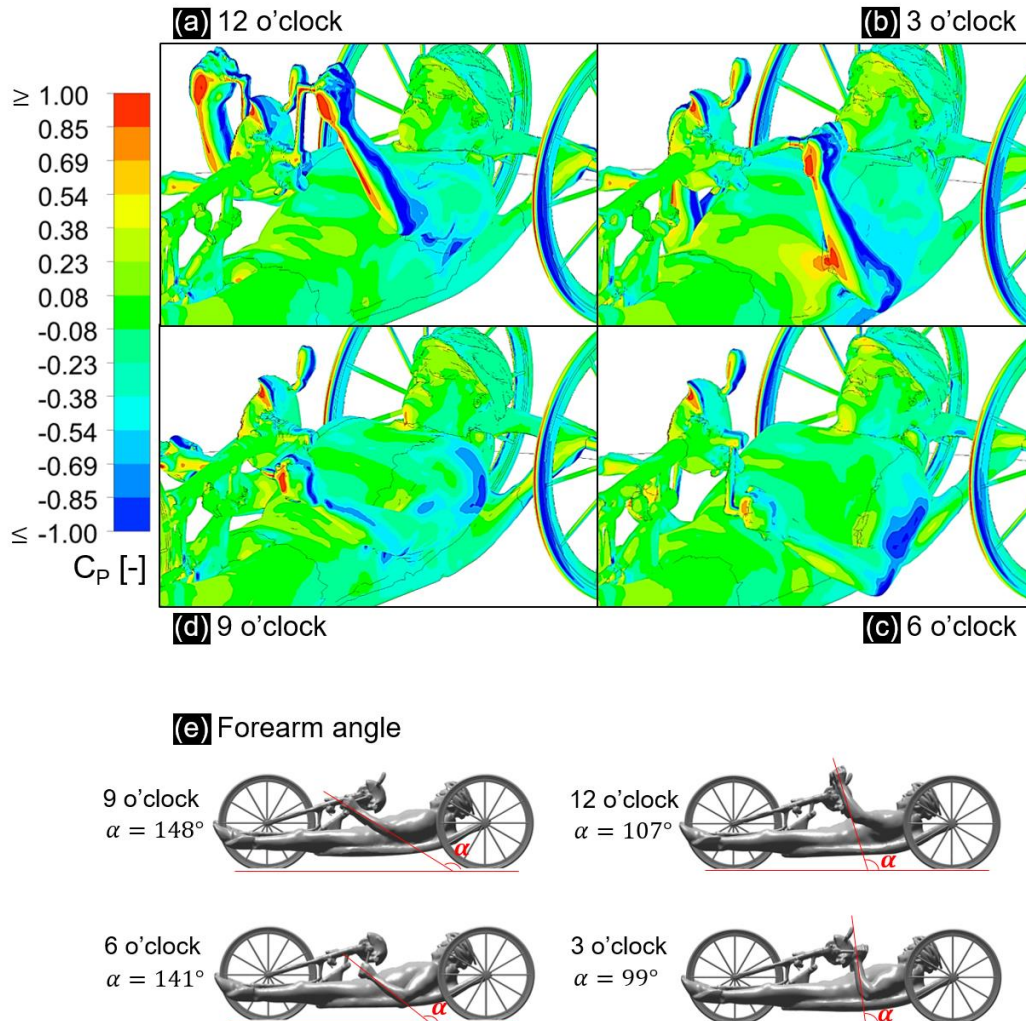


Figure 10.6. Pressure coefficient contours for 0° yaw for: (a) 12 (b) 3 (c) 6 (d) 9 o'clock arm crank positions, (e) the angle α denotes the clockwise angle between the forearm and the ground surface.

Normalised mean velocity contours in a horizontal plane that intersects with the upper arm (bicep-tricep) of the athlete illustrate the interaction of the flow from the forearms to the upper arms, and how it impacted flow separation from the arms of the athlete (Figure 10.7). Figure 6d suggests that flow separation occurred close to the shoulder when the athlete adopts a 9 o'clock position. A steeper angle of the upper arm relative to the horizontal ground plane is present when a 6 o'clock arm-crank position is adopted, resulting in flow separating along the length of the upper arm geometry. Figure 10.7b illustrates the resulting mean velocity fields around the upper arms for the 6 o'clock arm-crank position, showing the direction of the wake flow from the forearms that interacted with the upper arms. While the aerodynamic interaction between the forearms and the upper arms plays a role in the locations of flow separation, the orientation of the arms themselves plays a larger role. When the forearms or upper arms were close to a horizontal position, the flow remained attached along a larger part of the length of the arm. However, if the forearms or upper arms deviate more from a horizontal position, they present a shape similar to a tilted cylinder against the oncoming air, promoting flow separation around the surface of the arms.

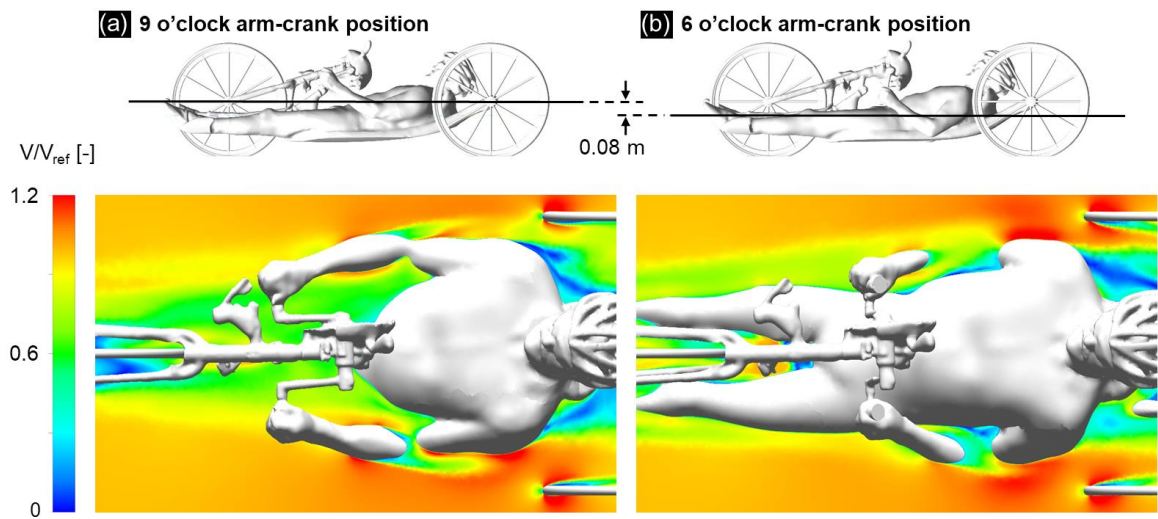


Figure 10.7. Normalised velocity contours in a horizontal plane for (a) the 9 o'clock, and (b) the 6 o'clock arm-crank positions, at 0° yaw.

10.4 Discussion

The 6 o'clock arm-crank position is the commonly adopted arm-crank position for hand-cyclists during hill descents to maximise their aerodynamic efficiency. Results from this study however demonstrated that the 9 o'clock arm-crank position has a lower drag area than the 6 o'clock position for all yaw angles tested. However, an advantage of the 6 o'clock position is that it may

provide respite to the athlete, while the 9 o'clock position might require additional effort to hold. Further research is recommended to quantify the trade-off between energy consumption and aerodynamics for hand-cyclists between holding the 6 and 9 o'clock arm-crank positions.

It is possible to convert the drag area differences to potential seconds saved in the descent phases (without any athlete power output) of race events (Table 1), where adopting the 9 o'clock arm-crank position instead of the 6 o'clock position could prove beneficial. By making a comparison over a descent of 500 m assuming a constant 0° yaw and a 15 m/s reference velocity, adopting the 9 o'clock position instead of the 6 o'clock position could save 0.8 s. On the other hand, compared to the 6 o'clock position, adopting the 12 o'clock and 3 o'clock positions would result in an additional 1.1 s for both positions respectively. The 9 o'clock arm-crank position offers a minimum saving of 0.3 s at 20° and a max of 0.8 s at 0° yaw over the 6 o'clock arm-crank position for a 500 m distance, assuming a reference velocity of 15 m/s for the 6 o'clock position at each yaw angle. The seconds saved or lost that are presented in Table 1 for each arm-crank position assume that the yaw angle is held constant for the 500 m descent. In reality, the land topography and twisting track routes result in a range of yaw angles being experienced over a single descent, particularly longer descents such as 2 km distance. However, if the assumption were made that there were no wind conditions over a 2 km descent where a hand-cyclist would constantly be at $\approx 0^\circ$ yaw, the 9 o'clock arm-crank position would save up to 3.1 s over the 6 o'clock position. These comparisons assume that the athletes are not providing propulsive power during these stages, but remain static in their aerodynamic positions.

Table 10.1. A comparison of time saved (+) or lost (-) against the 6 o'clock arm-crank position at a reference velocity of 15 m/s, for each yaw angle tested over a 500 m distance.

Positions (o'clock)	Yaw angle				
	0°	5°	10°	15°	20°
9	+0.8	+0.5	+0.4	+0.7	+0.3
12	-1.2	-0.9	-0.9	-1.1	-1.3
3	-1.1	-0.9	-0.3	-0.2	-0.5

There are several simplifications associated with the present study. Firstly, only static geometries were considered in the wind tunnel experiments and CFD simulations. In reality, the wheels are rotating along with the athlete's arms as they rotate the crank about its 360° cycle. Secondly, all surfaces on the hand-cycle model were modelled as smooth walls with zero roughness. The surface of the athlete varies in reality, due to skin, hair and the skinsuit. Furthermore, the anthropometry of individual athletes may play a role in the aerodynamics of different arm-crank positions, and this research is limited to a singular athlete.

The numerical simulations were observed to overestimate the drag of the hand-cyclist between 5°-20° yaw. This was primarily attributed to the turbulence modelling within RANS simulations. The SST k- ω (Menter, 1994) turbulence model was used for this research, as it has been found to provide reasonable aerodynamic force predictions in other cycling applications (Defraeye, 2010; Mannion et al., 2018a, 2018b). Mannion et al. (2018c) showed that the Spalart-Allmaras (Spalart & Allmaras, 1992) turbulence model underestimated the drag of a hand-cyclist in yaw conditions by comparison to the SST k- ω . Nevertheless, RANS simulations are inherently limited as they only solve the turbulence statistics.

In reality, the air velocity experienced by a hand-cyclist is a combination of the wind speed (head wind, tail wind or cross wind) and the travelling speed of the hand-cycle. The boundary layer on the raised platform was not representative of a boundary layer experienced by a hand-cyclist in real-world cycling conditions. In reality, the boundary layer on the ground in the approach flow only pertains to the wind speed, not the travelling speed. In the wind tunnel however, the boundary layer on the platform pertains to the combination of wind speed and travelling speed. Although the boundary layer height is only 60 mm, this will cause some differences with reality. Note that the validation process for the numerical simulations accounted for the boundary layer on the platform by including the geometry of the upper-surface of the platform in the simulations as a no-slip wall (Figure 10.2a).

Belloli et al. (2014) performed wind tunnel experiments on “arm powered” (H1-H4 category (UCI, 2017)) and “arm-trunk powered” (H5 category (UCI, 2017)) hand-cyclists in “aerodynamic” positions and “propulsive” phases (Belloli et al., 2014); the aerodynamic position featured a 6 o’clock arm-crank position for the arm powered H1-H4 category hand-cyclist, and the propulsive phase featured the hand-cyclists rotating the cranks. An increase in recorded C_{DA} values (5%) was reported for the H1-H4 category hand-cyclist for the propulsive phase against the aerodynamic position tested at 0° yaw. A coarse comparison can be made between the wind tunnel experiments by Belloli et al. (2014) and the results from this study by averaging the drag found for the four arm-crank positions tested at 0° yaw and comparing to the percentage increase found for the propulsive stage by Belloli et al., (2014). A 2.3% increase was found from the 6 o’clock arm-crank position at 0° yaw to the averaged drag of the four arm-crank positions. In reality, dynamic simulations are required to make a full comparison, with the same ratio of cycling cadence to riding velocity. This is recommended for future research, along with variations to this ratio to determine if it contains a relationship to the aerodynamic drag of the hand-cyclist.

Further research should include additional arm-crank positions for analysis with 15° differences between the positions tested in the 360° arm-crank cycle suggested. Fully dynamic studies of the arm-crank rotation with a temporal resolution small enough to acquire meaningful drag data

over the crank-arm rotation cycle would provide further information. Wind tunnel experiments are ideally suited for this research as they allow for actual athletes to be tested dynamically with no geometric simplifications that are associated with computational research. However, fully dynamic CFD simulations would provide a wealth of flow-field data for the aerodynamics of an arm-crank rotation cycle. Further research could also be conducted on the H5 category (upright) hand-cycle to determine if the aerodynamics of the arm-crank rotation cycle follows a similar, or its own unique trend.

Improving the aerodynamics of the 3 and 12 o'clock arm-crank position could yield net drag savings when the athlete is hand-cycling. A custom designed skinsuit with sleeves that delay flow separation on the athlete's forearms for these arm-crank positions could reduce the net drag of the hand-cyclist. Juhl (2013) showed that the rotational velocity of a hand-cyclist arm-crank reaches its peak between the 3 and 12 o'clock positions, providing further indication that aerodynamic optimisation research for these positions might yield drag savings for the hand-cyclist. In addition, the application of a non-circular chain-ring could have potential aerodynamic benefits for the arm-crank cycle of a hand-cyclist. Juhl (2013) discussed the application of an oval shaped chain ring opposed to a traditional circular ring to improve hand-cyclists race performance by measuring athlete oxygen uptake, however, the aerodynamic implications of a non-concentric shaped chain-ring have not been explored.

10.5 Conclusion

This study utilised CFD simulations validated with wind tunnel experiments to investigate the aerodynamics of four arm-crank positions at yaw angles in 5° increments between 0°-20°. A good agreement was found between the CFD simulations and the wind tunnel experiments for the validation of the 6 o'clock arm-crank position, with a maximum deviation of 5.4% at 10° yaw. Contrary to the common practice among hand-cyclists who maintain a 6 o'clock arm-crank position during descent stages of races, the 9 o'clock arm-crank position was found to have the lowest C_{DA} (m^2) value throughout all the yaw angles tested. Therefore the 9 o'clock arm-crank position can be recommended for hand-cycling races due to its superior aerodynamic performance. Time savings of up to 0.8 s might be possible over a 500 m descent by adopting the 9 o'clock arm-crank position over the 6 o'clock arm-crank position, with a minimum C_{DA} of 0.155 m^2 found at 0° yaw, and a max of 0.177 m^2 at a yaw angle of 15° found for the 9 o'clock position. The 12 o'clock arm-crank position was found to experience the largest drag force recorded, with a max C_{DA} of 0.197 m^2 at 15° yaw. An additional impact to hand-cycling aerodynamics could be made through the optimisation of the arm-

crank rotation cycle via a non-concentric chain-ring, and specialised skin-suit designs focused on the 3 and 12 o'clock arm-crank positions.

10.6 References

- ANSYS Fluent. (2015). ANSYS Fluent theory guide. *Release 16.1 Documentation*. ANSYS Inc.
- Artec Europe. (2017). Artec Eva, 3D Scanners. Retrieved May 22, 2017, from <https://www.artec3d.com/3d-scanner/artec-eva>
- Automation, A. I. (2018). F/T Sensor Delta. Retrieved April 4, 2018, from www.atia.com/app_content/Documents/9230-05-1330.auto.pdf
- Belloli, M., Cheli, F., Bayati, I., Giappino, S., & Robustelli, F. (2014). Handbike aerodynamics: wind tunnel versus track tests. In *The 2014 conference of the International Sports Engineering Association, Procedia Eng.* (Vol. 72, pp. 750–755). Elsevier B.V. <http://doi.org/10.1016/j.proeng.2014.06.127>
- Blocken, B. (2014). 50 years of Computational Wind Engineering: Past, present and future. *Journal of Wind Engineering and Industrial Aerodynamics*, 129, 69–102. <http://doi.org/https://doi.org/10.1016/j.jweia.2014.03.008>
- Blocken, B. (2015). Computational Fluid Dynamics for urban physics: Importance, scales, possibilities, limitations and ten tips and tricks towards accurate and reliable simulations. *Building and Environment*, 91, 219–245. <http://doi.org/10.1016/j.buildenv.2015.02.015>
- Blocken, B., & Toparlak, Y. (2015). A following car influences cyclist drag: CFD simulations and wind tunnel measurements. *Journal of Wind Engineering and Industrial Aerodynamics*, 145(0), 178–186. <https://doi.org/10.1016/j.jweia.2015.06.015>
- Blocken, B., Toparlak, Y., & Andrienne, T. (2016). Aerodynamic benefit for a cyclist by a following motorcycle. *Journal of Wind Engineering and Industrial Aerodynamics*, 155, 1–10. <http://doi.org/https://doi.org/10.1016/j.jweia.2016.04.008>
- Crouch, T. N., Burton, D., Brown, N. a. T., Thompson, M. C., & Sheridan, J. (2014). Flow topology in the wake of a cyclist and its effect on aerodynamic drag. *Journal of Fluid Mechanics*, 748, 5–35. <http://doi.org/10.1017/jfm.2013.678>
- Crouch, T. N., Burton, D., LaBry, Z. A., & Blair, K. B. (2017). Riding against the wind: a review of competition cycling aerodynamics. *Sports Engineering*, 20(2), 81–110. <http://doi.org/10.1007/s12283-017-0234-1>
- Crouch, T. N., Burton, D., Thompson, M. C., Brown, N. A. T., & Sheridan, J. (2016). Dynamic leg-motion and its effect on the aerodynamic performance of cyclists. *Journal of Fluids and*

- Structures*, 65, 121–137. <http://doi.org/10.1016/j.jfluidstructs.2016.05.007>
- Debraux, P., Grappe, F., Manolova, A. V., & Bertucci, W. (2011). Aerodynamic drag in cycling: methods of assessment. *Sports Biomechanics*, 10(3), 197–218. <http://doi.org/10.1080/14763141.2011.592209>
- Defraeye, T., Blocken, B., Koninckx, E., Hespel, P., & Carmeliet, J. (2010). Computational fluid dynamics analysis of cyclist aerodynamics: Performance of different turbulence-modelling and boundary-layer modelling approaches. *Journal of Biomechanics*, 43(12), 2281–2287. <http://doi.org/10.1016/j.jbiomech.2010.04.038>
- Fintelman, D. M., Hemida, H., Sterling, M., & Li, F.-X. (2015). CFD simulations of the flow around a cyclist subjected to crosswinds. *Journal of Wind Engineering and Industrial Aerodynamics*, 144, 31–41. <http://doi.org/10.1016/j.jweia.2015.05.009>
- Franke, J., Hellsten, A., Schlünzen, H., & Carissimo, B. (2010). The best practise guideline for the CFD simulation of flows in the urban environment: an outcome of COST 732. *The Fifth International Symposium on Computational Wind Engineering (CWE2010)*, 1–10.
- Juhl, J. (2013). Non-circular chainring optimization for handcycling. *Journal of Loremipsum*, 1(January), 1–8. <http://doi.org/00.0000/j.jbiomech.2013.08.012>
- Mannion, P., Toparlar, Y., Blocken, B., Hajdukiewicz, M., Andrienne, T., & Clifford, E. (2018a). Improving CFD prediction of drag on Paralympic tandem athletes: Influence of grid resolution and turbulence model. *Sports Engineering*, 21(2), 123–135. <http://doi.org/10.1007/s12283-017-0258-6>
- Mannion, P., Toparlar, Y., Blocken, B., Clifford, E., Andrienne, T., & Hajdukiewicz, M. (2018b). Aerodynamic drag in competitive tandem para-cycling: road race versus time-trial positions. *Journal of Wind Engineering & Industrial Aerodynamics*, 179, 92–101. <https://doi.org/10.1016/j.jweia.2018.05.011>
- Mannion, P., Toparlar, Y., Blocken, B., Clifford, E., Andrienne, T., & Hajdukiewicz, M. (2018c). Analysis of crosswind aerodynamics for competitive hand-cycling. *Journal of Wind Engineering and Industrial Aerodynamics*, 180(August), 182–190. <https://doi.org/10.1016/j.jweia.2018.08.002>
- Menter, F. R. (1994). Two-equation eddy-viscosity turbulence models for engineering applications. *AIAA Journal*, 32(8), 1598–1605. <http://doi.org/10.2514/3.12149>
- Roache, P. J. (1994). Perspective: A method for uniform reporting of grid refinement studies. *Journal of Fluids Engineering*, 116(3), 405–413.
- Roache, P. J. (1997). Quantification of uncertainty in computational fluid dynamics. *Annual Review of Fluid Mechanics*, 29, 123–160. <http://doi.org/10.1146/annurev.fluid.29.1.123>
- Tominaga, Y., Mochida, A., Yoshie, R., Kataoka, H., Nozu, T., Yoshikawa, M., & Shirasawa, T.

- (2008). AIJ guidelines for practical applications of CFD to pedestrian wind environment around buildings. *Journal of Wind Engineering and Industrial Aerodynamics*, 96(10–11), 1749–1761. <http://doi.org/10.1016/j.jweia.2008.02.058>
- Spalart, P., & Allmaras, S. (1992). A one-equation turbulence model for aerodynamic flows. In *30th Aerospace Sciences Meeting and Exhibit*. American Institute of Aeronautics and Astronautics. <https://doi.org/http://doi.org/doi:10.2514/6.1992-439>
- UCI. (2017). Cycling Regulations, Part 16 Para-Cycling, version on 01/02/2017. Union Cycliste Internationale. Retrieved from http://www.uci.ch/mm/Document/News/Rulesandregulation/16/26/73/16-PAR-20170201-E_English.PDF

Discussion and future perspectives

11.1 Discussion

Para-cycling is a growing discipline in competitive cycling. New technologies and new research can enable athletes to push the boundaries on what was previously possible. Aerodynamic resistance is a key challenge for para-cycling that is not yet well researched, by comparison to its able-bodied counterpart. Despite advancements in wind tunnel technologies, on-track testing, and numerical methods such as Computational Fluid Dynamics (CFD), para-cycling aerodynamics was mostly unexplored, with practitioners and stake-holders deriving many of their decisions on aerodynamics from able-bodied sources. This was evident in helmet and wheel choice, postures and positioning, and bicycle/equipment design. Paralympic tandem and hand-cycling were the focus of this research with the aim to narrow the knowledge gap between para and able-bodied cycling aerodynamics. CFD and wind tunnel tests were the tools used for aerodynamic analysis in this thesis, with CFD simulations requiring extensive wind tunnel experiments for validation purposes, while further complementing the wind tunnel data with whole flow-field data to yield new insights into flow phenomena in para-cycling aerodynamics. Part I of the thesis considered tandem cycling aerodynamics, and Part II considered hand-cycling aerodynamics. The main findings are condensed and discussed in this chapter.

Part I – Tandem cycling

The sensitivity to numerical parameters when modelling tandem cycling aerodynamics using CFD was demonstrated in Chapter 3. The aim of this study was to inform practitioners what parameters to use in order to obtain reliable CFD results. It was found that tandem aerodynamics modelling is sensitive to both turbulence modelling and near-wall grid resolution. Novel quarter-scale wind tunnel experiments were key to providing validation data to benchmark the numerical simulations against, by providing individual and simultaneous aerodynamic force measurements for both the pilot and the stoker. It was found that the Shear Stress Transport (SST) $k-\omega$ turbulence model provided the most accurate results by comparison to the wind tunnel experiments at 0° yaw, with drag deviations of 4.0% and 4.2% for the pilot and stoker respectively. It was also found that a well

resolved boundary layer was required to accurately predict aerodynamic forces, with a y^* value of 1 or less recommended. These recommended parameters were in contrast to those commonly used in the literature for able-bodied solo cyclists, where the standard $k-\varepsilon$ turbulence model was found to provide good results for several studies using wall functions opposed to Low Reynolds Numbers Modelling (LRNM) methods to resolve the near-wall flow (Blocken et al., 2016; Blocken & Toparlar, 2015; Fintelman et al., 2015; Griffith et al., 2014; Blocken et al., 2013; Defraeye et al., 2010). It was expected that the standard $k-\varepsilon$ turbulence model would provide reasonable results for tandem cycling, due to the good performance of the turbulence model in the literature for solo cyclists that have similar postures and anthropometrics to a single tandem athlete, and from good results attained in other cycling and drafting related fields such as a following motorcycle and a following car. However, the application of the standard $k-\varepsilon$ turbulence model for tandem cycling resulted in the CFD model incorrectly predicting a greater drag force on the stoker (rear athlete), rather than on the pilot (front athlete). An interesting finding was that there was only an 8% difference in the total $C_D A$ of the tandem between the standard $k-\varepsilon$ and SST $k-\omega$, despite opposite drag distributions on the pilot and stoker. This finding highlighted the importance of breaking down the drag on a tandem (pilot, stoker and bicycle) to look at the aerodynamic forces in a logical manner, ensuring the CFD model is performing as expected. It was determined that the traditional method of only examining the total drag of a cyclist using numerical methods would be a major pitfall for any further research or optimisation studies on tandem cycling. The findings from this research also illustrated the requirement for comprehensive validation of tandem cycling when developing new CFD simulations, and that numerical settings validated for other cycling case studies do not necessarily apply to all cycling categories.

The conclusion made from tandem cycling aerodynamics that validated numerical parameters may not be applicable to all cycling disciplines, was found to be applicable to different scenarios within a single cycling discipline. Crosswind investigations for tandem cyclists revealed that no one turbulence model was suitable for all yaw angles investigated, with the SST $k-\omega$ model providing the most accurate predictions at 0° and 5° yaw, but the $k-kl-\omega$ turbulence model providing better accuracy at 10° , 15° and 20° yaw. This finding would indicate that tandem cycling aerodynamics is a more complicated phenomena than previously anticipated, and that using CFD as a tool for understanding the underlying physics and for aerodynamic optimisation may be a challenging task without a comprehensive suite of validation data. Moreover, the difficulty of aligning the CFD results with experimental data is another difficulty, with numerous parameters to be investigated. It is theorised that higher fidelity transient numerical techniques that allow for boundary layer resolution using low-Reynolds number modelling (LRNM) methods, such as scale adaptive simulation (SAS) or detached eddy simulation (DES), might be useful in attaining a higher level of accuracy. Furthermore, the

transient data that can be acquired from such simulations may yield further insights into the underlying physics of tandem cycling aerodynamics. However, the findings of the present research are useful for practitioners especially where computational resources are a key limitation, and higher fidelity techniques need to be validated in future research before they can be advised.

A first C_{DA} prediction of a range of tandem setups was made in Chapter 5, identifying where athletes may find aerodynamic improvements, and providing a better understanding of the drag forces experienced by the athletes. Solo cyclists were simulated using the athlete geometries from the tandem simulations to provide further insight into how the tandem athletes interact aerodynamically with each other by comparisons to isolated cyclists. Anthropometric bias was removed by using the same athlete for the pilot and stoker positions. A C_{DA} of 0.314 m^2 was observed for a tandem equipped for a road race, with (simplified) spoked wheels and standard road helmets, and with both athletes adopting aggressive dropped (crouched) postures. The equivalent C_{DA} for a solo able-bodied road cyclist in the literature is 0.248 m^2 (Kyle & Burke, 1984). A standard time-trial setup was investigated along with a second time-trial setup termed as the ‘frame-clench’ position which is unique to tandem cycling. The frame-clench setup was found to be the most accurate tandem setup with a C_{DA} of 0.286 m^2 (at 0° yaw), 2.4% less drag than the standard TT setup and 8.9% than the road race setup. It was found that the stoker provided a benefit to the pilot by grasping the frame underneath the saddle of the pilot, and thus “filling” some of the low-pressure volume region behind the pilot. Chapter 6 expanded on the tandem athlete studies by investigating the impact of the torso angle of the pilot and stoker on the aerodynamic drag. It was found that the higher torso angles adopted by the stoker had a larger impact on the total C_{DA} (pilot, stoker and bicycle combined) than that of the pilot. In addition, the lowest C_{DA} was calculated when the pilot adopted a sagittal torso angle of 25° , and the stoker adopted an angle of 20° . When the pilot adopted a larger torso angle than the stoker, the total C_{DA} of the tandem was reduced. It is noted that 20° was the smallest sagittal torso angle investigated due to limitations in positioning two athletes on the tandem bicycle. A hypothesis that aerodynamics are not a limitation to tandem athletes attaining more speed than a solo cyclist was confirmed in chapter 5. Theoretically, a tandem can have two athletes that output twice the power of a solo cyclist, but with reduced aerodynamic penalties for the tandem athletes due to the drafting phenomena from their close proximity. If a tandem and a solo cyclist were both to maintain the same velocity, and given similar anthropometrics of all athletes involved, the two tandem athletes would consume up to 67.4% of the energy a solo rider would be required to expend. This of course, is an idealised scenario, and real world results may vary. However, the increased efficiency regarding aerodynamics and power output from having two athletes on a single bicycle is a useful confirmation of the potential for tandem cyclists, and may push tandem athletes to achieve higher performance in future competitive events.

Computational approaches such as LES/DES have not been used within this research, primarily due to their computational expense, and the acceptable level of accuracy that could be acquired with RANS modelling. Simulations were planned within a limited capacity of computational resources. Upon validating RANS methods for tandem and hand-cycling aerodynamics simulations, it was determined that investigating a larger number of cycling scenarios/variations would yield a larger repository of useful information for stakeholders in para-cycling, than a smaller number of high fidelity LES/DES simulations on a handful of specific scenarios/variations. As the knowledge gap in para-cycling aerodynamics diminishes, high fidelity simulations using LES/DES will undoubtedly be required to further the fundamental understanding of para-cycling aerodynamics, and to find new performance improvements. Solving high Reynolds number flows using LES/DES methods can challenge computational resources, and testing at lower velocities may be an option to maximise the use of available resources. However, Reynolds number similarity between experimental and numerical data remains critical for validation purposes, and it is recommended that this practice is maintained in any future research.

Part II – Hand-cycling

The first hand-cycle aerodynamics investigations in this thesis are described in Chapter 7. Sensitivity studies to numerical parameters were conducted with comparison data from wind tunnel experiments to validate the simulations. Hand-cycling simulations were not found to be as sensitive to turbulence modelling or near-wall grid resolution as tandems at 0° yaw, with y^* values below 10 provided accurate results, along with a choice of the T-SST, $k-kl-\omega$, SST $k-\omega$ and Spalart-Allmaras turbulence models for 0° yaw. The $k-\varepsilon$ based turbulence models did not provide good agreement with the wind tunnel experiments. Both the SST $k-\omega$ and Spalart-Allmaras were also tested under crosswind conditions and provided similar levels of accuracy to each other under the yaw angles tested. While the results of the hand-cycling sensitivity studies held some similarities to the tandem cycling investigations, such as the lesser performance of the $k-\varepsilon$ based turbulence models and the higher accuracy found for low y^* grids, it is not surprising to some extent that modelling hand-cycling aerodynamics using CFD did not present the same difficulties as tandem cycling. The two bluff bodies of the tandem athletes in close proximity to each other presents numerous challenges in resolving the wake flow from the pilot and stoker, flow reattachment and separation, and vortex generation and interactions. Hand-cycling presents a more streamlined silhouette, which could partially explain the good performance found for the Spalart-Allmaras turbulence model which was developed for aerodynamic flows in the aeronautical industry. The reduced sensitivity of hand-cycling aerodynamics to CFD parameters, would allow for CFD to be a valuable tool for aerodynamic

optimisation and design purposes in the hand-cycling industry. It is highly recommended that new hand-cycle designs should be developed with aerodynamics in mind, and that CFD is used in the design process. Furthermore, there is potential for new apparel to be designed with aerodynamics in mind for para-cycling. This includes helmets and skinsuits that are not in the typical orientation found for these items on a traditional cyclist. The flow-field information and level of accuracy that CFD can provide for hand-cycling aerodynamics, as demonstrated by this thesis, is ideally suited to inform design decisions in this regard.

The influence of wheel selection on hand-cycling aerodynamics was investigated with both geometrically simplified static wheel geometries, and also accurate geometrical models of the commercial Zipp 404 deep-section spoked wheel and the Zipp Sub9 disk wheel, with wheel rotation accounted for. However, it is noted that the spokes of the Zipp 404 wheel were removed to reduce computational costs, and were termed as ‘free-spoked’ wheels. The aim of these studies were to determine if a broad definition could be made regarding optimal wheel selection for aerodynamic purposes. I.e. should an athlete use disk wheels or some combination of spoked and disk wheels together? Numerical studies comparing static and geometrically simplified spoked and disk wheel options suggested that using only disk wheels would be preferable to using all spoked wheels. However, to test this in further detail, different wheel combinations were investigated using accurate geometrical representations of commercially available wheels. These combinations were termed as all disk (combination I), all free-spoked (combination II), front free-spoked – rear disk (combination III), and front disk – rear free-spoked (combination IV) wheel combinations. It was found that using combination I was not the most favourable aerodynamic solution overall, against initial expectations. Combination IV provided lower C_{DA} values than the all disk setup, over a yaw range between 0° - 20° and for maximum and minimum rear wheel spacing, indicating clear aerodynamic performance improvement. Furthermore, combination IV resulted in lower lateral forces than wheel combinations that included rear disk wheels, reducing the risk of roll-over. The implications of these findings are that hand-cyclists could potentially corner at higher velocities, thus reducing overall track times. It is noted that these findings were for the specific wheel types tested, which were designed with aerodynamic drag performance in mind. For example, the standard shallow-rim 36 spoke wheels would not be likely to provide better drag performance than disk wheels. The under-performance of using three disk wheels was found to be partly due to the two parallel wheels on the rear axle. A low-pressure region was found to be generated between the two rear disk wheels which accelerated the flow and impacted the hand-cycle frame and athlete surfaces upstream of the rear disk wheels. Larger drag forces were recorded on the athlete and frame surfaces when disk wheels were used due to increased suction, when compared to spoked wheels. These findings on wheel selection are useful for athletes in the H1-H4 hand-cycling categories, as a potentially cost effective means to optimise

aerodynamic performance while also reducing the risk of roll-over in high crosswind conditions and cornering scenarios. A simple change of wheels might lead to significantly improved track times.

It was initially hypothesised that reduced rear wheel spacing would increase the channelling effect between the two wheels, and thus increasing the suction drag on the athlete and hand-cycle frame upstream. However, the opposite was found, with reduced drag for smaller rear wheel spacings (55 cm – 70 cm range) with both disk and spoked wheels. This was attributed to the wheels entering the wake field of the athlete and thus negating the channelling effect. The implications of smaller rear wheel spacings are negative effects on the stability of a hand-cyclist, increasing the risk of roll-over in high-speed cornering. It is advised that athletes consider stability as a priority to aerodynamic optimisation, to reduce the risk of injury. Given specific tracks, and specific wind conditions on the day, minimal rear wheel spacing might be suitable in some competitive events to reduce aerodynamic drag if roll-over is not determined as a viable event.

Furthering the investigations on wheels, the optimal wheel diameter selection for hand-cycling aerodynamics was researched. Combinations of 20-inch and 26-inch diameter wheels were simulated, using a simplified static spoked wheel as the template for the wheel geometry. The pitch angle of the hand-cycle was found to impact the aerodynamic drag from combinations of the aforementioned wheel sizes. A smaller diameter wheel on the front axle coupled with larger wheels on the rear axle negatively impacted the drag of the athlete and hand-cycle frame, while the opposite combination had a positive impact. An overall conclusion was that 20-inch deep-section spoked wheels at minimum spacing on the rear axle, coupled with a 26-inch disk wheel on the front axle, is likely to be the best overall aerodynamic solution regarding wheel choice. However, this conclusion is based off the results presented in the research chapters and is not a product of this specific scenario being simulated, which is recommended for future research. Furthermore, in light of the findings for the aerodynamics of two parallel disk wheels on the rear axle of the hand-cycle, it is not known if two smaller diameter disk wheels would negate the channelling effect found for the larger disk wheels tested in this thesis. Furthermore, smaller rear wheels would lower the centre of gravity of the hand-cyclist, and would likely improve stability and decrease the risk of roll-over. This may reduce the risk of roll-over when smaller rear wheel spacings are implemented, but further research is advised before adopting this approach.

Arm-crank positioning for hand-cycle athletes was investigated in this thesis, for the application of hill-descents and as a means for optimisation accessible for all athlete, both amateur and professional. Clock times were allocated to four primary arm-crank positions viewed from the athletes left side; the 3, 6, 9 and 12 o'clock positions. The 6 o'clock position is often used by hand-cyclists in descent phases of race events due to the perception that the lowest position on the arm-

crank rotation cycle will provide the most aerodynamic solution. It was found that the 9 o'clock position provided a superior aerodynamic result for all yaw angles tested. Reduced flow separation on the forearms and upper arms from the near-horizontal arm positions in the 9 o'clock position was the key factor for this improvement. A gain of 0.8 s over a 500 m descent if athletes adopted the 9 o'clock position over the 6 o'clock position, assuming zero wind conditions. Such gains could be significant in timed events, particularly when applied to time-trials, and are accessible for all athletes.

11.2 Future perspectives

This research investigated tandem and hand-cycling aerodynamics using wind tunnel experiments and CFD simulations. It presents the first known aerodynamics study of tandem cycling in the literature, and the first study of hand-cycling using CFD simulations. However, the scope of para-cycling aerodynamics leaves much left to be explored. Tandem cycling presents a large scope for additional research. To date, there is no evidence of published material on tandem aerodynamics outside of the present research. This research has focused on two identical athletes for the pilot and stoker to remove anthropometric biasing. Within this template for tandem aerodynamics research, there is scope for further research to determine the influence of helmet selection and skin suits. Different helmets and skin suits may be suitable for the pilot and stoker. However, this research should also be extended to include a range of individual athletes with differing anthropometric proportions to provide a broad range of benchmarks useful for practitioners. Moreover, there is scope for new helmet and skin suit designs unique to tandem cycling.

All aerodynamic studies involving athletes can be considered athlete dependent or morphologically dependent to some degree. All athletes are anthropometrically different to some level, and thus, most athletes can be individually optimised for aerodynamics. This applies to hand-cycling and tandem cycling to different degrees. An argument could be made that the aerodynamics of hand-cycling are less 'morpho-dependent' or 'athlete dependent' than traditional solo cycling due to the relatively fixed position of the athlete who lies in a recumbent position. However, the aerodynamics of tandem cycling is considerably more athlete dependent than traditional solo cycling due to two athletes being present on the tandem bicycle. The potential for athlete dependency in tandem cycling, and the resulting applicability of this research, was partially taken into account by using the same athlete for both the pilot and stoker positions. Thus, no drag inferences can be made by citing differences in the anthropometrics of the pilot and stoker. A clear future step in this research,

would be to account for athlete dependency in both hand-cycling and tandem cycling. A large number of athletes could be tested to get statistical indicators of the prevailing aerodynamic drag trends with common anthropometric features. Another example of where this would be of interest, would be the aerodynamic impact of having a pilot or stoker of larger or smaller proportions to the other athlete. Furthermore, changes to postures and positioning also fall under the branch of ‘morpho-dependency’ and should be considered for future research.

Fundamental research with high-fidelity simulation is recommended for tandem cycling using transient methods such as detached eddy simulation (DES), that uses RANS methods to solve near-wall flow and large eddy simulation (LES) to solve the flow outside of the wall bounded regions. The transient information available from such simulations could further the knowledge on the underlying physics of tandem cycling, which would inform further future optimisations. Furthermore, this or other high-fidelity flow methodologies could potentially present a single approach to solving tandem aerodynamics problems using CFD, such as various posture and equipment combinations, racing scenarios, and crosswinds. Given the ever-increasing capabilities of modern computing, it is expected to be feasible to conduct such studies in the near future.

Tandem cycling involves two pairs of synchronised rotating legs. The problem of modelling a single pair of rotating legs for a solo cyclist using CFD has not yet been addressed in the literature, and a tandem bicycle with two athletes increases the difficulty significantly. Overset meshing has shown promise for this potential research endeavour, and has successfully been applied to a cyclist outside of the academia (Beves, 2016). Thus, the application of overset meshing to simulate the rotation of tandem cyclist legs remains feasible. In addition, the same application of overset meshing could be applied to the arm-crank rotation of hand-cycling. Wind tunnel experiments for investigating the effect of rotating legs/arms do not present the same challenge as the computational approach, however, the same degree of information cannot easily be ascertained from the experimental approach. It is difficult to extract drag data from both tandem athletes separately, and not all flow visualisation methods (such as smoke tests) provide the same level of detail available from CFD simulations.

The aerodynamics of rotating wheels is yet to be fully explored within the context of para-cycling, as it has not yet been investigated for para-cycling disciplines outside of hand-cycling. Both wind tunnel and CFD methods are feasible for investigating the effects of rotating wheel aerodynamics on tandem cycling, and perhaps tricycles.

Wheel aerodynamics were found to be a major influential factor for the aerodynamic performance of hand-cycling in this research. However, there are many wheel types yet to be tested, including two-spoke, tri-spoke, bladed spokes, and spoked wheels with various rim depths. The influence of spokes

has only been briefly investigated within this research due to the computational demand associated with modelling the spokes using CFD. There is no clear consensus from athletes/teams on the most aerodynamic wheel setup for hand-cycling, judging from the variation present at competitive events. In addition, there is scope for new wheel designs that are unique to hand-cycling, whether for the front wheel or the two rear wheels. Key improvements would include reducing the extent of the under-pressure region between the two rear wheels, reducing the magnitude of the lateral forces experienced by the three wheels under crosswind conditions, and optimising the aerodynamic interaction of the front and rear wheels in crosswind conditions. Furthermore, some of the findings of this study on H1-H4 category hand-cyclists may be applicable to H5 hand-cyclists and tricycles, which also employ two parallel rear wheels, and this is an open area for further research.

Drafting is also a common occurrence in hand-cycling, with drafting bumpers fitted to hand-cycles to prevent the front wheel of a trailing hand-cyclist from entering between the two rear wheels of a second leading hand-cyclist. However, there has been no study to date to the best knowledge of this author investigating the aerodynamic effects of drafting in hand-cycling, which could influence racing strategy.

The aerodynamics of the H5 competitive hand-cycling category was not explored in this research. The H5 category can be described as an upright position for athletes with less severe loss of function, who can also use their torso to provide power to the crank rotation. In addition, tricycle aerodynamics remains unexplored, along with prosthetics for Paralympic class C cyclists (to the best knowledge of the author). Furthermore, the modelling of athletes and cycles where an athlete is missing one or more limbs has not yet been addressed.

Finally, crosswinds research remains an integral part of cycling aerodynamics research. The present research could be expanded to include smaller increments in yaw angle to determine the absolute angle that maximum drag occurs at for both the pilot and stoker tandem athletes, and for hand-cyclists, for a range of cycling equipment variations.

11.3 References

Beves, C. (2016). *CFD simulation of a pedalling cyclist*. Retrieved from <https://www.linkedin.com/pulse/long-live-revolution-christopher-beves/>

Blocken, B., Defraeye, T., Koninckx, E., Carmeliet, J., & Hespel, P. (2013). CFD simulations of the

aerodynamic drag of two drafting cyclists. *Computers & Fluids*, 71, 435–445.
<http://doi.org/10.1016/j.compfluid.2012.11.012>

Blocken, B., & Toparlar, Y. (2015). A following car influences cyclist drag: CFD simulations and wind tunnel measurements. *Journal of Wind Engineering and Industrial Aerodynamics*, 145(0), 178–186. <http://doi.org/10.1016/j.jweia.2015.06.015>

Blocken, B., Toparlar, Y., & Andrienne, T. (2016). Aerodynamic benefit for a cyclist by a following motorcycle. *Journal of Wind Engineering and Industrial Aerodynamics*, 155, 1–10. <http://doi.org/https://doi.org/10.1016/j.jweia.2016.04.008>

Defraeye, T., Blocken, B., Koninckx, E., Hespel, P., & Carmeliet, J. (2010). Computational fluid dynamics analysis of cyclist aerodynamics: Performance of different turbulence-modelling and boundary-layer modelling approaches. *Journal of Biomechanics*, 43(12), 2281–2287. <https://doi.org/10.1016/j.jbiomech.2010.04.038>

Fintelman, D. M., Hemida, H., Sterling, M., & Li, F.-X. (2015). CFD simulations of the flow around a cyclist subjected to crosswinds. *Journal of Wind Engineering and Industrial Aerodynamics*, 144, 31–41. <http://doi.org/10.1016/j.jweia.2015.05.009>

Griffith, M. D., Crouch, T., Thompson, M. C., Burton, D., & Sheridan, J. (2014). Computational fluid dynamics study of the effect of leg Position on cyclist aerodynamic drag. *The American Society of Mechanical Engineers, Journal of Fluids Engineering*, 136. <http://doi.org/10.1115/1.4027428>

Kyle, C. R., & Burke, E. R. (1984). Improving the racing bicycle. *Mechanical Engineering*, 106(9), 34–45.

Chapter 12

Conclusions

This thesis provides greater understanding to athletes, coaches, sport scientists, and fellow researchers on the underlying physics of tandem and hand-cycling aerodynamics, the optimal athlete positioning and equipment selection for aerodynamic optimisation, and best practice guidelines for CFD simulations concerning tandem and hand-cycling studies. Para-cyclists can realise the velocities that able-bodied cyclists can achieve, and can exceed them in some situations. Hence, aerodynamics optimisation is an important aspect of developing and improving para-cycling performances. An absence of tandem and hand-cycling aerodynamics research was found in the literature, despite the attention received by traditional able-bodied cyclists. Novel wind tunnel experiments coupled with CFD simulations were used for the aerodynamics investigations in this study to provide a well-rounded approach with the whole flow-field data from CFD coupled with the aerodynamic forces from wind tunnel experiments. The main objectives of this research were divided between tandem cycling (Part I) and hand-cycling (Part II), and were as follows:

Part I: Tandem cycling

- Turbulence modelling and near-wall grid resolution sensitivity
- Crosswind considerations
- Aerodynamic analysis of variations in competitive race setups/configurations
- Aerodynamic impact of pilot and stoker torso angles

Part II: Hand-cycling

- Turbulence modelling and near-wall grid resolution sensitivity
- Crosswind considerations
- Optimal wheel selection for aerodynamics
- Aerodynamic impact of arm-crank positioning

Initial research focused on determining suitable methodologies for the CFD modelling of tandem and hand-cycling aerodynamics, instead of relying on the literature of able-bodied solo cyclists. This was due to inconsistent drag findings when utilising different turbulence models and/or grid resolutions for para-cycling applications. Validated CFD simulations were then used in wider comparison studies that included different postures and positioning, cycling equipment, and crosswind scenarios.

The key conclusions from investigating tandem cycling aerodynamics are summarised with the following points:

- The SST $k-\omega$ turbulence model provided the most accurate predictions for tandem cycling at yaw angles of 0° and 5° , and the $k-kl-\omega$ model for yaw angles of 10° , 15° and 20° .
- $K-\varepsilon$ turbulence models and low resolution near-wall grids ($y^* > 30$) incorrectly predicted the stoker to experience more drag than the pilot at 0° yaw.
- Resolving the boundary layer with an appropriate grid was required for accurate results. It is thus recommended to keep the average y^* value below 1.
- At 0° yaw, and inferring no anthropometric bias for the athletes, and with both athletes adopting a relatively aggressive posture (“on the drops”) for a road race event, a C_{DA} of 0.314 m^2 was predicted for the tandem. A maximum C_{DA} of 0.337 m^2 was predicted for the tandem at 15° yaw, and a minimum C_{DA} of 0.305 m^2 was predicted at 20° yaw;
- The drag force was found to be distributed over the pilot, stoker and tandem bicycle by 52%, 27%, and 21% respectively at 0° yaw, and by 39%, 33% and 28% respectively for the maximum drag force recorded at 15° yaw.
- The ‘frame-clench’ setup provided the best aerodynamic performance of the four setups tested; an upright setup, a crouched road race setup, a standard time-trial setup, and the so-called ‘frame-clench’ TT setup where the stoker grasps the tandem frame instead of the bars. A drag saving of 2.4% was found for the frame-clench setup over the traditional TT setup.
- It was found that the position of the stoker influenced the aerodynamics of the pilot. By comparison to isolated cyclists and depending on the posture adopted, the pilot can save up to 15% drag from the stoker, while the stoker can save up to 58% from the pilot.
- Higher torso angles adopted by the stoker were found to be more detrimental to the total drag of the tandem than equivalent torso angles adopted by the pilot, highlighting the importance of ‘shielding’ the stoker in the wake of the pilot. The most advantageous sagittal torso angle combination tested was 25° for the pilot and 20° for the stoker.

The key conclusions from investigating hand-cycling aerodynamics can be summarised as follows:

- Hand-cycling aerodynamics modelling was found to be less sensitive to the choice of turbulence model compared to tandem cycling. A range of turbulence models can provide good results at 0° yaw conditions, most notably of which was the SST $k-\omega$ turbulence model which also provided accurate drag and lateral force predictions in $0^\circ - 20^\circ$ yaw conditions.
- An average y^* value less than 10 can provide good aerodynamic predictions for hand-cycling. However, a y^* less than 1 is recommended for increased accuracy.

- The choice of wheels was found to be a key influencing factor for the drag of a hand-cyclist. The three wheels of a hand-cyclist influence the aerodynamics to a larger degree than the two wheels of traditional able-bodied cycling. This is in part due to the hand-cyclist being within the vertical coordinate of the wheel geometries.
- Using 20-inch as opposed to 26-inch diameter wheels reduced the C_{DA} of the hand-cyclist by 8.9%, primarily through the lower drag experienced by the wheels themselves. Combining a 26-inch front wheel with 20-inch rear wheels also reduced the total drag by 7.0%, by comparison to using only 26-inch wheels.
- An under-pressure region was found between the rear disk wheels on a hand-cycle, increasing suction drag on the athlete and frame surfaces. However, the total drag of the hand-cyclist was found to be lower than when simplified spoked wheels were used, due to the reduction in drag experienced by the wheel themselves.
- Disk wheels were found to have a large impact on the predicted lateral forces, with a drag to lateral force ratio of 1:5.6 for the TT setup with disk wheels at 20° yaw, compared to 1:1.6 for the spoked road setup. The use of disk wheels was found to impact the roll-over moment in crosswind conditions, potentially affecting the safety of the athletes.
- The maximum C_{DA} predicted for hand-cycling setups occurred at 15°. Minimum drag occurred at 0° yaw. This finding was found to hold regardless of the wheel types and wheel combinations used when accurate wheel geometries were modelled, and wheel rotation was accounted for.
- A wheel selection of a front disk wheel coupled with deep dish spoked wheels on the rear axle was found to provide the most favourable aerodynamics throughout the yaw range investigated, balancing low drag with low lateral forces.
- The minimum allowable rear wheel spacing of 55 cm by the UCI was found to reduce the total drag for both spoked and disk wheels in comparison to the maximum allowable spacing of 70 cm. This was due to the wheel geometries entering the wake field of the athlete and hand-cycle frame. However, it is noted that smaller rear wheel spacing could impact the stability of the hand-cyclist and increase the risk of roll-over.
- It was found that the arm crank position of 9 o'clock is preferable to the traditional 6 o'clock position adopted by athletes for hill descents. By using the 9 o'clock position, athletes could save up to 0.8 s over a 500 m descent.

The novel findings of this research highlight the challenges in modelling para-cycling aerodynamics using CFD, and the plethora of ways for optimising tandem and hand-cycling aerodynamics. This research can inform practitioners of the sport on how to approach optimising their aerodynamics, without compromising their safety. Furthermore, it offers a starting platform for

continued research with CFD guidelines, reference values for aerodynamic drag and lateral forces, and recommendations for further research into para-cycling aerodynamics, which is a field rich in potential for imminent investigation.

The numerical simulation of para-cycling aerodynamics contains its own unique difficulties, and numerical parameters should be validated for use in each sub-category, especially in those not considered in this research such as H5 category hand-cycling, tricycles, prosthetics/amputees. Specific validation is also required for different cycling scenarios, such as crosswinds, drafting or overtaking manoeuvres. CFD is a very useful tool for aerodynamics investigations, however, its use is cautioned for tandem cycling, with a high level of care required to determine the validity of the simulations. Tandem cycling, hand-cycling, and other para-disciplines have high potential for further optimisation. It is advised that aerodynamics are considered in the design process for new bicycle, hand-cycles and equipment. CFD guidelines from this research, along with the findings for aerodynamic drag and lateral forces, can be utilised by designers, researchers and practitioners of the sport to inform further developments. On the other hand, practitioners of the sport can also attain useful information for aerodynamic optimisation without the need to buy new bicycles/hand-cycles. For example, this thesis provides information for the postures that tandem athletes should adopt to reduce aerodynamic drag. Similar advice is provided for hand-cycling aerodynamics, to the athlete's arm-crank positioning and wheel choice. By providing insights into the fundamental flow characteristics for typical competitive setups, it is also hoped that this can further fuel aerodynamic optimisation developments through increased understanding of the underlying physics.

About the author

Paul Mannion was born on the 26th of August, 1994. He completed his bachelors of mechanical engineering in 2015, at the National University of Ireland Galway. During his undergraduate degree, he designed the aerodynamic outer bodies of the highly successful GEEC 1.0 & 2.0; Ireland's more energy efficient vehicles. Upon completion of his bachelors, Paul started his dual PhD degree between the National University of Ireland Galway, Ireland, and Eindhoven University of Technology, the Netherlands. During his PhD, he collaborated with Sport Ireland Institute, Cycling Ireland, and Paralympics Ireland. In addition, a key collaboration of the PhD was with KU Leuven and the University of Liège, Belgium. Paul also worked part time with InMotion, on the aerodynamics of their IM01 LeMans prototype.

Paul Mannion has published 8 ISI journal papers, of which 7 as first author, and two peer review conference papers. His conference paper for EACWE 2017 was selected for the special issue with the Journal of Wind Engineering and Industrial Aerodynamics. Paul has also presented at both the 2017 and 2018 Burgers Symposiums as well as contributed to the Gallery of Motion and poster collections at both of these events. Paul is a reviewer for the journals 'Wind Engineering and Industrial Aerodynamics,' 'Sports Engineering,' and 'Disability and Rehabilitation: Assistive Technology.' In addition, he has been invited to and has published two articles with the Engineers Ireland online journal, and Paul has also presented at the Engineers Ireland CPD event on computational fluid dynamics: The role and challenges of Computational Fluid Dynamics in engineering applications. Paul has contributed to extra-curricular academic activities, including designing and delivering a course titled "Engineering in Modern Transport, from car racing to cycling" for the Youth Academy Project in NUI Galway in both 2016 and 2018, and also participated in the 2016 Dutch Design Week 'Mind the Step' exhibition.

Publications and dissemination

Journal papers (published):

- [1] Mannion, P., Toparlar, Y., Blocken, B., Hajdukiewicz, M., Andrianne, T., & Clifford, E. (2018). Improving CFD prediction of drag on Paralympic tandem athletes: Influence of grid resolution and turbulence model. *Sports Engineering*, 21(2) 123-135.
<https://doi.org/10.1007/s12283-017-0258-6>
- [2] Mannion, P., Toparlar, Y., Blocken, B., Clifford, E., Andrianne, T., & Hajdukiewicz, M. (2018). Aerodynamic drag in competitive tandem para-cycling: road race versus time-trial positions. *Journal of Wind Engineering & Industrial Aerodynamics*, 179, 92–101.
<https://doi.org/10.1016/j.jweia.2018.05.011>
- [3] Mannion, P., Toparlar, Y., Blocken, B., Clifford, E., Andrianne, T., & Hajdukiewicz, M. (2018). Analysis of crosswind aerodynamics for competitive hand-cycling. *Journal of Wind Engineering and Industrial Aerodynamics*. 180, 182–190.
<https://doi.org/10.1016/j.jweia.2018.08.002>
- [4] Mannion, P., Toparlar, Y., Clifford, E., Hajdukiewicz, M., Andrianne, T., & Blocken, B. (2019). On the effects of crosswinds in tandem aerodynamics: an experimental and computational study. *European Journal of Mechanics – B/Fluids*. 74, 68-80. <https://doi.org/10.1016/j.euromechflu.2018.11.001>
- [5] Mannion, P., Toparlar, Y., Clifford, E., Hajdukiewicz, M., Andrianne, T., & Blocken, B. (2019). The impact of arm-crank position on the drag of a Paralympic hand-cyclist. *Computer Methods in Biomechanics and Biomedical Engineering*.
<https://doi.org/10.1080/10255842.2018.1558217>

- [6] Mannion, P., Toparlar, Y., Blocken, B., Hajdukiewicz, M., Andrianne, T., & Clifford, E. (2019). Impact of pilot and stoker torso angles in tandem para-cycling aerodynamics. *Sports Engineering*. <https://doi.org/10.1007/s12283-019-0301-x>
- [7] Mannion, P., Toparlar, Y., Clifford, E., Hajdukiewicz, M., Andrianne, T., & Blocken, B. (2019). Aerodynamics analysis of wheel configurations in Paralympic hand-cycling: a computational study. *Journal of Mechanics – B/Fluids*. 76, 50–65. <https://doi.org/10.1016/j.euromechflu.2019.01.011>
- [8] Blocken, B., van Druenen, T. Toparlar, Y., Malizia, F., Mannion, P., Andrianne, T., Marchal, T., Maas, G.J., Diepens, J. (2018). Aerodynamic drag in cycling pelotons: new insights by CFD simulation and wind tunnel testing. *Journal of Wind Engineering and Industrial Aerodynamics*. 179, 319-337. <https://doi.org/10.1016/j.jweia.2018.06.011>

Journal papers (under review):

- [9] Mannion, P., Toparlar, Y., Blocken, B., Hajdukiewicz, M., Andrianne, T., & Clifford, E. (2019). CFD analysis of hand-cycle aerodynamics: turbulence model and grid sensitivity analysis and impact of wheel choice. *Under review*.

Conference papers (in proceedings):

- [1] Mannion, P, Clifford, E, Blocken, B, Hajdukiewicz, M. (2016). Assessing aerodynamic performance in cycling using computational fluid dynamics. *Civil Engineering Research in Ireland (CERI 2016)*. 29th-30th August 2016, Galway, Ireland.
- [2] Mannion, P., Toparlar, Y., Blocken, B., Hajdukiewicz, M., Andrianne, T., Clifford, E. An investigation of tandem cycling aerodynamics. *The 7th European and African Conference on Wind Engineering (EACWE 2017)*. 4th-7th July 2017, Liège, Belgium.

Other publications:

- [1] Mannion, P., Hajdukiewicz, M., Blocken, B., and Clifford, E. (2016). Competitive cycling: pushing the boundaries of engineering. *Engineers Ireland Journal*. March Issue 2016. <http://www.engineersjournal.ie/2016/03/22/competitive-cycling-pushing-the-boundaries-of-engineering/>
- [2] Mannion, P., Clifford, E., Blocken, B., Toparlar, Y., and Hajdukiewicz, M. (2018). Computational fluid dynamics for Para-cycling aerodynamics. *Engineers Ireland Journal*. July Issue 2018. <http://www.engineersjournal.ie/2018/07/10/computational-fluid-dynamics-para-cycling-aerodynamics/>